VOLUME 7 NUMBER 1 2016 ISSN 2218-7987

International Journal of Mathematics and Physics

Al-Farabi Kazakh National University

International Journal of Mathematics and Physics is publishing two numbers in a year by al-Farabi Kazakh National University, al-Farabi ave., 71, 050040, Almaty, the Republic of Kazakhstan
website: http://ijmph.kaznu.kz/

Any inquiry for subscriptions should be send to:
Prof. Tlekkabul Ramazanov, al-Farabi Kazakh National University
al-Farabi ave., 71, 050040, Almaty, the Republic of Kazakhstan
e-mail: Tlekkabul.Ramazanov@kaznu.kz

 Printed in Kazakhstan

Editorial

The most significant scientific achievements are attained through joint efforts of different sciences, mathematics and physics are among them. Therefore publication of the Journal, which shows results of current investigations in the field of mathematics and physics, will allow wider exhibition of scientific problems, tasks and discoveries.

One of the basic goals of the Journal is to promote extensive exchange of information between scientists from all over the world. We propose publishing service for original papers and materials of Mathematical and Physical Conferences (by selection) held in different countries and in the Republic of Kazakhstan.

Creation of the special International Journal of Mathematics and Physics is of great importance because a vast amount of scientists are willing to publish their articles and it will help to widen the geography of future dissemination. We will also be glad to publish papers of scientists from all the continents.

The Journal will publish experimental and theoretical investigations on Mathematics, Physical Technology and Physics. Among the subject emphasized are modern problems of Calculus Mathematics, Algebra and Mathematical Analysis, Differential Equations and Mechanics, Informatics and Mathematical Modeling, Calculus of Approximations and Program Systems, Astronomy and Space Research, Theoretical Physics and Plasma Physics, Chemical Physics and Radio Physics, Thermophysics, Nuclear Physics and Nanotechnology.

The Journal is issued on the base of al-Farabi Kazakh National University. Leading scientists from different countries of the world agreed to join the Editorial Board of the Journal.

The Journal will be published two times a year by al-Farabi Kazakh National University. We hope to receive papers from many laboratories which are interested in applications of the scientific principles of mathematics and physics and are carrying out researches on such subjects as production of new materials or technological problems.

UDC 519.63;519.684;539.87

Abdigaliyeva A.N.

Faculty of Mechanics and Mathematics,
al-Farabi Kazakh National University, Almaty, Kazakhstan
e-mail: abdigalieva_an@mail.ru

Modelling of the turbulent energy decay based on the finite-difference and spectral methods

Abstract: The work deals with the modeling of turbulent energy using finite-difference and spectral methods. Simulation of the turbulent process is based on the filtered three-dimensional unsteady Navier-Stokes equations, for the closure of the main equation the dynamic model is used. The mathematical model is solved numerically, the equation of motion is solved by a finite-difference method, the equation for pressure is solved by spectral method. Also new algorithm for the numerical solution of the Poisson equation for finding pressure is developed. In the results of simulation, the change of turbulent kinetic energy over the time, the integral length scale, the change of longitudinal-transverse correlation functions are obtained, and longitudinal and transverse one-dimensional spectra are defined.
Key words: turbulent energy, finite-difference method, spectral method, Poisson equation, cyclic penta-diagonal scheme.

Introduction

Despite of the large number of works devoted to the modeling of turbulent processes in various fields, modeling of complex transitional and turbulent motions using the tools and applications of modern computer technology, new algorithms and approaches of applied mathematics remains relevant direction for scientists involved in applied research. This is explained by the fact that turbulent flow, characterized by a pronounced nonstationarity and nonlinearity of the processes, the presence of large displacements environment diverse, complex interactions, and dissipation of energy can not be accurately described mathematically. The problem of turbulence is still not solved. A study of turbulent processes necessary in connection with large number of devices, where there is turbulent phenomena and natural processes, where also dominated the chaos. From the standpoint of modern fluid mechanics, turbulence is contained a very useful information for engineering practice.

The main objective of the theory of turbulence - the study of the overall dynamics and the nature of turbulence, i.e. the study of the evolution of large-scale structures and statistical representation of the turbulent motion over the time.

In nature and technology, turbulent motion - is the most common form of the movement of liquids or gases. However, a quite universal and valid method for calculating turbulent flows does not exist. This is due to the complexity of the turbulent flow. Turbulence is caused by instability of laminar flow, and its character is determined by the geometry of the flow. Instability leads to the formation of wavy structures that can absorb energy from the main flow. As the wave is grown, the energy will be transferred to other forms of disturbances due to nonlinear effects, and cause disordered ripple, which is usually regarded as a manifestation of turbulence [1-4].

In this work, we make an attempt for solving this problem by using the large eddy simulation method. The idea is to impose in the phase space the initial condition for the field of velocities that satisfies the condition for continuity. Thus the main spectral equation can not be solved and a given initial condition phase space is translated into the physical space using a Fourier transform. The obtained field of velocities is used as the initial condition for the filtered Navier–Stokes equation. Then, the unsteady three dimensional Navier–Stokes equations are solved to simulate the degeneration of the isotropic turbulence.

The isotropic medium in turbulence undergoes a very rapid homogeneous deformation; then, all the characteristic sizes and any averaged characteristics of turbulence are constant, but variable in time. In

 Printed in Kazakhstan

order to determine turbulent characteristics, it is necessary to numerically model the time variation change in all the parameters and the degeneration of the isotropic turbulence at different Reynolds numbers.

Formulation of the problem

The numerical modeling of the problem is based on the solution of unsteady filtered Navier–Stokes equations with the continuity equation in the Cartesian coordinate system:

$$\begin{cases} \dfrac{\partial \overline{u}_i}{\partial t} + \dfrac{\partial}{\partial x_j}\left(\overline{u}_i \overline{u}_j\right) = -\dfrac{1}{\rho}\dfrac{\partial \overline{p}}{\partial x_i} + \dfrac{1}{\mathrm{Re}}\dfrac{\partial^2 \overline{u}_i}{\partial x_j \partial x_j} - \dfrac{\partial \tau_{ij}}{\partial x_j}, \\ \dfrac{\partial \overline{u}_i}{\partial x_i} = 0, \\ \tau_{ij} = \overline{u_i u_j} - \overline{u}_i \overline{u}_j, \end{cases} \tag{1}$$

where $\overline{u_i}$ – are velocity components, $\overline{p}$ – is the pressure, t – is the time, v – is the kinematic coefficient of viscosity, $\tau_{i,j}$ – is the sub grid tensor responsible for small scale structures to be simulated, i, j – 1, 2, 3.

For modeling the sub grid tensor a viscosity model is used and it is represented as:

$$\tau_{ij} - \frac{\delta_{ij}}{3}\tau_{kk} = -2\nu_T \overline{S}_{ij}, \tag{2}$$

where $\nu_T = C_S \Delta^2 \left(2\overline{S}_{ij}\overline{S}_{ij}\right)^{1/2}$ – is the turbulence viscosity; C_S – is the empirical coefficient; $\Delta = \left(\Delta_i \Delta_j \Delta_k\right)^{1/3}$ – is the width of the grid filter; $\overline{S}_{ij} = \frac{1}{2}\left(\frac{\partial \overline{u}_i}{\partial x_j} + \frac{\partial \overline{u}_j}{\partial x_i}\right)$ – is the value of the tensor of deformation of velocities [5].

Boundary conditions are taken as periodic in all directions. The initial values for each component are assigned as functions dependent on wave numbers in the phase space:

$$E(k) = A \times 12\pi k^m \exp^{-\frac{m}{2}\left(\frac{k}{k_0}\right)^2} \tag{3}$$

where $A = \dfrac{\frac{3}{2}u^2{}_0 m^{(m+1)/2}\sqrt{2}}{12\pi k_0{}^{m+1}(m-1)!!\sqrt{\pi}}$; $E(k)$ – energy spectrum.

For this problem a variation parameter m and the wave number k_0, which determine the type of turbulence, are chosen. In figure 1 for modeling decay of homogenous turbulence k_0 = 10 and m = 8 are taken.

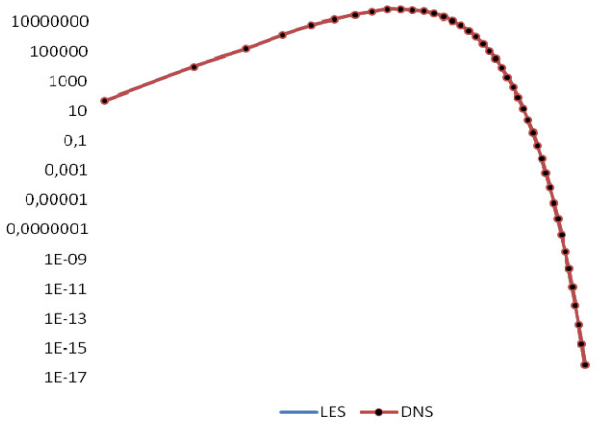

Figure 1 – Energy of the initial level of turbulence based on the fixed wave number k_0 = 10 and power of spectrum m = 8

Numerical method

For solving the Navier–Stokes equation (1), we use a splitting scheme by physical parameters that consist of three stages. At the first stage, the Navier–Stokes equation is solved, without taking pressure into account. For approximation of the convective and diffusion terms of the equation a compact scheme of a fourth order of accuracy $O(t^3, h^4)$ is used. The intermediate field of velocity is found by the fractional step method using the cyclic

penta-diagonal matrix method [5]. At the second stage the Poisson equation is solved, which is satisfies the continuity equation with considering the velocity field from the first stage. Obtained the pressure field is used at the third stage for the recallculate of the final velocity field [6].

To solve the three-dimensional Poisson equation the Fourier transform method, which consists of several steps is used. The resulting intermediate velocity field does not satisfy the continuity equation. The exact expression for the new velocity field is obtained by adding to the intermediate field the term corresponding to the pressure gradient:

$$\overline{u}_1^{n+1} = \overline{u}_1^* - \tau \frac{L_3}{L_1}\frac{\partial p}{\partial x_1}; \tag{4}$$

$$\overline{u}_2^{n+1} = \overline{u}_2^* - \tau \frac{L_3}{L_2}\frac{\partial p}{\partial x_2}; \quad \overline{u}_3^{n+1} = \overline{u}_3^* - \tau \frac{\partial p}{\partial x_3}.$$

Substituting the data in the continuity equation we get:

$$\frac{L_3}{L_1}\frac{\partial \overline{u}_1^*}{\partial x_1} + \frac{L_3}{L_2}\frac{\partial \overline{u}_2^*}{\partial x_2} + \frac{\partial \overline{u}_3^*}{\partial x_3} - \tau\left(\frac{L_3^2}{L_1^2}\frac{\partial^2 p}{\partial x_1^2} + \frac{L_3^2}{L_2^2}\frac{\partial^2 p}{\partial x_2^2} + \frac{\partial^2 p}{\partial x_3^2}\right) = 0. \tag{5}$$

Carrying out the transformation, we obtain the Poisson equation for the pressure field:

$$\frac{L_3^2}{L_1^2}\frac{\partial^2 p}{\partial x_1^2} + \frac{L_3^2}{L_2^2}\frac{\partial^2 p}{\partial x_2^2} + \frac{\partial^2 p}{\partial x_3^2} = \frac{1}{\tau}\left(\frac{L_3}{L_1}\frac{\partial \overline{u}_1^*}{\partial x_1} + \frac{L_3}{L_2}\frac{\partial \overline{u}_2^*}{\partial x_2} + \frac{\partial \overline{u}_3^*}{\partial x_3}\right). \tag{6}$$

The equation for pressure is approximated at the point i, j, k takes the following form:

$$\frac{P_{i+1jk} - 2P_{ijk} + P_{i-1jk}}{\Delta x^2} + \frac{P_{ij+1k} - 2P_{ijk} + P_{ij-1k}}{\Delta y^2} + \frac{P_{ijk+1} - 2P_{ijk} + P_{ijk-1}}{\Delta yz^2} = F_{ijk} \tag{7}$$

$$F_{i,j,k} = \frac{1}{\tau}\left(\frac{L_3}{L_1}\frac{\overline{u}^*_{1\,i+\frac{1}{2},j,k} - \overline{u}^*_{1\,i-\frac{1}{2},j,k}}{\Delta x_1} + \frac{L_3}{L_2}\frac{\overline{u}^*_{2\,i,j+\frac{1}{2},k} - \overline{u}^*_{2\,i,j-\frac{1}{2},k}}{\Delta x_2} + \frac{\overline{u}^*_{3\,i,j,k+\frac{1}{2}} - \overline{u}^*_{3\,i,j,k-\frac{1}{2}}}{\Delta x_3}\right) \tag{8}$$

Pressure P_{ijk} in the physical space goes into the next phase using next dysfunctional:

$$P_{ijk} = \sum_{k_3}\sum_{k_2}\sum_{k_1} \hat{p}(k_1,k_2,k_3) \times e^{\mathrm{I}\left(\frac{2\pi ik_1}{N_1} + \frac{2\pi jk_2}{N_2} + \frac{2\pi kk_3}{N_3}\right)} \tag{9}$$

$$F_{ijk} = \sum_{k_3}\sum_{k_2}\sum_{k_1} \hat{F}(k_1,k_2,k_3) \times e^{\mathrm{I}\left(\frac{2\pi ik_1}{N_1} + \frac{2\pi jk_2}{N_2} + \frac{2\pi kk_3}{N_3}\right)} \tag{10}$$

For the Poisson equation a boundary conditions are taken as periodic. For solving the Poisson equation we use spectral method in combination with Fourier transform. Substituting (9) and (10) expressions in equation (7) and performing transformation we get:

$$\hat{p}(k_1,k_2,k_3)=\frac{\hat{F}(k_1,k_2,k_3)}{2\left[\frac{\cos(\frac{2\pi k_1}{N_1})-1}{dx^2}+\frac{\cos(\frac{2\pi k_2}{N_2})-1}{dy^2}+\frac{\cos(\frac{2\pi k_3}{N_3})-1}{dz^2}\right]}$$

At the final stage the inverse Fourier transform is performed to obtain the solution of the Poisson equation.

Numerical results

As the result of modeling, the characteristics of the isotropic turbulence are defined. According to the semiempirical theory, the integral scale of turbulence grows with time. The calculation was performed in the area of $L_B=2\pi$ at the grid size of 128x128x128 in space, the time step is dt = 0.001, the kinematic viscosity is ν = (2π) u0 / 500, with the dimensionless parameter of Re = 500. Characteristic values of the speed, and time are taken equal: $u_0 = 1$, $T_0=\frac{L_B}{u_0}=1$.

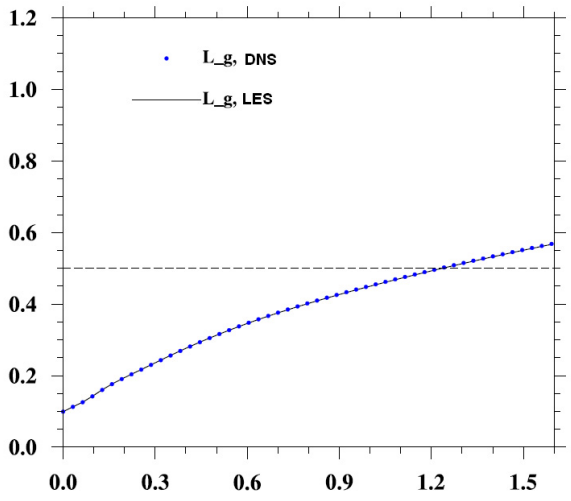

Figure 2 – The changing of integral turbulence scale, calculated at Re = 500, comparison of LES and DNS

In figure 2 results of changing of the integral scale of turbulence over the time, using dimensionless variables *Re* = 500 by simulation LES and DNS are compared. Figure 3 shows the results of the influence of the viscosity on the isotropic turbulence decay of the kinetic energy, calculated in *Re* = 500 and compared with data obtained by the LES. From Figures 2 and 3 can be seen that the integral turbulence on the expiry of the time scale is increased, while the decay of kinetic energy by the time all is rapidly approaching to zero. Also comparing of results LES and DNS has shown that during settlements is not revealed any abnormalities.

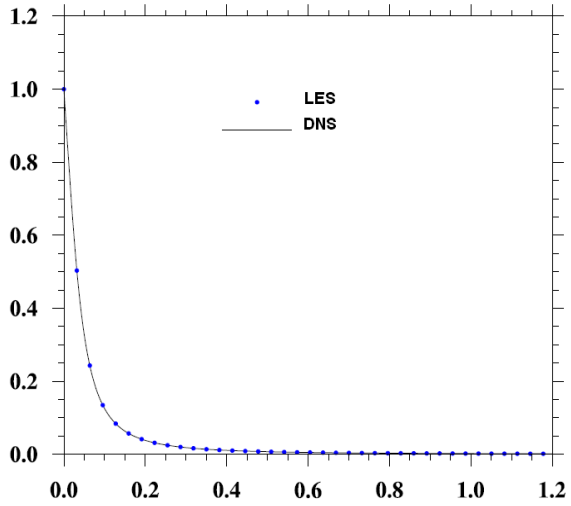

Figure 3 – The changing of turbulent kinetic energy over the time, calculated at Re = 500, comparison of LES and DNS

The correlation coefficients express the average by the volume, a correlation ratio between velocity components at various points. Figure 4 and Figure 5 shows the change of the longitudinal and transverse correlation function *f(r, t)* and *g(r, t)* by the time, calculated at Re = 500. We can see that with the growth of *r* values of functions tends to zero. Comparison of LES and DNS methods of calculation shows that don't occur any significant changes. The changing the longitudinal and transverse dimensional spectrum at different time points is possible to see in figures 6 and 7 respectively.

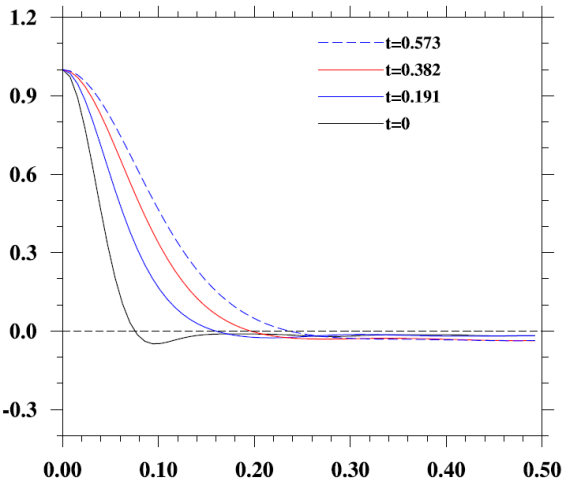

Figure 4 – The changing of longitudinal correlation function *f(r, t)* by the time, calculated at *Re* = 500:
1) *t* = 0.573; 2) *t* = 0.382; 3) *t* = 0.191; 4) *t* = 0

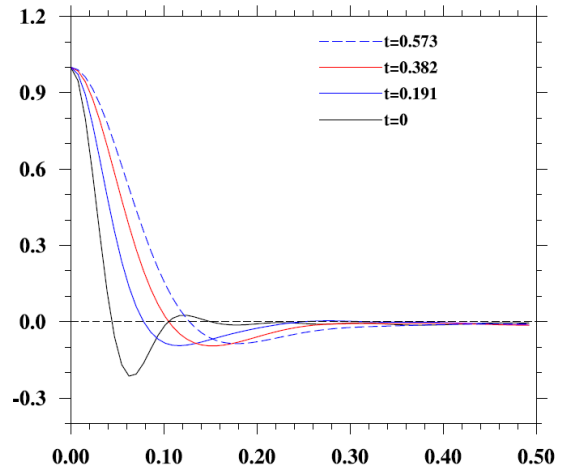

Figure 5 – The changing of transverse correlation function *g(r, t)* over the time, calculated at *Re* = 500:
1) *t* = 0.573; 2) *t* = 0.382; 3) *t* = 0.191; 4) *t* = 0

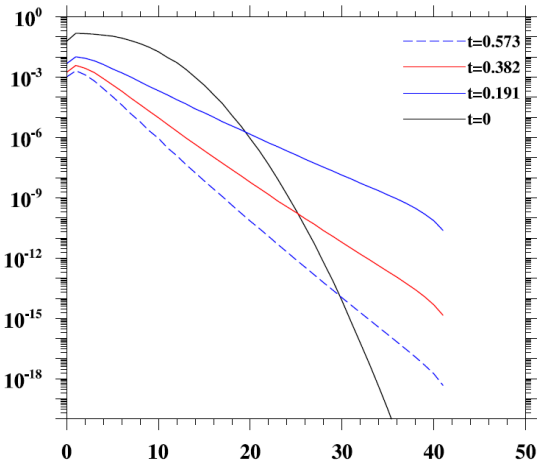

Figure 6 – The changing of a longitudinal one-dimensional spectrum over the time, calculated at *Re* = 500

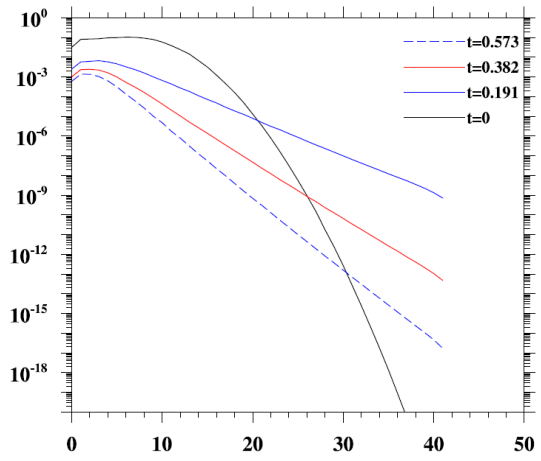

Figure 7 - The changing of a transverse one-dimensional spectrum over the time, calculated at *Re* = 500

Conclusion

In this paper, the numerical simulation of the kinematic viscosity decay the influence on homogeneous isotropic turbulence based on the finite-difference method is considered, and the comparison results with spectral method is shown. The results of numerical modeling, obtained in this paper are fully consistent with results of the authors [7].

Thus, new algorithm for the numerical solution of the Poisson equation for finding pressure is developed. Based on the constructed model the large-scale numerical simulations of isotropic turbulence by LES are carried out and comparison with results of DNS is made. All physical processes and phenomena of homogeneous turbulence are detected in the course of numerical simulation.

References

1. Monin A.S. Yaglom A.M. Statistical Fluid Mechanics, P. 2. – M.: Nauka, 1967. – 720 p.
2. Khintce I.O. Turbulence, its mechanism and theory. – M.: Fizmatgiz, 1963. – 680 p.

3. Ferziger J.H. Large eddy simulation of turbulent flows // AIAA J., 1977. – Vol 15. – No 9. – P. 1261-1267.

4. Sagaut P. Large eddy simulation for incompressible flows. – Heidelberg: Springer-Verl., 2002. – 423 p.

5. Samarskii A.A., Nikolaev E.S. Methods for solving grid equations. – M.: Nauka, 1978. – P. 73-120.

6. Abdibekov U.S., Zhumagulov B.T., Zhakebayev D.B., Zhubat K.Z. Modelling of the decay of isotropic turbulence by the LES // Mathematical Models and Computer Simulations. Springer. – 2013. – Vol. 5. – No 4. – P. 360–370.

7. Wang L.P, Ayala O, Gao H, Andersen C, Mathews K. Study of forced turbulence and its modulation by finite-size solid particles using the lattice Boltzmann approach // Comput. & Math. with Applications. – 2014. – No 67. – P. 363-380.

UDC 53.072; 53:681.3

[1*]Shmygaleva T.A., [2]Shmygalev E.V., [2]Kupchishin A.I.,
[1]Cherykbaeva L.Sh., [1]Temirbekova Zh.E.

[1]Faculty of Mechanics and Mathematics, al-Farabi Kazakh National University, Almaty, Kazakhstan
[2]Kazakh National Pedagogical University named after Abai, Almaty, Kazakhstan
[*]e-mail: shmyg1953@mail.ru

Communication cascade processes with Markov chains

Abstract: The work executed within the framework of cascade-probability method, the essence of which is to obtain and further use of cascade-probability functions (CPF) for the different particles. CPF sense the probability that a particle generated at a certain depth *h'* reaches a certain depth *h* after the *n*-th number of collisions. We have considered the interaction of ions with solids and communication processes of radiation defect with Markov processes and Markov chains. Displaying obtain recurrence relations for the simplest of CPF Chapman-Kolmogorov equations. In this case the particle after the collision does not change its direction of movement, the flow rate is independent of time, and hence the penetration depth. recurrence relations are also obtained for the RAF taking into account losses of energy to the ions of the Chapman-Kolmogorov equation, the intensity of the flow depends on the depth of penetration.
Key words: cascade-probability, ions, defect formation, Markov chain, Markov processes.

Introduction

It should be noted that the previously [1,2] connection issues cascade-probability functions, the energy spectra of primary ejected atoms (PEA), the concentration of defects in C, and the secondary particle fluxes *N*, integral multiplicities and others not considered a Markov process. The study of these relationships it possible to expand their knowledge about the processes taking place in materials when passing through these high-energy particles and a different look at these phenomena, in particular, with common positions. Practically all hitherto obtained analytical expressions for the CPF, the energy spectra of secondary particles and passing *N* and concentration of defects *C* and other can be derived from the Chapman-Kolmogorov equation, set the appropriate physical and mathematical models.

The processes of the passage of particles through a substance and the formation of radiation-induced defects in it can be viewed as a Markov process continuous in time and discrete in the number of collisions. The final expression for ψ, *N* and *C* are represented as sums of integrals and products of the corresponding conditional probabilities and the normalization coefficients, depending on the type and energy of the particles, reaction channels, differential and integral cross sections for interaction, energy loss, the elementary act of the parameters of the medium density, etc..

The main results

Consider the process of interaction of charged particles with matter in the generation of radiation defects in solids irradiated by electrons, protons, alpha particles, and ions.

It is assumed that the primary particle (electron, proton, alpha particle or ion) formed at a depth h' cooperates with the material as follows:

1. The charged particle loses energy by ionization and excitation (the main type of energy loss). These losses are considered to be continuous in the depth of the passage of particles.

2. The primary particles are formed of PEA, and hundreds of interactions with the electrons of the medium (ionization losses) occurs in approximately several interactions on the formation of PEA.

3. PEA forms Frenkel pairs (vacancy and interstitial atom) in the case of electron irradiation and cascading area in the case of the proton, alpha and ion irradiation.

4. For the electron is considered relativistic case, since the kinetic energy of the electrons is comparable to or greater than the energy of the

electrons of peace, interaction cross section is taken in the form of a cross section of the McKinley-Feshbach or Mott, the ionization losses are calculated from the Bethe-Bloch formula.

5. For protons, alpha particles, and ions considered non-relativistic case, the interaction cross section is selected as a section of Rutherford, the ionization losses of protons and alpha particles are calculated from the Bethe-Bloch formula for ions are taken from the table parameters of spatial distribution of the ion-implanted impurities (Kumakhov-Komarova).

Let us consider system *S*, representing process of interaction of particles with matter and tests one, two, three collisions. Such a process is a stochastic process with a discrete number of collisions and continuous in time, and hence the particle penetration depth. The transitions of the system *S* from state to come under the influence of some event streams. As we consider the ordinary event streams without after effects, they are Poisson. If the events form a Poisson flow, the number of events that fall at any time $(t_0, t_0 + \tau)$, the plot has a law of probability distribution [3-5]:

$$\rho_n = \frac{a^n}{n!} e^{-a}, \qquad (1)$$

where a – the mathematical expected number of points falling on the plot:

$$a = \int_{t_0}^{t_0+\tau} \lambda(t) dt, \qquad (2)$$

$\lambda(t)$ – flux density or intensity..

Poisson process is called stationary Poisson or just stream if $\lambda(t) = const$,

At a constant flow rate

$$a = \lambda t. \qquad (3)$$

The distribution in the form of (1) obtained by the outstanding French mathematician of the last century, S.D. Poisson.

In our case, state of the system are connected direct connection with one a sibling item. This scheme is a random process applies to a scheme of pure breeding, the process itself is a process of pure breeding. The set of states is system intransitive, unlocked, terminal, non-performing and non-recurrent state, the end state of the system is absorbing. The interaction of particles with matter is also a Markov process, since all the probabilities in the future depend only on the condition of the process is at the moment and do not depend on the manner in which this process took place in the past. A Markov chain is a kind of Markov process, in which the future depends on the past through the present [3-5].

The process of ion interaction with matter, including solid, as described by a Markov chain as the conditional probability of each event during this test are uniquely determined by the result of the previous state. A Markov chain is completely described by specifying all the possible transition probabilities, which are written in the form of *k*-th order square matrix [3-6].

A Markov chain is a process with discrete state and discrete time, so to go on Markov processes with discrete states and continuous time Markov chains to ask ourselves a sufficiently small interval depths Δh, so small that none of Poisson flows acting on the system, almost could not in the depth interval Δh appear more than events [3,4]. Define for each pair of states (S_i , S_j), between which a transition $S_i \rightarrow S_j$, transition probability $\psi_{ij}(h, \Delta h) = \psi_{ij}(k)$, which corresponds to a penetration depth [3-6]. Suppose that at a certain depth h' at an angle γ to the chosen direction (relative to the perpendicular to the sample surface) generated particle (nucleon, electron, positron, primary line of an atom). We assume that after the collision, it does not change its direction, intensity does not depend on the flow of time, and consequently, the penetration depth, that is

$$\lambda(h) = \lambda = const \qquad (4)$$

In the future, instead of all the time we consider the depth of penetration. Using the well-known equation of the Kolmogorov-Chapman for Markov processes, namely [5]:

$$p_{in}(\tau, t) = \sum_{v} p_{iv}(\tau, s) p_{vn}(s, t), \qquad (5)$$

where $\tau < s < t$, we obtain a recurrence relation for the transition probabilities:

$$\psi_{in}(h',h,\alpha_0)=\sum_{\nu}\psi_{i\nu}(h',h'',\alpha_0)\psi_{\nu n}(h'',h,\alpha_0) \tag{6}$$

But since the process is always continuous in the depth of penetration and a particle at some depth, instead of the amount we have the integral, which is taken over the entire depth of h' to h. Thus, we get the following relations:

$$\psi_n(h',h,\alpha_0)=\int_{h'}^{h}\psi_k(h',h'',\alpha_0)\frac{dh''}{\alpha_0}\psi_{n-k-1}(h'',h,\alpha_0), \tag{7}$$

$$\Psi_n(h',h,\alpha_0)=\int_{h'}^{h}\Psi_{n-k-1}(h',h'',\alpha_0)\frac{dh''}{\alpha_0}\Psi_k(h'',h,\alpha_0),\ k=1\div(n-1). \tag{8}$$

Or in a simpler form:

$$\Psi_n(h',h,\alpha_0)=\int_{h'}^{h}\Psi_0(h',h'',\alpha_0)\Psi_{n-1}(h'',h,\alpha_0)\frac{dh''}{\alpha_0}, \tag{9}$$

$$\psi_n(h',h,\alpha_0)=\int_{h'}^{h}\psi_{n-1}(h',h'',\alpha_0)\psi_0(h'',h,\alpha_0)\frac{dh''}{\alpha_0}, \tag{10}$$

where $\psi_n(h',h,\alpha_0)$ - probability to experience n particle collisions, reaching a depth h - the probability of transition in n steps ; $\alpha_0=\lambda\cos\gamma$; $\psi_{n-1}(h',h'',\alpha_0)$ - probability test particle (n-1) collision - transition probability for (n-1) step; $\psi_0(h'',h,\alpha_0)$ - the probability that the particle will reach a depth of h, without experiencing any impact - the probability of transition for step 1; $\frac{dh''}{\alpha_0}$ - the probability that the particle experiences collision at a depth h''.

In (1) we obtain when n=0, the probability that the particle will reach a depth h, without suffering any collision:

$$\psi_0(h',h,\alpha_0)=e^{-a}=e^{-\frac{h-h'}{\alpha_0}}, \tag{11}$$

where $a=\frac{h-h'}{\alpha_0}$.

Using recursive relation (10) we obtain the probability that the particle will reach a depth h,, experienced with one, two, n for the case of collision, and when λ and θ not changed after collision [1, 2, 7]

$$\psi_n(h',h,\alpha_0)=\left(\frac{h-h'}{\alpha_0}\right)^n\frac{1}{n!}\exp\left(-\frac{h-h'}{\alpha_0}\right). \tag{12}$$

In our case, the Markov chain is not homogeneous, since the transition probabilities ψ_k, $k=0,1,\ldots n$ change at each step the k, the flow rate does not depend on the depth of penetration, that is everything flows, S transform the system from one state to another, are the simplest stationary Poisson. This Markov chain has a stationary mode, because it does not has an ergodic property. The simplest CPF in the extreme case, at $\frac{h-h'}{\alpha_0}=\alpha$, the transition to the Poisson distribution.

Consider the case where after the collision of the particle does not change its direction of movement, the flow rate is time dependent, and consequently the penetration depth, i.e. [8]:

$$\lambda(h)=\frac{1}{\lambda_0}\left(\frac{1}{a(E_0'-kh'')}-1\right). \tag{13}$$

But since the process is always continuous in the depth of penetration and a particle at some depth, instead of the amount we have the integral, which is

taken over the entire depth of h' to h. Thus, we get the following relations:

$$\psi_n(h',h,E_0)=\int_{h'}^{h}\psi_k(h',h'',E_0)\psi_{n-k-1}(h'',h,E_0)\ \frac{1}{\lambda_0}\left(\frac{1}{a(E_0'-kh'')}-1\right)\ \mathrm{dh}'' \ , \tag{14}$$

$$\psi_n(h',h,E_0)=\int_{h'}^{h}\psi_{n-k-1}(h',h'',E_0)\psi_k(h'',h,E_0)\ \frac{1}{\lambda_0}\left(\frac{1}{a(E_0'-kh'')}-1\right)\ \mathrm{dh}'' \tag{15}$$

Or in a simpler form:

$$\psi_n(h',h,E_0)=\int_{h'}^{h}\psi_{n-1}(h',h'',E_0)\psi_0(h'',h,E_0)\frac{1}{\lambda_0}\left(\frac{1}{a(E_0'-kh'')}-1\right)dh'' , \tag{16}$$

where h', h - the depth of the generation and registration of the incident ion, E_0 - the initial ion energy, $\psi_n(h',h,E_0)$ - likely to experience n particle collisions, reaching depth h, $\psi_{n-1}(h',h'',E_0)$ - likely to experience particle n-1 collision, having a depth of h' to h'', $\psi_0(h'',h,E_0)$ - the probability that the particle will reach a depth of h, without experiencing any collisions, λ_0, a, E_0', k – approximation parameters.

Where we have CPF expression in the form of ions [8]:

$$\psi_n(h',h,E_0)=\frac{1}{n!\,\lambda_0{}^n}\left(\frac{E_0-kh'}{E_0-kh}\right)^{-l}\exp\left(\frac{h-h'}{\lambda_0}\right)*\left[\frac{\ln\left(\frac{E_0-kh'}{E_0-kh}\right)}{ak}-(h-h')\right]^n , \tag{17}$$

n - the number of interactions.

The energy spectrum of primary ejected atoms is calculated by the formula [8]:

$$W(E_0,E_2,h)=\sum_{n=n_0}^{n_1}\int_{h-k\lambda_2}^{h}\psi_n(h')\exp\left(-\frac{h-h'}{\lambda_2}\right)\frac{w(E_1,E_2,h')dh'}{\lambda_1(h')\lambda_2} , \tag{19}$$

where $\psi_n(h')$ – cascade-probability function in modified form; λ_1, λ_2 – runs on an ion - atomic and atom – atom collisions, respectively; k – an integer greater than one; n_0, n_1 – initial and final value of the number of interactions in the domain of cascade-probability functions, $w(E_1,E_2,h')$ - CPF range in the elementary act, E_2 – the energy of the primary knock-on atom.

Expression concentration of vacancy clusters under ion irradiation solid-state is given by [8]:

$$C_k(E_0,h)=\int_{E_c}^{E_{2\max}}W(E_0,E_2,h)dE_2 , \tag{20}$$

$E_{2\max}$ – the maximum possible energy to atom.

Formula (19) can also be written as an equation of the Kolmogorov-Chapman, the incident particle is an ion. It is obvious that the interaction of ions with solids, primary education ejected atoms is also described by a Markov chain.

In the expression for the spectrum of primary ejected atoms (19) under the integral contains the product of the probabilities.

Here they are:

$$1.\ \psi_n(h') = \frac{1}{n!\lambda_0^n}\left(\frac{E_0}{E_0 - kh'}\right)^{\frac{1}{\lambda_0 ak}} \exp\left(\frac{h'}{\lambda_0}\right)\left(\frac{\ln\left(\frac{E_0}{E_0 - kh'}\right)}{ak} - h'\right)^n = \psi_{ik}, \qquad (21)$$

ψ_{ik} – the probability that it reaches a depth h' after (n-1) - th collision, provided that the previous event occurred, namely at a certain depth of the primary particle was generated - ion.

2. $w(E_0, E_2, h') = \psi_{km}$ – the conditional probability that the initially-formed line of the atom with the energy E_2 of the ion with the energy E after n-fold impact.

3. $\exp\left(-\frac{h-h'}{\lambda_2}\right)/\lambda_2 = \psi_{ms}$ – the conditional probability that PEA formed at a depth h' of n-fold ion interaction with the substance to reach the depth h.

Spectrum PEA $W(E_0, E_2, h)$ is likely that from the 1st to the energy E_0 of the ion formed a certain number of secondary particles with an energy E_2 at a depth h.

In general, all the functions $\psi_{ik}, \psi_{km}, \psi_{ms}$ are the probabilities for the transition of the Markov chain, respectively, from the i-th state to the k-th; of k-th in the m-th; of m- th to s-th.

Then the Kolmogorov-Chapman equation can be written as follows:

$$\psi_{ij} = \sum_k \sum_m \Psi_{ik} \cdot \Psi_{km} \cdot \Psi_{ms}, \qquad (22)$$

$\psi_{ij} = W$ – probability of transition from i -th state in about j-th.

Since the the system state are continuous at depth, the expression (22) is converted to the following:

$$W(E_0, E_2, h) = \psi_{ij} = \sum_{n=0}^{n_1} \int_0^h \psi_{ik} \cdot \psi_{km} \cdot \psi_{ms} \qquad (23)$$

Markov chains are used in various areas of research. The chemistry of enzymatic activity, the Michaelis-Menten kinetics, may be viewed as a Markov chain, where at each time step, the reaction proceeds in a certain direction. While Michaelis-Menten kinetics is quite simple, much more complex reaction networks can also be modeled using Markov chains [9]. In physics, the growth (and composition) copolymers can be modeled using Markov chains. Based on reactivity ratios of the monomers which constitute the growing polymer chain, the chain structure may be calculated. [10] Markov chains are used in finance and economics, to simulate various phenomena, including asset prices and the collapse of the market [11,12]. In our work shows the relationship of the interaction of particles with matter and radiation defect formation in solids irradiated by ions with Markov chains and Markov processes, ie, Recurrence relations for the cascade-probability functions, expressions for the spectra of primarily sputtered atoms and the concentration of radiation-induced defects of Markov chains. Similarly, we can show the connection between the processes of radiation defect formation in solids irradiated by electrons, protons, alpha particles with Markov processes and Markov chains.

Thus, the particle interaction process with a solid education and radiation defects in solids irradiated by charged particles can be described by Markov chains and Markov processes. Unlike others, our research are used in radiation physics of solids. You can also use Markov chains and Markov processes in space research.

Conclusion

Therefore, it is shown that the particle interaction with matter and the process of formation of radiation defects in solids irradiated with ions, is a Markov chain. In our case, the Markov chain is not homogeneous, since the transition probabilities ψ_k, $k = 0, 1, \ldots n$ change at each step the k, the

intensity of the flow depends on the depth of penetration, that is everything flows, *S* transform the system from one state to the other, are non-stationary Poisson. Conditional probabilities $\psi_0, \psi_1, \psi_2, \psi_3 \ldots \psi_n$ are transition probabilities for inhomogeneous Markov chains, has no steady state. The elementary cascade-probability function does not account for energy losses due to ionization and excitation directly in the process of generating a primary ejected atoms. This Markov chain has a stationary mode, because it does not has an ergodic property.

The paper considers the relationship with Markov chains and Markov processes for models describing particle interactions with matter and the process of formation of radiation defects in the ion irradiation. In the future we plan to use a Markov chain for the cascade-probability functions for unstable particles, mu- mesons, pi- mesons, neutrons, positrons.

References

1. Boss E.G., Kupchyshyn A.I. The solution of physical problems cascaded probabilistic method. – Alma-Ata: Science, 1988. – 112 p.

2. Boss E.G., Kupchyshyn A.I. The solution of physical problems cascaded probabilistic method. – Alma-Ata: Science, 1998. – 144 p.

3. Guter R.S., Ovchinsky B.V. Fundamentals of Probability Theory. – M .: Education , 1967. – 159 p.

4. Kolmogorov A.N. Basic concepts of probability theory. – M .: Science, 1974. – 119 p.

5. Feller W., An Introduction to Probability Theory and Its Applications. – M .: Mir, 1984. – 527 p.

6. Wentzell A.D, Course of the theory of random processes. – M .: Nauka, 1996. – 400 p.

7. Kupchishin A.I Interaction of radiation with matter. Cascaded probabilistic method (methodical development for students of physics and mathematics). – Almaty, 1986. – 68 p.

8. Boos E.G., Kupchishin A.A., Kupchishin A.I., Shmygalev E.V, Shmygaleva T.A.. Cascaded probabilistic method, the solution of the radiation-physical problems, Boltzmann equations. Communication with Markov chains. Monograph. – Almaty.: KazNPU named after Abai, research institutes and KazNU named after Al-Farabi. – 2015. – 388 p.

9. Kutchukian P., Lou D., Shakhnovich E. "FOG: Fragment Optimized Growth Algorithm for the de Novo Generation of Molecules occupying Druglike Chemical" // Journal of Chemical Information and Modeling. – 2009. – Vol. 49, No 7. – P. 1630–1642.

10. Kopp V.S., Kaganer V.M., Schwarzkopf J., Waidick F., Remmele T., Kwasniewski A., Schmidbauer M. "X-ray diffraction from nonperiodic layered structures with correlations: Analytical calculation and experiment on mixed Aurivillius films" // Acta Crystallographica Section a Foundations of Crystallography 68. – 2011. 148.doi:10.1107/S0108767311044874. edit

11. Prasad N.R., Ender R.C., Reilly S.T., Nesgos G. "Allocation of resources on a minimized cost basis" // 1974 IEEE Conference on Decision and Control including the 13th Symposium on Adaptive Processes 13. – 1974. – Vol. 402, No 3.

12. Hamilton J. "A new approach to the economic analysis of nonstationary time series and the business cycle" // Econometrica. – 1989. – Vol. 57, No. 2.

UDC 53.072; 53:681.3

[1*]Shmygaleva T.A., [2]Kupchishin A.I., [2]Shmygalev E.V., [1]Cherykbaeva L.Sh., [1]Temirbekova Zh.E.

[1]Faculty of Mechanics and Mathematics, al-Farabi Kazakh National University, Almaty, Kazakhstan
[2]Kazakh National Pedagogical University named after Abai, Almaty, Kazakhstan
[*]e-mail: shmyg1953@mail.ru

Computer modeling of radiation processes in solids is under ion irradiation

Abstract: The paper deals with the process of ion interaction with matter and the formation of radiation defects. The process of producing the cascade-probability functions (CPF) used further in the calculation of the spectra of primary sputtered atoms (PSA) and the concentration of radiation-induced defects. Presented CPF calculation algorithm is based on the number of interactions and the depth of particle penetration. The models calculate the spectra of primary sputtered atoms and the concentration of radiation defects in materials irradiated by different ions. This takes into account the atomic weight of the incident particle and the target, all options are: atomic weight of the incoming particle is less than the atomic number of the target, the atomic weight of the incoming particle is commensurate with target atomic number, atomic weight of the incoming particle larger atomic number of the target. The regularities of the behavior concentration of radiation defects.
Key words: Radiation defect formation, cascade and probabilistic function, primary beaten-out atom, an ion, the flying particle, a target.

Introduction

The process of ion interaction with matter and their passage through matter is a challenge to create the physical and mathematical models [1]. First of all, this is due to a catastrophic increase in the interaction cross sections of electrons and atoms of the medium. At the same depth of penetration of the ions in the material with increasing mass of the incoming particles decreases dramatically. In calculating the cascade-probability functions in this case it is necessary to use special methods and techniques. Set type of incident particles and the target is a huge amount of items. It is possible to consider various situations when the mass number of incoming ions A^1 smaller mass number of the target A^2, ie, $A_1 < A_2$, a case where A_1 becomes comparable with A_2, and finally completely unique processes, when $A_1 > A_2$. As shown by preliminary analysis, all of these cases be taken into account - in each of them manifest their laws.

In addition, by using a certain kind of projectile particles in concrete material can be formed preassigned structure and chemical compounds is quite stable over a wide temperature range. Naturally, in this and physicochemical properties of these compounds are different from the original. Work in this direction is carried out in the framework of cascade-probability method.

In [1] cascade-probability functions, taking into account the energy loss of electrons, protons and α--particles, performed their mathematical analysis, obtained by the mathematical model for calculating the spectrum of the primary-sputtered atoms (PSA) and the concentration of radiation defects and made their calculations were derived PC. For ions mathematical models of CPF get much more complicated. This is due to the fact that the cross section of interaction calculated by the formula Rutherford large ranges approximately from $n*10^7$ to $n*10^{12}$ (barns), where n - an integer, and running penetration is very small and is approximately $10^{-6} – 10^{-3}$ cm. Fluctuations due to the fact that with increasing atomic number of the element of interaction cross section increases and penetration mileage decreases.

The main results

For ions in contrast to the electrons, protons and α-particle approximation the dependence of the cross section of the energy factor is represented as follows [2]:

$$\sigma(h) = \sigma_0\left(\frac{1}{a(E_0 - kh)} - 1\right), \qquad (1)$$

where σ_0, a, E_0, k - approximation coefficients.

Cascade-probability functions with regard to the ion energy loss can be obtained from the following recurrence relation [2]:

$$\psi_n(h', h, E_0) = \int_{h'}^{h} \psi_{n-1}(h', h'', E_0)\psi_0(h'', h, E_0)\frac{1}{\lambda_0}\left(\frac{1}{a(E_0 - kh'')} - 1\right)dh'' \quad (2)$$

In view of the above obtained recorded mathematical model CP - function energy taking into account the loss of ions in the form [2]

$$\psi_n(h', h, E_0) = \frac{1}{\lambda_0{}^n}\left(\frac{E_0 - kh'}{E_0 - kh}\right)^{-l} \exp\left(\frac{h - h'}{\lambda_0}\right) * \sum_{i=0}^{n} \frac{(-1)^i \ln^{n-i}\left(\frac{E_0 - kh'}{E_0 - kh}\right)(h - h')^i}{i!(n-i)!a^{n-i}k^{n-i}}. \quad (3)$$

Transforming the expression (3), we have

$$\psi_n(h', h, E_0) = \frac{1}{n!\lambda_0{}^n}\left(\frac{E_0 - kh'}{E_0 - kh}\right)^{-l} \exp\left(\frac{h - h'}{\lambda_0}\right) * \left[\frac{\ln\left(\frac{E_0 - kh'}{E_0 - kh}\right)}{ak} - (h - h')\right]^n. \quad (4)$$

Conditional probabilities ψ_0, ψ_1, ψ_2, ... ψ_n are transition probabilities for the Markov chain. When $k \to 0$, or $\alpha \to \infty$, CPF considering the energy loss becomes simple, and, consequently, in the Poisson distribution.

Calculation of cascade-probability functions, taking into account the energy loss of ions, represented by the expression (4), is particularly difficult for large values of the n (which is what we have in fact in most cases).

The following convenient upgraded formula for calculating used for calculating CPF:

$$\psi_n(h', h, E_0) = \exp\left[-\ln(n!) - n * \ln(\lambda_0) - \frac{1}{\lambda_0 ak}\ln\left(\frac{E_0 - kh'}{E_0 - kh}\right) + \frac{h - h'}{\lambda_0} + n * \ln\left(\frac{\ln\left(\frac{E_0 - kh'}{E_0 - kh}\right)}{ak} - (h - h')\right)\right], \quad (5)$$

where n - the number of interactions, h',h - the depth of ion generation and detection, λ_0, a, E_0, k - the parameters of the approximation.

The calculation of the concentration radiation defects under ion irradiation is performed by the formula [3]:

$$C_k(E_0, h) = \int_{E_c}^{E_{2\max}} W(E_0, E_2, h)dE_2, \quad (6)$$

$$E_{2\max} = \frac{4m_1c^2 m_2c^2}{(m_1c^2 + m_2c^2)^2}E_1, \quad (7)$$

m_1c^2 – the rest energy of the ion.

The spectrum of primary sputtered atoms is determined by the following equation [3]:

$$W(E_0, E_2, h) = \sum_{n=n_0}^{n_1} \int_{h-k\lambda_2}^{h} \psi_n(h')\exp\left(-\frac{h - h'}{\lambda_2}\right)\frac{w(E_1, E_2, h')dh'}{\lambda_1(h')\lambda_2}, \quad (8)$$

where n_0, n_1 - initial and final value of the number of interactions in the domain of cascade-probability functions.

Cascade-probability functions $\psi_n(h')$ in expression (8) is as follows

$$\psi_n(h') = \frac{1}{n!\lambda_0^n}\left(\frac{E_0}{E_0 - kh'}\right)^{\frac{1}{\lambda_0 ak}} \exp\left(\frac{h'}{\lambda_0}\right)\left(\frac{\ln\left(\frac{E_0}{E_0 - kh'}\right)}{ak} - h'\right)^n, \quad (9)$$

$$\text{where } \lambda_1(h') = \frac{1}{\sigma_0 n_0\left(\frac{1}{a(E_0 - kh')} - 1\right)} * 10^{24} \text{ (cm)}, \qquad \lambda_2 = \frac{1}{\sigma_2 n_0} * 10^{24} \text{ (cm)}. \quad (10)$$

Cross section σ_2 is calculated by the formula of Rutherford. The spectrum of PSA in the elementary act is calculated by the following formula [3]:

$$\varpi(E_1, E_2) = \frac{d\sigma(E_1, E_2) \Big/ dE_2}{\sigma(E_1)}, \quad (11)$$

$$\frac{d\sigma(E_1, E_2, h)}{dE_2} = 4\pi a_0^2 E_r^2 z_1^2 z_2^2 \frac{1}{E_1 E_2^2} 10^{24} \quad (12)$$

Substituting the expression for $w(E_1, E_2, h')$ in the formula (6), (8) we obtain:

$$C_k(E_0, h) = \frac{E_d E_{2\max}}{E_{2\max} - E_d} \int_{E_c}^{E_{2\max}} \frac{dE_2}{E_2^2} \sum_{n=n_0}^{n_1} \int_{h-k\lambda_2}^{h} \psi_n(h') \exp\left(-\frac{h-h'}{\lambda_2}\right) \frac{dh'}{\lambda_1(h')\lambda_2}. \quad (13)$$

Doing transformation, we arrive at the following expression:

$$C_k(E_0, h) = \frac{E_d}{E_c} \frac{E_{2\max} - E_c}{E_{2\max} - E_d} \sum_{n=n_0}^{n_1} \int_{h-k\lambda_2}^{h} \psi_n(h') \exp\left(-\frac{h-h'}{\lambda_2}\right) \frac{dh'}{\lambda_1(h')\lambda_2}. \quad (14)$$

Calculate the concentration of radiation defects by the formula (14), if we substitute $\psi_n(h')$ its expression in the form (9), it is impossible, as every member of CPF overflow occurs. The expression for $\psi_n(h')$ use in the form (5).

For light incident particles and light curves of targets increases, reaching a maximum and then decreases to zero. With the increase of the initial energy of the particle curves are shifted to the right. With the increase in the concentration of E_c values threshold energy decreases, and the curves are much lower, the transition through a maximum is carried out smoothly. At energies E_0 =100 keV curve decreases. With the increase in atomic weight of the incident particles function value at the maximum point is increased and thus pass above the curves, while the depth value decreases. With increasing atomic number of the target for the same value of a function of the incident particle at the maximum point slightly increased depth value decreases.

The calculation results are shown in Figures and Tables 1.2 to 1.2.

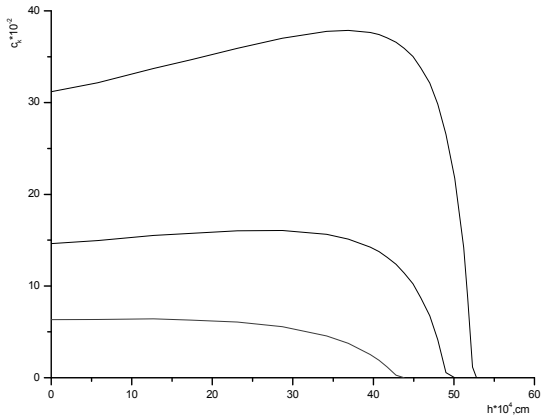

Figure 1 – The dependence of the concentration of radiation defects on the depth under ion irradiation for silver in titanium at E_0= 1000, E_c= 50 (1), 100 (2), 200 (3) keV

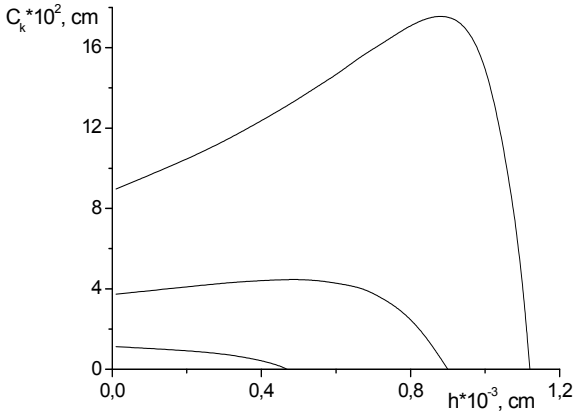

Figure 2 – Dependency of concentration radiation defects of depth by irradiating nitrogen ions, titanium for E_0 = 500 keV, 50 keV E_c = (1), 100 keV (2), 200 keV (3)

Table 1 – The boundaries of the area of determining the concentration of radiation defects in the aluminum titanium at E_c = 50 keV and E_0 = 1000 keV

h*10⁴, cm	**$C_к$, cm**	**E_0, keV**	**n_0**	**n_1**
0,1	3286,5	1000	7	139
1,4	3560,9	900	645	1155
3	3964,6	800	1645	2410
4,5	4419,5	700	2735	3698
6,2	5068	600	4172	5344
7,9	5908,4	500	5882	7260
9,7	7124,1	400	8100	9707
10,6	7910,7	350	9427	11156
11,5	8858,2	300	10951	12811
11,9	9358	280	11707	13628
12,3	9907,8	260	12521	14507
12,7	10513,5	240	13404	15457
13,1	11178,9	220	14365	16490
13,5	11906,1	200	15421	17621
13,9	12689,6	180	16589	18871
14,3	13508,5	160	17898	20268
14,7	14298,7	140	19383	21850
15,2	15536,3	120	21570	24174
15,6	15644,2	100	23691	26421
16	13843,2	80	26303	29183
16,2	11101,2	70	27876	30843
16,4	5544,9	60	29700	32765
16,6	-5926,2	50	31870	35049

Table 2 – The boundaries of the area of determining the concentration of radiation defects in titanium silver for the E_U = 50 keV, E_0 = 800 keV

h*10 ^{4}, cm	$C_к$, cm	E_0, keV	n_0	n_1
0,01	3050,95	800	0	22
0,57	3149,61	700	192	441
1,14	3247,18	600	476	830
1,70	3330,05	500	786	1229
2,25	3379,15	400	1114	1623
2,52	3378,35	350	1284	1835
2,79	3348,35	300	1459	2048
2,90	3324,76	280	1532	2132
3,0	3288,37	260	1599	2213
3,11	3242,87	240	1673	2297
3,21	317,84	220	1742	2367
3,32	3096,25	200	1819	2459
3,42	2983,01	180	1889	2545
3,53	2833,87	160	1967	2626
3,63	2625,95	140	2040	2713
3,73	2323,90	120	2113	2806
3,87	1914,65	100	2216	2922
3,95	1244,71	80	2276	2981
4,0	758,55	70	2314	3055
4,06	102,06	60	2360	3080
4,14	0	50	2421	3156

Conclusion

In work ions interaction process with substance and radiation defects formations is considered. Process receiving the cascade and probabilistic functions (CPF) used further at calculation ranges the primary beaten-out atoms (PBOA) and concentration on radiation defects is described. The calculation algorithm on CPF depending on interactions number and depth on particles penetration is presented. Calculation models on primary beaten-out atoms ranges and radiation concentration defects in the materials irradiated with various ions are developed. Thus the nuclear weight on the flying particle and target is considered, all options are considered: the nuclear weight the flying particle is less than atomic number on a target, the nuclear weight on the flying particle is commensurable with a target atomic number, the nuclear weight on the flying particle is more than a target atomic number. Regularities on concentration behavior on radiation defects are revealed.

References

1. Kupchishin A.A., Kupchishin A.I., Shmygaleva T.A.. Computer modeling of radiation-physical problems. Monograph. – Almaty. Publishing house "Kazakh University". – 2007. – 432 p.

2. Kupchishin A.A., Kupchishin A.I., Shmygaleva T.A. and others. Computer simulation and experimental study of radiative processes in iron and hard alloys. Monograph. – Almaty.: KazNPU named after Abai, FTTS, LLP "KAMA" NIIETF KazNU named after Al-Farabi. – 2010. – 263 p.

3. Boos E.G., Kupchishin A. A., Kupchishin A. I., Shmygalev E. V, Shmygaleva T. A.. Cascaded probabilistic method, the solution of the radiation-physical problems, Boltzmann equations. Communication with Markov chains. Monograph. – Almaty: KazNPU named after Abai, research institutes and KazNU named after Al-Farabi. – 2015. – 388 p.

UDC 517.518

*Embergenova Zh.K., Sikhov M.B.

Faculty of Mechanics and Mathematics,
al-Farabi Kazakh National University, Almaty, Kazakhstan
*e-mail: e_jansaya@mail.ru

Estimates of the best approximations of functions with a spectrum with a given majorant

Abstract: Assessment of the best approximations of functions through its modulus of smoothness (direct theorems of approximation theory or theorems of Jackson type) and of modulus of smoothness through its best approximation in a given metric (inverse theorems of approximation theory or theorems similar to Bernstein's theorem) by orthogonal systems have been the subject of research of many generations of mathematicians. Earlier, inhis research MirbulatSikhov obtained non-removable direct and inverse theorems of approximation theory for various metricsfor trigonometric polynomials with arbitrary spectrum defined by the general form of the majorant function $\Lambda(t)$ under certain conditions of regularity for functions $\Lambda(t)$ .The article presents precise assessment of best approximations by trigonometric polynomials of functions of the Besovclass where the spectrum of the best approximation functions is determined by a majorant function of a special type $\Omega(t)=\prod_{j=1}^{d} t_j^{r}\left(\log\frac{1}{t_j}\right)_{+}^{-\gamma_j}$. The relevance of this topic is determined by the numerical analysis, particularly with the development of computer technology. This topic is naturally linked to the further development of the tasks aiming to estimate the closest approximation of a function, approximation of inequalities of Bernstein and Nikolskiy, and of approximation theory [1-8].
Key words:the best approximation, assessment of the best approximation, modulus of continuity.

Introduction

The basic concepts of approximation theory are the concepts of best approximation and the modulus of continuity that reflect constructive and structural properties of the function, respectively.In one-dimensional case, the relationship between these two fundamentally different characteristics of functions was first established by D. Jackson and S. Bernstein. This problem allows different multidimensional generalizations – depending on the approximation method and on the definition of differences used that generate the corresponding modulus of smoothness. All of these studies are related to the theorems of Jackson and Bernstein (or to the direct and inverse theorems of approximation theory) in the setup of this paper for trigonometric polynomials. The main difficulties encountered in the study of solutions to the problems of this type arethe difficulties in determining the type of the estimation needed, in figuring out how the parameters are estimated, and in showing that they can't be improved.

Let $\pi_d=[-\pi,\pi]^d-d-$ dimensional cube. Let $L^p(\pi_d)$ $(1\le p\le\infty)$ be the set of all measurable 2π periodic functions in each d variable $f(x)=f(x_1,...,x_d)$ such that,

$$\|f\|_p=(2\pi)^{-d}\left(\int_{\pi_d}|f(x)|^p\,dx\right)^{\frac{1}{p}}<\infty,\ 1\le p<\infty$$

$$L_0^p(\pi_d)=\left\{f\in L^p(\pi_d):\int_{-\pi}^{\pi}f(x)dx_j=0(j=1,...,d)\right\}$$

 Printed in Kazakhstan

For a subset B of the Euclidean space R^d denote by B_0 and B_+ the set consisting of all elements of $x=(x_1,x_2,...,x_d)\in B$ where each component is non-negative and positive, respectively. Let Z^d denote R^d integer lattice. For $n\in Z_+^d$ suppose that $\|n\|_1=n_1+...+n_d$, $2^{-n}=\left(2^{-n_1},...,2^{-n_d}\right)$.

For $f\in L^p(\pi_d)$ we can identify a mixed modulus of smoothness of order $k\in Z_+\equiv Z_+^1$

$$\Omega_k(f;t_1,...,t_d)_p=\sup_{\substack{|h_j|\le t_j\\ j=1,...,d}}\left\|\Delta_h^k f(x)\right\|_p\left(t\in[0,1]^d\right),$$

where $\Delta_h^k f(x)=\Delta_{h_d}^k...\Delta_{h_1}^k f(x)$, $\Delta_{h_d}^k=\Delta_{h_j}^1\left(\Delta_{h_j}^{k-1}\right)$,

$$\Delta_{h_j}^1 f(x)=f\left(x_1,...,x_j+h_j,...,x_d\right)-$$
$$-f\left(x_1,...,x_j,...,x_d\right).$$

For these numbers $1\le p<\infty, 0<r_1\le...\le r_d$ Nikolskiy class $SH_p^{r_1,...,r_d}$ by definition consists of all functions $f\in L^p(\pi_d)$ such that for a mixed modulus of smoothness of order

$$k>r_d\ \Omega_k(f;t)_p\le\prod_{j=1}^d t_j^{r_j}$$

holds.

A more precise classification of the functions of smoothness in the metric $L^p(\pi_d)$ consists of the replacementof the function $t_j^{r_j}$ in the definitionbycommon functions such as modulus of smoothness $w_j(t_j)$.

If $f\in L^p(\pi_d)$, then let $E_G(f)_p$ denote the best approximation (on L^p) of the function f with polynomials from *T(G)*, where G – is a finite set of points Z^d, and

$$T(G)=\left\{t(x):t(x)=\sum_{n\in G}c_n e^{i(n,x)}\right\}$$

The spectrum G will be definedon $[0,1]^d$ by a continuous function $\Lambda(t)=\Lambda(t_1,...,t_d)$ that is non-decreasing in each variable and such that $\Lambda(t)>0$ and $\Lambda(t)=0$ depending on whether $\prod_{j=1}^d t_j>0$ or $\prod_{j=1}^d t_j=0$.

By $SB_{q,\theta}^{\Omega}(1\le q<\infty, 0<\theta\le\infty)$ let's denote the space of functions $f\in L_0^q(0,1)^d$, for which the semi normis bounded as is shown below

$$\|f\|_{SB_{q,\theta}^{\Omega}}=\left(\int_{[0,\pi]^d}\left[\Omega_k(f;t)_q/\Omega(t)\right]^\theta\prod_{j=1}^d t_j^{-1}dt\right)^{\frac{1}{\theta}}\le 1$$

For $1<r<l,\gamma_j$ and $t_j\ge 0, j=1,...,d$ let's define the function $\Omega(t)$ as follows: if $t_j>0, j=1,...,d,$ then

$$\Omega(t)=\prod_{j=1}^d t_j^r\left(\log\frac{1}{t_j}\right)_+^{-\gamma_j}$$

$$\text{if}\prod_{j=1}^d t_j=0,\text{then}\,\Omega(t)=0,$$

$$\left(\log\frac{1}{t_j}\right)_+=\max\left\{\log_2\frac{1}{t_j};1\right\}$$

Further, without loss of generality let's assume that $\gamma_1\le...\le\gamma_d$.

Consider the sets

$$\chi(N)=\left\{s=(s_1,...,s_d):s_j\in Z_+, j=1,...,d, \prod_{j=1}^d 2^{rs_j}s_j^{\gamma_j}\le N\right\},$$

$$Q(N)=\bigcup_{s\in\chi(N)}\rho(s),$$

where

$$\rho(s)=\left\{k=(k_1,...,k_d):k_j\in Z,2^{s_j-1}\le|k_j|<2^{s_j},j=1,...,d\right\}$$

Also, consider

$$\Gamma(N,\Omega)=\left\{k=(k_1,...,k_d):|k_j|\in N,j=1,...,d,\Omega\left(\frac{1}{|k_1|},...,\frac{1}{|k_d|}\right)\ge\frac{1}{N}\right\},$$

i.e.

$$\Gamma(N,\Omega)=\left\{k=(k_1,...,k_d):|k_j|\in Z_+,j=1,...,d,\prod_{j=1}^{d}|k_j|^r\left(\log|k_j|\right)_+^{\gamma_j}\le N\right\}$$

$$\Gamma^{\perp}(N,\Omega)=Z_+^s\setminus\Gamma(N,\Omega)$$

For functions of mixed modulus of smoothness let's assume that

$$\theta(\Omega,N)=\Gamma(\Omega,2^lN)-\Gamma(\Omega,N),$$

i.e.

$$\theta(N)=\left\{s=(s_1,...,s_d):s_j\in Z_+,j=1,...,d,N<\prod_{j=1}^{d}2^{rs_j}s_j^{\gamma_j}\le 2^lN\right\}.$$

$A(N)<<B(N)$ means that there exists $C>0$ that does not depend on N such that $A(N)\le CB(N)$.

The functions of one variable $\varphi(\tau)\ge 0$ will satisfy condition (S) if $\varphi(x)/\tau^{\alpha}$ is almost increasing for some $0<\alpha<1$, i.e. there is a number $C>0$ that does not depend on τ_1 and τ_2, such that

$$\frac{\varphi(\tau_1)}{\tau_1^{\alpha}}\le C\frac{\varphi(\tau_2)}{\tau_2^{\alpha}},\ 0<\tau_1\le\tau_2\le 1.$$

To prove our main results we need the following results.

Lemma 1 [2]. Let $\Lambda(t)$ satisfy (S). Then for $0<p<\infty$

$$\sum_{n\in\Gamma^{\perp}(N,\Lambda)}\left(\Lambda\left(2^{-n}\right)\right)^p<<\sum_{n\in\theta(N,\Lambda)}\left(\Lambda\left(2^{-n}\right)\right)^p$$

Lemma 2 [2]. Let $\Lambda(t)$ satisfy (S) for $0<\alpha<1$ such that $\alpha>\beta>0$. Then for $0<p<\infty$

$$\sum_{n\in\Gamma^{\perp}(N,\Lambda)}\left(\Lambda\left(2^{-n}\right)2^{\|n\|_1\beta}\right)^p<<\sum_{n\in\theta(N,\Lambda)}\left(\Lambda\left(2^{-n}\right)2^{\|n\|_1\beta}\right)^p$$

Lemma 3 [6].For $n\in\theta(N)$ the following holds

$$2^{\|n\|_1}\asymp N^{1/r}\prod_{j=1}^{d}n_j^{-\gamma_j/r}$$

Lemma 4 [7].The following sum

$$\sum_{n\in\theta(N)}\prod_{j=1}^{d} n_j^{-\gamma_j}, \qquad \gamma_1 \le \ldots \le \gamma_d$$

is equal to:

1) $(\log N)^{d-1-\gamma_1-\ldots-\gamma_d}$, if $\gamma_d < 1$;

2) $(\log N)^{\nu-1-\gamma_1-\ldots-\gamma_d}(\log\log N)^{\nu-1}$, if $\gamma_\nu < 1 = \gamma_{\nu+1} = \ldots = \gamma_{\nu+\mu} < \gamma_{\nu+\mu+1}$;

3) $(\log N)^{-1}(\log\log N)^{\nu-1}$, if $\gamma_1 = \ldots = \gamma_\nu = 1 < \gamma_{\nu+1}$;

4) $(\log N)^{-\nu_1}$, if $1 < \nu_1$.

Mirbulat Sikhov previously proved the following theorems:

Theorem 1 [8]. Let $1 < p < q < \infty, 1 \le \theta \le \infty$ and $\Lambda(t)-$ be the function of mixed modulus of smoothness of order k. If $f(x) \in SB^{\Lambda}_{p.\theta}$ and

$$\sum_{n\in Z_+^d}\left[2^{\|n\|_1\left(\frac{1}{p}-\frac{1}{q}\right)}\Lambda\left(2^{-n}\right)\right]^{\rho} < \infty$$

where $\rho = \dfrac{\theta q}{\theta - q}$ for $q < \theta$ and $\rho = \infty$ where $q \ge \theta$, then $f(x) \in L_0^q(\pi_s)$ and

$$\|f(x)\|_q << \left(\sum_{n\in Z_+^d}\left[2^{\|n\|_1\left(\frac{1}{p}-\frac{1}{q}\right)}\Lambda\left(2^{-n}\right)\right]^{\rho}\right)^{\frac{1}{\rho}},$$

$$E_{Q(N,\Lambda)}(f)_q << \left(\sum_{n\in\Gamma^{\perp}(N,\Lambda)}\left[2^{\|n\|_1\left(\frac{1}{p}-\frac{1}{q}\right)}\Lambda\left(2^{-n}\right)\right]^{\rho}\right)^{\frac{1}{\rho}}$$

Theorem 2 [8]. Let $1 < p < q < \infty, 1 \le \theta \le \infty$ and $\Lambda(t)-$ be the function of mixed modulus of smoothness of order k .If $f(x) \in SB^{\Lambda}_{p.\theta}$, then the following inequality holds

$$E_{Q(N,\Lambda)}(f)_q << \left(\sum_{n\in\Gamma^{\perp}(N,\Lambda)}\left(\Lambda\left(2^{-n}\right)\right)^{\rho}\right)^{\frac{1}{\rho}}$$

where $\rho = \dfrac{\theta p_0}{\theta - p_0}$ for $p_0 < \theta$ and $\rho = \infty$ for $p_0 \ge \theta$ and $p_0 = \min(p,2)$.

Theorem 3. Let $1 < p < q < \infty, 1 \le \theta \le \infty$, $q < \theta$, $\gamma_1 \le \ldots \le \gamma_d$ and $0 < r < 1$. If $f(x) \in SB^{\Omega}_{p.\theta}$ and

$$\sum_{n\in Z_+^d}\left[2^{\|n\|_1\left(\frac{1}{p}-\frac{1}{q}\right)}\Lambda\left(2^{-n}\right)\right]^{\rho} < \infty$$

where $\rho = \dfrac{\theta q}{\theta - q}$, then $f(x) \in L_0^q(\pi_s)$ and

$$E_{Q(N)}(f)_q << N^{\frac{1-r}{r}} \cdot \Phi(N,d,q,p,r)$$

where $\Phi(N,d,q,p,r)$ is equal to:

1) $(\log N)^{\frac{d-1-\gamma_1-\ldots-\gamma_d}{\rho}}$, if $\gamma_d < 1$;

2) $(\log N)^{\frac{\nu-1-\gamma_1-\ldots-\gamma_d}{\rho}}(\log\log N)^{\frac{\nu-1}{\rho}}$, if $\gamma_\nu < 1 = \gamma_{\nu+1} = \ldots = \gamma_{\nu+\mu} < \gamma_{\nu+\mu+1}$;

3) $(\log N)^{-\frac{1}{\rho}}(\log\log N)^{\frac{\nu-1}{\rho}}$, if $\gamma_1 = \ldots = \gamma_\nu = 1 < \gamma_{\nu+1}$;

4) $(\log N)^{-\frac{\nu_1}{\rho}}$, if $1 < \nu_1$.

where $\tau = \left(\dfrac{1}{p} - \dfrac{1}{q}\right)\rho$, $\gamma_j = \dfrac{b_j \tau}{r}$, $\gamma_1 \le \ldots \le \gamma_d$

Proof . By Theorem 1, Lemma 2, Lemma3, we have

$$E_{Q(N)}(f)_q << \left\{ \sum_{n\in\Gamma^{\perp}(N,\Lambda)} \left[2^{\|n\|_1\left(\frac{1}{p}-\frac{1}{q}\right)} \Lambda\left(2^{-n}\right) \right]^{\rho} \right\}^{\frac{1}{\rho}} << \left\{ \sum_{n\in\theta(N)} \left[2^{\|n\|_1\left(\frac{1}{p}-\frac{1}{q}\right)} \Lambda\left(2^{-n}\right) \right]^{\rho} \right\}$$

$$<< \frac{1}{N} \left\{ \sum_{n\in\theta(N)} 2^{\|n\|_1 \rho\left(\frac{1}{p}-\frac{1}{q}\right)} \right\}^{\frac{1}{\rho}} << \frac{1}{N} N^{\frac{1}{r}} \left(\sum_{n\in\theta(N)} \prod_{j=1}^{d} n_j^{-\gamma_j} \right)^{\frac{1}{\rho}}$$

By Lemma 4

1) $N^{\frac{1-r}{r}} (\log N)^{\frac{d-1-\gamma_1-\ldots-\gamma_d}{\rho}}$, if $\gamma_d < 1$;

2) $N^{\frac{1-r}{r}} (\log N)^{\frac{\nu-1-\gamma_1-\ldots-\gamma_d}{\rho}} (\log\log N)^{\frac{\nu-1}{\rho}}$, if $\gamma_\nu < 1 = \gamma_{\nu+1} = \ldots = \gamma_{\nu+\mu} < \gamma_{\nu+\mu+1}$;

3) $N^{\frac{1-r}{r}} (\log N)^{-\frac{1}{\rho}} (\log\log N)^{\frac{\nu-1}{\rho}}$, if $\gamma_1 = \ldots = \gamma_\nu = 1 < \gamma_{\nu+1}$;

4) $N^{\frac{1-r}{r}} (\log N)^{-\frac{\nu_1}{\rho}}$, if $1 < \nu_1$.

Theorem 4. Let $1 \le q < p < \infty$ or $1 < q = p < \infty$. $1 \le \theta \le \infty$ and $\Lambda(t)$ - be the function of mixed modulus of smoothness of order k. If $f(x) \in SB^{\Lambda}_{p.\theta}$, then the following inequality holds

$$E_{Q(N,\Lambda)}(f)_q << \frac{n^{\rho(s-1)}}{2^{nr}}$$

where $\rho = \dfrac{\theta p_0}{\theta - p_0}$ for $p_0 < \theta$ and $\rho = \infty$ for $p_0 \ge \theta$ and $p_0 = \min(p,2)$.

Proof. By Theorem 2 and Lemma 2

$$E_{Q(N,\Lambda)}(f)_q << E_{Q(N,\Lambda)}(f)_p << \left(\sum_{n\in\Gamma^{\perp}(N,\Lambda)} \left(\Lambda\left(2^{-n}\right)\right)^{\rho} \right)^{\frac{1}{\rho}} << \left(\sum_{n\in\theta(N)} \left(\Lambda\left(2^{-n}\right)\right)^{\rho} \right)^{\frac{1}{\rho}}$$

Taking into account that $|\theta(N)| \asymp (\log)^{d-1}$ (see. [7]), we have

$$E_{Q(N,\Lambda)}(f)_q << \frac{1}{N^r} |\theta(N)|^{\rho(s-1)} \le \frac{1}{2^{nr}} (n)^{\rho(s-1)}$$

$$E_{Q(N,\Lambda)}(f)_q << \frac{n^{\rho(s-1)}}{2^{nr}}.$$

Conclusion

In this paper we obtained estimates of the best approximations of functions of the Besovclass by trigonometric polynomials when the spectrum of the best approximations of a function is determined by a majorant function of a special type $\Omega(t) = \prod_{j=1}^{d} t_j^r \left(\log \frac{1}{t_j} \right)_+^{-\gamma_j}$.

Earlier, in his research Mirbulat Sikhov obtained non-removable direct and inverse theorems of approximation theory for various metrics for trigonometric polynomials with arbitrary spectrum defined by the general form of the major ant function $\Lambda(t)$ under certain conditions of regularity for functions $\Lambda(t)$.

References

1. Temlyakov V.N. Approximation of functions with bounded mixed derivative // Trudy. –Vol.178.– M: Science, 1986. – 112 p. (in Russian)

2. Pustovoitov N.N. Approximation of multidimensional functions with a given major ant of mixed moduluos of continuity. //Matem. zametki. 1999. –Vol.65, No 1. – P.107-117(in Russian)

3. Sikhov M.B. Some problems in the theory of multi-dimensional approximations of different metrics // Kazakh National Al-Farabi – Almaty: Kazakh University, 2010 (in Russian)

4. Sikhov M.B. On direct and inverse theorems of approximation theory with a given majorant// Analysis Mathematica. – Vol. 30, No 2. – 2004. – P. 137-146 (in Russian)

5. Sikhov M.B. Inequalities of Bernstein and Jackson – Nikolskii and evaluation norms of derivatives of the Dirichlet // Math. – Vol.80. – 2006. – P. 95-104 (in Russian)

6. Pustovoitov N.N. The ortho-diameters of multivariate periodic functions, majorant of mixed moduluos of continuity which contains as power and logarithmic factors //Anal. Math. – 2008. – Vol. 34. – P. 187-224 (in Russian)

7. Pustovoitov N.N. On the approximation of periodic functions by linear methods of the classes // Matem. sbornik. – 2012. – Vol.203,No 1. – P. 91-113 (in Russian)

8. Sikhov M.B. Approximation of functions of several variables with a given majorant space Besov // Mathematical journal. – 2002. – Vol.2, No 2. – P. 95-100 (in Russian)

UDC 532.517.4.519.6

*Issakhov A., Yessenkozha A.M.

Faculty of Mechanics and Mathematics,
al-Farabi Kazakh National University, Almaty, Kazakhstan
*e-mail: alibek.issakhov@gmail.com

Mathematical modelling of air flow in the human respiratory system

Abstract: Nasal inspiration is important for maintaining the internal milieu of the lung, since ambient air is conditioned to nearly alveolar conditions (body temperature and fully saturated with water vapor) on reaching the nasopharynx. In this work conducted a two-dimensional computational study of transport phenomena in model transverse cross sections of the nasal cavity of normal human noses based on the two dimensional Navier-Stokes equation. For discretization Navier-Stokes equation used finite volume method.Projection method applied for solution of the Navier-Stokes equations. The results suggest that during breathing via the normal human nose there is ample time for heat and water exchange to enable equilibration to near intraalveolar conditions. A normal nose can maintain this equilibrium under extreme conditions. The turbinates increase the rate of local heat and moisture transport by narrowing the passageways for air and by induction of laminar swirls downstream of the turbinate wall.
Key words: Respiratory air conditioning, alveolar condition, 2D modeling, heat transfer, Navier-Stokes equations, finite volume method.

Introduction

The nasal cavity balances the inhaled air to the internal condition of the body with amazing efficiency. In Cole, [2] Inglestedta, [3] and Webb [4] papers were general agreement that the air inhaled through the nasal cavity reaches the alveolar condition (fully saturated with water vapor at temperature of the body) to the time when it reaches the throat and it is practically independent of the condition of ambient air which enters through the nares. These findings were supported by Farley and Patel [5], who collected in vivo data of air temperature from various locations along the upper airways throughout the respiratory cycle, and Hannah and Scherer [6], who measured the local mass transfer coefficients on the plaster model of the human upper respiratory tract.

Numerical studies have focused on the assessment of the dampening and regulating the temperature of the nasal cavity. In addition, as the surgical procedures are now being used at an increasing rate to restore the structure and functions of the nose [8]. For example, aromatic inhalations are used to improve airflow and to reduce congestion, and rhinoplastic procedures used to overcome injuries or aesthetic deformations. These artificial intervention cause local changes, and can affect the efficiency of transport phenomena. However, the exact characteristics of intranasal and distribution of transport phenomena is still unknown even to normal (or healthy) state [15, 16].

Experimental study of the nasal cavity is impossible, due to a complex internal structure and size, because by putting a measuring instrument or probe into the nasal cavity causes a flow disturbance. Therefore, mathematical modeling is the only approach for the study of air flow in the nasal cavity.

The purpose of this study was to use the numerical modeling to study the dynamic capacity of the nasal cavity, the process of heating and moisturizing of inhaled air.

Formulation of the problem

The structure of the nasal cavity provides a very sophisticated way to airflow. The complex structure of the nasal cavity and the full three-dimensional analysis of the flow of steam, the heat transfer in the inside of the nasal mucosa requires significant computational resources, which prevent systematic analysis of relevant factors.

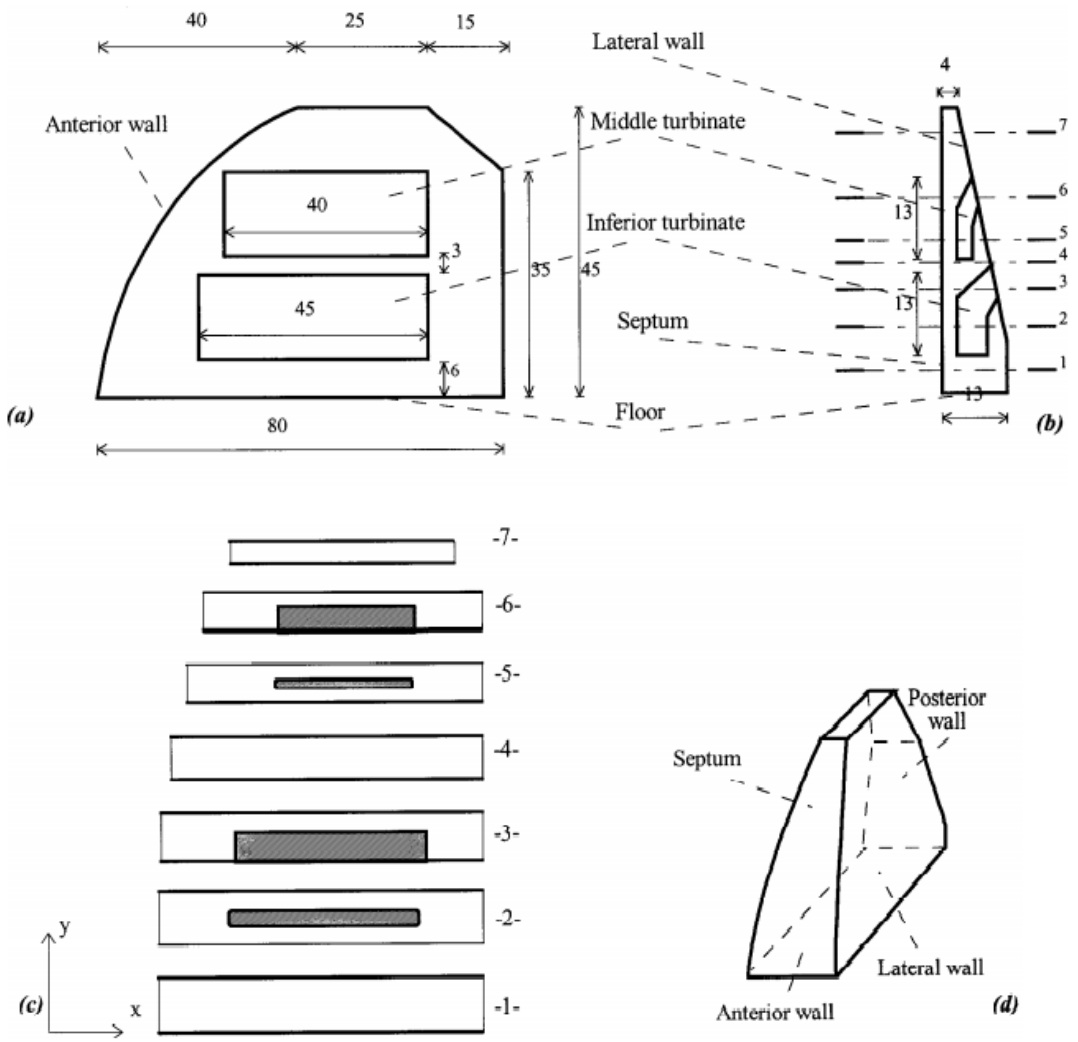

Figure 1 – Simplified nose models: a) longitudinal section, b) coronal section, c) the cross-section at height h = 3, 13, 17, 20, 26, 33, 40 mm from the bottom of the nasal cavity, d) a perspective view

Taking into account the available computing resources, a comprehensive study of transport mechanisms was conducted with two-dimensional simulation through transverse cross section of the nose.

In addition, the following assumptions were made:

- The walls of the nasal cavity and nasal turbinates are assumed to be rigid structures.
- Air flow in the nasal cavity is considered as a laminar flow, and the air as an incompressible medium.
- No-slip conditions are assumed at the interface between the air and the surface of the nasal cavity.

Subtle features of the nose do not have the exact size, as there are differences in the structure of the nasal cavities of healthy people, so we can't determine the exact model of the "normal nose".Thus, we had devised a simplified model of nose, where major essential features were identified. The sizes were taken fromaverage dimensions of human nasal cavity.

The physical area of the problem is the second cross-section (Figure 1 (c) "-2"), which is important for the study because a significant proportion of the air flow moves in this area, and it has a complex structure due to the main functions of the nasal cavity are performed.

The mathematical model is based on the Navier-Stokes equations, including the continuity equation, motion equation and the temperature transport equation [11, 12, 13]. Discretization was performed by finite volume method [9, 10, 14].

$$\nabla U = 0,$$

$$\frac{\partial U}{\partial t} + (U \cdot \nabla)U = -\frac{1}{\rho}\nabla p + v\nabla^2 U,$$

$$\frac{\partial T}{\partial t} + (U \cdot \nabla)T = \frac{k}{\rho c_p}\nabla^2 T,$$

where U is the velocity vector, t is time, p is fluid pressure , c_p is specific heat at constant pressure, T is temperature, ρ, v and k are the fluid density, kinematic viscosity and thermal conductivity, respectively, and ∇^2 is the Laplacian.

The boundary condition for the entrance of the inhaled air is given in the form of the profile, and ambient air temperature is taken as 25 ℃:

$$u_{in}(t, x = 0, y) = \left[2\sin^2\frac{\pi}{2} - 1\right] \times \frac{(12y - y^2)}{36}$$

$$T_{in}(t, x = 0, y) = 25°C$$

On the walls of the nasal cavity and nasal turbinate:

$$u_{wall}(t, x, y) = 0,\ v_{wall}(t, x, y) = 0,$$
$$T_{wall}(t, x, y) = 37°C$$

Initial conditions:

$$u_0(t = 0) = 0,$$

$$T_0(t = 0) = 32°C.$$

Numerical algorithm

For the numerical solution of this system of equations is used projection method[14, 17]. At the first stage it is assumed that the transfer of momentum is carried out only by convection and diffusion. Intermediate velocity field is calculated by the fourth order Runge-Kuttamethod [13]. In the second stage, based on the found intermediate velocity field, one solves pressure field. Poisson equation for the pressure field is solved by Jacobi method. In a third step it is assumed that the transfer is carried out only by the pressure gradient. In the fourth stage, temperature transport equation is calculated by the fourth order Runge-Kutta method [13, 15, 16].

I. $$\int_\Omega \frac{\vec{u}^* - \vec{u}^n}{\tau} d\Omega = -\oint_{\partial\Omega} (\nabla \vec{u}^n \vec{u}^* - \upsilon \Delta \vec{u}^*) n_i d\Gamma$$

II. $$\oint_{\partial\Omega} (\Delta p) d\Gamma = \int_\Omega \frac{\nabla \vec{u}^*}{\tau} d\Omega$$

III. $$\frac{\vec{u}^{n+1} - \vec{u}^*}{\tau} = -\nabla p.$$

IV. $$\int_\Omega \frac{T^{n+1} - T^n}{\tau} d\Omega = -\oint_{\partial\Omega} (\nabla \vec{u}^n T - \frac{k}{\rho c_p} \Delta T) n_i d\Gamma$$

Computational mesh was created in Point Wise. The area was divided into 10 sub-areas to run on the software package ITFS-MKM (on the high-performance cluster T-Cluster at the Mechanics and Mathematics Faculty of al-Farabi Kazakh National University.).

The results of simulations

As a result of the numerical simulation of aerodynamics of the human nasal cavity, the following data were obtained; to verify the calculations used data from the paper [1], which describes the profiles of the longitudinal component of the velocity and temperature at three locations: at a distance x_1 = 17 mm, x_2 = 49 mm and x_3= 80 mm from the entrance (Figure 2.).

Figure 3 compares profiles between the velocitiesfrom calculation results and data from the paper Naftali S. [1]. Figure 4 shows a comparison of temperature profiles between the sections and the data from paper [1].

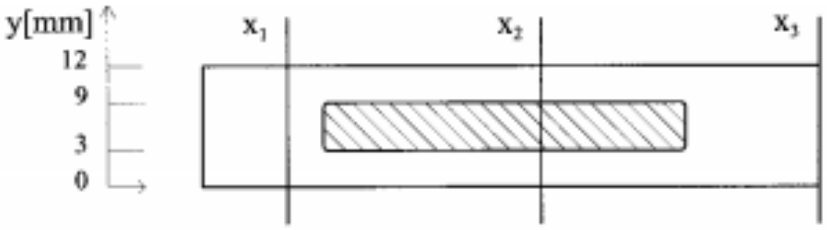

Figure 2 – Evaluation of the three zones for temperature and velocity of the cross-section

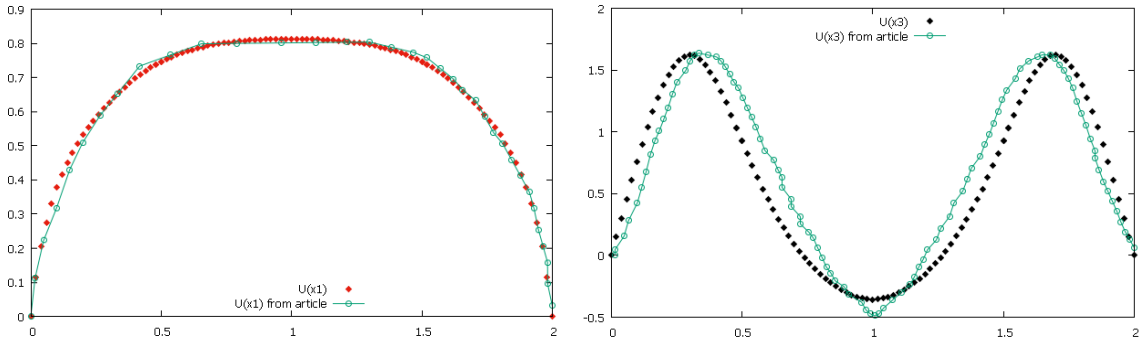

Figure 3 – Comparison of velocity component profiles with the numerical results from the paper [1] on x_1 = 17mm and x_3 = 80mm

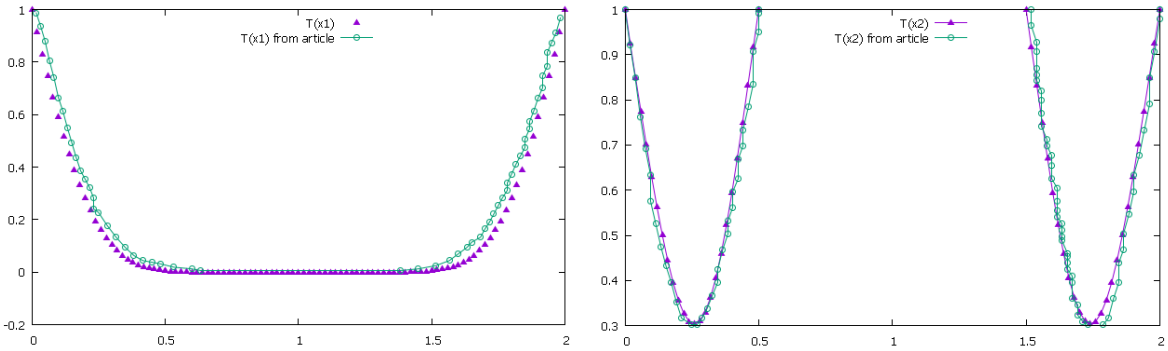

Figure 4 – Comparison of temperature profiles with the numerical results from the paper [1] on x_1 = 17mm and x_2 = 49mm

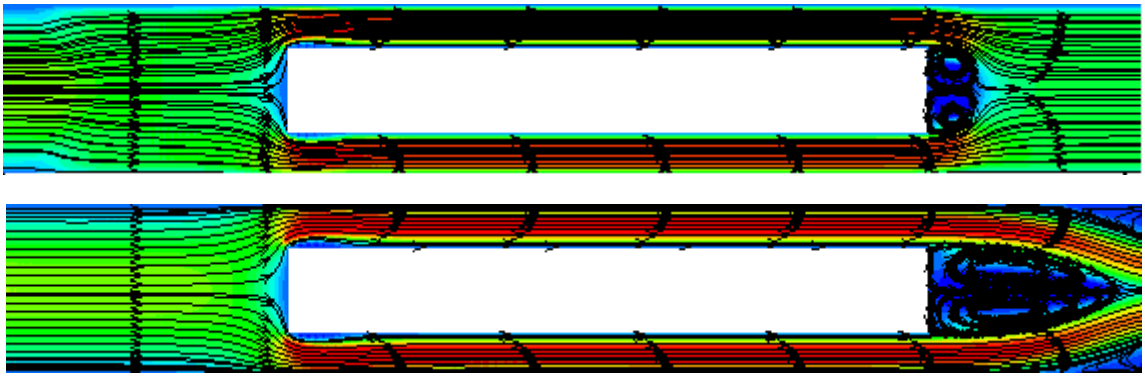

Figure 5 – The longitudinal components of the flow rate
to the cross-sectional lines with streamtracesfor different time layers

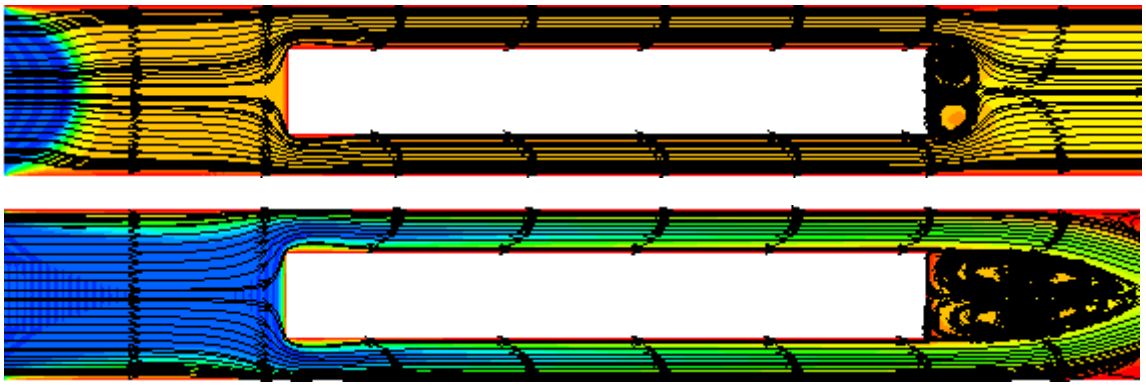

Figure 6 – Temperature for the cross-sectional lines with streamtraces
for different time layers

Figure 5 shows a longitudinal velocity component in cross section with streamtraces for different time layers. Along the streamtraces visible vortices which appear due to walls of the turbinates, which play an important role in the process of heating the air. Figure 6 shows the calculated temperature region with the flow lines for any time layers. From the figures it can be seen that the passage in the downstream narrow spaces of the nasal cavity air is heated.

Conclusion

Thus, in the research of nasal cavity we can conclude that nasal wall heats transfer air, also produces vortices which have a great importance for the transition into the alveolar air condition before reaching the nasopharynx. Studies of the nasal cavity are actually important, because nowadays thenumber of people with nasal breathing problems are increasing; this problem can be resolved by surgery, where it is important to optimally operate the structure of the nose and nasal cavity for the sake of correct functioning owing to the fact that normal breathing should be carried out with the help of the nose.

References

1. Naftali S., Schroter R. C., Shiner R. J., Elad D. Transport Phenomena in the Human Nasal Cavity: A Computational Model // Annals of biomedical engineering. – 1998. – P. 831-839.

2. Cole P. Some aspects of temperature, moisture and heat relationships in the upper respiratory tract // J. Laryngol. Otol. 67. – 1953. – P. 669–681.

3. Ingelstedt S. Studies on conditioning of air in the respiratory tract // Acta Oto-Laryngol. Suppl. 131. – 1956. – P. 1–80.

4. Webb P. Air temperatures in respiratory tracts of resting subjects // J. Appl. Physiol. 4. – 1951. – P. 378–382.

5. Farley R. D., and Patel K. R. Comparison of air warming in human airway with thermodynamic model // Med. Biol. Eng. Comput. 26. – 1988. – P. 628–632.

6. Hanna L. M., and Scherer P. W. Measurement of local mass transfer coefficients in a cast model of the human upper respiratory tract // J. Biomech. Eng. 108. – 1986. – P. 12–18.

7. McFadden E. R. Respiratory heat and water exchange: Physiological and clinical implications // J. Appl. Physiol. 54. – 1983. – P. 331–336.

8. Maran A.G.D., and Lund V.J. Clinical Rhinology. – New York: Thieme Medical.– 1990.

9. Anderson D., TannehilDzh., Pletcher R. Vyichislitelnaya gidromehanika i teploobmen. – M..: Mir, 1990. –337 p.

10. Anderson D., Tannehill Dzh., Pletcher R. Vyichislitelnaya gidromehanika i teploobmen. –M.: Mir, 1990. –384 p.

11. Fletcher K. Vyichislitelnyie metodyi v dinamike zhidkostey. – M.: Mir, 1991. – 552 p.

12. Rouch P. Vyichislitelnaya gidrodinamika. – M.: Mir, 1972. – 612 p.

13. Chung T.J. Computational fluid dynamics. – 2002. – 1034 p.

14. Issakhov A., Mathematical modeling of the discharged heat water effect on the aquatic environment from thermal power plant // International Journal of Nonlinear Science and Numerical Simulation. – 2015. Vol. 16. – No 5. – P. 229–238.

15 Issakhov A., Mathematical modeling of the discharged heat water effect on the aquatic environment from thermal power plant under various operational capacities // Applied Mathematical Modelling. –2016. – Vol. 40, No 2. – P. 1082–1096

16 Issakhov A. Large eddy simulation of turbulent mixing by using 3D decomposition method // J. Phys.: Conf. Ser. – 2011.– Vol. 318. – No 4. – P. 1282-1288.

17 Chorin A.J. Numerical solution of the Navier-Stokes equations // Math. Comp. – 1968. – Vol. 22. – P. 745-762.

UDC 519.63; 519.684

*Issakhov A., Shubay A.

Faculty of Mechanics and Mathematics,
al-Farabi Kazakh National University, Almaty, Kazakhstan
*e-mail: alibek.issakhov@gmail.com

Mathematical modelling of blood flow in vascular system of the brain with pathological changes

Abstract: The paper presents numerical study of blood flow in vascular system without stenosis and with pathological changes. The Navier – Stokes system of equation is used for modeling of liquid flow in blood vessels. The numerical algorithm was based on projection method. At first stage, it is assumed that the transfer of the movement of amount occurred is due to convection and diffusion. The intermediate regions of velocity are determined by using the 5-step Runge – Kutta method algorithm. At second stage the intermediate velocity field is used to define the pressure field. The Poisson equation for pressure field is solved by Jacobi method. The numerical results are checked by comparing analytical solutions for the Poiseuille flow with numerical results. The influence of the blood velocity flow on behavior of the liquid in vascular system of brain was investigated. One of the characteristic features of blood flow in blood vessels affected by stenosis is an appearance of vortex currents, which manifests as a pathology, as opposite to normal blood circulation. The results of this work can be used in mathematical modeling investigations of blood circulation in brain and solving problems in practical medicine.
Key words: Navier-Stokes equation, Poiseuille flow, atherosclerotic plaque, stenosis, pathological changes in the blood vessels.

One of the most difficult and important problems of medicine is curing of the pathology of cerebral circulation. Because of the cerebrovascular disease spreading prevention and operative therapy of dysfunction of brain circulation very actual nowadays. The death rate from insult reaches 35% in Kazakhstan (450000 insults), herewith the risk of insult increases with age rise, particularly at the age of 65 – 80. Insult is serious complication of vascular heart diseases, which is located in the first three reasons of death and in some cases the death rate of insult exceeds the death rate of heart attack. The probability of disability is very high in case of patients suffered from insult, 20% of them return to work, 60% of patients have neurological disorders, 20% of patients need constant nursing care. The rise of the patients number with vascular brain diseases is depend on a lot of factors and connected with the age rise and the increase of weight of elderly people.

Formulation of the task

In the work is made formulation of the problem and the equations of blood flow in vessels of the thick – wall hyper elasticity vessel. It is assumed that blood is homogeneous incompressible Newtonian medium. Vessel is considered as thick – wall cylinder form hyper elastic material. Blood is affected by changing pressure gradient.

For a description of blood movement, the no stationary two – dimensional Navier – Stokes equations with constant density and kinematic viscosity are used [1, 2]:

$$\begin{cases} \dfrac{\partial u}{\partial x}+\dfrac{\partial v}{\partial y}=0 \\ \dfrac{\partial u}{\partial t}+u\dfrac{\partial u}{\partial x}+v\dfrac{\partial u}{\partial y}=-\dfrac{1}{\rho}\dfrac{\partial p}{\partial x}+\vartheta\left(\dfrac{\partial^2 u}{\partial x^2}+\dfrac{\partial^2 u}{\partial y^2}\right) \\ \dfrac{\partial v}{\partial t}+u\dfrac{\partial v}{\partial x}+v\dfrac{\partial v}{\partial y}=-\dfrac{1}{\rho}\dfrac{\partial p}{\partial y}+\vartheta\left(\dfrac{\partial^2 v}{\partial x^2}+\dfrac{\partial^2 v}{\partial y^2}\right) \end{cases} \quad (1)$$

where p – pressure, u, v – velocity component, ρ density, x, y – space coordinates, t – time, ν – kinematic viscosity. In this work by using this system of equation is modeled two problems stenos is in cerebral vessels are modeled in the work.

First problem is healthy vessel (figure 1).

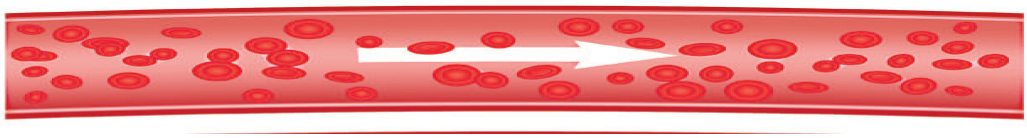

Figure 1 – Healthy vessel

Second problem is stenosis on one of the vascular wall (figure 2):

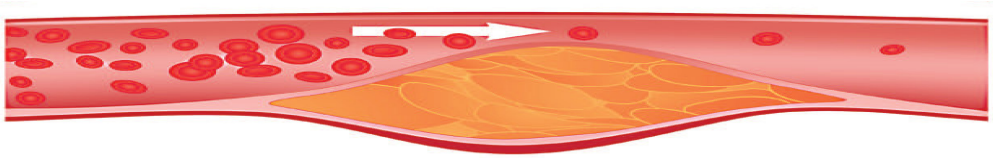

Figure2 – Vessel with atheroma

Numerical algorithm

For solving of the system of equations (1) is used projection method [7, 10]. At first stage, it is assumed that the transfer of the movement of amount occurred is due to convection and diffusion. The intermediate regions of velocity are determined by using the 5-step Runge – Kutta method algorithm. At second stage the intermediate velocity field is used to define the pressure field. The Poisson equation for pressure field is solved by Jacobi method. At the third stage, it is assumed that the transfer if carried out only by pressure gradient. Below is given the numerical algorithm in mathematical form [8, 9]:

$$\text{I.}\quad \int_{\Omega}\frac{\vec{u}^{*}-\vec{u}^{n}}{\tau}d\Omega=-\oint_{\partial\Omega}\left(\nabla\vec{u}^{n}\vec{u}^{*}-\upsilon\Delta\vec{u}^{*}\right)n_i d\Gamma$$

$$\text{II.}\quad \oint_{\partial\Omega}(\Delta p)d\Gamma=\int_{\Omega}\frac{\nabla\vec{u}^{*}}{\tau}d\Omega$$

$$\text{III.}\quad \frac{\vec{u}^{n+1}-\vec{u}^{*}}{\tau}=-\nabla p$$

The results of numerical estimations

The system of equations (1)is closed by following boundary conditions: for the velocity components on the wall no slip is set, in inlet — parabolic profile, in outlet— outlet boundary conditions. For the pressure the Neumann conditions were set in all boundaries.

Poiseuille flow (the first problem) is viscous flow going through a tube with determined diameter and theoretically infinite length. At figure 3, a geometric parameters are given, which were used in solving of this problem. The basis of the research work is taken from work Schlichting G. [6].

In work [6] the tube with length L and radius l were used with Reynolds number *Re* = 100. And $\frac{L}{l}=10$ (figure 3)

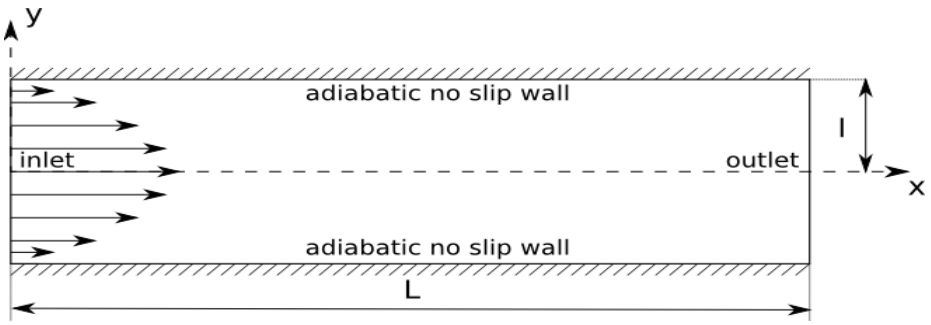

Figure 3 – Computational domain

At figure 4, shown comparison of numerical and analytical solution of streamwise velocity at points $x/L = 0$ and $x/L = 9$ is presented. Results taken form research matches with analytical solution very well.

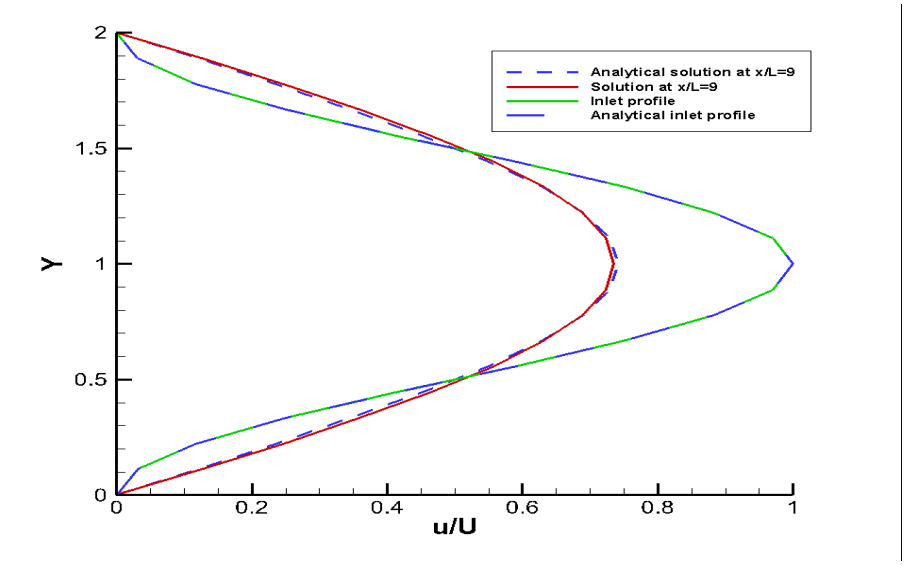

Figure 4 – Velocity profile on points $x/L = 0$ and $x/L = 9$

At figure 5, the velocity field for the number Re=100 is presented for different time lays. From figure 5, we can make following conclusions, that the speed of blood flow in the norm is laminar and the velocity profile is parabolic. The movement of blood speed in the center of vessel turns out much bigger than movement velocity near the vascular wall. Wherein the blood layer adjoining to the vascular vessel is almost stationary, the next blood layer moves a small distance, the blood portion located in the center part of vascular vessel moves big distance. Thus, the velocity profile distributionforms in vessels.

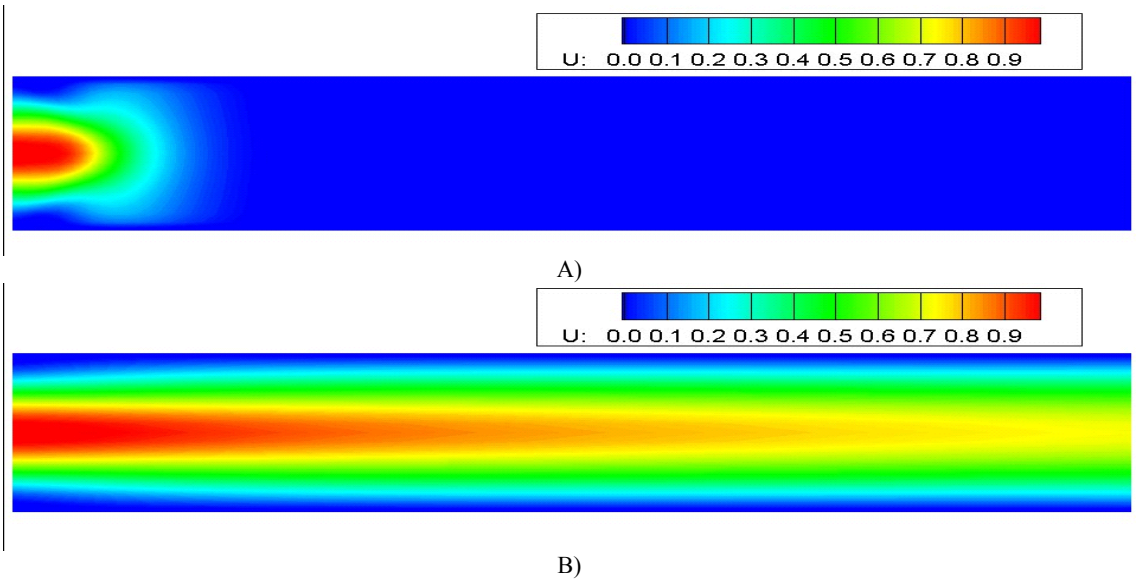

Figure 5 – Contour of velocity fieldRe=100at various time layers(A) t=0, B) t=10)

Table 1 – Properties of vessels and blood.

Vessels	$D[cm]$	$V\left[\frac{cm}{s}\right]$	$\rho\left[\frac{gr}{cm^3}\right]$	$\mu\left[\frac{gr}{cm\cdot s}\right]$	T[°C]
Artery 1) Carotid	0,15-0,25	20	1,05	0,0255-0,03	40-41
2)Vertebral artery	0,15-0,25	25	1,05	0,0255-0,03	40-41
3)Infraorbital artery	0,15-0,25	15	1,05	0,0255-0,03	40-41
4)Internal carotid artery	0,15-0,25	75	1,05	0,0255-0,03	40-41
Arteriole	0,005-0,01	45	1,05	0,0255-0,03	40-41
Veins: 1) Cava	0,5-3	10-20	1,05	0,0255-0,03	40-41
2) Venule	0,004-0,005	0,3-1	1,05	0,0255-0,03	40-41
Capillaries	0,00045-0,0007	0,2-0,3	1,05	0,0255-0,03	40-41

For the second problem, the blood flow in vein is modeled numerically, which gives an opportunity to make a picture of the flow cased by stenosis. It complements the information which might be received in experimental researches and allows determining the effect of a wall shape, flow type and character on the disease's degree. Such parameters as distribution of velocity along axis, vessels diameter, density, blood viscosity for the determination of physiological and pathological conditions in vessels. The special flow characteristic in vessels affected by stenosis is the appearance of intermediate regimes of flow, which are considered as pathological in contradistinction to normal flow regime. Due to growth of atherosclerotic plague the narrowing of canal is happening, which in its turn, leads to velocity rise in vessel and appearance of turbulence regime, which has bad effect on vessels of brain. In vessels of brain laminar flow appears in the low values of blood speed. In turn, flow with stenosis such features as division of flow on further eddy zones in vessels appears. The data for the numerical modeling is taken from the table 1 [3, 4, 5].

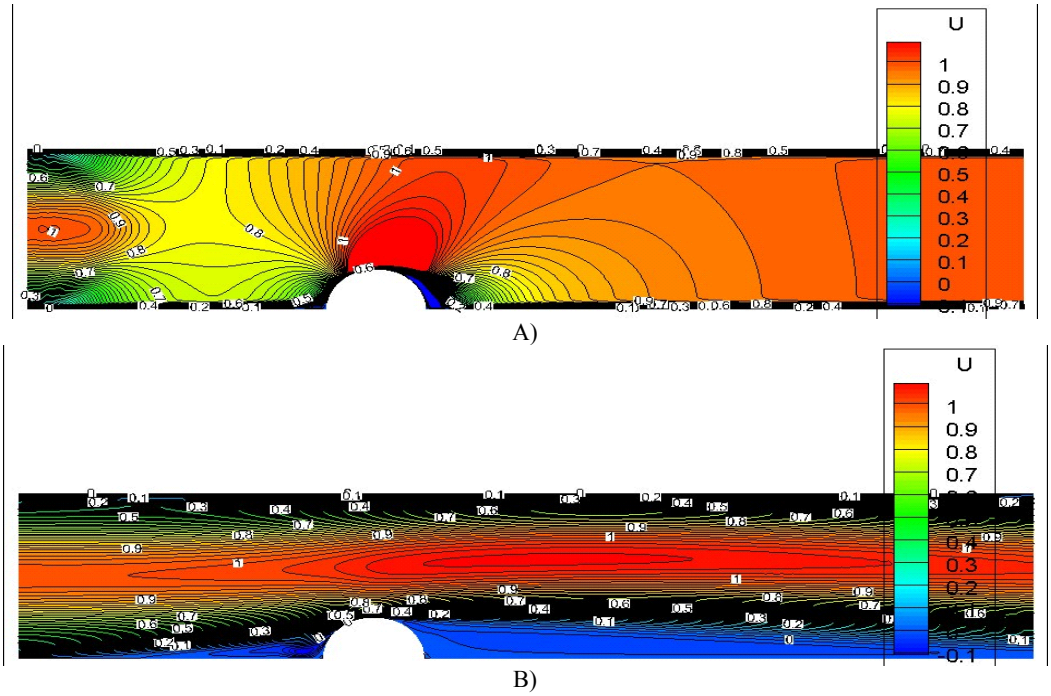

Figure 6 – Contour of velocity field with stenosis for speed $\upsilon = 15\,\frac{cm}{s}$ in different time layers (A) t = 0, B) t = 10).

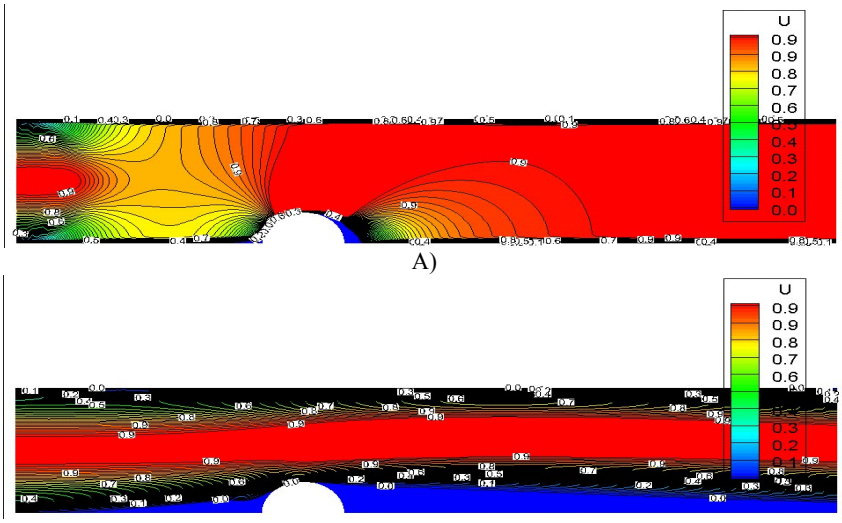

Figure 7 – Contour of velocity field with stenosis for speed $\upsilon = 20\frac{cm}{s}$ in different time layers (A) t = 0, B) t = 10)

The estimated area is given at figure 6, which shows an atherosclerotic plague. For the numerical modeling of stenosis in brain vessel the next parameters are used: vessel diameter D=0.01 mm., kinematic viscosity μ =0,03 $\frac{gr}{cm \cdot s}$.

At figures 6-8 the velocity field of blood flow with atherosclerotic plague in vessel of brain is presented for different time layers and different velocities. As it can be seen from the figures, vortex field appears behind the atherosclerotic plague. Wherein, blood velocity grows, making vortex field in zone of narrowing of vessel, which in its turn can transformed in turbulence flow. In the end, the atherosclerotic plaque can increase in size. At figures 9-11, presents the different vertical velocity profiles with stenosis for different numbers of velocity. At figures 10-11 are shown the velocity profiles before passing atherosclerotic plaque. The fracture in the velocity profile at figure 12 indicates the appearance of tearing off zone.

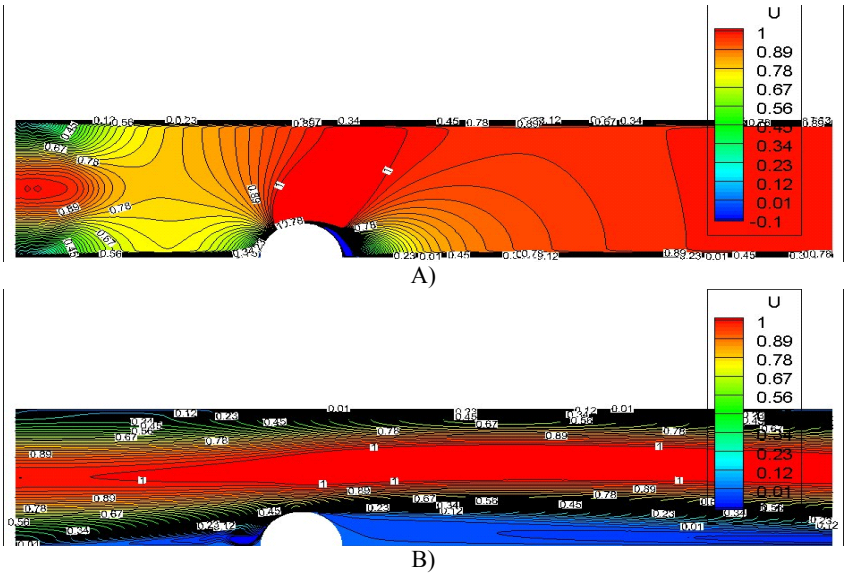

Figure 8 – Contour of velocity field with stenosis for speed $\upsilon = 25\frac{cm}{s}$ in different time layers (A) t = 0, B) t = 10).

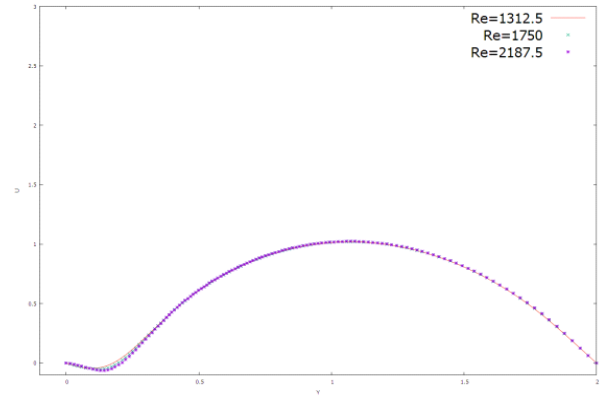

Figure 9 –Vertical velocity profile with stenosis for different velocity x = 2,56

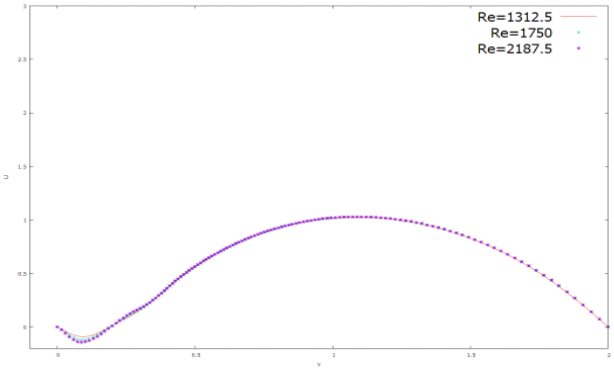

Figure 10 –Vertical velocity profile with stenosis for different velocity x = 2,85

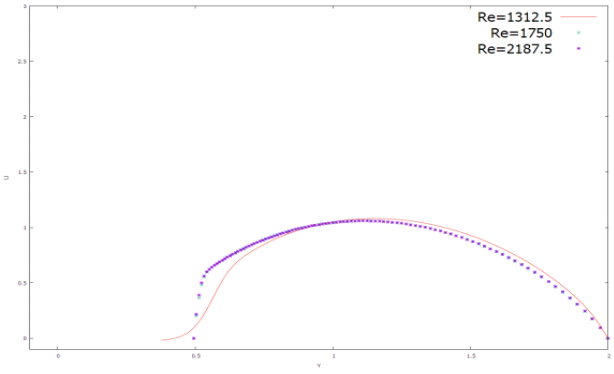

Figure11 –Vertical velocity profile with stenosis for different velocity x = 3,45

As plaque grow, the lumen decrease gradually, which can lead to its complete occlusion with time. The plagues growth is dangerous because its part can tear off and travel through bloodstream getting into a smaller vessel and plugging it up.In this type of stenosis, the violation of the blood supply in particular brain area happens. In slow stenosis development of arteries, the cerebrovascular insufficiency develops. The main manifestations are disturbance of memory, eyesight, speech, changes in emotional sphere, different movement disorders.

Conclusion

The numerical method is tested in example of Poiseuilleflow. According to numerical result the graph of Poiseuille flow profile, the numerical method gives satisfactory result. It allows us to apply this numerical method to the blood flow problem in vessels of brain with pathological diseases which we are interested in.

Numerical modeling of atherosclerotic plaque in vessels of brain gives an opportunity to make a picture of flow, which caused by stenosis.Further information can be obtained from experimental researches, which allows us to determine type, character of flow and degree of disease. For the detection of physiological and pathological processes in vessel, important parameters are velocity distribution along the axis and drop of pressure. One of the characteristics of blood flow in blood vessels affected with stenosis is the appearance of eddy flow regime, which pathology is comparing with a normal blood circulation. In laminar regime of blood flow in vessels of brain the flow occurs in low values of speed's numbers. When there is a stenosis in vessels a blood consumption decrease greatly because of eddy zones appearance. Taking the Navier – Stokes equation as a base in this work, movements of blood in vessels of brain are modeled numerically. The behavior of the blood flow is researched with different velocity, availability of atherosclerotic plaques that allows to diagnose disease at early stages and to choose right ways of therapeutic treatment and prevention. The results of this work might be used in solving of tasks of clinical medicine.

References

1. Skobtsov Yu.A., Rostov Yu.V., Overko B.S. Modelirovanie i vizualizatsia povedeniya potokov krovipri patologicheskikh protsessakh – Donetsk: Izatel'Zaslavskiy A. Yu. – 2008. – 212 p..

2. Zabielski L., Mestel A. Unsteady blood flow in a helically symmetric pipe // Journal of Fluid Mechanics. – 1998. – Vol. 370. – P. 321- 345.

3. Smirnov V. M. Fiziologiyacheloveka. izd – M.: Meditsina, 2002. – 608 p.

4. Tsvibel' V., Pellerito Dzh. Ul'trazvukovoe issledovanie sosudov. izd. – M.: Vidar, 2008. – 644 p.

5. Tazyukov F. Kh., Dzhafar M. Khassan, Khalaf Kh. A., Snigerev B.A., Safa Kh. Abdul Rakhman Techeniekrovi v simmetrichnoi krovenosnoiarterii so stenozom // Rossiyskiy zhurnal biomekhaniki. – 2012. – Vol. 16. – No 1(55). – P. 46–56.

6. Schlichting G. Teotiya pogranich negosloya. izd. – M.: Nauka, 1974. – 708 p.

7. Issakhov A., Mathematical modeling of the discharged heat water effect on the aquatic environment from thermal power plant // International Journal of Nonlinear Science and Numerical Simulation. – 2015. – Vol. 16, No 5. – P. 229–238.

8. Issakhov A., Mathematical modeling of the discharged heat water effect on the aquatic environment from thermal power plant under various operational capacities // Applied Mathematical Modelling. – 2016. – Vol. 40, No 2. – P. 1082–1096

9. Issakhov A. Large eddy simulation of turbulent mixing by using 3D decomposition method // J. Phys.: Conf. Ser. – 2011. – Vol. 318. – No 4. – P. 1282-1288.

10. Chorin A.J. Numerical solution of the Navier-Stokes equations // Math. Comp. – 1968. – Vol. 22. – P. 745-762.

UDC 519.63; 519.684

* Issakhov A., Shaibekova A.A.

Faculty of Mechanic-Mathematics,
al-Farabi Kazakh National University, Almaty, Kazakhstan
*e-mail: alibek.issakhov@gmail.com

Mathematical modelling of flow around obstacles with complex geometric configuration in a viscous incompressible medium

Abstract. In this paper, we numerically investigate flow around obstacles with complex geometric configuration in a viscous incompressible environment. The Navier-Stokes equations were used to modeling the flow around obstacles with complex geometric configuration. The numerical algorithm was constructed by using projection method. At the first stage the intermediate speed is determined by the 5-step Runge-Kutta method. At the second stage the results of intermediate velocity used to determine the pressure field. Poisson equation for the pressure field is solved numerically by using the Jacobi method. The numerical algorithm is tested at flow around the square cylinder and compared with experimental data, which gives good results. Also, in this work simulated non-stationary flow around one and two cylinders obstacles arranged opposite each other.
Key words: The Navier-Stokes equations, finite volumes method, Karman vortex shedding, an aerodynamic tube.

Introduction

One of the main problems of the mechanics is the study of viscous incompressible environment. Flow around obstacles with complex geometric configuration, such as flow around a cylinder with a circular cross-section, is well-studied problem. In many mechanical engineering applications, separated flows often appear around any technical object. Tall buildings, monuments, and towers are permanently exposed to wind. Particular attention to the aerodynamic stability of constructions began to pay after some unfortunate incidents such as the collapse of a hanging bridge over the river Tacoma (USA, November 7, 1940), three towers on the thermal power plant Ferry bridge (England, November 1, 1965), the accident at the Nuclear Power Plant Turkey Point (USA, 1985). Very often, research is conducted on the examples of two-dimensional cylinder flow problems varying cross-sectional shape: circular, square, rectangular, elliptical, etc. In this paper tested numerical algorithm as an example of flow of the square cylinder and a study of non-stationary two-dimensional flow over a cylinder and two cylinders with a circular cross-section, located opposite each other.

Mathematical formulation of the problem

To describe the motion of the liquid and the gas around the geometric configuration of a viscous incompressible unsteady environment used two-dimensional Navier-Stokes equations with constant density and kinematic viscosity: In our case, the system consists of two equations: motion equations and the continuity equation.

$$\begin{cases} \dfrac{\partial u}{\partial x}+\dfrac{\partial v}{\partial y}=0 \\ \dfrac{\partial u}{\partial t}+u\dfrac{\partial u}{\partial x}+v\dfrac{\partial u}{\partial y}=-\dfrac{1}{\rho}\dfrac{\partial p}{\partial x}+\vartheta\left(\dfrac{\partial^2 u}{\partial x^2}+\dfrac{\partial^2 u}{\partial y^2}\right) \\ \dfrac{\partial v}{\partial t}+u\dfrac{\partial v}{\partial x}+v\dfrac{\partial v}{\partial y}=-\dfrac{1}{\rho}\dfrac{\partial p}{\partial y}+\vartheta\left(\dfrac{\partial^2 v}{\partial x^2}+\dfrac{\partial^2 v}{\partial y^2}\right) \end{cases}$$

where u, v – velocity components, p – pressure, ρ – density, v – the kinematic viscosity, t – time, x, y - space coordinates.

In this paper for testing the numerical method is considered a two-dimensional problem of flow around a square cylinder in a viscous incompressible environment. Results obtained from a numerical simulation were compared with

 Printed in Kazakhstan

experimental data provided in paper [3]. Also in this work considered two problems with flow around: 1) structure with a circular cross-sectional shape; 2) two structures with a circular cross-sectional shape located opposite each other.

Numerical algorithm

Projection method is used to solve the Navier-Stokes equations (1) [7, 10]. It is assumed that the transfer of momentum carried out only by convection and diffusion in the first step. The intermediate velocity field is determined by the 5-step of Runge-Kutta method. In the second stage, due to the known intermediate velocity field, the pressure field is found. Poisson equation for the pressure field is solved by Jacobi method [4]. In the third step it is assumed that the transfer is carried out only by the pressure gradient [8, 9], i.e.:

$$\text{I. } \int_{\Omega} \frac{\vec{u}^{*} - \vec{u}^{n}}{\tau} d\Omega = -\oint_{\partial\Omega} \left(\nabla \vec{u}^{n} \vec{u}^{*} - \upsilon \Delta \vec{u}^{*} \right) n_i d\Gamma$$

$$\text{II. } \oint_{\partial\Omega} (\Delta p) d\Gamma = \int_{\Omega} \frac{\nabla \vec{u}^{*}}{\tau} d\Omega$$

$$\text{III. } \frac{\vec{u}^{n+1} - \vec{u}^{*}}{\tau} = -\nabla p$$

Experimental system of viscous flow over a square cylinder

Consider the problem of two-dimensional square-shaped cross-flow cross-section of the tubular body limitless laminar flow. [4]. A rectangular Plexiglas channel (Dimensions (m): L = 0.9255 stream wise; B = 0.01 transverse; W = 0.1 span wise) was used as the primary test section in a closed-loop configuration. A stainless steel square cylinder of diameter (D = 0.0025 m) was symmetrically affixed with the help of two miniature screws at a distance of 0.693 m from the inlet to the test section. The blockage ratio (β = D/B) was fixed at 0.25.The device D (Dimensions (m): L = 0.4; B = 0.2; W = 0.5) was connected to the test section using an intermediate channel (Dimensions (m): L = 0.5; B = 0.04; W = 0.1). This device effectively distributes the flow at the entrance to ensure a uniform and constant flow rate at the inlet of the test section. This channel had the hole (0.25 inch diameter) which was used to inject a colored dye through a streamlined stainless steel tube (1 mm diameter).

Furthermore, the apparatus 1 m length were installed inside the machine, to remove any swirl. Water flow comes from HT tank by a pump P to reservoir CHT1. CHT1 tank was connected to the apparatus through D FV valve regulating the amount of water flow. For smooth transition of the water flow from the apparatus A to the intermediate conduit used QE1, QE2 elliptical equipment. (Figure 1).

The Figure 2 illustrates a scheme of the test section that shows lines across which the time-averaged velocity profiles were measured. Physical scheme and the boundaries of computational domain are shown in Figure 1.

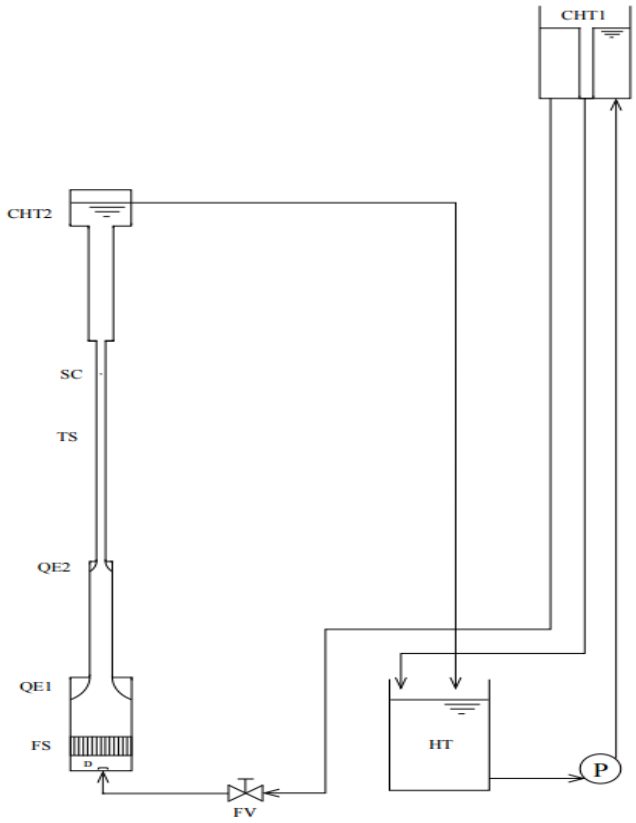

Figure 1 – Scheme of experimental system

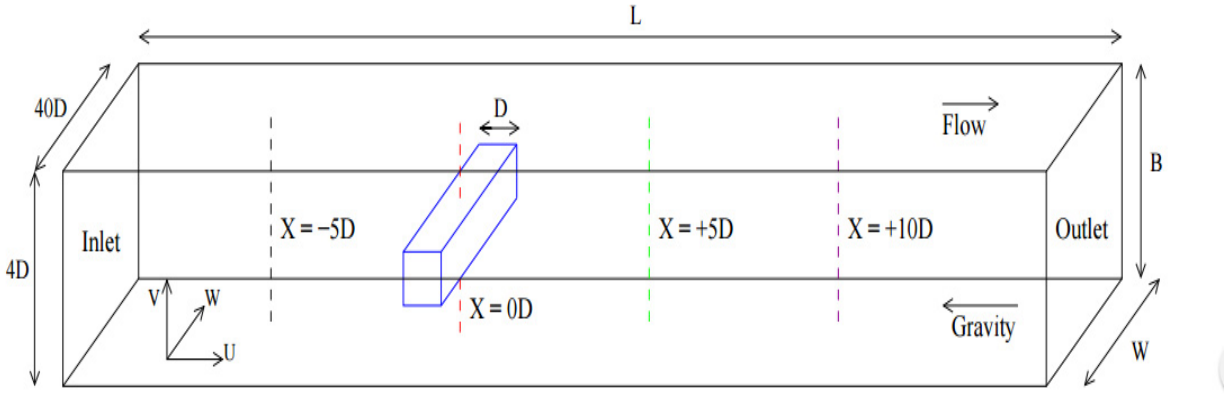

Figure 2 – Scheme of test section

Results of numerical simulation

The system of equations (1) is closed by the following boundary conditions: for the velocity components are set on the wall no slip condition and not overflow and at the inlet – parabolic profile, at the exit – "outlet" boundary conditions. For the pressure on all borders set Neumann conditions. The parameters of the computational domain are presented in Figure 3 for the numerical simulation of flow around square cylinder problem in a viscous incompressible environment and comparing the results with the known results.

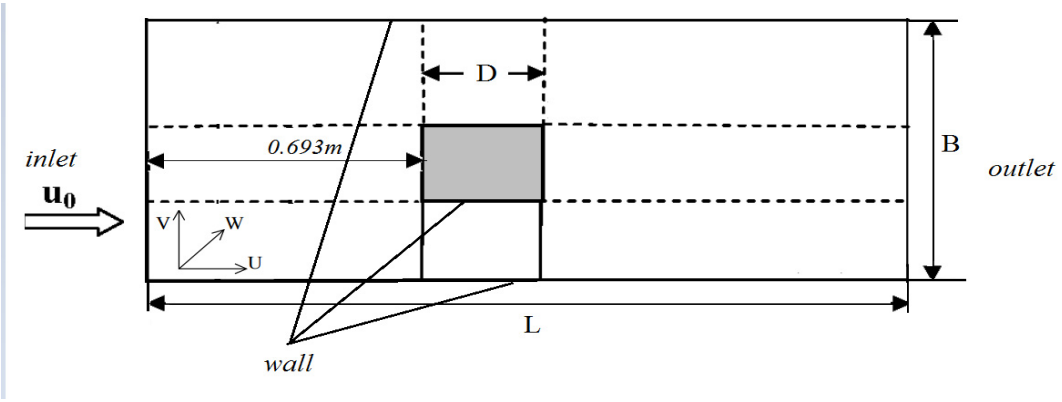

Figure 3 – Scheme of flow around a square cylinder in a viscous incompressible environment

By using a numerical algorithm to the problem of flow around a square cylinder, the following (Figure 4) was obtained:

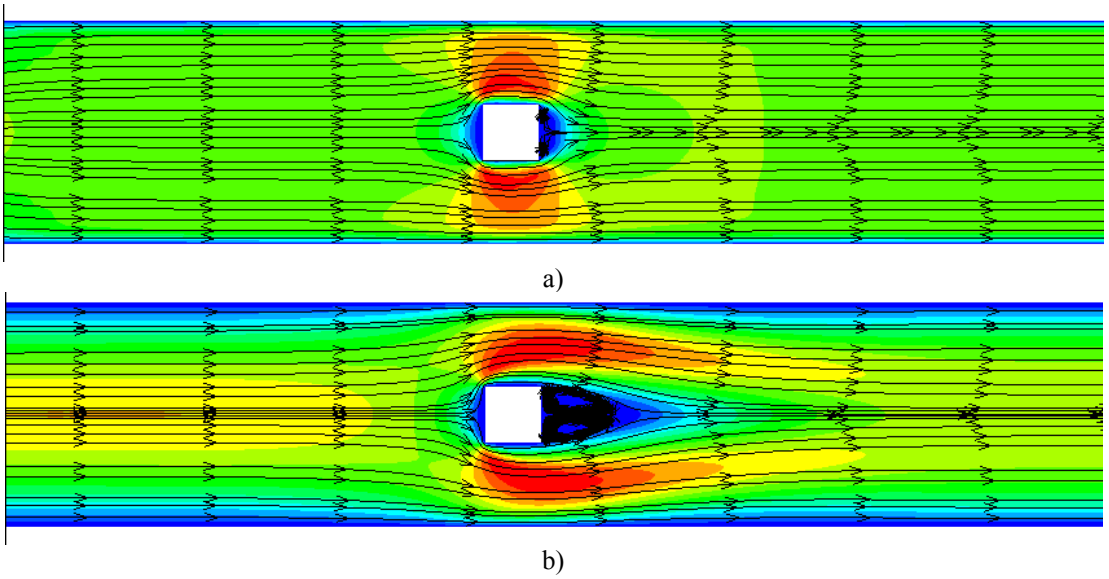

Figure 4 – The components of the velocity and streamlines the flow around a square cylinder with the number of Reynolds number Re = 46 for different time layers a) t = 0.5 sec; b) t = 2 sec; a) t = 3.5 sec

The numerical study of flow around square cylinder viscous flow charts velocity profiles were obtained and compared with the numerical and experimental results, given in paper [3]. (Figure 5) From Figure 5 it can be seen that this problem from the numerical study results are in good agreement with the experimental data [3].

With the help of the developed program of calculations to determine the velocity field over time, acting on a streamlined cylinder circular shape in a viscous incompressible environment including at Re = 1000 on a uniform mesh size of 225 × 500 was performed. In the case of low Reynolds number, the smaller the critical Reynolds number Re * is formed within the stationary unseparated. According to published papers, the critical Reynolds number for flow past a circular cylinder is equal to Re*(40-50) [5].

Figure 6 indicates that at Re = 1000 is one of the vortices of the circular cylinder becomes so long that it breaks off and floats downstream with the fluid. The liquid for the cylinder is twisted again and formed new vortices. This process is known as Karman vortex shedding flow [5] (Figure 6).

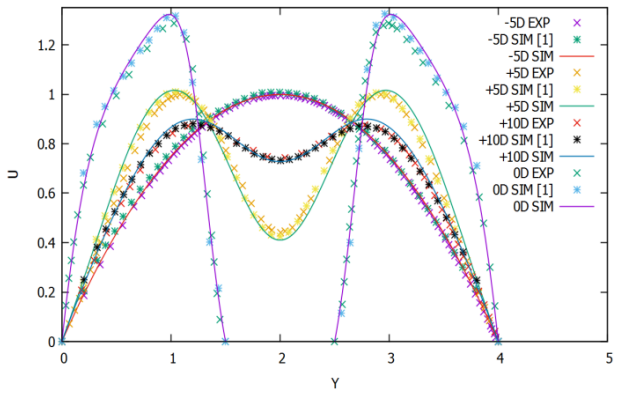

Figure 5 – Velocity profiles in certain parts of the computational domain at Re = 46

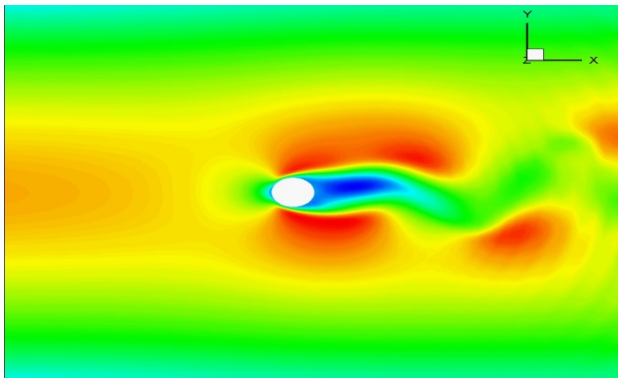

Figure 6 – Velocity contours at a Reynolds number of 1000 and t= 2 sec.

Flow around two circular cylinders located opposite each other was examined at Re = 1000 distance between the cylinders L = 1, the height of the computational domain D = 2.2. Depending on the distance between the two cylinders are formed different types of flows [5].

Figure 7 shows the flow rates at various time points when the distance between the cylinders is L = 2,2. With these arrangement of cylinders formed two vortices that behave more independently. (Figure 7).

By reducing the distance between the cylinders, it can be seen that the vortices formed near the cylinders influence each other [6].

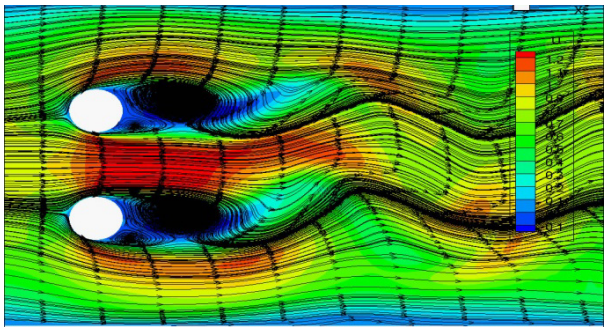

Figure 7 – Velocity contours at a Reynolds number of 1000 and t= 2 sec.

Conclusion

In carrying out work on the basis of numerical solution of two-dimensional Navier-Stokes equations conducted test calculations of the method used for the problem of flow around a square cylinder in a viscous medium, and studied flow around a circular cylinder.

As a result of the study, the data obtained can be used during the installation and location of the building constructions, taking into account the aerodynamic elasticity.

It should be noted that the advantages discussed in the approach are: simplicity of software implementation schemes of high order of spatial sampling, the effectiveness of its application for the calculation of the steady and unsteady flows.

References

1. Chung T.J. Computational fluid dynamics //Cambridge University Press. – 2002. – 1012 p.

2. Fletcher K. Computational Methods in Fluid Dynamics (Russian) – M., 1991. –552 p.

3. Madhavan S. Transition to three-dimensional models for flow past a confined square cylinder. PhD thesis, University of Alberta, Edmonton, AB. – Canada, 2011.

4. Anderson D., Tannehill John., Pletcher R. Computational fluid mechanics and heat transfer (Russian). – M., 1990. – 337 p.

5. Kozlov I.M., Dobergo K.V., Gnesdilov N.N. Application Of RES methods for computation of

hydrodynamic flows by an example of 2D flow past a circular cylinder for Re=5-200 // International Journal of Heat and Mass Transfer. – 2011. –Vol. 54. – P. 887-893.

6. Belov I. Interaction of the Non-Uniform Flows with the Obstacles. – M.: Engineering, 1983. – 166 p.

7. Issakhov A., Mathematical modeling of the discharged heat water effect on the aquatic environment from thermal power plant // International Journal of Nonlinear Science and Numerical Simulation. – 2015. – Vol. 16. – No 5. – P. 229–238, doi:10.1515/ijnsns-2015-0047.

8. Issakhov A., Mathematical modeling of the discharged heat water effect on the aquatic environment from thermal power plant under various operational capacities // Applied Mathematical Modelling. – 2016. – Vol. 40. – No 2. – P. 1082–1096

9. Issakhov A. Large eddy simulation of turbulent mixing by using 3D decomposition method // *J. Phys.: Conf. Ser.* – 2011. –Vol. 318, No 4. – P. 1282-1288, doi:10.1088/1742-6596/318/4/042051.

10. Chorin A.J. Numerical solution of the Navier-Stokes equations // Math. Comp. – 1968. – Vol. 22. – P. 745-762.

UDC 519.863

*Mereyeva Z.A., Turganbayeva A.R.

Faculty of Mechanics and Mathematics,
al-Farabi Kazakh National University, Almaty, Kazakhstan
*e-mail: zere_mereeva@mail.ru

Application of ant colony algorithm for vehicle routing problems

Abstract: In recent years, mathematical methods based on the natural mechanisms of making decisions are extensively appliedin optimization problems.Repeated studies have shown that the most of the processes occurring in the nature are organized very efficiently. In particular, a number of scientific observations were held, which objects were the ant colonies. During the observation, it was found that the length of the path, laid from the anthill to a food source by ants, was close to the optimum value. Moreover, when the environment changes ant colony quickly adapts and finds new shortcuts.In order to improve the efficiency and quality of vehicle routing problem solution new approaches and algorithms are offered. Swarm intelligence algorithms refer to such a type of methods. Developed modifications of the algorithms will improve the quality of the solutions. Quality of the solutions of vehicle routing problems has direct affect on the pricing of the product. The paper provides an overview of numerical methods for solving vehicle problems and the algorithm of ant colonies is considered in details as an example.
Key words: vehicle routing problems, swarm intelligence, ant colony optimization algorithms.

Introduction

Ant is not quick-witted. Single ant is unable to take the slightest decision. The fact that it is extremely primitive: all its actions are reduced to elementary reactions to the environment and its congeners. Ant is not able to analyze, draw conclusions and look for solutions.

These facts, however, disagree with the success of ant as the species. They exist on the planet over 100 million years, building huge anthills, providing them with all necessary and even leading real wars. In comparison with the utter helplessness of individuals, the achievements of ants seem to be unthinkable.

Ants are able to achieve such success because of their sociality. They live only in groups - colonies. All ants of the colony form so-called swarm intelligence. The individuals that make up the colony should not be intelligent: they should only engage in certain, very simple rules, and then the entire colony will be effective.

In recent years, mathematical methods based on the natural mechanisms of making decisionsobtainmore and more applications in optimization problems.

Repeated studies have shown that the most of the processes occurring in the nature are organized very efficiently. In particular, a number of scientific observations were held, which objects were the ant colonies. During the observation, it was found that the length of the path, laid from the anthill to a food source by ants, was close to the optimum value. Moreover, when the environment changes ant colony quickly adapts and finds new shortcuts.

The results of these studies inspired by an Italian mathematician Marco Dorigo to create an approach known as "Ant Algorithm", which has gained widespread use in optimization problems. This algorithm was considered in the works of Kazharov A.A., Kureichik V.M [1], Novikov A.K. [2].

Setting a vehicle routing problem

Capacitated Vehicle Routing Problem (CVRP) isa combinatorial optimization problem in which the set of routes to distant points of several customers should be determined for parks of the vehicles located in one or more depots, herewith the total weight of all orders on each route must not exceed the carrying capacity of the vehicle carrying freight.

The main purpose of the researchis the minimization of the vehicle park and the total distance traversed by all types of transport. Graphical illustration of the problem is shown in Figure.

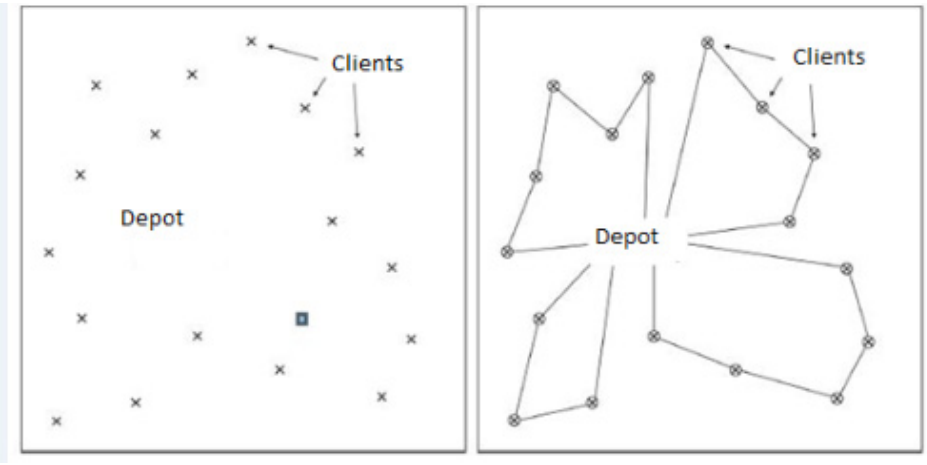

Figure – Graphical illustration of a routing problem

This problem can be represented as a graph *G(V, E)*, where:

$V = \{v_0, v_1, ..., v_n\}$ is a vertex set (v_0 isa depot, $v_{1..n}$is a customer);

E a plurality of ribs $\{(v_i, v_j) \mid i \neq j\}$;

C non- negative matrix of distances(path cost) c_{ij}between consumers;

q_i the volume of cargo shipped the *i*-th customer;

m the number of vehicles;

W capacity constraint of one vehicle;

R_i the route of *i*-th vehicle (*i*=1...m);

(R_i) the route cost R_i;

There are following restrictions on the problem:

- each route begins and ends at the depot;
- each node is part of the route only once;
- each node is visited by only one car;
- the total weight of the order for all the vertices in the route does not exceed W.

The solution of the problem will be a partition of the whole V set of vertices on the routes and the order of traversal on that route.

Basic concepts of the ant algorithm

The basic idea of the ant algorithm is to model the behavior of ant colony in the search path to a food source. Despite the fact that a single ant (system agent) is rather primitive, and alone ant is not able to make optimal decisions, the behavior of the colony in its entirety is reasonable. The intelligence of such kind of system grounded by low-level interaction between agents that occurs via a chemical substance - pheromone laid by ant on its way. Choosing the direction of movement, each agent of the system is based on the experience of previous generations (the amount of pheromone deferred by the colony previously). Thus, the most ants preferred this route, the greater will be delayed pheromone on it, and therefore, the probability, that the next ant will move in this direction, increases. However, this positive feedback can quickly lead to the fact that this route will be the only one, and all the ants will move only in one way. Therefore, in the process of evaporation of pheromone a negative feedback loop is introduced, which ensures us to study new routes.

The behavior of the ants and their properties on choosing the path are described:

1) The ants have their own "memory", which is presented as a list of vertices in which the ant has already been.

2) The ants have a "vision". The quantity, which is inversely proportional to the length of a rib, is accepted as the vision of the ant: $\eta_{ij} = 1/D_{ij}$.

3) The ant is able to pick up the trail of pheromone, which will determine the desire of the ant to pass the rib. Pheromone level at time *t* on the rib D_{ij} will meet $\tau_{ij}(t)$.

4) The transition probability of an ant from vertex *i* to vertex *j* will be determined by the following equation:

$$\begin{cases} P_{ij,k}(t) = \dfrac{\left[\tau_{ij}(t)\right]^{\alpha} \cdot \dfrac{1}{\left[D_{ij}(t)\right]^{\beta}}}{\sum\limits_{l \in J_{i,k}} \left[\tau_{il}(t)\right]^{\alpha} \cdot \left[\eta_{il}(t)\right]^{\beta}}, j \in J_{i,k} \\ P_{ij,k}(t) = 0, j \notin J_{i,k}, \end{cases} \quad (1)$$

where:

α isan empirical coefficient of "the greed" of the algorithm;

β is empirical coefficient of "the herd" of the algorithm;

$J_{i,k}$ is a list of vertices, that have not yet been visited by the ant.

5) On the path each ant lays pheromone, the amount of which is determined by the following formula:

$$\Delta\tau_{ij}(t)=\begin{cases}\dfrac{Q}{L_{k(t)}},(i,j)\in T_k(t)\\ 0,(i,j)\notin T_k(t)\end{cases}, \qquad (2)$$

where Q is a parameter having a value of the order of the optimal path, L_k *(t)* is the length of the route T_k *(t)*.

6) Evaporation of pheromone is determined by the following expression:

$$\tau_{ij}(t+1)=(1-p)*\tau_{ij}(t)+\sum_{k=1}^{m}\Delta\tau_{ij,k}(t), \qquad (3)$$

where m is the number of ants, p is evaporation coefficient *(0 ≤ p ≤ 1)*.

7) The maximum weight of the load, which is able to move each ant on one path does not exceed the value of W.

Description of the ant algorithm for the CVRP problem

The set of vertices $V = \{v_0, v_1, ...,v_n\}$, to which the position and weight of the goods to be delivered to each of the vertices are given, goes as input data for this problem.

At the preparatory stage, there is a need to calculate the distance matrix D between all nodes, set the initial amount of pheromone on all arcs, as well as to determine the coefficients α, β, Q, p. The correct choice of these factors has a significant impact on the resulting optimal response of the algorithm.

Then, the loop is initialized on all the ants. Each ant starts to move from the top to the top. To select the next vertex transition probability is estimated to each of the vertices, that has not yet visited by ant. Probability values depend on the value inversely proportional to the length of the arc connecting the current and selected top, as well as the amount of pheromone on a given arc. Probability is calculated according to the rule (1). Then, a random number is generated and the next vertex is selected depending on what probabilistic range it fells to.

If load capacity of ant W has reached the maximum possible load capacity W_{max}, he has to return to the starting vertex (depot), and then continue to bypass the remaining vertices. This process is completed as soon as the list of $J_{i,k}$ not visited by ant vertices becomes empty.

After traversing all the vertices a number of pheromone on route traversed by ant is updated by the formula (2) and evaporation of the pheromone on all the vertices is updated according to the formula (3).

In the next step the length of route L traversed by k-th ant is compared with the best long routes on the current L *. If the value is less than the current best, then we update the information on the best route.

The algorithm ends when all the ants take over all vertices. A lot of routes T* and the total length of L* are the answer to the problem.

Conclusion

The Ant Algorithms are well suited for use in conjunction with the local search procedures, allowing to find starting points for them quickly.

An important feature of the Algorithm is that due to the negative feedback, even after a large number of iterations, the set of solutions are investigated at the same time, which lets minimize the delay time in the local extremes.

Solution of vehicle problems of routing by using classical method allows to get the result of absolute certainty. However, in the real problems the dimension of input data is high. In this case, the time spent on the search for solutions by using classical method becomes unacceptable. In such cases, the application of The Ant Algorithm, which allows to find a solution that is close in size to the optimum in a short time, is extremely effective.

References

1. Kazharov A.A., Kureichik V.M. Ant algorithms for solving transport problems // News of RAS. Theory and management systems. – 2010. – No 1. – P. 32-45.

2. Novikov A.K. Application of ant algorithm in transport routing problems // Youthscientific and technical bulletin. – 2015. – No 11.

3. Bonavear E., Dorigo M. Swarm Intelligence: from Natural to Artificial Systems – Oxford: University Press. – 1999. – 307 p.

4. Shtovba S.D. Ant algorithms // Exponenta Pro. Mathematics in applications. – 2003. – No 4. – P. 70-75.

5. Svami M., Thulasiraman K. Graphs, netsandalgorithms. – M.: Mir, 1984. – 454 p.

6. Varlamov O.O. Evolutionary databases and knowledge bases for adaptive synthesis of intellectual systems. Mivarnoe informational space. – M: Radio and connection, 2002. – 286 p.

UDC 517.962

*Orazov S.K., Tungatarov N.N.

Faculty of Mechanics and Mathematics,
al-Farabi Kazakh National University, Almaty, Kazakhstan
*e-mail: orazov_sayat@mail.ru

Difference scheme stability investigation for model of barotropic viscous gas

Abstract: In this paper, the technique of convergence of research and the stability difference schemes for the equations of gas dynamics in the presence of an electric field. The work consists in the strict mathematical definition of the conditions of stability and convergence of difference schemes, which relate to the long posed problems of computational mathematics. The studies enable significant progress in the study of the convergence and stability of difference schemes for gas dynamic tasks. The results of the thesis could be used for a wide class of problems of mathematics and mechanics. In the proof of the stability and convergence of difference schemes used by well-known theorems and inequality. All results are formulated as theorems.
Key words: difference scheme, stability investigation, gas dynamic, convergence, electric field, barotropic viscous gas.

Introduction

Many mathematical modern science and technology problems arising in practice, related to the solution of the equations of gas dynamics. Despite the numerous number of methods currently used to solve these equations, work on their further study continues to be important and relevant. Therefore, the problem encountered in the study of the mechanics of the problems are of great scientific and practical interest, as their decision is related to the further development of the theory of differential equations and difference schemes. With their help, we can solve many problems of mechanics, physics and engineering, which are, in one way or another, to the equations of gas dynamics. Such as the aerodynamics of aircraft, astrophysics, weather forecast and more.In practice, more common problem when the gas-dynamic flow affect various additional factors, such as electric, magnetic and gravitational fields, heat conduction and electrical, chemical, and others. Given these events, it follows a lot of problems and difficulties in the correct mathematical formulation and decisions. The solution of such problems analytical method is not always possible, due to the nonlinearity and complexity of the equations. The mathematical problem of determining the solutions of the equations describing the motion of a continuous medium is reduced to finding the unknown functions of three space variables and time, for example, speed, volume, pressure, temperature, density, electric and magnetic intensity. This problem is often very difficult, and it requiresto bring in additional solutions schematization associated with specific physical problems, and make valid simplify their mathematical formulation. Among the gas dynamics models important place occupied by the system of Navier-Stokes equations for viscous compressible fluid. The model takes into account both the compressibility and thermal conductivity and viscosity of the medium. This system is very complicated, it has a complex type, and the equations included in it, the non-linear. Therefore often used and other more simple model of a viscous gas. In particular, if we consider the barotropic motion, the energy equation is detached, although in this case, the system retains the main features - non-linearity and a component type.

Problem description and statement

This section describes the motion of a viscous heat-conducting gas and ions of one species in an electric field. The flow region $\Omega = (0,1)$ has impermeable walls. This chapter is devoted to the study of convergence and stability of a difference scheme for electric gas dynamic model, without taking into account the diffusion coefficient of ions, i.e., and ion mobility factor has the form $b_1 = b / \rho$,

 Printed in Kazakhstan

$b = const > 0$. In this case we consider the so-called pump mode, when the relative velocity of the ions $u_{relative} = bE > 0$ everywhere in $Q_T = \Omega \times (0,T)$.

When you study the issues of sustainability and convergence of the problem is convenient to use Lagrangian coordinates. Keeping to the mass Lagrangian variable the same notation, denoting the specific volume of the system of equations can be written as follows:

$$\frac{\partial v}{\partial t} = \frac{\partial u}{\partial x}, \tag{1}$$

$$\frac{\partial u}{\partial t} = -\frac{\partial p}{\partial x} + \mu \frac{\partial}{\partial x}\left(\frac{1}{v}\frac{\partial u}{\partial x}\right) + \varepsilon E \frac{\partial E}{\partial x}, \tag{2}$$

$$\frac{\partial \theta}{\partial t} = -p\frac{\partial u}{\partial x} + \chi \frac{\partial}{\partial x}\left(\frac{1}{v}\frac{\partial \theta}{\partial x}\right)_x + \mu \frac{1}{v}\left(\frac{\partial u}{\partial x}\right)^2 + b\varepsilon v E^2 \frac{\partial E}{\partial x}, \tag{3}$$

$$\frac{\partial E}{\partial t} = -bE\frac{\partial E}{\partial x}, \tag{4}$$

$$p = \frac{R\theta}{v}, \tag{5}$$

Conditions at the boundaries *x=0, x=1* and the initial data are

$$u(0,t) = u(1,t) = 0,\ E(0,t) = 0,$$

$$\frac{\partial \theta(0,t)}{\partial x} = \frac{\partial \theta(1,t)}{\partial x} = 0, \tag{6}$$

$$u(x,0) = u_0(x),\ v(x,0) = v_0(x),$$

$$\theta(x,0) = \theta_0(x),\ E(x,0) = E_0(x),\ x \in \overline{\Omega} \tag{7}$$

And $v_0(x),\quad \theta_0(x)$ - are strictly positive and bounded functions.

$$0 < m_0 \le (v_0(x), \theta_0(x)) \le M_0 < \infty,\ x \in \overline{\Omega}.$$

We can assume that the specific volume has the property

$$\int_0^1 v_0(x)dx = 1.$$

The difference scheme for the problem

To construct a difference scheme, approximately describing this differential problem is necessary to replace the differential region of the argument continuous variation of a discrete area of change and replace the continuous functions to grid functions and set the difference analogue for the boundary and initial conditions.

In the area $\overline{Q}_T = \overline{\Omega} \times [0,T]$ we introduce the rectangular grids $Q_{h\Delta t}$ and $Q^1_{h\Delta t}$. For grid $Q_{h\Delta t}$ points (x_i, t_{n+1}) will be assigned grid functions speed u_i^{n+1} and voltage E_i^{n+1} to the "half-integer" grid $Q^1_{h\Delta t}$ points $(x_{i-1/2}, t_{n+1})$ - grid functions specific volume $v_{i-1/2}^{n+1}$ and temperature $\theta_{i-1/2}^{n+1}$. Approximating the system of electric gas dynamics differential equations (1.5) - (1.7) with the difference analogs of derivatives we consider the following difference scheme:

$$v_{i-1/2\bar{t}}^{n+1} = u_{i\bar{x}}^{n+1},\ i = 1,..., N, \text{m} \tag{8}$$

$$u_{i\bar{t}}^{n+1} = \mu\left(\frac{u_{i\bar{x}}^{n+1}}{v_{i-1/2}^{n+1}}\right)_x - R\left(\frac{\theta_{i-1/2}^{n+1}}{v_{i-1/2}^{n+1}}\right)_x + \frac{\varepsilon}{2}\left(E_{i+1}^{n+1} + E_i^{n+1}\right)E_{i\dot{x}}^{n+1},\quad i = 1,..., N-1, \tag{9}$$

$$\theta_{i-1/2\bar{t}}^{n+1} = -R\frac{\theta_{i-1/2}^{n+1}}{v_{i-1/2}^{n+1}}u_{i\bar{x}}^{n+1} + \mu\frac{\left(u_{i\bar{x}}^{n+1}\right)^2}{v_{i-1/2}^{n+1}} + \frac{b\varepsilon}{2}v_{i-1/2}^{n}\left(E_i^{n+1} + E_i^{n}\right)E_i^{n+1}E_{i\dot{x}}^{n+1} + \chi\left(\frac{\theta_{i-1/2\bar{x}}^{n+1}}{v_{i-1/2}^{-n+1}}\right)_x,\quad i = 1,..., N-1, \tag{10}$$

$$E_{i\bar{t}}^{n+1} = -bE_i^{n+1}E_{i\bar{x}}^{n+1},\ i = 1,...,N-1,$$
$$n = 0,...,M-1, \qquad (11)$$

and here is $\bar{v}_{i-1/2}^{n+1} = \frac{v_{i-1/2}^{n+1} + v_{i-1/2}^{n}}{2}$. Initial and boundary conditions

$$u_0^{n+1} = u_N^{n+1} = 0,\ E_0^{n+1} = 0,$$
$$\theta_{1/2\bar{x}}^{n+1} = \theta_{N+1/2\bar{x}}^{n+1} = 0,\ n = 0,...,M-1, \qquad (12)$$

$$u_i^0 = u_0(x_i),\ v_{i-1/2}^0 = v_0(x_{i-1/2}),$$
$$\theta_{i-1/2}^0 = \theta_0(x_{i-1/2}),\ E_i^0 = E_0(x_i), \qquad (13)$$
$$x_i \in \Omega_h,\ \ x_{i-1/2} \in \Omega_h^1$$

Also $v_{i-1/2}^0, \theta_{i-1/2}^0$ – strictly positive bounded functions

$$0 < m_0 \le \left(v_{i-1/2}^0, \theta_{i-1/2}^0\right) \le M_0 < \infty,$$
$$i = 1,...,N.$$

We can assume that the difference analog of the specific volume and tensions have properties

$$\sum_{i=1}^{N} v_{i-1/2}^0 h = 1,\ E_{i\bar{x}}^0 \ge 0,\ E_0^0 = 0.$$

Difference equations (1) - (4) approximate the differential equation (5), respectively, with orders $O\left(h^2 + \Delta t\right),\ \ O\left(h + \Delta t\right),\ \ O\left(h^2 + \Delta t\right),\ O\left(h + \Delta t\right)$.

Upper and lower bounds for the difference analog of the specific volume

Due to the fact that the system (1.5) is non-linear, for the convergence of research and the stability of the difference scheme (2.1) - (2.6), it is necessary to obtain estimates for the difference of its decision in the rules grid analogues of Sobolev spaces. So we need to prove an auxiliary lemma.

Lemma 1. If $\left(u^0, E^0\right) \in W_{2h}^1\left(\Omega_h\right)$, $\left(v^0, \theta^0\right) \in W_{2h}^1\left(\Omega_h^1\right)$, moreover $0 < m_0 \le \left(v_{i-1/2}^0, \theta_{i-1/2}^0\right) \le M_0 < \infty,\ i = 1,...,N$. Then for the difference solution $\left(u,\ v,\ \theta,\ E\right)$ of the scheme (2.1) – (2.6) there are a priori estimates

$$\sum_{i=1}^{N}\left[\frac{\varepsilon}{2}\left(E_i^{n+1}\right)^2 v_{i-1/2}^{n+1} + \left(v_{i-1/2}^{n+1} - R\ln v_{i-1/2}^{n+1} - 1\right) + \frac{\left(u_i^{n+1}\right)^2}{2} + \left(\theta_{i-1/2}^{n+1} - \ln\theta_{i-1/2}^{n+1} - 1\right)\right]h +$$
$$+ \sum_{m=0}^{n}\sum_{i=1}^{N}\left[\chi\frac{\left(\theta_{i-1/2\bar{x}}^{m+1}\right)^2}{\theta_{i-3/2}^{m+1}\theta_{i-1/2}^{m+1}\bar{v}_{i-1/2}^{m+1}} + \mu\frac{\left(u_{i\bar{x}}^{m+1}\right)^2}{\theta_{i-1/2}^{m+1}v_{i-1/2}^{m+1}} + \frac{b\varepsilon}{2}\frac{v_{i-1/2}^{m}}{\theta_{i-1/2}^{m+1}}\left(E_i^{m+1} + E_i^{m}\right)E_i^{m+1}E_{i\bar{x}}^{m+1}\right]h\Delta t \le C_0 < \infty, \qquad (14)$$

$$\sum_{i=1}^{N}\left[\frac{\varepsilon}{2}\left(E_i^{n+1}\right)^2 v_{i-1/2}^{n+1} + \frac{1}{2}\left(u_i^{n+1}\right)^2 + \theta_{i-1/2}^{n+1}\right]h \le C_1 < \infty, \qquad (15)$$

$$\frac{1}{2}\left\|E^{n+1}\right\|^2 + \sum_{m=0}^{n}\sum_{i=1}^{N} b\left(E_i^{m+1}\right)^2 E_{i\bar{x}}^{m+1}h\Delta t \le C_2 < \infty, n = 0,...,M-1. \qquad (16)$$

Proof. **Let's multiply (8) to** $\frac{\varepsilon}{2}\left(E_i^{n+1}\right)^2 + 1 - \frac{R}{v_{i-1/2}^{n+1}}$, **(9) to** u_i^{n+1}, **(10) to** $1 - \frac{1}{\theta_{i-1/2}^{n+1}}$, (11) to $\frac{\varepsilon}{2}\left(E_i^{n+1} + E_i^{n}\right)v_{i-1/2}^{n}$. Then, (8) (10) and (11) sum over i to N, equation (9) sum over i to N-1. All equations sum together and over m. To the sum of the right-hand side of the new expression, we apply the formula for summation by parts. Then, revealing the difference derivatives with respect to time and discarding the positive terms on the left-hand side, we obtain estimate (14)

$$\sum_{i=1}^{N}\left[\frac{\varepsilon}{2}\left(\left(E_i^{n+1}\right)^2 v_{i-1/2}^{n+1}-\left(E_i^0\right)^2 v_{i-1/2}^0\right)+\left(v_{i-1/2}^{n+1}-v_{i-1/2}^0\right)+\frac{1}{2}\left(\left(u_i^{n+1}\right)^2-\left(u_i^0\right)^2\right)-\right.$$
$$\left.-R\left(\ln v_{i-1/2}^{n+1}-\ln v_{i-1/2}^0\right)+\left(\theta_{i-1/2}^{n+1}-\theta_{i-1/2}^0\right)-\left(\ln\theta_{i-1/2}^{n+1}-\ln\theta_{i-1/2}^0\right)\right]h+$$
$$+\sum_{m=0}^{n}\sum_{i=1}^{N}\left[\mu\frac{\left(u_{\bar{i}x}^{m+1}\right)^2}{\theta_{i-1/2}^{m+1}v_{i-1/2}^{m+1}}+\frac{b\varepsilon}{2}\frac{v_{i-1/2}^{m+1}}{\theta_{i-1/2}^{m+1}}\left(E_i^{m+1}+E_i^m\right)E_i^{m+1}E_{\bar{i}x}^{m+1}+\chi\frac{\left(\theta_{i-1/2\bar{x}}^{m+1}\right)^2}{\theta_{i-1/2}^{m+1}\theta_{i-3/2}^{m+1}v_{i-1/2}^{-m+1}}\right]h\Delta t\le C_3.$$

To obtain (15) we multiply (8) to $\frac{\varepsilon}{2}\left(E_i^{n+1}\right)^2$, (9) to u_i^{n+1}, (10) remain unchanged, (11) multiply to $\frac{\varepsilon}{2}\left(E_i^{n+1}+E_i^n\right)v_{i-1/2}^n$. Then sum (8), (10) and (11) for from 1 to N, and (9) on the sum from 1 to N-1. Then we add together all the equations and sum over m from 0 to n. At the right side of the new expression the amount will be reduced after the application of the formula for summation by parts to the last three sums. We expand the derivatives with respect to time and sum over m, we have the estimate (15)

$$\sum_{i=1}^{N}\left[\frac{\varepsilon}{2}\left(E_i^{n+1}\right)^2 v_{i-1/2}^{n+1}-\frac{\varepsilon}{2}\left(E_i^0\right)^2 v_{i-1/2}^0+\theta_{i-1/2}^{n+1}-\theta_{i-1/2}^0+\frac{\left(u_i^{n+1}\right)^2}{2}-\frac{\left(u_i^0\right)^2}{2}\right]h+\sum_{m=0}^{n}\sum_{i=1}^{N}\left(u_{i\bar{t}}^{m+1}\right)^2 h\left(\Delta t\right)^2=0.$$

To obtain (16) we multiply (11) to $E_i^{n+1}h\Delta t$ on and sum and m, we have required estimate 16

$$\sum_{m=0}^{n}\sum_{i=1}^{N}E_i^{m+1}E_{i\bar{t}}^{m+1}h\Delta t=-\sum_{m=0}^{n}\sum_{i=1}^{N}b\left(E_i^{m+1}\right)^2E_{i\bar{x}}^{m+1}h\Delta t,$$

or

$$\sum_{i=1}^{N}\frac{1}{2}\left(\left(E_i^{n+1}\right)^2-\left(E_i^0\right)^2\right)h+\sum_{m=0}^{n}\sum_{i=1}^{N}\frac{1}{2}\left(\Delta t\right)^2\left(E_{i\bar{t}}^{m+1}\right)^2h\Delta t+\sum_{m=0}^{n}\sum_{i=1}^{N}b\left(E_i^{m+1}\right)^2E_{i\bar{x}}^{m+1}h\Delta t=0.$$

Lemma 2. Let the conditions of Lemma 1 and $\Delta t=O\left(h^{\alpha+2}\right)$, $0<\alpha<1$. Then $E_{i\bar{x}}^n\ge 0$, $n=1,...,M$, $i=1,...,N$ and for the difference analogue of the specific volume the estimate is

$$0<m_1\le v_{i-1/2}^{n+1}\le M_1<\infty,\ i=1,...,N,\quad n=0,...,M-1, \tag{17}$$

here $m_1,M_1>0$.

Let's proof that lemma, so we can get estimates. Let's write (9) as

$$u_{i\bar{t}}^{n+1}=\mu\left(\frac{u_{i\bar{x}}^{n+1}}{v_{i-1/2}^{n+1}}\right)_x-R\left(\frac{\theta_{i-1/2}^{n+1}}{v_{i-1/2}^{n+1}}\right)_x+\frac{\varepsilon}{2}\left(\left(E_i^{n+1}\right)^2\right)_x, \tag{18}$$
$$i=1,\ldots,N-1,\ n=0,\ldots,M-1.$$

Let's potentiate and express

$$v_{j-1/2}^{n+1}=\frac{v_{j-1/2}^{0}v_{i^*(n)-1/2}^{n+1}}{v_{i^*(n)-1/2}^{0}}\exp\left\{\frac{1}{\mu}\sum_{i=i^*(n)}^{j-1}\left(u_i^{n+1}-u_i^0\right)h-\frac{1}{\mu}\sum_{m=0}^{n}\left[R\frac{\theta_{i^*(m)-1/2}^{m+1}}{v_{i^*(m)-1/2}^{m+1}}+\mu\cdot z_{i^*(m)-1/2}^{m+1}-\right.\right.$$

$$\left.\left.-\frac{\varepsilon}{2}\left(E_{i^*(n)}^{m+1}\right)^2-R\frac{\theta_{j-1/2}^{m+1}}{v_{j-1/2}^{n+1}}-\mu\cdot z_{j-1/2}^{m+1}+\frac{\varepsilon}{2}\left(E_j^{m+1}\right)^2\right]\Delta t\right\}. \tag{19}$$

We introduce the notation

$$B(n,j)=\frac{v_{i^*(n)-1/2}^{0}}{v_{j-1/2}^{0}}\exp\left\{\frac{1}{\mu}\sum_{i=i^*(n)}^{j-1}\left(u_i^0-u_i^{n+1}\right)h+\frac{1}{\mu}\sum_{m=0}^{n}\left(\frac{\varepsilon}{2}\left(E_j^{m+1}\right)^2-\mu z_{j-1/2}^{m+1}\right)\Delta t\right\}, \tag{20}$$

$$I(n)=\exp\left\{\frac{1}{\mu}\sum_{m=0}^{n}\left(R\frac{\theta_{i^*(n)-1/2}^{m+1}}{v_{i^*(n)-1/2}^{m+1}}+\mu z_{i^*(m)-1/2}^{m+1}-\frac{\varepsilon}{2}\left(E_{i^*(m)}^{m+1}\right)^2\right)\Delta t\right\}. \tag{21}$$

From (19) using (20) and (21), we obtain the following equation

$$v_{j-1/2}^{n+1}=v_{i^*(n)-1/2}^{n+1}\left(B(n,j)\right)^{-1}\left(I(n)\right)^{-1}\exp\left\{\frac{1}{\mu}\sum_{m=0}^{n}R\frac{\theta_{j-1/2}^{m+1}}{v_{j-1/2}^{m+1}}\Delta t\right\}. \tag{22}$$

Let us show that the inequality under conditions $b>0, E_{i\bar{x}}^{0}\geq 0,$ where $E_{i\bar{x}}^{n+1}\geq 0, i=1,...,N, n=0,...,M-1.$ Let us note $E_{i\bar{x}}^{n+1}=\omega_i^{n+1},$ where $\omega_i^0\geq 0.$ Let us prove that $\omega_i^{n+1}\geq 0$ for all iand n. Take the difference derivative forward from both sides of the equation (11). Then replace and multiply on equality, sum over from 0 to, using (12), we can write

$$\sum_{i=0}^{N-1}2\left(\omega_{i+1}^{n+1}\right)^{-}\left(\left(\omega_{i+1}^{n+1}\right)^{-}\right)_{\bar{t}}h\Delta t+\sum_{i=0}^{N-1}2b\left(\left(\omega_{i+1}^{n+1}\right)^{-}\right)^3h\Delta t=-\sum_{i=1}^{N-1}2b\left(\omega_{i+1}^{n+1}\right)^{-}\left(\left(\omega_{i+1}^{n+1}\right)^{-}\right)_{\bar{x}}h\Delta t.$$

Then, by replacing we obtain

$$2\left(\omega_{i+1}^{n+1}\right)^{-}\left(\left(\omega_{i+1}^{n+1}\right)^{-}\right)_{\bar{x}}h=\left[\left(\left(\omega_{i+1}^{n+1}\right)^{-}\right)^2\right]_{\bar{x}}h+h^2\left[\left(\left(\omega_{i+1}^{n+1}\right)^{-}\right)_{\bar{x}}\right]^2,$$

$$2\left(\omega_{i+1}^{n+1}\right)^{-}\left(\left(\omega_{i+1}^{n+1}\right)^{-}\right)_{\bar{t}}\Delta t=\left(\left(\omega_{i+1}^{n+1}\right)^{-}\right)^2-\left(\left(\omega_{i+1}^{n}\right)^{-}\right)^2+(\Delta t)^2\left[\left(\left(\omega_{i+1}^{n+1}\right)^{-}\right)_{\bar{t}}\right]^2.$$

By the following amounts apply the formula for summation by parts

$$-\sum_{i=1}^{N-1}bE_i^{n+1}\left[\left(\left(\omega_{i+1}^{n+1}\right)^{-}\right)^2\right]_{\bar{x}}h\Delta t=-bE_N^{n+1}\left(\left(\omega_N^{n+1}\right)^{-}\right)^2\Delta t+bE_0^{n+1}\left(\left(\omega_1^{n+1}\right)^{-}\right)^2\Delta t+$$

$$+\sum_{i=0}^{N-1}bE_{ix}^{n+1}\left(\left(\omega_{i+1}^{n+1}\right)^{-}\right)^2h\Delta t=-bE_N^{n+1}\left(\left(\omega_N^{n+1}\right)^{-}\right)^2\Delta t+\sum_{i=0}^{N-1}bE_{ix}^{n+1}\left(\left(\omega_{i+1}^{n+1}\right)^{-}\right)^2h\Delta t.$$

And we have

$$\left\|\left(\omega^{n+1}\right)^{-}\right\|^2-\left\|\left(\omega^{n}\right)^{-}\right\|^2+\sum_{i=0}^{N-1}(\Delta t)^2\left[\left(\left(\omega_{i+1}^{n+1}\right)^{-}\right)_{\bar{t}}\right]^2 h+$$

$$+\sum_{i=1}^{N-1}bE_i^{n+1}\left(\left(\left(\omega_{i+1}^{n+1}\right)^{-}\right)_{\bar{x}}\right)^2 h^2\Delta t+\sum_{i=1}^{N-1}b\left(\left(\omega_{i+1}^{n+1}\right)^{-}\right)^3 h\Delta t=-bE_N^{n+1}\left(\left(\omega_N^{n+1}\right)^{-}\right)^2\Delta t.$$

Using previous estimates we obtain

$$\left(v_{j-1/2}^{n+1}\right)^{-1}\le C_5N_1=\left(m_1\right)^{-1}\text{or}\,v_{j-1/2}^{n+1}\ge m_1>0,$$
$$j=1,\ldots,N,\,n=0,\ldots,M-1. \qquad (23)$$

Using Granuoll's lemma, we conclude that

$$M_v^{n+1}\le M_1 \text{ или } v_{i-1/2}^{n+1}\le M_1, \qquad (24)$$
$$i=1,\ldots,N,\,n=0,\ldots,M-1.$$

Conclusion

The study of fluid dynamics problems for a wide class of their applicability in a variety of devices electric gas dynamic generator, ion-convection pump, accelerators, feeders, cages in which the conductive medium moves through the channel or pipe in the presence of an electric field, continues to be important and relevant. This thesis studied the questions of convergence and stability of implicit difference schemes for one-dimensional problems gas dynamics. The investigations are as follows:

- constructed difference scheme for model of barotropic viscous gas in the electric field;
- obtained a priori estimates of the first decision of a difference scheme for model of barotropic viscous gas in the electric field;
- a priori estimates for higher derivatives of the solution of a difference scheme for model of barotropic viscous gas in the electric field;
- the convergence and stability of a difference scheme for model of barotropic viscous gas in the electric field;

References

1. Otmar Stuetzer O. Apparent viscosity of a charged fluid // The Physics of Fluids / Published by the American Institute of Physics. – December, 1961. – Vol. 4. – No 4. – P. 1226-1237.

2. Shohet Y. Errors and Stability of the Entry Problem Equations in Laminar Magneto hydrodynamic Flow // The Physics of Fluids / Published by the American Institute of Physics. – June, 1963. – Vol. 6. – No 6. – P. 797-802.

3. Smith C.V., Melcher J.R. Electrohy-drodynamicall induced spatially periodic celluar stokes – flow // The Physics of Fluids – November, 1967. – Vol. 10. – No 11. – P. 2315-2322.

4. Itaya N. The existence and uniqueness of the solutions of the equations describing compressible viscous fluid flow. // Proc. Japan. Acad. – 1970. – Vol. 46. – No 4. – P. 379-382.

5. Tani A. On the first initial boundary value problem of compressible viscous fluid motion // Publisher Res. Institute Mathematical Science. – 1977. – Vol. 13. No 1. – P. 193-251.

UDC 629.191

[1*]Zhilisbayeva K., [1]Doszhan N., [2]Saspayeva A.

[1]Faculty of Mechanics and Mathematics, al-Farabi Kazakh National University, Almaty, Kazakhstan
[2]National center space researches and technologies, Almaty, Kazakhstan
[*]e-mail: zhilisbaeva@mail.ru

Changing the magnetic field intensity during the motion of spacecraft

Abstract: In this paper the change of the intensity vector of geomagnetic field during the motion of the spacecraft in orbit in direct dipole model was investigated. The dependences of the intersection point coordinates of the vector intensity of the geomagnetic field with the unit radius Earth sphere were found, their graphs were built and their extremes were determined. The relations of the intersection point velocity of the vector intensity of the geomagnetic field to the unit radius Earth sphere were found, their graphs were built and their extremes determined. The graphs of each component of the geomagnetic field along the trajectory of the spacecraft and the combined graphs were built.
Key words: Magnetic field intensity, direct dipole, spacecraft, rotational motion, orientation.

Introduction

Among the spacecrafts (SC) functioning currently the majority are low-altitude (altitude less than 1000 km) spacecrafts. It is due to the broad area of use: scientific, technological and educational satellites.

To control flight and experiments conducted on the board of low-altitude spacecraft in near real timeit is needed to create a motion control system in order to solve the problem of determining the orientation quickly and autonomously. For example, information about the state vector of spacecraft with scientific and technological experiments carried out on the board is necessary for the correct interpretation of the results. Herewith, the requirements of accuracy of somestate vector elements of the spacecraft (e.g., orientation) may be low (approximately 5 ° error).

Magnetometers and sun sensors became widespread in the attitude control systems because of their high reliability and efficiency.

A lot of papers devoted to the development of methods focused on determination of orientation of the magnetometric measurements.

It is important to note that an unambiguous one-time definition of orientation only by magnetometric measurements is impossible.

The problem of removing the ambiguity of determining the orientation by magnetometric measurements is achieved either by using a model of movement relative to the center of mass or by aggregation of magnetometric data with information from the additional measuring device.

Currently existing methods of determining the orientation can be divided into two classes: the methods with usage of the movement relative to the center of mass (CM) (integral methods) and methods without usage of them (local).

The relevance of the research topic: In all satellite missions relevant issue is the problem of satellite orientations. The bulk of the logic and algorithms orientations are put into the base instrument onboard the satellite subsystems. Relevance of the topic of this research is to develop algorithms for determining the orientation of the magnetometric satellite, based on a three-axis magnetometer data aggregation.

Development and improvement of systems of orientation of magnetometric satellite. Each study in this subject is a new data, new calculations and new improved algorithms.

Purpose: The aim is to study the existing on-board subsystems designed to determine the orientation used on spacecraft for various purposes, including the development of algorithms for determining the orientation of magnetometric satellite.

Research objectives:

- To develop algorithms for determining the orientation of the magnetometric satellite based on magnetometric data aggregation;

- To study the existing on-board subsystems to determine the orientation used in the magnetometric satellites and their analysis;
- Numerical calculations and analysis of the results.

Methods

Integral methods. The main idea is in usage of a mathematical model of the motion relative to the CM in order to combine measurements taken at a sufficient interval for the treatment of dimensional time.

Determination of orientation using the mathematical model of the motion relative to the CM may be performed on the basis of measurements of one direction. At the same time, however, significant change of direction of the vector being measured in the dimensional range is necessary; otherwise orientation of the spacecraft can be determined only up to an arbitrary rotation about the vector.

Integral methods are not applicable in the case of presence of significant underestimated disturbing moments acting on the spacecraft. Also, this method of determining the orientation is not applicable to solution of the problem of determining the orientation in the time scale near the real.

Local methods. The basis of the local methods of simultaneous determination of the orientation is a method of matching measurements of two or more vectors in the two coordinate systems. As the measured parameters in the calculation of the angular position of the spacecraft values, which characterizessome directions in connected with spacecraft coordinate system, known a priori at the base (the absolute, orbital or in another convenient) coordinate system, are used. If several directions for the spacecraftare determined at the same time, then the number of measurement functions will be sufficient to calculate the matrix of orientationat any moment of time obtaining measurements.

Local methods for determining the orientation are preferred to solve the problem of promptly determining the orientation on board of the spacecraft.

Based on the above solvable goal and objective of the thesis is being formed.

Theoretical and practical significance of the research

The practical significance of the research is the design of onboard subsystems for magnetometric satellite and study of Earth's magnetic field.

Due to the fact that magnetometric measurements are used in research work, it is necessary to consider the model of Earth's magnetic field (EMF).

In the first approximation, the magnetic field of the Earth is considered as a dipole, which it's axis is called geomagnetic axis and it's angle with the Earth rotational axis is ≈ 11,5° (Fig.1).

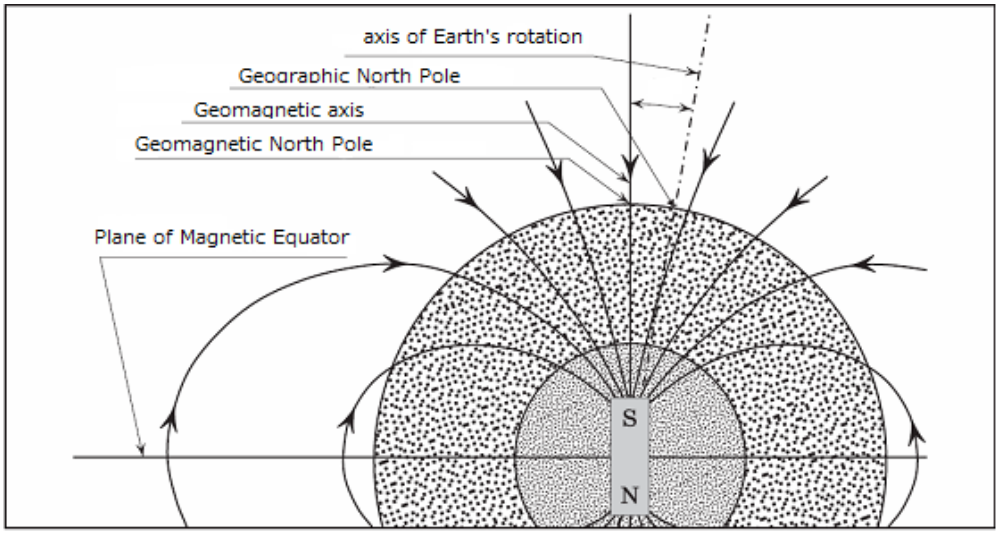

Figure 1 – Earth's magnetic field

The Earth's magnetic field represented as maps of isolines or analytically as relations ofthe intensity to geographical coordinates of the observation point. Analytical representation is more suitable for the study of the influence of Earth's magnetic field on the satellite's motion. Currently, the main part of the Earth's magnetic field is usually described by infinite series:

$$U = \overline{R}_E \sum_{n=1}^{\infty} \sum_{m=0}^{n} \left[\left(J_n^m \cos m\lambda + i_n^m \sin m\lambda \right) \left(\frac{\overline{R}_E}{R} \right)^{n+1} + \left(E_n^m \cos m\lambda + e_n^m \sin m\lambda \right) \left(\frac{R}{\overline{R}_E} \right)^{n} \right] \widetilde{P}_n^m \cos\theta \qquad (1)$$

where, $\widetilde{P}_n^m \cos\theta$ – is associated Legendre function of the first kind; λ – geographic longitude; θ – addition to the latitude of the observation point; $\overline{R}_E$ – the average radius of the Earth; R – the distance from the Earth's center to the observation point; J_n^m, i_n^m – constant coefficients corresponding to the outer part of the Earth's magnetic field; E_n^m, e_n^m – constant coefficients corresponding to the inner part of the Earth's magnetic field;

In tasks of the magnetic control and orientation in the analytical representations of EMF, the external sources are not considered.

The components of the full vector of the magnetic field of the Earth

The earth's magnetic field usually considered in a geographic coordinate system $OX_gY_gZ_g$, whose axes are directed: OX_g – along the geographic meridian to the north; OY_g – along the parallel to the east; OZ_g – along the vertical to center of the Earth (Fig.2), where, $\vec{X}$ – Northern component directed along the axis OX_g, $\vec{Y}$ – Eastern component directed along the axis OY_g, $\vec{Z}$ – Vertical component directed along the axis OZ_g, $\vec{T}$ – Full intensity vector, $\vec{H}$ – horizontal component located in a horizontal plane, D – Magnetic declination, J – magnetic inclination.

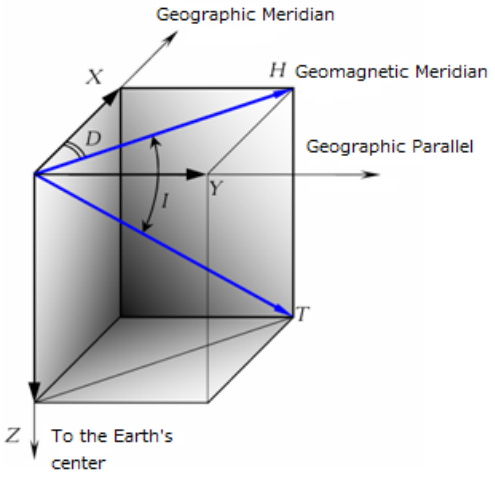

Figure 2 – The components of the full vector of the magnetic field of the Earth

In the study of motion of the spacecraft in the earth's magnetic field the geomagnetic field is represented as dipole field which located in the center of the earth and possessing a magnetic moment $M_E = 8{,}07 \cdot 10^{25}\ G \cdot cm^3$. In the dipole approximation, the different characteristics of the magnetic field are calculated using simple analytical equations:

$$U = \frac{M_E}{R^2} \cos\theta, \qquad (2)$$

$$Z = -\frac{\partial U}{\partial z_g} = \frac{\partial U}{\partial R} = -\frac{2M_E}{R^3} \cos\theta, \qquad (3)$$

$$H = -\frac{\partial U}{\partial x_g} = -\frac{\partial U}{R\partial\theta} = \frac{M_E}{R^3} \sin\theta, \qquad (4)$$

$$T = \frac{M_E}{R^3}\sqrt{1+3\cos^2\theta}\,, \qquad (5)$$

$$tgJ = \frac{Z}{H} = -3ctg\theta = tg\Phi\,, \qquad (6)$$

where, U – dipole potential, Φ – geomagnetic latitude(the angle between the radius vector drawn from the center of the Earth, and the plane of the geomagnetic equator), $\theta = \frac{\pi}{2} - \Phi$ - addition to the magnetic latitude.

Graphs of the magnetic field along the trajectory of the spacecraft

The following characteristics of spacecraft were used as example:

Class orbit – LEO, type of orbit – sun-synchronous, inclination – 98.2°, eccentricity – 0.00190988187027, perigee – 685.0 km, apogee – 712.0 km, period – 98.74 min. According to these data by calculation program were built the graphics of components $\vec{X}$, $\vec{Y}$, $\vec{Z}$ and full intensity vector $\vec{T}$ of EMF along its trajectory (Figures 3-7).

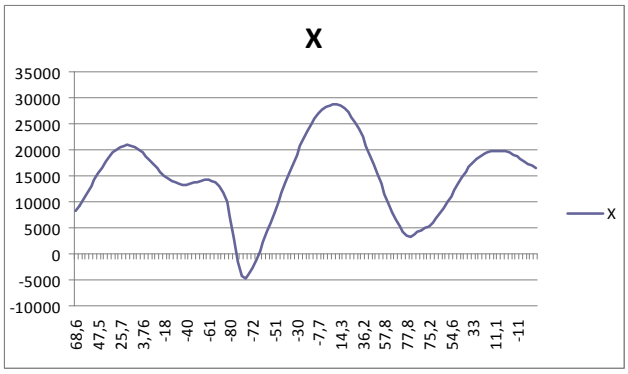

Figure 3 – Graph of X component of the Earth magnetic field along the trajectory of the spacecraft

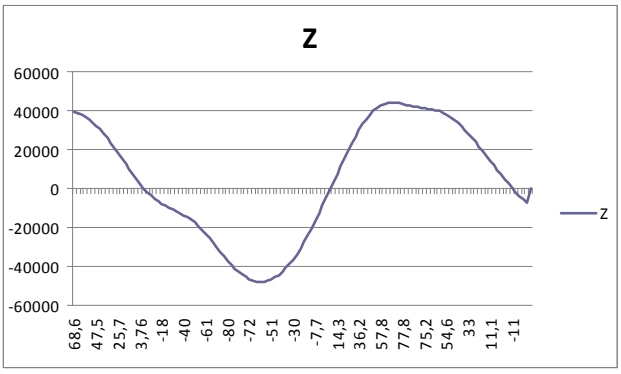

Figure 5 – Graph of Z component of the Earth magnetic field along the trajectory of the spacecraft

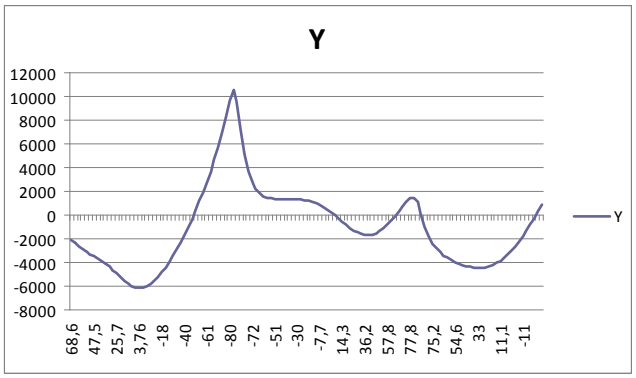

Figure 4 – Graph of Y component of the Earth magnetic field along the trajectory of the spacecraft

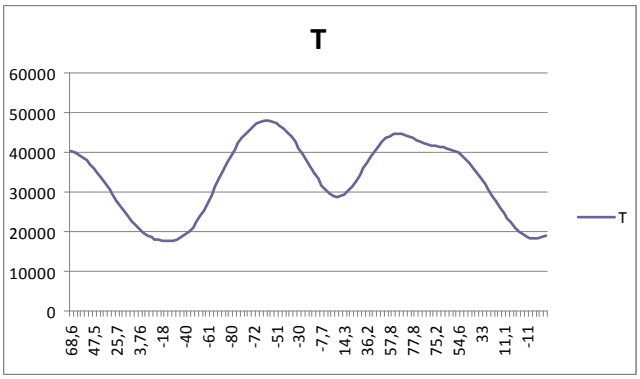

Figure 6 – Graph of intensity T of the Earth magnetic field along the trajectory of the spacecraft

For clarity and analysis, changes in the components of the magnetic field of the Earth resulting curves are combined and represented on one graph (Fig.7).

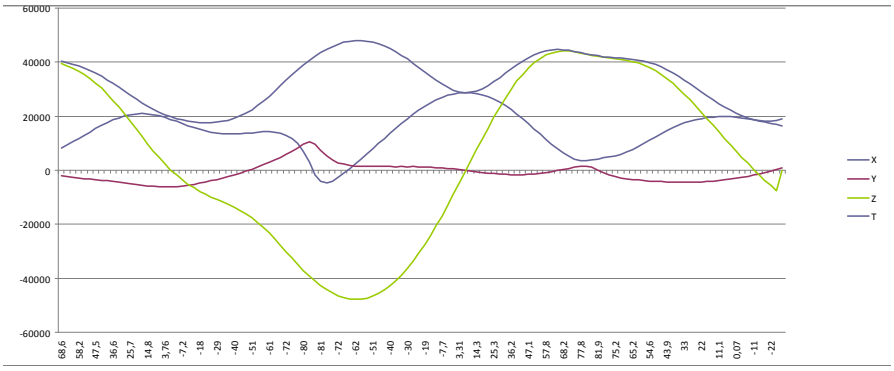

Figure 7 – Graphs of components of the Earth magnetic field along the trajectory of the spacecraft

Simulation of the geomagnetic field perceived by the spacecraft

During the motion of center of mass of a satellite along the orbit, vector of geomagnetic intensitymoves in a complicated manner in space changing at each point of the orbit.

Vector of the dipole field in a point in space with the radius vector $\vec{R}$ represented as

$$\vec{H}^E = \frac{\mu_e}{R^5}\left[R^2\vec{k}_e - 3\left(\vec{k}_e, \vec{R}\right)\vec{R}\right] \qquad (7)$$

where, $\vec{H}^E$ – the dipole geomagnetic field; μ_e – constant of Earth Magnetism (the magnetic moment of the Earth's dipole); $\vec{k}_e$ – ort of dipole axis (in a first approximation coincides with the Earth's axis of rotation), antiparallel to the magnetic moment of the Earth.

To describe the changes in vector $\vec{H}^E$ when the satellite moves in orbit in direct dipole model derive two right geocentric coordinate systems $O\overline{XYZ}$ and $OXYZ$, planes $O\overline{XY}$ and OXY lie in the Earth's equatorial plane(OX axis directed to the ascending node of the satellite orbit), and $O\overline{Z}$, OZ axes coincides with the Earth's axis of rotation. Ω_1 angle – longitude of the ascending node, ω_π – longitude in pericenter, ν – true anomaly of the satellite center of mass, u – argument of latitude. The projections of the $\vec{H}^E$ vector to the axis of the system $OXYZ$ are:

$$H_X^E = -\frac{3\mu_e}{2R^3}\sin i \sin 2u$$
$$H_Y^E = -\frac{3\mu_e}{2R^3}\sin 2i \sin^2 u \qquad (8)$$
$$H_Z^E = \frac{\mu_e}{R^3}(1 - 3\sin^2 i \sin^2 u)$$

The module of the magnetic intensity is determined by the formula:

$$\left|H^E\right| = \frac{\mu_e}{R^3}\sqrt{1 + 3\sin^2 i \sin^2 u} \qquad (9)$$

If the orbital geocentric coordinate system $O\overline{xyz}$ (fig.8) is implemented, $O\overline{z}$ axis of which coincides with the normal to the orbital plane of the satellite and $O\overline{x}$ axis passes through the ascending node of the orbit, then formulas (8) and (9) will be:

$$H_{\overline{x}}^E = -\frac{3\mu_e}{R^3}\sin i \sin u \cos u,$$
$$H_{\overline{y}}^E = \frac{\mu_e}{R^3}\sin i(1 - 3\sin^2 u), \qquad (10)$$
$$H_{\overline{z}}^E = \frac{\mu_e}{R^3}\cos i.$$
$$\left|H^E\right| = \frac{\mu_e}{R^3}\sqrt{1 + 3\sin^2 i \sin^2 u}.$$

Changing the coordinates of the magnetic field intensity during the motion of spacecraft in orbit in the direct dipole model

To investigate the changes of the $\vec{H}^E$ vector along the trajectory of the spacecraft derive $Ox_1y_1z_1$ geocentric coordinate system, which in case of $i \le 90^0$ is obtained from $OXYZ$ coordinate system by counterclockwise rotating at an angle about the OX axis (fig.8). Surface described by intensity vector in the dipole model for $\nu_1 \le 90^0$ case, is a cone (Fig.8).

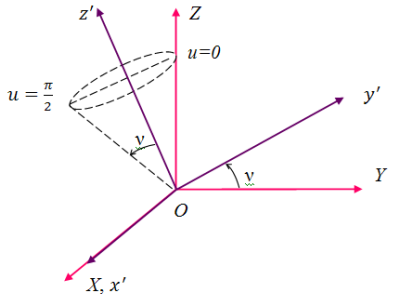

Figure 8 – Moving of an intensity vector $\vec{H}^E$

where, ν_1 is an angle determined from equations:

$$tg\nu_1 = \frac{1.5\sin 2(\pi - i)}{1 - 3\sin^2(\pi - i) + \sqrt{1 + 3\sin^2(\pi - i)}} = \frac{1.5\sin 2i}{1 - 3\sin^2 i + \sqrt{1 + 3\sin^2 i}}, \quad (11)$$

$$tg(\nu_1 - (\pi - i)) = \frac{2 - \sqrt{1 + 3\sin^2(\pi - i)}}{1 + \sqrt{1 + 3\sin^2(\pi - i)}} tg(\pi - i) = -\frac{2 - \sqrt{1 + 3\sin^2 i}}{1 + \sqrt{1 + 3\sin^2 i}} tgi = tg(\nu_1 + i) \quad (12)$$

To identify patterns in the distribution of $\vec{H}^E$ vector combine base of $\vec{H}^E$ with the center of the Earth's sphere of unit radius, then the points of intersection of the sphere with the $\vec{H}^E$ vector will be:

$$x_1 = -\frac{1.5\sin(\pi - i)\sin 2u}{\sqrt{1 + 3\sin^2(\pi - i)\sin^2 u}} = \frac{1.5\sin i \sin 2u}{\sqrt{1 + 3\sin^2 i \sin^2 u}},$$

$$y_1 = \frac{\sin\nu_1 - 3\sin(\pi - i)\cos(\nu_1 - (\pi - i))\sin^2 u}{\sqrt{1 + 3\sin^2(\pi - i)\sin^2 u}} = \frac{\sin\nu_1 + 3\sin i\cos(\nu_1 - i)\sin^2 u}{\sqrt{1 + 3\sin^2 i \sin^2 u}}, \quad (13)$$

$$z_1 = \frac{\cos\nu_1 + 3\sin(\pi - i)\sin(\nu_1 - (\pi - i))\sin^2 u}{\sqrt{1 + 3\sin^2(\pi - i)\sin^2 u}} = \frac{\cos\nu_1 - 3\sin i\sin(\nu_1 + i)\sin^2 u}{\sqrt{1 + 3\sin^2 i \sin^2 u}}.$$

All the functions in (13) are π-periodical by argument of latitude, so it is sufficient to investigate onlyvalues $u \in (0, \pi)$.

The basic laws ofmotion of intensity vector along a trajectory of the spacecraft on cone can be detected by analyzing changes of x_1 and y_1 coordinates for a half-turn of the spacecraft in orbit. To do this, derivatives of the x_1 and y_1 functions are obtained:

$$\frac{dx_1}{du} = -\frac{3\sin(\pi - i)}{\sqrt{(1+3\sin^2(\pi - i)\sin^2 u)^3}}\left(\cos 2u - 3\sin^2(\pi - i)\sin 4u\right) = \\ = -\frac{3\sin i}{\sqrt{(1+3\sin^2 i\sin^2 u)^3}}\left(\cos 2u - 3\sin^2 i\sin 4u\right), \tag{14}$$

$$\frac{dy_1}{du} = \frac{1.5\sin i\sin 2u(-2\cos(\nu_1 + i) - 3\cos(\nu_1 + i)\sin^2 i\sin^2 u + \sin\nu_1\sin i)}{\sqrt{(1+3\sin^2 i\sin^2 u)^3}}. \tag{15}$$

Substituting the value of the inclination of the orbit of spacecraft to the (11)-(15) formulas, we will have:

$$tg(\nu_1 + 98.2^0) = -\frac{2 - \sqrt{1+3\sin^2 98.2^0}}{1+\sqrt{1+3\sin^2 98.2^0}}tg98.2^0, \tag{16}$$

$$tg98.2^0 = \frac{1.5\sin 196.4^0}{1-3\sin^2 98.2^0 + \sqrt{1+3\sin^2 98.2^0}}, \tag{17}$$

$$x_1 = -\frac{1.5\sin 98.2^0\sin 2u}{\sqrt{1+3\sin^2(98.2^0)\sin^2 u}},$$

$$y_1 = \frac{\sin\nu_1 + 3\sin 98.2^0\cos(\nu_1 - 98.2^0)\sin^2 u}{\sqrt{1+3\sin^2 98.2^0\sin^2 u}}, \tag{18}$$

$$z_1 = \frac{\cos\nu_1 - 3\sin 98.2^0\sin(\nu_1 + 98.2^0)\sin^2 u}{\sqrt{1+3\sin^2 98.2^0\sin^2 u}},$$

$$\frac{dx_1}{du} = -\frac{3\sin 98.2^0}{\sqrt{(1+3\sin^2 98.2^0\sin^2 u)^3}}\left(\cos 2u - 3\sin^2 98.2^0\sin 4u\right), \tag{19}$$

$$\frac{dy_1}{du} = \frac{3\sin 98.2^0\sin 2u(\sin\nu_1\sin 98.2^0 - 2\cos(\nu_1 + 98.2^0) - 3\cos(\nu_1 + 98.2^0)\sin^2 98.2^0\sin^2 u)}{2\sqrt{(1+3\sin^2 98.2^0\sin^2 u)^3}} \tag{20}$$

Using the MAPLE program the formulas (18) – (20)were implemented and the graphs of changes of x_1 and y_1 coordinates and $\dot{x}_1$, $\dot{y}_1$ velocities of intensity vectors of the geomagnetic field along the trajectory of the spacecraft were built (Figures 9-13).

The following characteristics of spacecraft were used as example:

Class orbit – LEO, type of orbit – sun-synchronous, inclination – 98.2°, eccentricity – 0.00190988187027, perigee – 685.0 km, apogee – 712.0 km, period – 98.74 min.

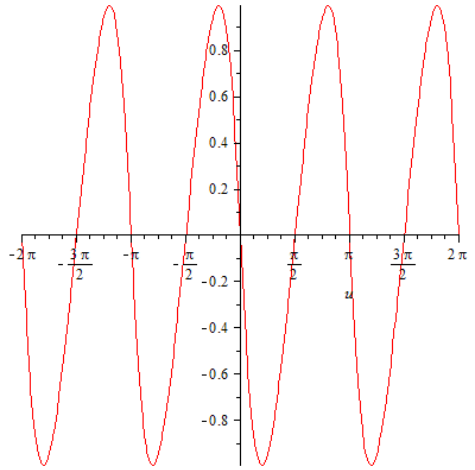

Figure 9 – Change of the x_1 coordinate of intensity vector of the geomagnetic field along the trajectory of spacecraft

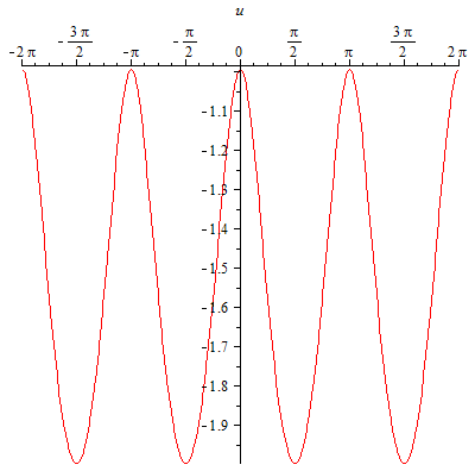

Figure 10 – Change of the y_1 coordinate of intensity vector of the geomagnetic field along the trajectory of spacecraft

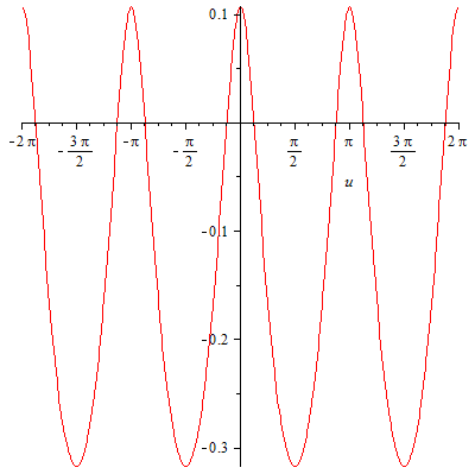

Figure 11 – Change of the Z_1 coordinate of intensity vector of the geomagnetic field along the trajectory of spacecraft

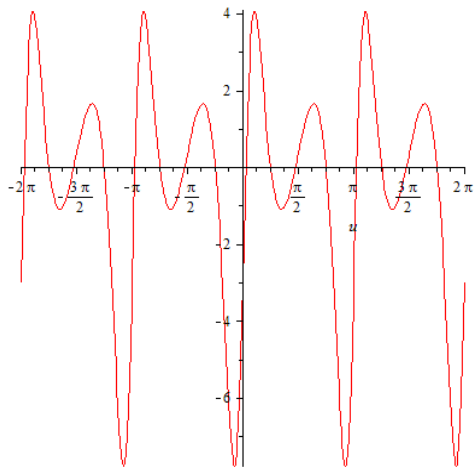

Figure 12 – Change of the $\dot{x}_1$ velocity of intensity vector of the geomagnetic field along the trajectory of spacecraft

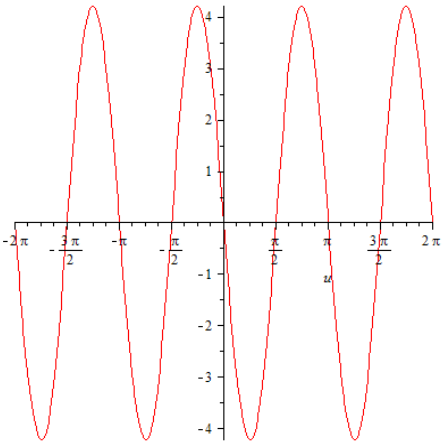

Figure 13 – Change of the $\dot{y}_1$ velocity of intensity vector of the geomagnetic field along the trajectory of spacecraft

Conclusion

The change of the intensity vector ofgeomagnetic field during the motion of the spacecraft in orbit in direct dipole model was investigated.The dependences of the intersection point coordinates of the vector intensity of the geomagnetic field with the unit radius Earth sphere were found,their graphs were built and their extremes were determined.The relations of the intersection point velocity of the vector intensity of the geomagnetic field to the unit radius Earth sphere were found, their graphs were built and their extremes determined.

The graphs of each component of the geomagnetic field along the trajectory of the spacecraft and the combined graphs were built.

The orientation of the satellite relative to the geomagnetic coordinate system was determined.

The projections of intensity of the geomagnetic field in view of components of the geomagnetic field were determined.

These results make it possible to assess the influence of each component of the geomagnetic field on the rotational motion of the satellite, to determine the optimal orientation of the satellite in the geomagnetic field, to develop necessary for this system of magnetic stabilization, etc.

References

1. Parkinson U. Vvedenie v geomagnetism. – Moscow: Mir, 1986 (inRussian)

2. Azad R. O probleme vozniknoveniya magnitnogo polya u vrashchayushchikhsya ob"ektov (Kratkii obzor rabot) // Vestnik RUDN. – 2001. – Vol.1, No 9. – P. 20-26 (in Russian)

3. Gauss K.F. Izbrannye trudy po zemnomu magnetizmu.– M.: Izd-vo ANSSSR. – 1952 (in Russian)

4. Alpatov A.P., Dranovskii V.I., Saltykov Yu.D., Khoroshilov V.S. Dinamika kosmicheskikh apparatov s magnitnymi sistemamiupravleniya. – M.: Mashinostroenie, 1978 (in Russian)

5. Kovalenko A.P. Magnitnye sistemy upravleniya kosmicheskimiletatel'nymi apparatami. – M.: Mashinostroenie, 1975 (in Russian)

6. Beletskii V.V., Khentov A.A. Vrashchatel'noe dvizhenie namagnichennogo sputnika. – M.: Nauka, 1985 (in Russian)

7. Sarychev V.A., Ovchinnikov M.Yu. Magnitnye sistemyorientatsii iskusstvennykh sputnikov Zemli. – M.: VINITII. – 1985 (in Russian)

8. Beletskii V.V. Dvizhenie iskusstvennogo sputnika otnositel'notsentra mass. – M.: Nauka, 1965 (in Russian)

9. Beletskii V.V.Dvizhenie sputnika otnositel'no tsentra mass vgravitatsiannom pole. –M.: Izd-vo MGU. – 1975(in Russian)

10. Yanovskii B.M. Zemnoi magnetizm. –M.: Gostekhizdat. – 1953 (inRussian)

11. Landau L.D., Livshits E.M. Teoreticheskaya fizika. – M.: Nauka. – 1988 (in Russian)

12. Khentov A.A. Passivnaya stabilizatsiya iskusstvennykh sputnikov po magnitnomu polyu Zemli // Kosmicheskie issledovaniya. – 1967. –Vol 5, No 4. – P. 540-553.

13. [http://www.ngdc.noaa.gov/IAGA/vmod/igrf.html]

14. http://www.magnolia.com.ru/db/satellites/133/

15. http://cwer.ws/node/234534/

UDC 004.75

*Sarsembayev M., Turdalyuly M., Omarova P.

Faculty of Mechanic-Mathematical,
al-Farabi Kazakh National University, Almaty, Kazakhstan
*e-mail: magatrone@mail.ru

Cloud data-processing system for the automated generation of combustion models

Abstract: Demands of energy for the twenty-first century and beyond will require the development of alternative, renewable fuel sources. Validating an alternative fuel source or fuel additive inherently comes from a posteriori knowledge: run a series of experiments whose results will assist in determining whether additional experiments should be conducted. Unfortunately, this knowledge is acquired at the expense of the fuel.The development of data-processing system of this type will not only timely and promptly provide engineers predictive chemical models of combustion processes of real fuels, but also will create a basis for organizing and coordination of fundamental data on the thermodynamic and kinetic properties of the hydrocarbon molecules, mechanisms of combustion of the individual components of real fuels and mixtures thereof. As an example, it suffices to mention that due to the inconsistency of data used by different research groups at the same time there are multiple versions of this simple combustion of fuel such as hydrogen, not to mention the much more complex hydrocarbon fuels.PrIMe (Process Informatics Model)- is a new approach for developing predictive models of chemical reaction systems that is based on the scientific collaborator paradigm and takes full advantage of existing and developing cyber infrastructure.

Key words: Cloud data-processing system, combustion models,PriMe, Modeling, combustion, global systems, web-based application, collaborative science.

Develop and maintain up to date detailed predictive models of chemical combustion is impossible without real software tools for analysis, processing and storage of large volumes of initial theoretical and experimental data. Furthermore, the process of continuous renewal of existing and new generation of chemical models is associated with a large number of computations.

Analysis of recent publications on the subject of the development of the kinetic schemes actual fuel combustion suggests that the current system, fully implement the set of computational modules and databases to automate this work, are not used because of the absence. Basically, researchers use computational modules that could be the private components of such a system.

Private task generating kinetic schemes combustion of hydrocarbons was solved a number of research groups [3,6]. RMG is the most advanced system among the cited systems [7] (reaction mechanism generation), the main advantage of which is extensible architecture. The essence of the extensible architecture is to create a hierarchy of derived classes of reaction centers in the molecules of hydrocarbons (and the corresponding rate constants of elementary processes) and the corresponding database, allowing the user to expand the database that is automatically reflected on the results of the hydrocarbon generation kinetic combustion schemes. Unfortunately, the main disadvantage of this system is the lack of direct assessment of the uncertainties in the rate constants of reactions of classes that give her isolated from the follow-up mechanism for the advancement of the generated.

Of particular importance of the presence of chemical mechanisms it has predictive in modeling real-world fuel combustion processes. This is due not only to the high importance of practical problems to be solved, but above all to the fact that computer modeling using detailed chemical information, is an essential part of the modern cycle development and optimization of power plants, which is essential to the achievement of the required parameters for today.

The task of developing and maintaining up to date detailed predictive self-consistent models of real chemical fuel combustion requires today address the following issues: effective use of the latest models of experimental and theoretical data on

the thermodynamic and chemical properties of hydrocarbon molecules; coherence patterns (property of the same materials and basic processes in different models must be the same); use to verify the model of the widest possible range of experimentally measured characteristics of the selected burning fuel (or fuel group); chemical recovery of values of model parameters on the basis of direct and indirect experimental measurements, the use of information about the accuracy of the model parameters for the analysis of uncertainty propagation and evaluation of the reliability of results in multiscale modeling of engineering.

Solution of these problems requires the analysis, processing and storage of large volumes of initial theoretical and experimental data. Furthermore, the process of continuous renewal of existing and new generation of chemical models is associated with a large number of computations. These problems can not be solved without the involvement of a modern information infrastructure: optimal computational algorithms and data management technologies and computing tasks in heterogeneous distributed systems. The scientific problem to be solved by the project aims is to develop the theoretical foundations of a new generation of data-processing system for the automated design of chemical models of real burning hydrocarbon fuels with the assessment of the reliability of the simulation results.

The closest prototype of the universal system, implemented to date, is a web service PrIMe [1,2], created and supported by the group of Professor M. Frenklach. This system implements the functionality associated optimization of kinetic schemes and disseminating the analysis of uncertainties in the modeling process. It is worth noting that at the heart of this system lies Data Collaboration concept, the essence of which is to collect all available direct and indirect experimental information on the combustion process and its subsequent use for the prediction of the required properties of combustion processes. This concept is universal and can be extended to other subject areas. The main limitation of this system is the lack of libraries of models of combustion processes and efficient parallel solvers running on high-performance systems. Also, the possibility of a system limited to a single set of methods for inverse kinetic problem (methods of sequential quadratic programming) solutions, whose capacity may not be enough in the analysis of combustion kinetic schemes of large hydrocarbons.

PrIMe – Process Informatics Model- is a new approach for developing predictive models of chemical reaction systems that is based on the scientific collaboratory paradigm and takes full advantage of existing and developing cyber infrastructure. The primary goals of PrIMe are collecting and storing data, validating the data and quantifying uncertainties, and assembling the data into predictive models with quantified uncertainties to meet specific user requirements. The principal components of PrIMe include: a data Depository, which is a repository of data provided by the community [4,8], a data Library for storage of evaluated data, and a set of computer-based tools to process data and to assemble data into predictive models. Two guiding principles of PrIMe are: open membership- a qualified individual or industrial organization can register to participate in the project; and open source- all submitted data, tools and models will be in the public domain.

The objective of this project was to sustain and extend the development of the PrIMe cyber infrastructure for the practical use by the Combustion community. PrIMe (Process Informatics Model) is a new approach for developing predictive models of chemical reaction systems that is based on the scientific col laboratory paradigm. The primary goals of PrIMe are collecting and storing data, validating the data and quantifying uncertainties, and assembling the data into predictive models with quantified uncertainties to meet specific user requirements. The principal elements of PrIMe include: a data Warehouse which is a repository of data provided by the community, a data Library which archives community-evaluated data, and computer-based tools to process data and to assemble data into predictive models.

Optimizing combustion efficiency and understanding the mechanisms that prevent full energy utilization of fuels relies on detailed knowledge of the underlying physics and chemistry [7]. These systems are generally complex enough that models have been used to explore the effectof different feed and reactor conditions and have been successful in optimizing fuel mixtures and combustor performance. However, the models are extremely complex and often controversial. The data, which parameterize the models and are compared to model predictions, are themselves complex and often open to interpretation. Further, they are developed by multiple labs using different technologies. To keep track of models, parameters,

and data in an integrated framework has proven a necessity in the field of Combustion. The PrIMe initiative is designed to fill this need. In its scientific content, PrIMe is a system approach aimed at establishing the infrastructure, both scientific and CI, in support of developing predictive models of combustion.

The initial phase and development of PrIMe CI has focused on underlying chemical reaction models. There are several important reasons for this strategy. First, modeling of a combustion process begins with a reaction model, which determines the concentrations of chemical specifies and the heat flux, and hence it is only natural to start the new development from this founding stage. It has been our experience1 that most disagreements between models and experiments and most controversies begin with and trace to the selected reaction model. Another factor for starting with reaction models is the fact that chemical kinetics has accumulated much needed data and the missing data can be evaluated using quantum and reaction-rate theories. And finally, the scientific underpinning of the process, also illustrating the feasibility of the approach, has been piloted by the GRI-Mech project.

The PrIMe Workflow Application (PWA) is a web-based application that unifies the components of PrIMe into a single interface [5]. The purpose of this document is to describe the PrIMe Workflow Application architecture and its internal structure. The functionality of PWAcomponents is depicted in the form of Use Case diagrams. Class diagrams, consistencydiagrams, data-base scheme, and components diagrams are used to demonstrate systemdesign and component interaction.

The common structure of PrIMe is consists of the following components:

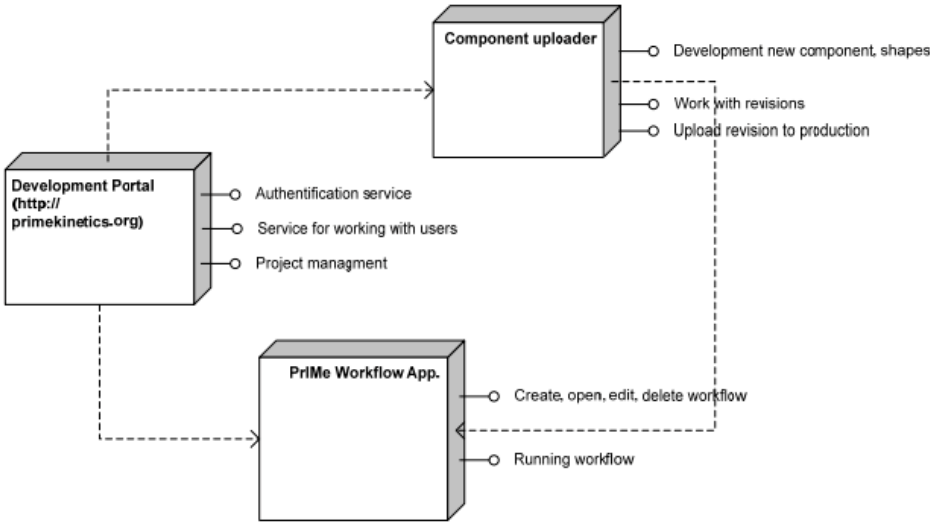

Figure – Components of the PrIMe structure

1. PrIMe Portal is responsible for system user management. It implements user authorization and authentication services, assigns user roles, and manages user permissions. Additionally, it enables users to collaborate. In the PrIMe portal one can find information such as the latest changes, documentation, and operating instructions. The Development Portal provides an interface for two additional systems – Scientific Component Uploader and PrIMe Workflow Application.

2. Scientific Component Uploader (SCU) is used to develop and deploy new scientific components. It allows the scientific component developer to upload a new scientific component, assign resources to components, and edit properties and configuration information of his/her previously developed components. All changes made by developers are stored as separate revisions, allowing a developer to open and edit any existing revisions. Only a user with administrator privileges can create a new revision and deploy it to the PrIMe Workflow Application (PWA).

3. PrIMe Workflow Application (PWA) is the "environment" where a user creates and executes

scientific workflow projects. The scientific workflow project is built using preconfigured scientific components that are linked together in a network. The user can set input and output information for each scientific component and, if applicable, the user.

References

1. M. Frenklach, Transforming data into knowledge-Process Informatics for combustion chemistry, Proceedings of the Combustion Institute, Vol 31, Issue 1, January 2007, Pages 125–140

2. Susnow, R.G.; Dean, M.A.; Green, W.H.; Peczak, P.; Broadbelt, L.J. Rate-Based Construction ofKinetic Models for Complex Systems. J. Phys. Chem. A 1997, 101, 3731-3740

3. Warth, V.; Battin-Leclerc, F.; Fournet, R.; Glaude, P.A.; Come G.M.; Scacchi, G. Computer based generation of reaction mechanisms for gas-phase oxidation. Comput. Chem. 2000, 24, 541-560

4. Rakiewicz A. and Truong. T. N. Application of chemical graph theory for automated mechanism generation. J. Chem. Inf. Comput. Sci., 2003, 43 (1), pp 36–44

5. E. Ranzi, T. Faravelli, P. Gaffuri, and A. Sogaro. Low-temperature combustion: automatic generation of primary oxydation reaction and lumping procedures. Combustion and Flame, 102:179, 1995

6. William H. Green, Joshua W. Allen, Beat A. Buesser, Robert W. Ashcraft, Gregory J. Beran, Caleb A. Class, Connie Gao, C. Franklin Goldsmith, Michael R. Harper, AmritJalan, Murat Keceli, Gregory R. Magoon, David M. Matheu, Shamel S. Merchant, Jeffrey D. Mo, Sarah Petway, Sumathy Raman, Sandeep Sharma, Jing Song, YurySuleymanov, Kevin M. Van Geem, John Wen, Richard H. West, Andrew Wong, Hsi-Wu Wong, Paul E. Yelvington, Nathan Yee, Joanna Yu; "RMG - Reaction Mechanism Generator v4.0.1", 2013

7. Benson, S.W. Thermochemical Kinetics: Methods for the Estimation of Thermochemical Data andRate Parameters2d ed., John Wiley & Sons, New York, 1973

8. www.primekinetics.org

UDC 539.171

[1]Burtebayev N., [1,2*]Alimov D.K., [3]Boztosun I., [1]Kerimkulov Z., [1]Nassurlla M., [1,2]Mukhamejanov Y.S., [2]Yushkov A.V., [1]Sakhiev S.K., [4]Janseitov D.M., [5]Bahtibayev A.N., [5]Pattaev A. and [6]Hamada Sh.

[1]Institute of Nuclear Physics, Almaty, Kazakhstan
[2]Department of Physics and Technology, al-Faraby KazNU, Almaty, Kazakhstan
[3]Faculty of Science Department of Physics, Akdeniz University, Antalya, Turkey
[4]Physics and Technology Department, Eurasian National University, Astana, Kazakhstan
[5]Natural Sciences Faculty, A. Yesevi IKTU, Turkestan, Kazakhstan
[6]Faculty of Science, Tanta University, Tanta, Egypt
[*]e-mail: Diliyo@mail.ru

Investigation of interaction processes of ^{3}He with ^{14}N nuclei at 50 and 60 mev

Abstract: Elastic scattering of ^{3}He on ^{14}N as example of 1p-shell nuclei at 50 and 60 MeV has been investigated within the framework of Optical Model. In the Optical Model analysis, both microscopic double-folding and phenomenological potentials for the real part of the complex nuclear potential have been used. For both microscopic double-folding and phenomenological analysis, the imaginary potential has taken to be Wood-Saxon volume shaped. It is noticed that while a normalization of the strength of the double-folding real potential is needed to explain the structure observed in the experimental data, a good agreement between experimental data is obtained for the phenomenological potential case.
Key words: optical model, double-folding potential, elastic and inelastic scattering, nucleon-nucleon interaction, fresco.

Introduction

The study of the interaction of ^{3}He with ^{14}N nuclei at low energies is of interest both from the point of view of establishing reliable values of the parameters of the internuclear interaction potential of ^{3}He and to study the mechanisms of cluster effect in scattering processes [1].

The elastic and inelastic experimental data of ^{3}He+^{14}N system has been measured in Institute of Nuclear Physics (INP), Almaty as a part of larger experimental research program of the scattering of ^{3}He on light-heavy nuclei with a mass range between 4 and 28. Experiment on the elastic and inelastic scattering of ^{3}He ions with energies 50 and 60 MeV on ^{14}N were carried out on the extracted beam of the isochronous cyclotron U-150M in INP Almaty, Kazakhstan. The spread of the beam energy was less than 1%.

Experimental details

In order to carry out measurements on gas targets a special device [2], a cylinder filled with the studied isotope having input and output windows for the accelerated particles beam made of iron foil (7 mg/cm^2) on indium seals, has been developed and manufactured. Nitrogen isotope ^{14}N (enrichment equal to 99.63%) target thickness was equal to 1.37-7.66 mg/cm^2. For the reaction products registration there is a window with radial diameter equal to cylinder quarter diameter made of Mylar (2.9 mg/cm^2). The exit window is arranged so that the geometrical axis of limiting collimator (having a slope relative to the horizontal plane of the scattering camera equal to 10^o), installed before turning spectrometer always intersects the center of the target gas. The target was mounted in the scattering chamber in two positions for measuring the angular range between 10^o to 96^o and from 84^o to 170^o; in last case it must be rotated around a vertical axis 180 ^{o}. Calculations of the thickness of the target was carried out using vacuum-gauge according to the formula:

$$d = \rho P t\,, \qquad (1)$$

where ρ – density of the gas under normal conditions, P – pressure, t – the visible part of the beam seen by collimator, defined as:

$$t = \left(R - d_1 l / \left(d_1 + d_2\right)\right) sin\alpha \left(1 / sin\left(\theta + \alpha\right) + 1 / sin\left(\theta - \alpha\right)\right)(2), \quad (2)$$

where d_1 and d_2 – collimator diaphragms, R – the distance from the center of the gas target to the current diaphragm d_1, l – distance between the diaphragms, α – angular uncertainty which, as shown in Figure 1, is calculated from the relationship:

$$tga = d_1 + d_2/2l \quad (3)$$

The geometry of the cross-section of the target gas in the reaction plane

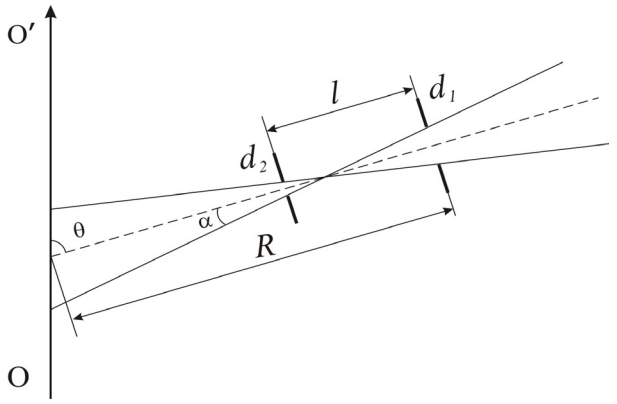

Figure 1 – 00` – direction of the ion beam, d_1 and d_2 – limiting collimator diaphragms, α- angular uncertainty, θ – scattering angle, R – the distance from the center of the target to the operating diaphragm (d_1) spectrometer, l – distance between the diaphragms

The value of the calculated thickness of the gas defined this way column is underestimated by up to 3% of the real at angle of 90 ^{o} and 1-2% at angle 170 ^{o} in the laboratory coordinate system (lcs). This decrease is due to both the deviation of the gas from the cylindrical cord due to the divergence of the beam after forming input collimator and the limited visibility of the cord conical solid angle of the detector, instead of flat sections that were used in the calculations.

The thickness of the gas target was determined by weighing or by energy loss of α - particles from a radioactive source with exactly 6-9%. Nuclear reaction products were detected by using telescope detectors consisting of surface-barrier silicon counters with a thickness - 10, 18, 33, 50, 100 micrometers or ionization chamber, the effective thickness may be smoothly changed in a broad range. In both variants, telescopes as E-counter used diffusion-drift silicon detectors with a sensitive layer thickness of 2 mm. The angular distributions of scattered particles in the investigated nuclei were measured in the angular range of 10˚-170˚ in laboratory coordinate system in steps 3˚ [3].

Experimental data ^{3}He+^{14}N measured at INP Almaty has been analyzed within the standard optical model and microscopic double-folding potentials using the computer code FRESCO. In the next section we present our optical model potentials and then show our results in section 4. We also present our conclusion and future plots in this section.

The Model

In the present calculations, we have used both phenomenological deep and double-folding real potentials with a volume type imaginary potential [4-8]. Our total real potential for these cases consists of the nuclear potential, $V_{Nuclear}$ and the Coulomb and centrifugal potentials, $V_{Coulomb}, V_{Centrifugal}$ respectively.

$$V_{total} = V_{Nuclear}\left(r\right) + V_{Coulomb}\left(r\right) + V_{Centrifugal}\left(r\right). \quad (4)$$

The phenomenological nuclear potential is assumed to have the square of a Woods-Saxon shape.

$$V_{Nuclear}\left(r\right) = \frac{-V_0}{\left(1 + exp\left(r - R\right)/a\right)^2}, \quad (5)$$

where

$$R = r_0\left(A_p^{1/3} + A_t^{1/3}\right) \quad (6)$$

The Coulomb potential [5] due to a charge $Z_p e$ interacting with a charge $Z_t e$ distributed uniformly over a sphere of radius R_C, is also added.

$$V_{Coulomb} = \frac{1}{4\pi\varepsilon_0}\frac{Z_p Z_t e^2}{r}, r \geq R_C, \quad (7)$$

$$\frac{1}{4\pi\varepsilon_0}\frac{Z_p Z_t e^2}{2R_C}\left(3-\frac{r^2}{R_C^2}\right), r < R_C, \quad (8)$$

where R_C = 4.62 fm is the Coulomb radius, and Z_p and Z_t denote the charges of the projectile p and the target nuclei t respectively.

Table 1 – Optical and Double-Folding potential parameters with normalization coefficient N_r

E_b(MeV)	V_0(MeV)	r_0(fm)	a_0(fm)	W_V (MeV)	r_V (fm)	a_V (fm)	N_r	R_C (fm)
50 DF	60	1.2	0.823	8.8 8.8	1.412 1.412	0.747 0.747	0.9	4.62
60 DF	55	1.2	0.823	9.8 9.8	1.318 1.318	0.747 0.747	0.9	4.62

Double-Folding potential [6] is calculated by using the nuclear matter distributions of both projectile and target nuclei together with an effective nucleon-nucleon interaction potential (v_{NN}) are used. Thus, the double-folding potential is

$$V_{DF}(r) = \int dr_1 \int dr_2 \rho_p(r_1)\rho_t(r_2)v_{NN}(r_{12}), \quad (9)$$

where $\rho_p(r_1)$ and $\rho_t(r_2)$ are the nuclear matter density of projectile and target nuclei, respectively. Gaussian density distributions (GD) have been used for both nuclei [4, 7] defined as:

$$\rho(r) = \rho_0 exp(-\beta r^2) \quad (10)$$

where β is adjusted to reproduce the experimental value for the rms radius of the ^{14}N=2.58 fm and ^{3}He=1.877 fm [8]. ρ_0 values can be obtained from the normalization condition

$$\int \rho(r) r^2 dr = \frac{A}{4\pi}, \quad (11)$$

where A is the mass number. We have chosen the most common one, the M3Y nucleon-nucleon realistic interaction. The M3Y has two form, one of them to M3Y-Reid and another is based on the so-called M3Y-Paris interaction [7]. In this work, we use the former form with the relevant exchange correction term due to the Pauli principle, given by

$$V_{NN}(r) = 7999\frac{\exp(-4r)}{4r} - 2134\frac{\exp(-2.5r)}{2.5r} + J_{00}(E)\delta(r)MeV, \quad (12)$$

where

$$J_{00}(E) = 276\left[1 - 0.005E_{Lab}/A_p\right]MeVfm^3. \quad (13)$$

Results and Conclusion

The results obtained by using the microscopic double-folding and phenomenological nuclear potentials with the above-described models are shown in Fig.1 in comparison with the experimental data. As it can be seen from this figure that the real part of the double folding potential requires a normalization in order to obtain a reasonable result. Without this normalization, N_r = 0.9, we could not get an agreement with the experimental data. The phenomenological Woods-Saxon typed potential has provided a better agreement with the experimental data as seen in the same figure with green line.

Double-Folding analysis could effectively tit the experimental data at the first hemisphere (angles lower than 70˚), while phenomenological analysis could tit the experimental data at backward angles. The resulting potentials can be used for model calculations of yields of nuclear reactions necessary for astrophysical applications.

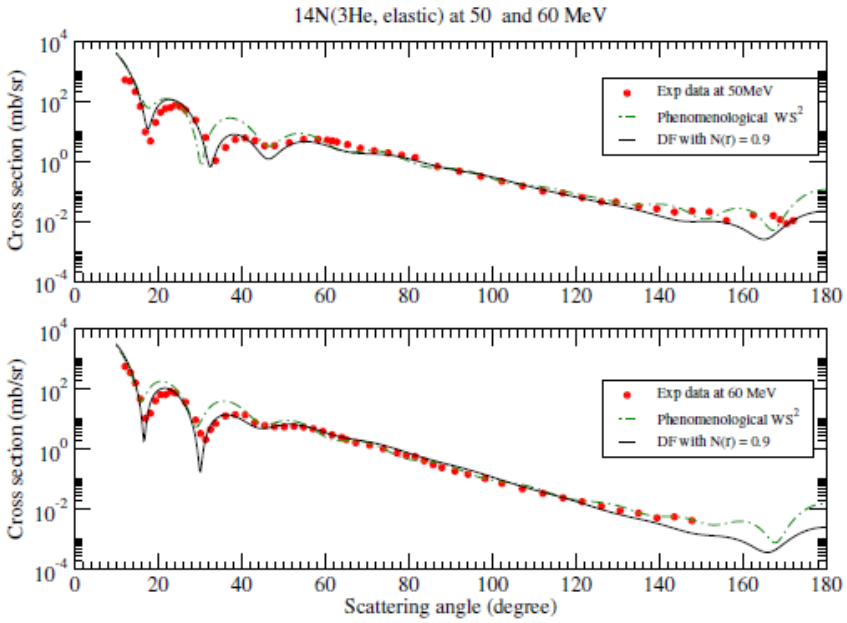

Figure 2 – The results of Double-Folding and phenomenological Wood-Saxon squared potentials in comparison with experimental data for ^{3}He+^{14}N system at 50 and 60 MeV

References

1. Burtebayev N., Hamada Sh., Kerimkulov Zh., Alimov D.K. and Yushkov A.V. Clusterization probability in ^{14}N nuclei // WASET. – 2014. – Vol. 86. – P. 630-634.

2. Duysebaev A.D., Ivanov G.H., Burtebayev N.T., Berger A.A., Arzumanova Z.M. Gas target // Izv. AN KazSSR. – 1984, – Vol. 4. – P. 73-74.

3. MAESTRO-32 MCA Emulator for Microsoft Windows 98. 2000. NT. and XP A65-B32 Software // Users Manual Software Version 6.

4. Burtebayev N., Alimov D.K., Boztosun I. and et.al. Interaction of 1*p* nuclei: Case of 14N+12C Elastic Scattering at 21.0 MeV // Journal of Physics. Conference Series. – Turkey. – 2015. – Vol. 590. – P. 1-5.

5. Kucuk Y. and Boztosun I. Global examination of the ^{12}C + ^{12}C reaction data at low and intermediate energies // Nucl. Phys. A. – 2006. – Vol. 764. – P. 160-180.

6. Stock R., Jahnke U., Hendrie D. L., Mahoney J., Maguire C. F., Schneider W.F.W., Scott D. K. and Wolschin G. Contribution of alpha cluster exchange to elastic and inelastic^{16}O+^{20}Ne scattering // Phys. Rev. C. – 1976. – Vol. 14. – P. 1824 – 1831.

7. Karakoc M. and Boztosun I. α−α double folding cluster potential description of the^{12}C+^{24}Mg system // Phys. Rev. C. – 2006. – 73. – 047601. – P. 1-4.

8. Vries H.De., Jager C.W.De. and Vries C. De. At. Data and Nucl. Data Tables. – 1987. – Vol. 36. – P. 495.

UDC 628.9:662.92; 538.953-405

Bolegenova S.A., Askarova A.S., Bekmukhamet A., Bolegenova S.,
Maximov V., *Ospanova Sh., Manabayeva R., Utelov S.

Al-Farabi Kazakh National University, IETP, al-Farabi 71, 050040 Almaty, Kazakhstan
*e-mail: shinar_ospanova87@mail.ru

3D modeling high temperature flows in the combustion chambers of the power plants

Abstract: In this paper the results obtained by the numerical method of modelling of Ekibastuz coal burning in BKZ-420 combustion chamber of Kazakhstan's coal-fired Power Plant are presented. They are devoted to the numerical simulation of combustion processes in the furnace boiler BKZ-420. Boiler's steam generating capacity 420 T/h. Boiler has six vertical pulverized coal burners arranged in two levels with three burners on the front wall of the boiler. High ash, low-grade coal from Ekibastuz burned in the furnace. Its ash content is 39 %, volatile – 24 %, humidity – 5 %, highest calorific value is 16 750 kJ/kg. In this research the main harmful gases distribution characteristics of the concentration of carbon oxides (CO and CO_2), nitrogen dioxide (NO_2), and oxygen O_2 are shown.
Key words: fuel, turbulent flow, numerical method, boiler, burner, high-energy fuel.

Introduction

It is now one of the fastest growing areas in sources in more efficient and economical way. The efficient combustion of solid fuel in combustion chambers and the efficient heat transfer to water and steam in steam generators are essential for the economical operation of power plants. Heat transfer problems pertaining to the combustion in industrial furances are great importance to the engineering designer of boilers and steam generators in most industrial flame applications, the achievement of high heat transfer rates is a main target and desirable. According to the IEA coal is estimated to remain the second largest source of energy also in the years to come [1-3]. Over the longer term, coal is even projected to again become the number one primary source of energy. Figure 1 is showing the past and future shares of primary energy amongst different sources. This scenario assumes the increase in coal consumption, based on the proven fossil fuel reserves and the future development of new technologies, the increase in utilisation of renewables, especially of biomass, and the decline of oil and gas consumption.

At the present work by means of 3D – Finite Volume (Fig-2) simulation tool FLOREAN developed at the institute for Heat and Fuel technology TU Braunschweig heat and mass transfer processes in furnaces with swirl burners in box-firing system are considered [4-5].

On the front wall of the BKZ-420 boiler furnace are six dual-flow pulverized coal burner (Fig. 2) on two levels include three stages. The extreme burner turned to the center of furnace by 8 degrees. We can see on the Figure 3 and in the opposite side wall of the burner area of second layer has a hole for feeding secondary air to the center turned 45 degrees and whose dimensions 14x60 sm. Productivity of one burner 12 t / h of Ekibastuz coal. In carrying out computational experiments at the initial stage you need to build the geometry of the object, as well as get it finite difference grid.

Industrial implementation of any new technology is not possible without preliminary analysis of advantages and disadvantages suggested method. The rapid development in computer sciences gives the advance to computational techniques to be used for simulation of complex combustion processes in industrial furnaces. Products of combustion contain different harmful substances and the emission of these components grows into a great problem. Industrial development causes an increase in hydro carbonaceous fuels' consumption. These fuels contain harmful and poisonous components such as carbonic oxide (CO), nitric oxide (NO), sulphur dioxide, acid sulphate, lead combinations and different hydrocarbons, etc.

To decrease emissions of harmful substances various methods are applied, including special fire regimes (organization of combustion process),

which suppresses the formation of harmful substances in flame and two-stage burning, when the burners work with low air surplus. In this way numerical experiments became one of the most effective and suitable means for detail analysis and in-depth study of physical and chemical phenomena.

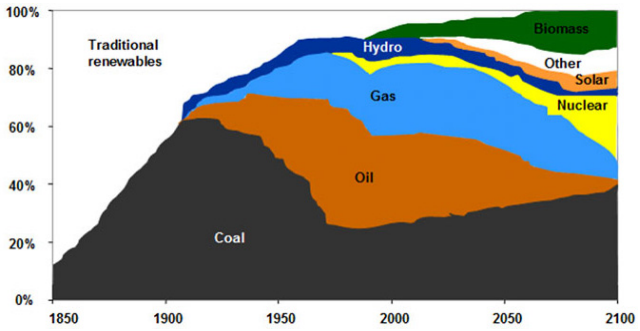

Figure 1 – Historic and future world primary energy mix (scenario 2100)
Source: World Coal Institute 2014

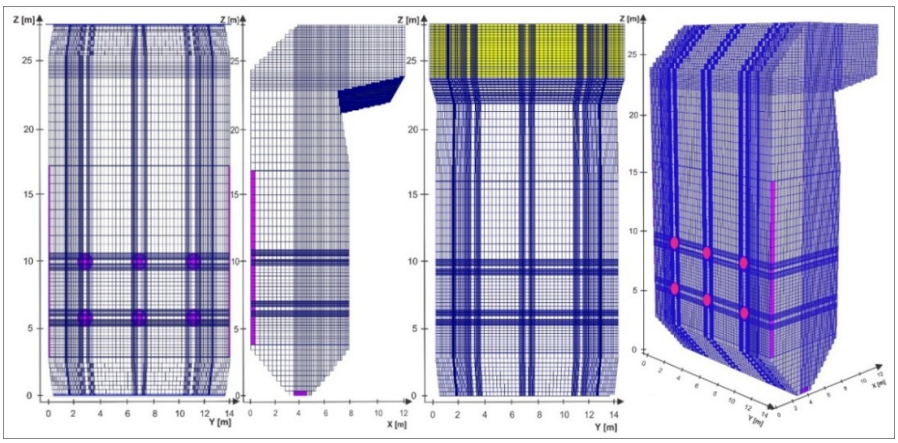

Figure 2 – General view of the BKZ-420 combustion chamber of the Almaty TPP-2 on the control volumes

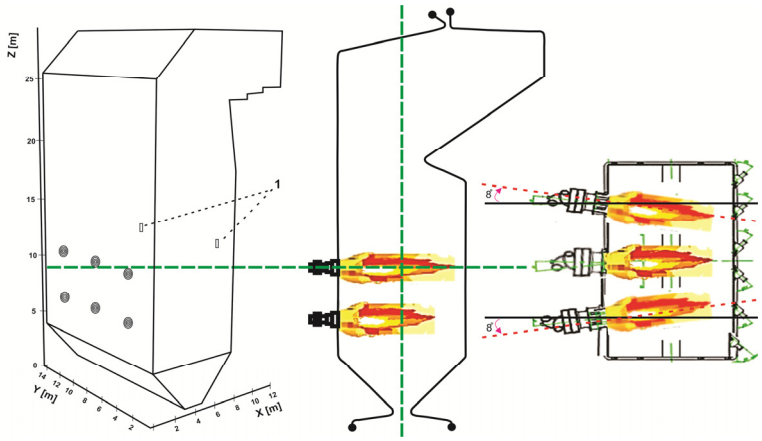

Figure 3 – General view of the BKZ-420 combustion chamber

Mathematical model

Among the methods of modeling the combustion of pulverized fuel most widely used method based on the Euler, an approach to describe the motion and heat transfer of the gas phase. This method uses the spatial balance equations for mass, momentum, the concentrations of gaseous components and energies for the gas mixture. To describe the motion of single particles and heat mass transfer of fuel along their trajectories used Lagrange approach. Turbulent flow structure is described by a two-parameter of k-ε model of turbulence, where k – the kinetic energy of turbulence, ε – turbulent energy of dissipation. The mathematical description of physical and chemical processes based on the solution of balance equations. In general, these equations contain four terms describing:

- change in the value of time;
- convective transfer;
- diffusive transfer;
- source or sink.

In general, for numerical solution the whole computational domain is divided into discrete difference grid point, or volume, continuous field variables is replaced by discrete values at the nodes of the grid, and derivatives in the differential equations are replaced by their approximate expressions in terms of the difference of function values at grid points. In the present study for the problem is solved using the method of control volume. The system of algebraic equations for the differential equation of control volume for each balanced value is as follows:

$$a_P\phi_P = \sum_n a_n\phi_n + S_\phi . \qquad (1)$$

Coefficients are determining the contribution of convective and diffusive flow in all directions at each point of control volume. As a result of approximation of equation were obtained algebraic equation for each control volume and for each unknown variable ϕ_n. For each cell in the computational domain used physical laws of conservation and differential equations describing these laws (transfer equation), integrated over the volume of each cell. FLOREAN is based on the numerical solution of the Reynolds averaged balance equations for mass, species, energy and momentum. It predicts gas flows, species concentrations, temperature fields due to combustion, radiation and convective heat transfer and the pollutant formation and destruction in furnace chambers. The mean flow equations are investigated by the *k-ε* turbulence model.

The changes of the concentrations of flue gas components and the fuel due to the combustion are taken into account in the source sink terms by appropriate sub models. In addition, in the source sink term the heat balance takes into account the energy release due to the combustion reactions and the significant heat transfer due to radiation using a six flux radiation model. Equation for conservation of thermal energy is written in terms of the enthalpy *h*. Radiation heat transfer is determined by 6 flux radiation models by Lockwood, etc. [6-7].

Pulverized coal flames are turbulent reacting two-phase flows. Particle presence is approximated as continuum and the mean particle velocity is assumed to be approximately equal to the gas phase velocity. In the standard *k-ε* model written basic transport equation of turbulent kinetic energy *k*:

$$\frac{\partial\left(\overline{\rho}k\right)}{\partial t} = -\frac{\partial\left(\overline{\rho}\,\overline{u}_j k\right)}{\partial x_j} + \frac{\partial}{\partial x_j}\left[\frac{\mu_{eff}}{\sigma_k}\frac{\partial k}{\partial x_j}\right] + P - \overline{\rho}\cdot\varepsilon \qquad (2)$$

where, P – production of turbulent kinetic energy, which is defined by the following equation:

$$P = \left[\mu_{turb}\cdot\left(\frac{\partial\overline{u_i}}{\partial x_j} + \frac{\partial\overline{u_j}}{\partial x_i}\right) - \frac{2}{3}\cdot\rho\cdot k\cdot\delta_{ij}\right]\cdot\frac{\partial\overline{u_i}}{\partial x_j} \qquad (3)$$

The equation for the turbulent kinetic energy dissipation ε was written as:

$$\frac{\partial\left(\overline{\rho}\,\varepsilon\right)}{\partial t} = -\frac{\partial\left(\overline{\rho}\,\overline{u}_j\varepsilon\right)}{\partial x_j} + \frac{\partial}{\partial x_j}\left[\frac{\mu_{eff}}{\sigma_\varepsilon}\frac{\partial\varepsilon}{\partial x_j}\right] + C_{\varepsilon,1}\cdot\frac{\varepsilon}{k}\cdot P - C_{\varepsilon,2}\cdot\frac{\varepsilon^2}{k}\cdot\overline{\rho}$$

The turbulent viscosity is determined by the equation of Prandtl – Kolmogorov:

$$\mu_t = C_\mu \cdot \rho \cdot \frac{k^2}{\varepsilon},$$

where these are empirical constants [8]:

$$C_\mu = 0.09; \quad \sigma_k = 1.00; \quad \sigma_\varepsilon = 1.30;$$

$$C_{1\varepsilon} = 1.44; \quad C_{2\varepsilon} = 1.92.$$

The boundary conditions for the turbulence model are defined as follows (kinetic energy of turbulence at the inlet):

$$k_{in} = 1.5(u_{i,in} Tu)^2$$

It should be noted that the modeling of flows in the presence of turbulence, which are taken as a basis for solving the equations for the turbulent characteristics (kinetic energy of turbulence and its dissipation), allows to obtain the desired accuracy of the solution, while excluding non-useful machine costs associated with obtaining it.

Results of CFD research

Simulation tool FLOREAN allows to get detailed information about furnace performance including velocities, temperature, thermal radiation and concentration distributions, etc. within the furnace and along the walls. The efficient combustion of solid fuel in combustion chambers and the efficient heat transfer to water and steam in steam generators are essential for the economical operation of power plants. This information is useful to evaluate the combustion process and to design optimal furnaces. FLOREAN will also be very useful in improving combustion process of different fuels in industrial boilers, optimizing operation and minimizing pollutant emission [9-11].

Consequently, the **FLOREAN** – code was used to predict thermal and hydrodynamic aspects of flue gases mixing in the near wall region and inside the furnace. In the case of **Over Fire Air** (OFA) technology of simulations show that effective mixing between flue gases and over-fire air is of essential importance for CO re-burning and low NOx emissions:

$$2CO + O_2 = 2CO_2 + 571 \text{ kJ/mol}.$$

The special importance during the combustion of pulverized coal gets the oxidation of carbon to carbon monoxide CO, as further CO, reacts with oxygen in the air, «burns down» to CO_2, while allocating thus the maximum energy equal to 571 kJ/mol [12]. Analysis of figures 4-5 shows that maximum values of carbon monoxide CO takes in the central section in location area of burners, because here there is observed the region of high temperatures (~1740 ºC), there is a large concentration of fuel carbon and oxidant's oxygen.

The figure 4 represents the three-dimensional distribution of the concentration of carbon monoxide CO in the lower section of the burner (Z=10,8 м) and the figure 5 shows the same disrtibution in the longitudinal sections (Y1 = 2.95m, Y3 = 11.47 m) of the combustion chamber.

Comparative analysis of the graphs in Figure 4 shows that the mass flow of additional air, which is equal to 5 kg/s, the maximum value of the CO concentration reaches $1.72 \cdot 10^{-2}$ kg/kg, and at 10 kg/s reaches the value of $9{,}3 \cdot 10^{-3}$ kg/kg. This is due to the fact that the value of air of 5 kg/s temperature in the combustion chamber more than at 10 kg/s and fuel oxidation process occurs actively. Analysis of Figure 4 shows that the concentration of carbon monoxide CO near the wall, which is opposite for the burners with holes is less for the case where the secondary air flow rate is 10 kg/s.

In the figure 5 there are represents the three-dimensional distribution of the concentration of carbon monoxide CO in the lower section of the burner (Z = 6.82 m) and longitudinal sections (Y1 = 2.95m, Y3 = 11.47m) of the combustion chamber. May be noted that the concentration of carbon monoxide CO in the whole cross-sections indicated as less than in the case where the additional air flow is 10 kg/s. Such a reduction in the concentration of CO can be explained by the greater concentration of oxidant (O_2) for this case, and a more complete combustion of the carbon to CO and its further conversion into CO_2.

The figure 6 shows the distribution of the mean values of the concentrations of carbon monoxide CO by height of the combustion chamber for two different values of the additional air mass flow through the holes which are located on the walls opposite for the burners.

We can see that as the three-dimensional color graphs on the carbon monoxide field at the outlet from the combustion chamber at a mass flow of air, equal to 5 kg/s, the concentration of carbon monoxide CO is higher compared with the case when the flow rate is 10 kg/s.

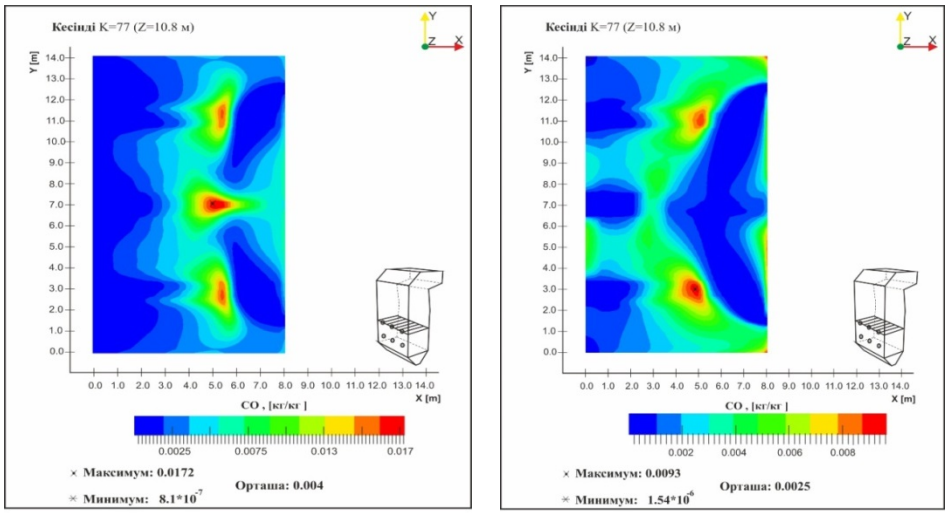

a) 5 kg/s b) 10 kg/s

Figure 4 – The distribution of the carbon monoxide concentration CO in the cross section of the combustion chamber in the zone of upper burners (h = 10.8 m)

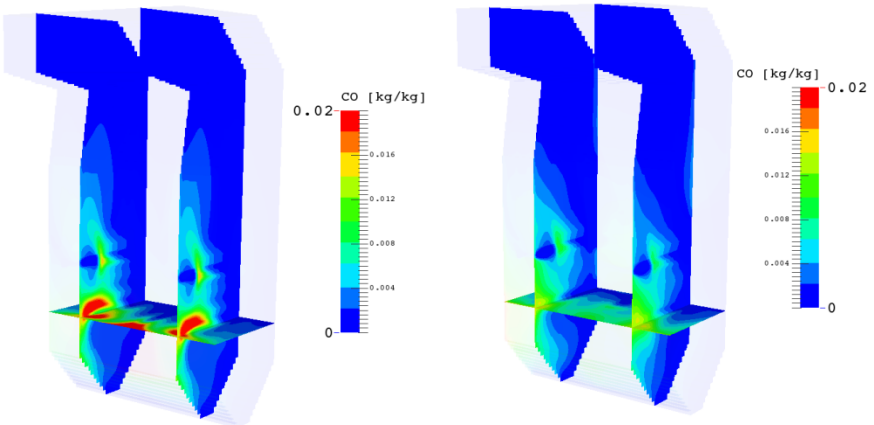

a) 5 kg/s b) 10 kg/s

Figure 5 – The three-dimensional distribution of the concentration of carbon monoxide CO in the lower section of the burner (Z = 6.82 m) and longitudinal sections (Y1 = 2.95m, Y3 = 11.47m) of the combustion chamber

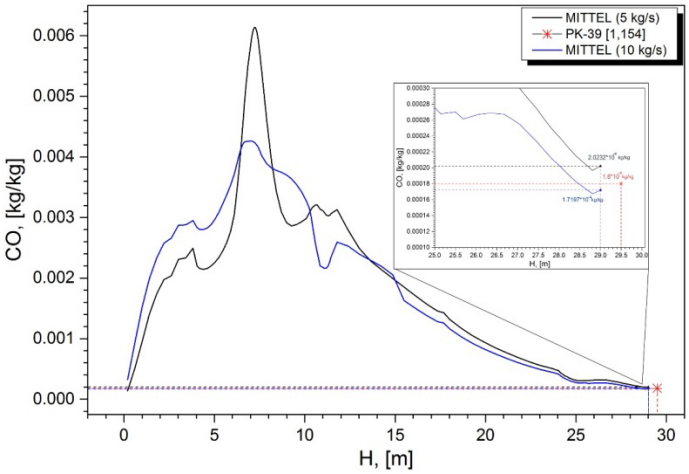

Figure 6 – The distribution of the concentration of carbon monoxide CO by height of the combustion chamber

Analysis of Figure 6 shows that the two curves reach a maximum in the location area of the burners. This is due to the largest concentration of entering in this part of the combustion chamber fuel 's carbon and oxidant's oxygen, the intensity of physical and chemical interactions between them, which gives a high temperature here and heat generation due to chemical reactions between the components of the fuel and oxidant.

Analysis of figures 7-8 shows that the distribution of carbon dioxide CO_2 is completely opposite to the character of the distribution of carbon monoxide CO. One can see that in the upper zone of burners at a height of 10.8 meters the average concentration of carbon dioxide CO_2 is

additional air through the holes in the wall of the combustion chamber, which are located opposite the burner devices is 10 kg / s, provides the optimal combustion mode.

Figure 9 provides a comparative graph of the distribution of average values of the carbon dioxide CO_2 by height of the combustion chamber for two values of air mass flow rate of 5 kg/s and 10 kg/s. By analyzing the graph it can be seen that in location area of the burners, and above them, the concentrations of carbon dioxide in the case when the flow rate of additional air through the holes in the wall of the combustion chamber which are located opposite the burners is 10 kg/s higher than for the air flow rate 5 kg/s. This is confirmed by the three-dimensional fields of concentrations of CO_2, presented in the Figures 7-8. Obviously this is due to the fact that in the case where the amount of secondary supplied air is greater, the combustion equal to 1.104 kg/kg for the additional flow rate of air – 5 kg/s and 0.11 kg/kg is for flow rate 10kg/s. In contrast to the distribution monoxide CO, the average concentration of carbon dioxide CO2 as it moves out of the combustion chamber increases and the outlet takes a value equal to 0.172 kg/kg for the flow rate of additional air – 5kg/s (Fig. 8a) and 0.164 kg/kg to flow rate 10 kg/s (Fig. 8b).

When flow rate of the additional air is equal to 10 kg/s at the outlet of the combustion chamber the concentration of carbon dioxide CO_2 4.65% is less than a flow rate of air 5kg/s, which corresponds to a maximum permissible standards accepted in current TPP. Therefore, we can conclude that the second case of combustion of fuel when the flow rate of reaction with formation of CO_2 is occurred more intensively.

At the outlet of the CO_2 concentration of the combustion chamber at high flow rate of air is less because the formation of carbon dioxide is dependent on the temperature values. In the case where the additional air flow rate is 10 kg / s, the temperature at the outlet of the combustion chamber is lowered by 58 ° C, create conditions for incomplete reaction afterburning CO to CO_2, which resulted in a decrease in the concentration of carbon dioxide at the outlet of the combustion chamber. Although this reduction is small and is 4.65% [13]. So we have to a greater flow of additional air CO2 concentration on the yield equal to 0.164 kg/kg to less rate – 0.172 kg/kg.

In the area of the burners (Fig. 10) the maximum concentration of NO_2 for additional air mass flow of 5 kg /s is 7812.4 mg /Nm^3, while for the 10 kg/s –

3256.6 mg/Nm^3. As one moves out of the combustion chamber (Fig. 11) there is a decrease the concentration of NO_2. The maximum concentration at the outlet of the combustion chamber for the base case is 879.8 mg/Nm^3, as proposed by us for the case is 680 mg/Nm^3.

At the outlet (Fig. 11) we have a mean concentration NO_2 =761mg / Nm^3 for additional air rate equal to 5 kg/s (Fig. 11a), and the average concentrations of NO_2 in the cross section at the outlet equal to 655 mg / Nm^3 to the flow rate -10kg /s (Fig. 11b), which is quite acceptable emission standards for NO2, adopted by the TPP. In the proposed variant of the coal combustion (additional air flow rate is 10 kg/s) decreased by 14% in comparison with the first case. So it can be seen that increasing submitted air rate further reduces the average concentration of nitrogen dioxide NO_2.

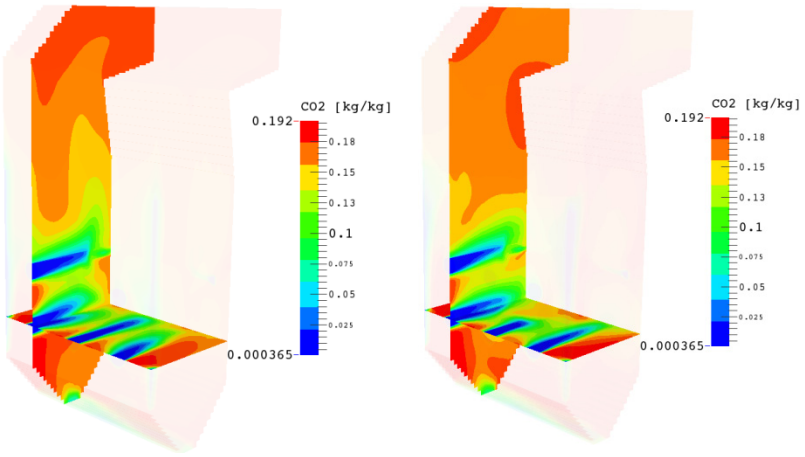

a) 5 kg/s b) 10 kg/s

Figure 7 – The three-dimensional distribution of carbon dioxide CO_2 in the lower section of the burners (Z = 6.82 m) and in the longitudinal section (Y1 = 2.95m) of the combustion chamber

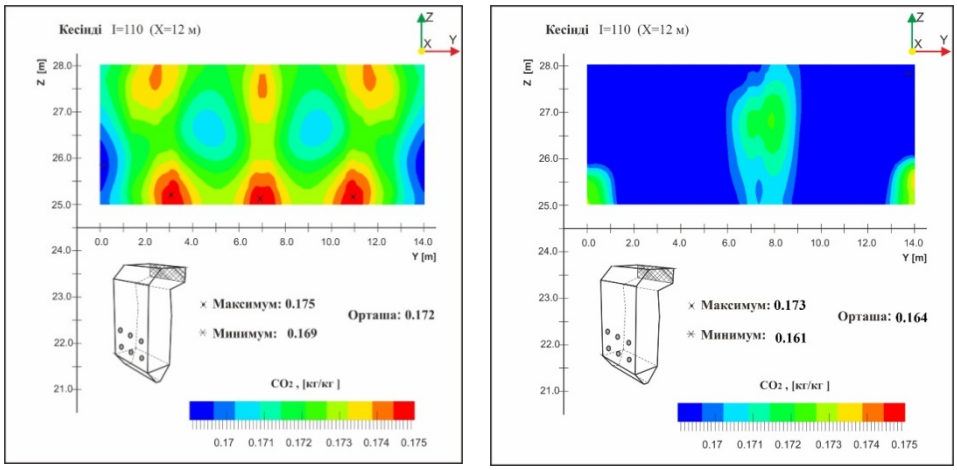

a) 5 kg/s b) 10 kg/s

Figure 8 – The distribution of the carbon dioxide CO_2 concentration at the outlet of the combustion chamber (X = 12 m)

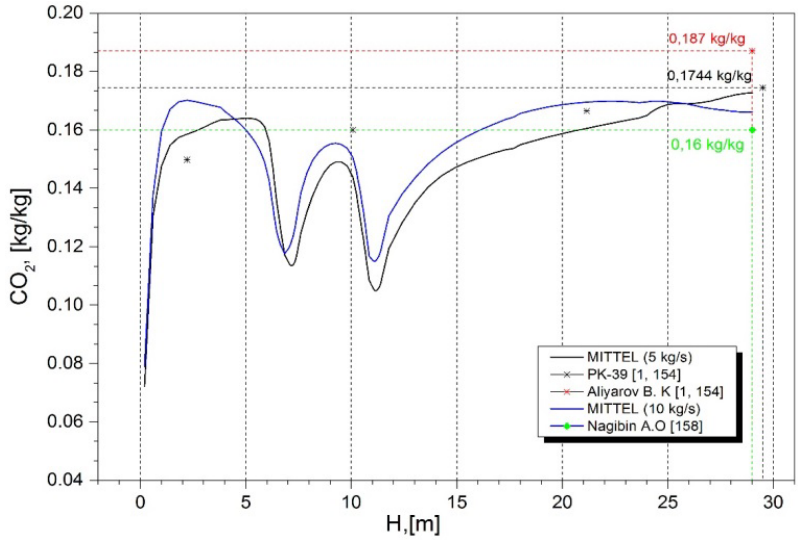

Figure 9 – Graph of distribution of average values of carbon dioxide CO_2 by height of the combustion chamber for different values of mass flow rate of additional air

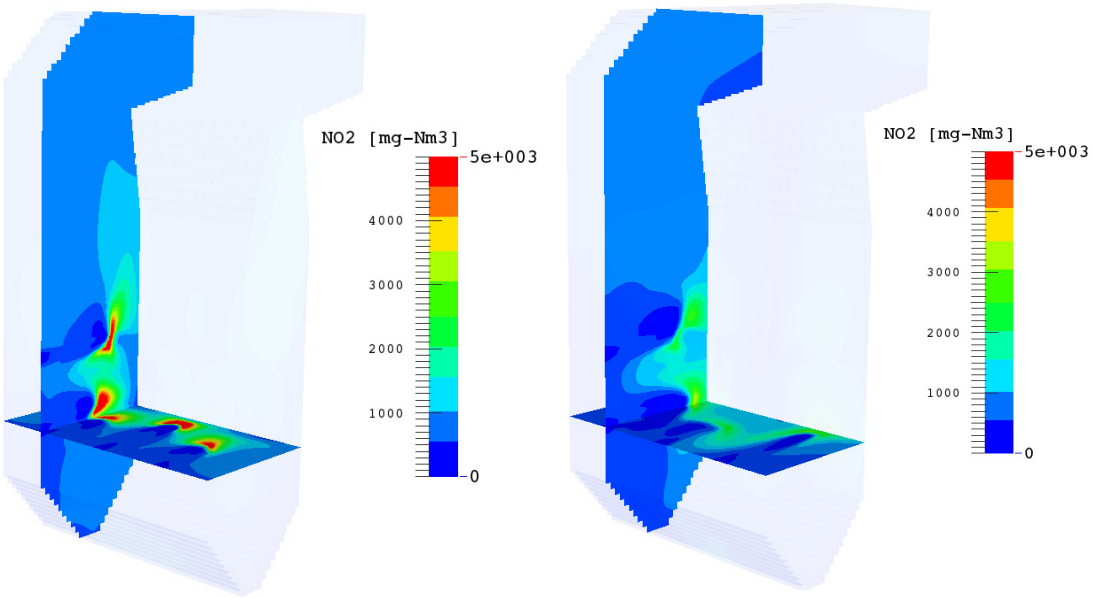

a) 5 kg/s b) 10 kg/s

Figure 10 – The three-dimensional distribution of the nitrogen dioxide NO_2 in the lower area of the burner (Z = 6.82 m) and in longitudinal section (Y1 = 2.95m) of the combustion chamber

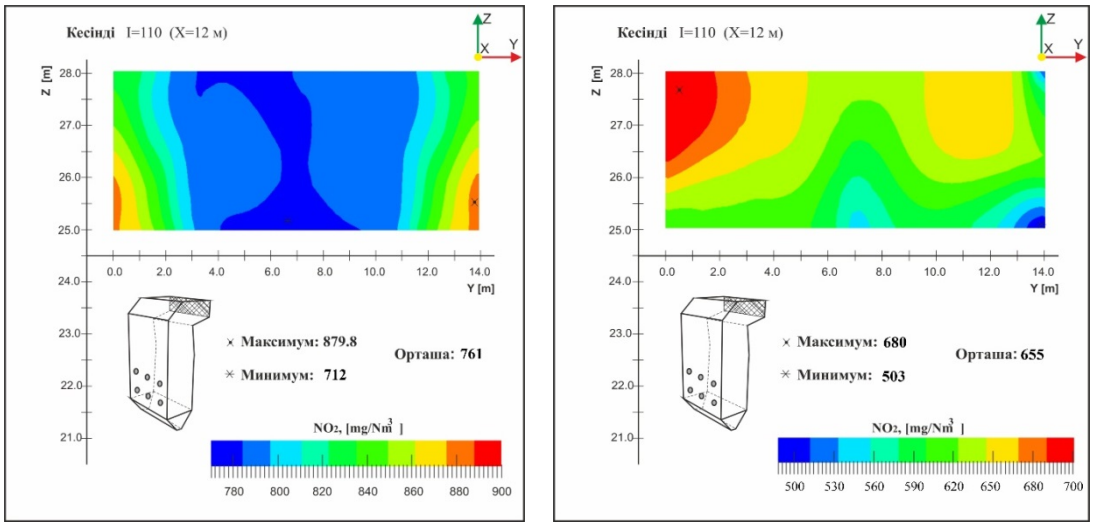

a) 5 kg/s b) 10 kg/s

Figure 11 – The concentration distribution of nitrogen dioxide NO_2 at the outlet of of the combustion chamber (X = 12 m)

Conclusion

This article has been developed optimal combustion technology of high-energy fuel and the best design parameters of the combustion chamber of the boiler BKZ-420 of the Almaty TPP-2 that improve the durability of the power equipment and reduce the emissions of harmful substances into the atmosphere. The proposed Ekibastuz coal combustion technology reduces the temperature of the furnace wall, opposite the burners on the 3000 ^{0}C, that is to 17.24%, and also reduces the average carbon monoxide concentration CO at the outlet of the furnace up to 15%, carbon dioxide CO_2 – 4.65%, and nitrogen dioxide NO2 – 14%.

The concentration of carbon monoxide can be reduced due to an increase in the excess air ratio in the combustion chamber and the high temperatures in it. However, increase in temperature in the combustion chamber invariably leads to increased formation of nitrogen oxides NOx (NO and NO_2), which are recognized at the present time, the most toxic environmental pollutants. 90% of the total amount of nitrogen oxides is nitrogen monoxide NO, which is further oxidized to NO2. The NOx cause acidification of atmospheric precipitation contribute to photochemical air pollution and the thinning of the ozone layer. Reducing the concentration of nitrogen oxides NOx, generated by combustion of coal is one of the main tasks in the development and operation of power devices [14-16].

During the flow rate of the additional air equal 10 kg/s at the outlet of the combustion chamber the concentration of carbon dioxide CO_2 4.65% is less than a flow rate of air 5kg/s, which corresponds to a maximum permissible standards adopted for TPP. So, we can conclude that the second case of combustion of fuel when the flow rate of additional air through the holes in the wall of the combustion chamber which located opposite the burner units is 10 kg / s, provide optimal combustion mode.

The results have scientific value and provide more insight into the mechanism of turbulent combustion of pulverized coal in the combustion chambers of power plants, which in turn contributes to the solution of fundamental problems of modern thermal physics, Macrokinetics, the theory of combustion explosion.

References

1. Messerle V.E., Lavrishcheva Ye.I., Karpenko E.I., et al. Plasma-supported coal combustion in boiler furnace // IEEE Transactions on Plasma Science. – 2007. – Vol. 35, No 6. – P.1607-1616.

2. Ustimenko A.B., Askarova A.S., Messerle V.E., Nagibin A. Pulverized coal torch combustion in a furnace with plasma-coal system //

Journal of Thermophysics and Aeromechanics**.** – 2010. – Vol.7, No 3. – P. 435-444**.**

3. Karpenko E.I., Messerle V.E. et al. Plasma enhancement of combustion of solid fuels // Journal of High Energy Chemistry. – 2006. – Vol. 40, No 2. – P.111-118.

4. D Askarova A.S., Lavrichsheva Ye., Leithner R., Müller H., Magda A. Combustion of low-rank coals in furnaces of Kazakhstan Coal-firing Power Plants // VDI Berichte. – 2007. –No 1088. – P. 497-502.

5. Vockrodt S., Leithner R., Schiller R., Buchman M. Firing technique measures for increased efficiency and minimization of toxic emissions in Kasakh coal firing // VDI BERICHTE. – Dresden. – 1999. – Vol. 1492. – P. 93-97.

6. B Abbas T., Costen P.G. and Lockwood F.C. Solid Fuel Utilisation: From Coal to Biomass Twenty-Sixth Symposium (International) on Combustion, The Combustion Institute, Pittsburgh. – 1996. – 3041 p.

7. Bolegenova S.A., Messerle V.E., Maksimov V.Yu. et al. Numerical Simulation of the Coal Combustion Process Initiated by a Plasma Source // Journal of Thermophysics and Aeromechanics. – 2014. – Vol. 21, No 6. – P.747-754.

8. Leithner, R., Müller, H. CFD studies for boilers Second M.I.T. Conference on Computational Fluid and Solid Mechanics – Cambridge. – 2003. – 172 p.

9. Karpenko Yu.E., Karpenko E.I., Askarova A.S. et al. Mathematical modeling of the processes of solid fuel ignition and combustion at combustors of the power boilers // 7-th International Fall Seminar on Propellants, Explosives and Pyrotechnics. Theory and Practice of Energetic Materials. – China. – 2007. – Vol. 7. – P. 672-683.

10. L Buchmann M.A., Askarowa A. Structure of the flame of fluidized-bed burners and combustion processes of high-ash coal // VDI BERICHTE. – 1997. – Vol. 1313. – P. 241-244.

11. Bekmukhamet A., Beketayeva M.T., Sh.S., Gabitova Z.K. et al. Numerical modeling of turbulence characteristics of burning process of the solid fuel in BKZ-420-140-7c combustion chamber // International Journal of Mechanics. – 2014. – Vol.8. – P.112-122.

12. Askarova A.S., Maksimov V.Yu., et al. Computational method for investigation of solid fuel combustion in combustion chambers of a heat power plant // Journal of High Temperature. – 2015. – Vol.53,No 5. – P. 751-757.

13. Bolegenova S.A., Bekmuhamet A., et al. Using 3d modeling technology for investigation of conventional combustion mode of bkz-420-140-7c combustion chamber // Journal of Engineering and Applied Sciences. – 2014. – Vol. 9. – P.24-28.

14. Messerle V.E., Maksimov V.Yu., et al. Numerical simulation of pulverized coal combustion in a power boiler furnace // Journal of High Temperature. – 2015. – Vol.53,No 3. – P.445-452.

15. Safarik P., Askarova A.S., et al. Numerical Modeling of Pulverized Coal Combustion at Thermal Power Plant Boilers // Journal of Thermal Science. – 2015. – Vol. 24,No 3. – P.275-282.

16. Loktionova I.V., Messerle V.E., et al. 3D modeling of the two-stage combustion of Ekibastuz coal in the furnace chamber of a PK-39 boiler at the Ermakovo district power station // Journal of Thermal engineering. – 2003. – Vol. 50, No 8. – P.633-638.

UDC 533.9.01

Askaruly A., Arkhipov Yu.V., *Davletov A.E., Yerimbetova L.T.

IETP, Al-Farabi Kazakh National University, Almaty, Kazakhstan
e-mail: askar@physics.kz

Finite-size effects in the interaction of dust particles in a plasma

Abstract. A pseudopotential model of interaction between dust particles is proposed to simultaneously take into account the finite-size and the screening effects. The consideration starts from the assumption that the dust particles are hard balls such that the interparticle distances are measured between their surfaces rather than between their centers. After that to derive the screened interaction potential between dust particles the density-response formalism is used in which the dielectric function of the plasma is taken in the form of the random-phase approximation. This procedure provides a simple analytic expression for the intergrain potential that numerically differs from the well-known Debye-Huckel (Yukawa) potential at small separations.
Key words: Dusty plasma, density-response formalism, finite-size effects, random-phase approximation.

Introduction

For the past few decades dusty plasmas have attracted a great deal of attention of plasma physics researchers since they are frequently encountered in various settings both in nature and in the laboratory. In particular, dusty plasmas appear in various astrophysical contexts [1-3], space and earth experiments [4-6], nanotechnology [7, 8], cancer therapy in medicine [9, 10], etc. Furthermore, as it happens in nuclear fusion researches [11, 12] and plasma etching in electronics [13, 14], solid microparticles readily penetrate into the plasma medium as a consequence of its contact with electrodes and chamber walls, thereby substantially modifying both surface properties of the confining material and the local plasma characteristics.

What makes dusty plasma a unique object for investigation is the presence of micron-sized dust particles, called grains, which are capable of acquiring a high, mostly negative, electric charge [15, 16] which invokes diverse manifestations of strong coupling effects [17]. For instance, first experiments with dusty plasmas clearly demonstrated that under certain conditions strong electrostatic interactions between grains took over their thermal kinetic energy resulting in the formation of the so-called plasma crystals [18-20]. The latter are quite similar, in physical properties, to ordered structures in liquids and solids, such that even phase transitions of the first and second orders are easily observed [21, 22].

In order to correctly describe the properties of non-ideal systems it is crucial to know the form of interaction energy between the constituent elements. As for dusty plasmas, the interaction potential between grains is conventionally taken in the form of the screened Coulomb (Yukawa) potential [23-25] which is only known to be valid for point-like dust particles immersed into the buffer plasma whose role is virtually reduced to shielding of the electric field. In this manuscript an effective potential of interparticle interaction in dusty plasmas is proposed to take into account finite dimensions of grains. The idea is to start counting distances between the surfaces of dust particles rather than between their centers [26] with subsequent application of the density-response formalism in which the dielectric function of the buffer plasma is taken in the form of the random phase approximation.

Dimensionless plasma parameters

Of interest in the following is the interaction of two dust particles immersed into the buffer plasma of electrons and ions. For the sake of simplicity the buffer plasma is considered to be a fully ionized hydrogen consisting of free electrons with the electric charge $-e$ and the number density n_e and of free protons with the electric charge e and the number density $n_p = n_e = n$. The microparticles are assumed to be hard balls of radius R and of the electric charge $-Z_d e$ such that their number density

 Printed in Kazakhstan

n_d is so small to satisfy the inequality $n_d Z_d << n$ which assures the total plasma neutrality.

To describe the state of the dust component of the plasma it is convenient to introduce the coupling parameter as

$$\Gamma = \frac{Z_d^2 e^2}{R k_B T}, \qquad (1)$$

where k_B stands for the Boltzmann constant and T denotes the medium temperature.

Coupling parameter (1) is not conventional since it represents the ratio of the electrostatic interaction energy of two grains, separated by the distance R, to their average kinetic energy of chaotic thermal motion.

Another suitable dimensionless parameter involved is the screening parameter defined as

$$\kappa = \frac{R}{\lambda_D}, \qquad (2)$$

where $\lambda_D = (k_B T / 8\pi n e^2)^{1/2}$ designates the Debye screening radius.

It has to be stressed that knowledge of dimensionless parameters (1) and (2) is perfectly enough to completely describe the interaction of two isolated hard balls placed into the buffer plasma.

Boundary condition

It is widely believed in the literature that the dust charge is determined by the normal component of the electric field strength at the particle surface. This inference is usually made from the following equation for the electric field strength $\mathbf{E}$ as applied to the cylindrical volume of the cross section S shown in Figure 1:

$$\oint \mathbf{E} \cdot \mathbf{dS} = 4\pi(\sigma S + \rho_{pl} V), \qquad (3)$$

where σ stands for the surface charge density on the dust particle and ρ_{pl} refers to the plasma charge density.

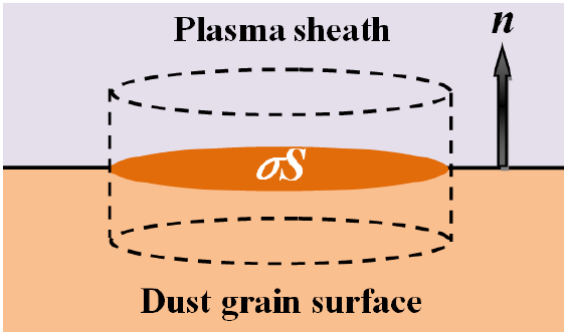

Figure 1 – To the derivation of the boundary condition.

Without any loss of generality the dust grain material can be assumed to be conductive so that the electric field strength under the grain surface turns zero and, then, applying eq. 1 to the infinitesimally thin cylinder, $V \to 0$, finally yields

$$E_n = 4\pi\sigma. \qquad (4)$$

Boundary condition (4) is incorrect from the viewpoint of plasma electrodynamics because the cylinder in equation (3) cannot be taken infinitesimally thin, otherwise one has to inevitably turn to consideration of the microscopic electric field which rapidly fluctuates over time in contrast to the macroscopically averaged electric field entering equation (3).

To correctly derive the boundary condition one has to use the following explicit equation for the dielectric displacement vector $\mathbf{D}$ which stems from the plasma electrodynamics:

$$\oint \mathbf{D} \cdot \mathbf{dS} = 4\pi\sigma S, \qquad (5)$$

When applied to a rather small cylinder still containing enough number of plasma particles to treat the electric field macroscopically, (5) gives rise to the correct boundary condition

$$D_n = 4\pi\sigma. \qquad (6)$$

for the dielectric displacement vector in a plasma near the dust surface.

Boundary condition (6) differs significantly from (4) because the displacement vector $\mathbf{D}$ is expressed in terms of the electric field strength $\mathbf{E}$ in the static case of plasma electrodynamics via the integral relation

$$\mathbf{D}(\mathbf{r}) = \int \varepsilon(\mathbf{r}-\mathbf{r}_1)\mathbf{E}(\mathbf{r}_1)\mathbf{dr}_1 , \qquad (7)$$

where $\varepsilon(\mathbf{r})$ stands for the plasma dielectric function defined in the configurational space.

It is, thus, rather clear how to accurately work out the problem of the intergrain interaction in the buffer plasma. One has to consider a spatially finite plasma with boundary condition (6) and spatially varying plasma parameters, i.e. to construct an exact theory of the plasma sheath. This is quite a complicated problem to solve analytically and all further simplified consideration is aimed at establishing what impact expression (6) has on the interaction between plasma particles and the dust grain.

Interaction model

It is well known [27] that in spatially infinite plasmas the Fourier transform of the screened interaction potential $\tilde{\Phi}(\mathbf{k})$ between the dust particles is expressed in terms of the Fourier transform of the true microscopic interaction potential $\tilde{\varphi}(\mathbf{k})$ and the plasma static dielectric function $\varepsilon(\mathbf{k})$ as:

$$\tilde{\Phi}(\mathbf{k}) = \frac{\tilde{\varphi}(\mathbf{k})}{\varepsilon(\mathbf{k})}, \qquad (8)$$

in which the static dielectric function can be taken in the form of the random phase approximation [28] as

$$\varepsilon(k) = 1 + \frac{k_D^2}{k^2}, \qquad (9)$$

where $k_D = 1/\lambda_D$ denotes the wavenumber inversed to the Debye screening radius.

Using the convolution theorem it is convenient in the sequel to rewrite relation (8) as

$$\Phi(\mathbf{r}) = \int \varepsilon^{-1}(\mathbf{r}-\mathbf{r}_1)\varphi(\mathbf{r}_1)\mathbf{dr}_1 , \qquad (10)$$

where the kernel is found from equation (9) as

$$\varepsilon^{-1}(r) = \delta(r) - \frac{k_D^2}{2\pi r}\exp(-k_D r) . \qquad (11)$$

To practically apply formulas (10) and (11), initially worked out for an infinite plasma, to a spatially finite plasma of interest it is proposed herein to treat dust grains as point-like charges by counting all distances r from the dust grain surfaces so that the interaction micropotential acquires the form:

$$\varphi(r) = \frac{Z_d^2 e^2}{r + 2R} . \qquad (12)$$

On substituting expressions (11) and (12) into (10), one ultimately gets

$$\Phi(r) = \varphi(r) - \frac{Z_d^2 e^2}{r}\left[1 - \exp(-k_D r) - k_D R\,\mathrm{B}(r)\right], \qquad (13)$$

where

$$\begin{aligned}\mathrm{B}(r) = {} & \exp(k_D(2R+r))\,\mathrm{Ei}(k_D(2R+r)) - \\ & -\exp(k_D(2R-r))\,\mathrm{Ei}(2k_D R) + \\ & +\exp(-k_D(2R+r))\left[\mathrm{Ei}(2k_D R) - \mathrm{Ei}(-k_D(2R+r)\right]\end{aligned} \qquad (14)$$

with the exponential integral function defined as

$$\mathrm{Ei}(x) = \int_x^{\infty} \frac{\exp(-t)}{t}\,dt . \qquad (15)$$

Note that it is ordinarily assumed in the literature that the screening effects start from the dust grain surface such that the Debye-like theory gives rise to the following interaction potential

$$\Phi(r) = \frac{Z_d^2 e^2}{(r+2R)(1+2k_D R)}\exp(-k_D r) . \qquad (16)$$

In Figure 2 a comparison is made between expressions (12), (13) and (16) at $\Gamma = 10$ and $\kappa = 0.5$. It is well seen that potentials (13) and (16) are effectively screened and micropotential (12) lies high above Yukawa potential (16) and the proposed potential (13) that has a gap at the origin caused by engaging of the plasma electrodynamics. It is worth

noting that the onset of the gap is a straightforward consequence of boundary condition (6).

Figure 3 demonstrates the intergrain interaction potential (13) as a function of the distance r and the screening parameter κ at the fixed value of the coupling parameter $\Gamma = 100$. It is clearly observed that the increase in the screening parameter results in stronger shielding of the intergrain interaction and, at the same time, in lowering of the potential at the origin.

It is worth mentioning that the constructed potential of the intergrain interaction can be used to calculate the static correlation functions which can then be applied to find thermodynamic properties or to even evaluate dynamic characteristics of the dust component using the theory of moments [29.30].

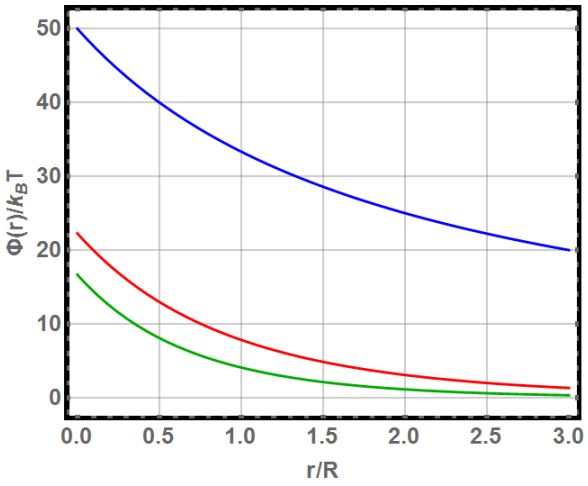

Figure 2 – The intergrain interaction potential at Γ=100 and k=1.0. Blue line: micropotential (12); green line: Yukawa potential (16); red line: screened potential (13).

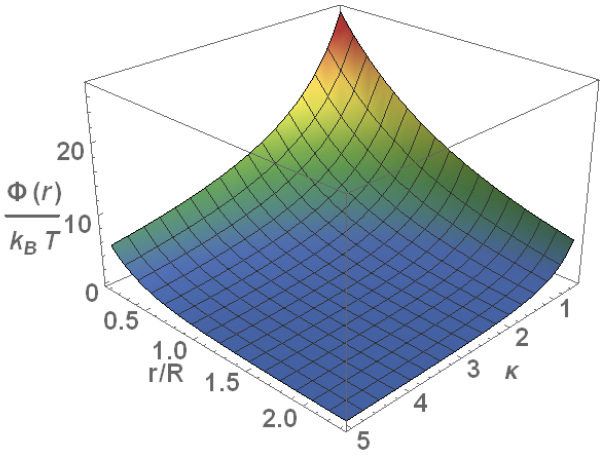

Figure 3 – The intergrain interaction potential as a function of the distance r and of the screening parameter k at Γ=100.

Conclusions

This paper has been solely concentrated on the problem of derivation of the interaction potential between two isolated dust particles immersed into a buffer plasma. The plasma electrodynamics has provided an important insight that the charge of the dust grain determines the normal component of the dielectric displacement vector near the grain surface. A simple model has been put forward to derive the screened interaction potential between dust grains. It is based on the idea of counting distances between dust particles surfaces with further application of the density-response formalism to account for the buffer plasma screening. The numerical results portray that a gap between the obtained potential and the micropotential appears at the origin and an increase in the screening parameter gives rise to stronger shielding of the interaction as well as to lowering of the potential at the origin.

Acknowledgements

The authors acknowledge the support from the state grant number 3120/GF4, funded by the Ministry of Education and Science of the Republic of Kazakhstan and A. Askaruly expresses gratitude for the financial support provided by the Ministry by a grant The Best Lecturer.

References

1. Forsberg M., Brodin G., Marklund M., Shukla P.K., Moortgat J. Nonlinear interactions between gravitational radiation and modified Alfvén modes in astrophysical dusty plasmas // Phys. Rev. D – 2006. – Vol. 74. – 064014.

2. Malmrose M.P., Marscher A.P., Jorstad S.G., Nikutta R., Elitzur M. Emission from Hot Dust in the infrared Spectra of Gamma-ray Bright Blazars // Astrophys. J. – 2011. – Vol. 732. – P. 116.

3. Seok J.Y., Koo B.-C., Hirashita H. Dust Cooling in Supernova Remnants in the Large Magellanic Cloud // Astrophys. J. – 2015. – Vol. 807. – P. 100.

4. Izvekova Yu.N., Popel S. I. Charged Dust Motion in Dust Devils on Earth and Mars // Contrib. Plasma Phys. – 2016. – Vol. 56. – P. 263.

5. Heidemann R.J., Couëdel L., Zhdanov S.K., Sütterlin K.R., Schwabe M., Thomas H.M., Ivlev A.V., Hagl T., Morfill G.E., Fortov V.E., Molotkov V.I., Petrov O.F., Lipaev A.I., Tokarev V., Reiter

Th., Vinogradov P. Comprehensive experimental study of heartbeat oscillations observed under microgravity conditions in the PK-3 Plus laboratory on board the International Space Station // Phys. Plasmas. – 2011. – Vol. 18. – 053701.

6. Fedoseev A.V., Sukhinin G.I., Abdirakhmanov A.R., Dosbolayev M.K., Ramazanov T.S. Voids in Dusty Plasma of a Stratified DC Glow Discharge in Noble Gases // Contrib. Plasma Phys. – 2016. – Vol. 56. – P. 234.

7. Szetsen L., Hsiu-Feng C., Chien-Ju C. Spectroscopic study of carbonaceous dust particles grown in benzene plasma // J. Appl. Phys. – 2007. – Vol. 101. – 113303.

8. Kundrapu M., Keidar M. Numerical simulation of carbon arc discharge for nanoparticle synthesis // Phys. Plasmas – 2012. – Vol. 19. – 073510.

9. Keidar M., Shashurin A., Volotskova O., Stepp M. A., Srinivasan P., Sandler A., Trink B. Cold atmospheric plasma in cancer therapy // Phys. Plasmas – 2013. – Vol. 20. – 057101.

10. Walk, R. M., Snyder, J. A., Scrivasan, P., Kirch, J., Diaz, S. O., Blanco F. C., Shashurin A., Keidar M., Sandler A. D. Cold atmospheric plasma for the ablative treatment of neuroblastoma // J. Pediatr. Surg. – 2013. – Vol. 48. – P. 63.

11. Winter J. Dust: A new challenge in nuclear research? // Phys. Plasmas, – 2000. – Vol. 7. – P. 3862.

12. Castaldo C., Ratynskaia S., Pericolli V., de Angelis U., Rypdal K., Pieroni L., Giovannozzi E., Maddaluno G., Marmolino C., Rufoloni A., Tuccillo A., Kretschmer M., Morfill G.E. Diagnostics of fast dust particles in tokamak edge plasmas // Nucl. Fusion – 2007. – Vol. 47, – P. L5.

13. Kokura H., Yoneda S., Nakamura K., Mitsuhira N., Nakamura M. and Sugai H. Diagnostic of surface wave plasma for oxide etching in comparison with inductive RF plasma // Jap. J. Appl. Phys. – 1999. – Vol. 38. – P. 5256.

14. Kersten H., Deutsch H., Stoffels E., Stoffels W.W., Kroesen G.M.W., Hippler R. Micro-disperse particles in plasmas: From disturbing side effects to new applications // Contrib. Plasma Phys. – 2001. – Vol. 41. – P. 598.

15. Khrapak S., Morfill G. Basic Processes in Complex (Dusty) Plasmas: Charging, Interactions, and Ion Drag Force // Contrib. Plasma Phys. – 2009. – Vol. 49. – P. 148.

16. Shukla P.K., Eliasson B. Fundamentals of dust-plasma interactions // Rev. Nod. Phys. – 2009. – Vol. 81. – P. 25.

17. Bonitz M., Henning C., Block D. Complex plasmas: a laboratory for strong correlations // Rep. Prog. Phys. – 2010. – Vol. 73. – 066501.

18. Vladimirov S.V., Ishihara O. On plasma crystal formation // Phys. Plasmas – 1996. – Vol. 3. – P. 444.

19. Morfill G.E., Thomas H. Plasma crystal // J. Vac. Sci. Technol. A – 1996. – Vol. 14, – P. 490.

20. Kählert H., Bonitz M. How Spherical Plasma Crystals Form // Phys. Rev. Lett. – 2010. – Vol. 104. – 015001.

21. Vaulina O.S., Vladimirov S.V., Petrov O.F., Fortov V. E. Criteria for Phase-Transitions in Yukawa Systems (Dusty Plasma) // AIP Conf. Proc. – 2002. – Vol. 649. – P. 471.

22. Kundu M., Avinash K., Sen A., Ganesh R. On the existence of vapor-liquid phase transition in dusty plasmas // Phys. Plasmas – 2014. – Vol. 21. – 103705.

23 Kalman G., Hartmann P., Donko Z., Golden K.J., Kyrkos S. Collective modes in two-dimensional binary Yukawa systems // Phys. Rev. E – 2013. – Vol. 87. – 043103.

24 Khrapak S.A., Thomas H.M. Fluid approach to evaluate sound velocity in Yukawa systems and complex plasmas // Phys. Rev. E – 2015. – Vol. 91. – 033110.

25 Khrapak S.A., Thomas H.M. Practical expressions for the internal energy and pressure of Yukawa fluids // Phys. Rev. E – 2015. – Vol. 91. – 023108.

26 Baimbetov F.B., Davletov A.E., Kudyshev Zh.A., Mukhametkarimov E.S. New Model of Dusty Plasma Particles Interaction // Contrib. Plasma Phys. – 2011. – Vol. 51. – P. 533.

27 Davletov A.E. A new model of intergrain interaction in dusty plasmas // J. Phys. A: Math. Gen. – 2006. – Vol. 39. – P. 4555.

28 Ichimaru S. Basic Principles of Plasma Physics (Benjamin/Cumming, Reading, 1973).

29 Arkhipov Yu.V., Askaruly A., Ballester D., Davletov A.E., Tkachenko I.M., Zwicknagel G.. Dynamic properties of one-component strongly coupled plasmas: The sum-rule approach // Phys. Rev. E – 2010. – Vol. 81. – 026402.

30 Arkhipov Yu.V., Ashikbayeva A.B., Askaruly A., Davletov A.E., Tkachenko I.M. Optical Properties of Kelbg-Pseudopotential-Modelled Plasmas // Contrib. Plasma Phys. – 2013. – Vol. 53. – P. 375.

UDC 530.145; 530.12; 539.12-17

[1*]Nurbakova G.S., [1]Habyl N., [2]Mukushev B.A., [1]Tyulemissov Zh.Zh.

[1]Department of Physics and Technology, al-Farabi Kazakh National University, Almaty, Kazakhstan
[2]Shakarim State University, Semey, Kazakhstan
[*]e-mail: guliya_nurbakova@mail.ru

Polarization observables in rare decay $B \to K^*(\to K\pi)l^+l^-$

Abstract: Our article is devoted to the study of the $B \to K^*(\to K\pi)l^+l^-$ decay. Rare decay $B \to K^*(\to K\pi)l^+l^-$ is one of the best modes to search for new physics beyond the Standard Model (SM). A large number of observables allow for unique tests of the SM contributions.
We calculate the relevant form factors in the framework of the covariant quark model with infrared confinement in the full kinematical momentum transfer region. The calculated form factors are used to evaluate branching fractions and polarization observables in the cascade decay $B \to K^*(\to K\pi)l^+l^-$. We compare the obtained results with available experimental data and the results from other theoretical approaches. We show the relation of our helicity formalism with an approach based on the transversality amplitudes which is widely used by both experimentalists and theorists.
Key words: relativistic quark model, confinement, B-meson, rare decay, form factor, polarization observables.

Introduction

It is generally believed that the decay mode $B \to K^*(\to K\pi)\,\mu^+\mu^-$ is one of the best modes to search for new physics beyond the SM. The angular distribution makes possible an independent measurement of several observables as a function of the dilepton invariant mass. A large number of observables obtained in this manner allows for unique tests of the SM contributions [1].

The measured ratio R_K by the LHCb Collaboration [2]

$$R_K = \frac{\mathrm{B}(B^+ \to K^+\mu^+\mu^-)}{\mathrm{B}(B^+ \to K^+e^+e^-)} = \\ = 0.745^{+0.090}_{-0.074}(stat.) \pm 0.036(syst.) \qquad (1)$$

in the region $1 < q^2 < 6\ \mathrm{GeV}^2$ was found to be compatible with the SM prediction only within 2.6 standard deviations.

The results of a measurement of form-factor independent angular observables in the decay $B^0 \to K^{*0}(892)\mu^+\mu^-$ were presented in [3]. The analysis is based on a data sample corresponding to anintegrated luminosity of $1.0\,\mathrm{fb}^{-1}$, collected by the LHCb experiment in pp collisions at a center-of mass energy of 7 TeV. Four observables are measured in six bins of the dimuon invariant mass squared, q^2, in the range $0.1 < q^2 < 19.0\ \mathrm{GeV}^2$. Agreement with the SM predictions is found for 23 of the 24 measurements. A local discrepancy, corresponding to 3.7 standard deviations, is observed in one q^2 bin for one of the observables.

Our article is devoted to the study of the $B \to K^*(\to K\pi)l^+l^-$ decay. We evaluate the relevant form factors in the framework of the covariant quark model with infrared confinement. Form factors are then exploited for evaluation of physical observables.

The covariant confined quark has been applied to a large number of elementary particle processes [4, 5]. This model can be viewed as an effective quantum field approach to hadronic interactions based on an interaction Lagrangian of hadrons interacting with their constituent quarks. The coupling strength is determined by the compositeness condition $Z_H = 0$ where Z_H is the wave function renormalization constant of the hadron. The hadron field renormalization constant Z_H characterizes the overlap between the bare hadron field and the bound state formed from the constituents. Once this constant is set to zero, the dynamics of hadron interactions is fully described by constituent quarks in quark loop diagrams with

local constituent quark propagators. Matrix elements are generated by a set of quark loop diagrams according to the $1/N_c$ expansion. The ultraviolet divergences of the quark loops are regularized by including vertex functions for the hadron-quark vertices which, in addition, describe finite size effects due to the non-pointlike structure of hadrons. Quark confinement was implemented into the model [6] by introducing an infrared cutoff on the upper limit of the scale integration to avoid the appearance of singularities in any matrix element. The infrared cutoff parameter λ is taken to have a common value for all processes. The covariant confined quark model contains only a few model parameters: the light and heavy constituent quark masses, the size parameters that describe the size of the distribution of the constituent quarks inside the hadron and the infrared cutoff parameter λ. They are determined by a fit to available experimental data.

Effective Lagrangian

The coupling of a meson $M\left(q_1\overline{q}_2\right)$ to its constituent quarks q_1 and $\overline{q}_2$ is described by the Lagrangian

$$L_{int}\left(x\right)=g_H M\left(x\right)\int dx_1\int dx_2 F_M\left(x,x_1,x_2\right)\overline{q}_2\left(x_2\right)\Gamma_M q_1\left(x_1\right)+h.c. \tag{2}$$

Here, Γ is a Dirac matrix which projects onto the spin quantum number of the meson field M(x). The function F_M is related to the scalar part of the Bethe-Salpeter amplitude and characterizes the finite size of the meson. To satisfy translational invariance the function F_H has to fulfil the identity $F_M\left(x+a;x_1+a,x_2+a\right)=F_M\left(x;x_1,x_2\right)$ for any four-vector a. In the following we use a specific form for the scalar vertex function

$$F_M\left(x;x_1,x_2\right)=\delta\left(x-x_1\omega_1-x_2\omega_2\right)\Phi_M\left(\left(x_1-x_2\right)^2\right), \tag{3}$$

where Φ_M is the correlation function of the two constituent quarks with masses m_{q_1}, m_{q_2} and the mass ratios $\omega_i=m_{q_i}/\left(m_{q_1}+m_{q_2}\right)$.

We choose a simple Gaussian form of the vertex function $\tilde{\Phi}_H\left(-k^2\right)$. The minus sign in the argument of this function is chosen to emphasize that we are working in the Minkowski space. One has

$$\tilde{\Phi}_H\left(-k^2\right)=exp\left(k^2/\Lambda_H^2\right) \tag{4}$$

where the parameter Λ_H characterizes the size of the meson. Since k^2 turns into $-k_E^2$ in the Euclidean space, the form (4) has the appropriate fall-off behavior in the Euclidean region. We emphasize that any choice for Φ_M is appropriate as long as it falls off sufficiently fast in the ultraviolet region of the Euclidean space to render the corresponding Feynman diagrams ultraviolet finite. We choose a Gaussian form for Φ_M for calculational convenience.

***B* – *K** form factors in the covariant quark model**

Herein our primary subject is the following matrix element, which can be expressed via dimensionless form factors:

$$\left\langle V_{[\overline{q}_1q_3]}(p_2,\varepsilon_2)\left|\,\overline{q}_2(O^\mu q_1)\,\right|P_{[\overline{q}_3q_2]}(p_1)\right\rangle=N_c g_P g_V\int\frac{d^4k}{(2\pi)^4 i}\tilde{\Phi}_P(-(k+w_{13}p_1)^2)\tilde{\Phi}_V(-(k+w_{23}p_2)^2)$$

$$\times tr\left[O^\mu S_1(k+p_1)\gamma^5 S_3(k)\not{\varepsilon}_2^\dagger S_2(k+p_2)\right]=\frac{\varepsilon_\nu^\dagger}{m_1+m_2}(-gP\cdot qA_0(q^2)+P^\mu P^\nu)A_+(q^2)+q^\mu P^\nu A_-(q^2) \tag{5}$$

$$+i\varepsilon^{\mu\nu\alpha\beta}P_\alpha q_\beta V(q^2),$$

$$\begin{aligned}
&\left\langle V_{[\bar{q}_1 q_3]}(p_2,\varepsilon_2)\,|\,\bar{q}_2(\sigma^{\mu\nu}q_\nu(1+\gamma^5))q_1)\,|\,P_{[\bar{q}_3 q_2]}(p_1)\right\rangle = \\
&= N_c g_P g_V \int \frac{d^4k}{(2\pi)^4 i}\tilde{\Phi}_P(-(k+w_{13}p_1)^2)\tilde{\Phi}_V(-(k+w_{23}p_2)^2) \\
&\times tr\left[\sigma^{\mu\nu}q_\nu(1+\gamma^5)S_1(k+p_1)\gamma^5 S_3(k)\not{\epsilon}_2^\dagger S_2(k+p_2)\right] \\
&= \varepsilon_\nu^\dagger(-(g^{\mu\nu}-q^\mu q^\nu/q^2)P\cdot q a_0(q^2)+(P^\mu P^\nu - q^\mu P^\nu P\cdot q/q^2)a_+(q^2)+i\varepsilon^{\mu\nu\alpha\beta}P_\alpha q_\beta g(q^2)).
\end{aligned} \tag{6}$$

Here, $P = p_1 + p_2$, $q = p_1 - p_2$, $\epsilon_2^+ \cdot p_2 = 0$, $p_i^2 = m_i^2$ The form factors defined in Eq. (6) satisfy the physical requirement $a_0(0) = a_+(0)$, which ensures that no kinematic singularity appears in the matrix element at $q^2 = 0$. We will use the latest fit done in Ref. [7]. The fitted values of the constituent quark masses m_q, the infrared cut-off λ, and the size parameters Λ_H are given in Table 1.

Our form factors are represented as three-fold integrals which are calculated by using NAG routines. They are shown in Figs. 1, 2. The results of our numerical calculations are well approximated by the parametrization

$$F(q^2) = \frac{F(0)}{1 - as + bs^2}, \qquad s = \frac{q^2}{m_1^2}. \tag{7}$$

The values of $F(0)$, a and b are listed in Table 2.

Polarization observables

Let us consider the polar angle decay distribution differential in the momentum transfer squared q^2. The polar angle is defined by the angle between $\vec{q} = \vec{p}_1 - \vec{p}_2$ and $\vec{k}_1$ ($\ell^+\ell^-$ rest frame) as shown in Figure 1. One has

$$\begin{aligned}
&\frac{d^2\Gamma}{dq^2 d\cos\theta} = \frac{|\mathbf{p}_2|\upsilon}{(2\pi)^3 4m_1^3}\cdot\frac{1}{8}\sum_{pol}|M|^2 = \frac{G_F^2}{(2\pi)^3}\left(\frac{\alpha|\lambda_t|}{2\pi}\right)^2\frac{|\mathbf{p}_2|\upsilon}{8m_1^2}\times \\
&\times\frac{1}{8}\left\{H_{11}^{\mu\nu}\cdot tr\left[\gamma_\mu\left(\not{k}_1 - m_\ell\right)\gamma_\nu\left(\not{k}_1 + m_\ell\right)\right] + H_{22}^{\mu\nu}\cdot tr\left[\gamma_\mu\gamma_5\left(\not{k}_1 - m_\ell\right)\gamma_\nu\gamma_5\left(\not{k}_1 + m_\ell\right)\right] + \right. \\
&\left. + H_{12}^{\mu\nu}\cdot tr\left[\gamma_\mu\left(\not{k}_1 - m_\ell\right)\gamma_\nu\gamma_5\left(\not{k}_1 + m_\ell\right)\right] + H_{21}^{\mu\nu}\cdot tr\left[\gamma_\mu\gamma_5\left(\not{k}_1 - m_\ell\right)\gamma_\nu\left(\not{k}_1 + m_\ell\right)\right]\right\} = \\
&= \frac{G_F^2}{(2\pi)^3}\left(\frac{\alpha|\lambda_t|}{2\pi}\right)^2\frac{|\mathrm{P}_2|\upsilon}{8m_1^2}\cdot\frac{1}{2}\left\{L_{\mu\nu}^1\cdot\left(H_{11}^{\mu\nu} + H_{22}^{\mu\nu}\right) - \right. \\
&\left. -\frac{1}{2}L_{\mu\nu}^2\cdot\left(q^2 H_{11}^{\mu\nu} + \left(q^2 - 4m_\ell^2\right)H_{22}^{\mu\nu}\right) + L_{\mu\nu}^3\cdot\left(H_{12}^{\mu\nu} + H_{21}^{\mu\nu}\right)\right\},
\end{aligned} \tag{8}$$

where $|\mathbf{p}_2| = \lambda^{1/2}\left(m_1^2, m_2^2, q^2\right)/2m_1$ is the momentum of the $K(K^*)$ - meson given in the B-rest frame and $\beta_l = \sqrt{1 - 4m_l^2/q^2}$.

The differential (q2, cos θ) distribution finally reads

$$\frac{d\Gamma\left(H_1 \to H_2 \bar{\ell}\ell\right)}{dq^2 d\left(\cos\theta\right)} = \frac{3}{8}\left(1+\cos^2\theta\right)\cdot\frac{1}{2}\left(\frac{d\Gamma_U^{11}}{dq^2}+\frac{d\Gamma_U^{22}}{dq^2}\right)$$
$$+\frac{3}{4}\sin^2\theta\cdot\frac{1}{2}\left(\frac{d\Gamma_L^{11}}{dq^2}+\frac{d\Gamma_L^{22}}{dq^2}\right)-\upsilon\cdot\frac{3}{4}\cos\theta\cdot\frac{d\Gamma_P^{12}}{dq^2} \quad (9)$$
$$+\frac{3}{4}\sin^2\theta\cdot\frac{1}{2}\frac{d\tilde{\Gamma}_U^{11}}{dq^2}-\frac{3}{8}\left(1+\cos^2\theta\right)\cdot\frac{d\tilde{\Gamma}_U^{22}}{dq^2}+\frac{2}{3}\cos^2\theta\cdot\frac{1}{2}\frac{d\tilde{\Gamma}_L^{11}}{dq^2}-\frac{3}{4}\sin^2\theta\cdot\frac{1}{2}\frac{d\tilde{\Gamma}_L^{22}}{dq^2}+\frac{3}{4}\frac{d\tilde{\Gamma}_S^{22}}{dq^2}.$$

After integrating over cos θ one obtains

$$\frac{d\Gamma\left(H_1 \to H_2 \bar{\ell}\ell\right)}{dq^2} = \frac{1}{2}\left(\frac{d\Gamma_U^{11}}{dq^2}+\frac{d\Gamma_U^{22}}{dq^2}+\frac{d\Gamma_L^{11}}{dq^2}+\frac{d\Gamma_L^{22}}{dq^2}\right)+\frac{1}{2}\frac{d\tilde{\Gamma}_U^{11}}{dq^2}-\frac{d\tilde{\Gamma}_U^{22}}{dq^2}+\frac{1}{2}\frac{d\tilde{\Gamma}_L^{11}}{dq^2}-\frac{d\tilde{\Gamma}_L^{22}}{dq^2}+\frac{3}{2}\frac{d\tilde{\Gamma}_S^{22}}{dq^2}, \quad (10)$$

where the partial helicity rates $d\Gamma_X^{ij}/dq^2$ and $d\tilde{\Gamma}_X^{ij}/dq^2$ $\left(X=U,L,P,S;i,j=1,2\right)$ are defined as

$$\frac{d\Gamma_{X_{ij}}}{dq^2} = \frac{G_F^2}{\left(2\pi\right)^3}\left(\frac{\alpha|\lambda_t|}{2\pi}\right)^2\frac{|\mathbf{p}_2 q^2\upsilon|}{12m_1^2}H_X^{ij}, \quad \frac{d\tilde{\Gamma}_{X_{ij}}}{dq^2} = \delta_{\ell\ell}\frac{d\Gamma_X^{ij}}{dq^2}, \quad \delta_{\ell\ell}\equiv\frac{2m_\ell^2}{q^2}. \quad (11)$$

The differential angular decay distribution in the Ref. [8] is expressed via the transversality amplitudes $A_\perp$, $A_\parallel$, A_0 and A_t. They are related to our helicity amplitudes as

$$A_\perp^{L,R} = N\frac{1}{\sqrt{2}}\left[\left(H_+^{(1)}-H_-^{(1)}\right)\mp\left(H_+^{(2)}-H_-^{(2)}\right)\right],$$
$$A_\parallel^{L,R} = N\frac{1}{\sqrt{2}}\left[\left(H_+^{(1)}+H_-^{(1)}\right)\mp\left(H_+^{(2)}+H_-^{(2)}\right)\right], \quad (12)$$
$$A_0^{L,R} = N\left[\left(H_0^{(1)}\mp H_0^{(2)}\right)\right],$$
$$A_t = -2N H_t^{(2)}$$

where the overall factor is given by

$$N = \left[\frac{1}{4}\frac{G_F^2}{(2\pi)^3}\left(\frac{\alpha|\lambda_t|}{2\pi}\right)^2\frac{|\mathbf{p}_2|q^2\upsilon}{12m_1^2}\right]^{\frac{1}{2}}.$$

We do not consider here the CP-violationg observables and scalar contributions $A_S \equiv 0$. Following Ref. [9] we choose, first, three natural observables: the differential branching fraction dB/dq^2, the forward-backward asymmetry A_{FB} and the longitudinal polarization

$$\frac{d\Gamma}{dq^2} = \int d\cos\theta_l d\cos\theta_K d\phi\frac{d^4\Gamma}{dq^2\, d\cos\theta_K\, d\cos\theta_l\, d\phi} = \frac{1}{4}(3J_{1c}+6J_{1s}-J_{2c}-2J_{2s}), \quad (13)$$

$$A_{FB} = \frac{1}{d\Gamma/dq^2}\left[\int_{1-}^{0}-\int_{0}^{1}\right]d\cos\theta_l\frac{d^2\Gamma}{dq^2\, d\cos\theta_l} = -\frac{3J_{6s}}{3J_{1c}+6J_{1s}-J_{2c}-2J_{2s}}. \quad (14)$$

$$F_L = -\frac{J_{2_c}}{d\Gamma/dq^2} = \frac{1}{2}\beta_l^2\frac{H_L^{11}+H_L^{22}}{H_{tot}}. \quad (15)$$

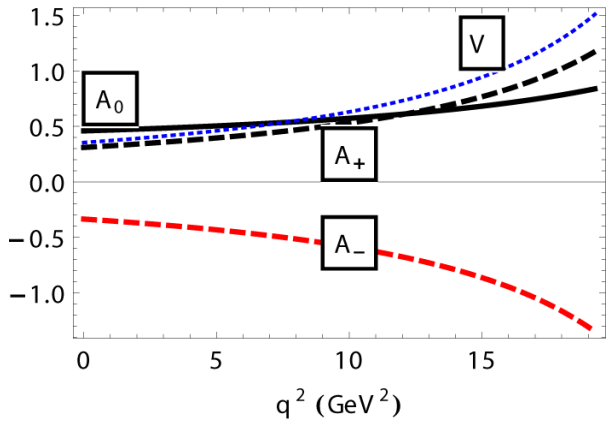

Figure 1 – The q^2-dependence of the $B - K^*$ transition V,A form factors

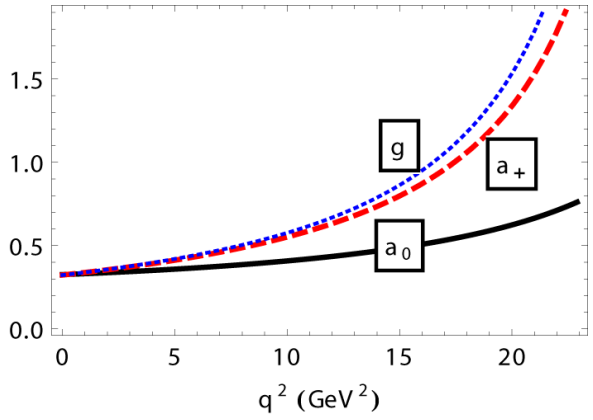

Figure 2 – The q^2-dependence of the $B - K^*$ transition T form factors

Table 1 – The fitted values of the model parameters in GeV.

$m_{u/d}$	0.241	Λ_K	1.02	Λ_{η_c}	2.06	Λ_{K^*}	0.75
m_s	0.428	Λ_D	1.71	Λ_{η_b}	2.95	Λ_{D^*}	1.51
m_c	1.67	Λ_{D_s}	1.81	Λ_ρ	0.61	$\Lambda_{D_s^*}$	1.71
m_b	5.05	Λ_B	1.96	Λ_ω	0.50	Λ_{B^*}	1.76
λ,	0.181	Λ_{B_s}	2.05	Λ_ϕ	0.91	$\Lambda_{B_s^*}$	1.71
Λ_π	0.87	Λ_{B_c}	2.50	$\Lambda_{J/\psi}$	1.93	Λ_Υ	2.96

Table 2 – Parameters for the approximated form factors in Eqs. (23) of the $B \to K^*$ transitions.

	A_0	A_+	A_-	V	a_0	a_+	G
$F(0)$	0.459	0.310	-0.335	0.354	0.326	0.323	0.323
a	0.439	1.252	1.306	1.345	0.457	1.249	1.350
b	-0.311	0.270	0.316	0.343	-0.290	0.268	0.349

Table 3 – Total branching fractions

Decay	Our	Experiments [10,12,13]
$B \to K^* \mu^+ \mu^-$	12.7×10^{-7}	$(9.24\pm0.93(stat)\pm0.67(sys))\times10^{-7}$
$B \to K^* \tau^+ \tau^-$	1.35×10^{-7}	-
$B \to K^* \gamma$	3.74×10^{-5}	$(4.21\pm0.18)\times10^{-5}$
$B \to K^* \nu\bar{\nu}$	1.36×10^{-5}	-
$B \to K \mu^+ \mu^-$	7.18×10^{-7}	$(4.29\pm0.07(stat)\pm0.21(sys))\times10^{-7}$
$B \to K \tau^+ \tau^-$	3.0×10^{-7}	-
$B \to K \nu\bar{\nu}$	0.60×10^{-5}	-

Table 4 – q^2–averages of polarization observables

	$B \to K^* l^+ l^-$							
	$< A_{FB} >$	$< F_L >$	$< P_1 >$	$< P_2 >$	$< P_3 >$	$< P_4 >$	$< P_5 >$	$< P_8 >$
μ	-0.23	0.47	-0.48	-0.31	0.0015	1.01	-0.49	-0.010
τ	-0.18	0.092	-0.74	-0.68	0.00076	1.32	-1.07	-0.0018

Conclusion

We calculate various physical observables semileptonic rare decay $B \to K^*(\to K\pi) l^+ l^-$. The values of the lepton and meson masses and the B-meson lifetime are taken from Ref. [11]. In Table 3 we give the numerical values for the total branching ratios and compare them with available experimental data. In Table 4 we give the q^2–averages of polarization observables.

Considering the outcoming numbers, it is difficult to make a clear statement about the level of agreement. Clearly, the branching fraction prediction is above both measured values. On the other hand one has to note the discrepancy which exists between the experimental values themselves and thus a question mark remains on this issue.

Acknowledgements

This work was supported by the Ministry of Education and Science of the Republic of Kazakhstan, grant 3091/GF4, state registration No. 0115RK01041.

References

1. Langenbruch C. LHCb Collaboration Latest results on rare decays from LHCb // http://arxiv.org/abs/1505.04160.

2. Aaij R. et al. LHCb Collaboration Test of lepton universality using $B^+ \to k^+ l^+ l^-$ decays // Phys. Rev. Lett. – 2014. – Vol.113. – P. 151-601.

3. Aaij R. et al. LHCb Collaboration Measurement of form-factor independent observables in the decay $B^0 \to k^{*0} \mu^+ \mu^-$ // Phys. Rev. Lett. – 2013. – Vol.111. – P. 191-801.

4. Zhaugasheva S.A., Nurbakova G.S., Saidullaeva G.G., Khabyl N. Form factors for $\mathrm{B} \to \mathrm{K} l^+ \mathrm{l}^-$ decay // International Journal of mathematics and physics 5. – 2014. – No. 2. – P. 52-56.

5. Zhaugasheva S.A., Saidullaeva G.G., Nurbakova G.S., Khabyl N., Bekbaev A.K. Rare bs - decays in the covariant quark model // International Journal of mathematics and physics 5. – 2014. – No. 2. – P. 68-76.

6. Branz T., Faessler A., Gutsche T., Ivanov M. A., K¨orner J. G., Lyubovitskij V. E. Relativistic constituent quark model with infrared confinement // Phys. Rev. D – 2010. – Vol.81. – P. 034010.

7. Ganbold G., Gutsche T., Ivanov M. A. and Lyubovitskij V. E. On the meson mass spectrum in the covariant confined quark model // J. Phys. G. – 2015. – Vol.42. – P. 075002.

8. Kruger F. and Matias J. Probing New Physics Via the Transverse Amplitudes of B0-> K*0(-> K-pi+) l+l- at Large Recoil // Phys. Rev. D. – 2005. – Vol.71. – P. 094009.

9. Matias J., Mescia F., Ramon M. and Virto J. Complete Anatomy of $B \to K^* ll$ and its angular distribution // JHEP. – 2012. – Vol.1204. – P. 104.

10. Descotes–Genon S., Hurth T., Matias J. and Virto J. Optimizing the basis of $B \to K^* ll$ observables in the full kinematic range // JHEP. – 2013. – Vol.1305. – P. 137.

11. Olive K. A. et al. Particle Data Group Collaboration // Chin. Phys. C. – 2014. – Vol.38. – P. 090001.

12. Aaij R. et al. LHCb Collaboration Differential branching fractions and isospin asymmetries of $B \to K^{(*)} \mu^+ \mu^-$ decays // JHEP. – 2014. – Vol.1406. – P. 133.

13. Pescatore L. LHCb Collaboration Rare decays at the LHCb experiment // http://arxiv.org/abs/1410.2411.

UDC 621.48

[1*]Manatbayev R.K., [2]Georgiev A., [2]Popov R., [2]Dzhonova-Atanasova D.,
[1]Kuikabayeva A.A., [1]Zulbukharova E.M.

[1]Physico-Technical Faculty, al-Farabi Kazakh National University, Almaty, Kazakhstan
[2]Plovdiv university Paisii Hilendarski, Plovdiv, Bulgaria
[*]e-mail: Rustem.Manatbayev@kaznu.kz

The effect of design parameters on energy characteristics of Darrieus rotor

Abstract. In the last 10-15 years the use of wind energy is growing. There are more than 20,000 wind power turbines with a total capacity of more than a few megawatts in the world. Kazakhstan has significant wind power resources. Resources of the Jungar gate and Shelek complex in Almaty region are the best known in this respect. Their capabilities for use in electricity generation of air flow are unique.
This article describes the main types of wind turbines and the benefits of Darrieus rotor over other wind turbines. The article provides the basic calculations to determine the effect of the wind turbine Darrieus design characteristics on its energy efficiency. This article shows the dependence of the maximum utilization coefficient of wind energy vertical axis windwheels from the number of blades with constant filling factor σ, from the number of blades with their constant width, from blades elongation λ. Design characteristics for 1 kW rotor were identified based on these results. Also, wind turbine scheme, that can provide thermal protection by warm air natural ventilation in the rotating elements of wind turbine which arises due to centrifugal forces, is shown.
Key words: Darrieus rotor, rotation shaft, windturbine, the fill factor, thermal protection, ideal rotor.

Introduction

In the last 10-15 years the use of wind energy is quick stepping to new peaks. There are more than 20,000 wind electric set so far in the world, the total capacity of which is more than a few megawatts.

The possibility of electric power generation is defined by the construction of wind turbines. All the wind turbines consist of blades that rotate axis connected to a generator, which generates a current.

The size and capacity of wind turbines are fluctuating widely. There are three main types of wind turbines: with horizontal axis, with vertical axis and channel.

Currently the horizontal axis or so called propeller type turbines are mainly used in the world. They compose more than 90% of the total number of wind farms, and some thousand companies are engaged in their serial production.

The vertical axis wind turbines were not developed for almost 40 years because of the improper conclusion on low rate of wind energy operation of vertical axis wind turbines. And only at the end of the last century, firstly Canadian and then American and British specialists have proved experimentally that these conclusions do not apply to the Darrieus rotor of blade lift [1].

This paper specifies that the propeller type wind turbines can significantly reduce the generated electricity with frequent changes in wind direction. When the wind direction is changed rapidly the wind wheel must accurately track these changes, but it is almost impossible to effectively orient the wind wheel when changing the wind direction due to delay in orientation mechanisms action.

Recently the majority of foreign companies began to give priority to the new type of wind turbine with vertical axis of Darrieus rotor (see Fig. 1). The turbine operates due to the occurrence of the lift on cover blades equidistant from a common axis of rotation.

The advantage of vertical axis wind turbines is the possibility of placing the generator on the turbine base. This eliminates the strong, most likely multi level angle drive of torque simplifying the requirements for the installation of equipment (exclude limitations on size and weight) and for the maintenance conditions (lack of shocks and vibrations). It facilitates the transmission of electricity generated.

 Printed in Kazakhstan

Figure 1 – Darrieus wind turbine

The operation of Darrieus rotor does not depend on flow direction. Consequently, the turbine at its base unit does not require positioner. Darrieus rotor is characterized by a high specific speed at low flow rates and high flow energy efficiency, and the area swept by rotor wings can be quite large.

The most technologically advanced is the H-rotor Darrieus. This type is of high-speed installation, coefficient of efficiency reaches 0.45. Rotor H-Darrieus differs by low noise level and total lack of infrasound. The wind turbine of this type has a simple structure and high reliability.

The experimental study of energy characteristics of Darrieus rotor has showed their significant dependence on the thickness of the blade profile. The same dependence on the profile thickness is observed for the traction force generated by flapping wings [4].

The experimental study results show significant dependence of the flow energy efficiency on the geometric parameters of the wind wheel. In this regard, it is important for constructor to know the maximum energy capability of the wind wheel, which can be "squeezed" out of it by designing. The concept of an ideal wind wheel is introduced in order to estimate the maximum energy capability. It refers to a virtual wind wheel running without loss. It is believed that the Darrieus rotor and propeller type wind wheel have the same maximum values of wind flow energy efficiency [5]. However, the experimental study conducted in recent years [6] has showed that the Darrieus rotor may have a higher energy characteristic than the propeller type wind wheel.

Harsh winters so common to Nordic countries, create a very serious problem – blades icing. And it is fraught with just a few troubles, says the Swedish meteorologist Stefan Söderberg, Research Officer of Weathertech Company in Uppsala: "When the ice crust is formed on blades, their aerodynamic characteristics are significantly deteriorated. As a result the wind turbine capacity is lost. This is at first. Secondly, a nice crust unbalances wind wheel, which leads to an increased wear of the bearing parts and the wind generator as a whole. Besides that because of the freezing of super-cooled rain or wet snow the aerodynamics of the blade is worsen, and sometimes you have to disconnect the wind turbine if the ice layer thickness exceeds a critical value. The same situation is observed in Finland, and in the north of Germany and in Switzerland and Russia. Finally, we cannot ignore the dangers connected with the fact that the pieces of the ice from the ends of the rotating blades can break away and scatter over long distances. Appelbo wind turbine in Sweden, for example, reported on 7-week turbine stop in winter 2002-2003. The Swedish statistical database of accidents contains in total about 1337 such records occurred between 1998 and 2003 - as a result, in general, downtime-161 523 hours. 92 accidents (7 percent) were due to the cold climate and as a result of 8022 hours (5 percent) - loss of production. Reports on low temperature downtime in a cold climate were 669 hours (8 percent), although due to the cases of icing were 7353 (92 percent). Downtime is reported due to icing in Finland in the period from 1996 to 2001 were 1208/495/196/581/739 and 4230 hours for the 19/21/29/38/61 and 61 turbines, respectively [7].

Calculation of the effects of the design parameters

Recently the extensive studies have been conducted to identify and simulate methods of preventing icing. The variety of methods developed by experts in alternative energy resource and air flying machine to solve this problem is offered all over the world. Most of these methods have been taken from the aircraft industry and can be divided into two categories: active and passive. Passive methods are based on the physical properties of the

blade for preventing ice accumulation, while active methods based on external system applied to the blade. Two types of systems can be used to prevent icing - in particular this is purging against icing and preventing icing. The first removes the ice from the surface after its formation, whereas the latter prevents early ice formation [8].

The methods of active protection for operation demand energy supply, and include thermal, chemical and pneumatic methods and act as the systems for purging of ice or anti-ice [9].

The development of a safe method of protection the operating wind electric set from adverse weather conditions is important. In this regard, the development of wind turbine with anti-icing system using natural ventilation flow turbine elements with warm air, not allowing wet snowflakes sticking on the surface of the machine and formation of ice, is proposed in this paper[10]. This paper deals with the development of thermal protection method of operating wind turbines and preservation of its operating capacity under the most severe climatic conditions in winter.

Therefore the task is to develop a design of the wind turbine Darrieus with thermal protection and to determine geometric parameters of the turbine of 1 kW capacity for the further development of semi-commercial sample of wind turbine of H-rotor type having an anti-icing system.

When designing a wind turbine constructor needs to know the influence of the main parameters on the performance of the rotor. Currently the main source of information for the design of wind wheels with Darrieus rotor is an experiment. The most complete and comprehensive experimental results are published in the works [2.11].

Thus, the calculations of the influence of design parameters on the energy characteristics of the rotor Darrieus have been done.

1) *The effect of blade elongation.* The blade elongation is one of the main rotor Darrieus design parameters that determines its aerodynamic characteristics. The aerodynamic loads level on blade, including torque significantly depends on the values of elongation. The nature of this dependence for a single blade is almost the same as for the wing. When elongating $\lambda<1$, the value of the aerodynamic load varies linearly from λ, and with the increase of the elongation these loads approach their asymptotic values at $\lambda> 5$.

2) *The effect of the number of blades.* Another important design parameter is the number of blades of the rotor Darrieus. In order to assess the effect of the number of blades on the rotor energy characteristics special investigation on the rotor models with different number of blades are held.

According to Fig.2 it is necessary to use blades with elongation of more than 6 to ensure acceptable wind energy efficiency.

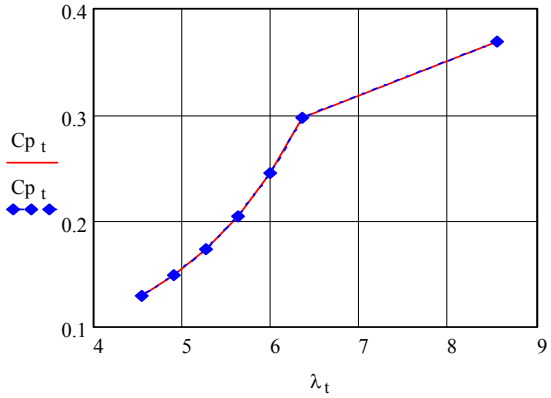

Figure 2 – The dependence of C_p on blade elongation (n = 2, b/D = 0.167, R = 1.65 m, *l* = altern.)

The experiment shows that the high energy characteristics have single-blade rotor. Although in this case, torque experiences a large ripple in time that causes dynamic problems. Increasing the number of rotor blades smoothes out torque characteristics, but it leads to a decrease in energy efficiency. This is especially appears, when increasing the number of blades to reduce their chord to preserve the constancy of the fill factor σ. In increasing the number of blades the preservation of the chord length is more effective. Fig. 3 shows the results of calculations on the study of the effect of the number of blades at constant fill factor. It is evident that with the increase of number of blades the wind energy efficiency is reduced. Fig. 4 shows that at constant width of blades the efficiency of C_P drops considerably less than at constant filling with the increase of the number of blades.

3) *The effect of blade thickness.* The effect of relative profile thickness of the blade on the amount of the maximum value of C_P coefficient at a different Re numbers is shown in [12]. The greatest effect is achieved for the blades with relative thickness of $0.15<\overline{c}<20$. The main feature of this effect is associated with a sharp drop of C_P for thin blades. It should be noted that the same dependence

character on relative thickness of the profile is observed for the traction force generated by flapping wings [4].

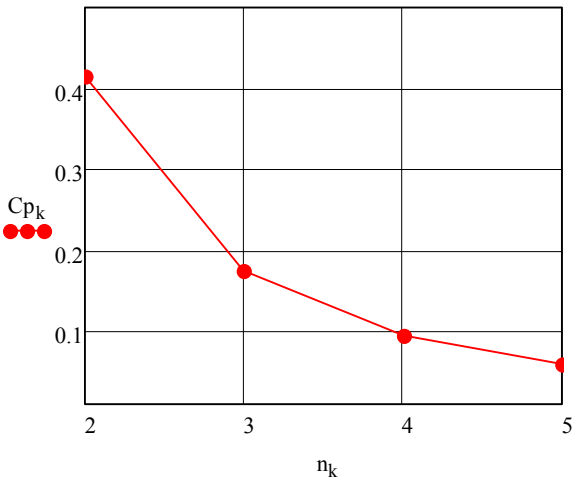

Figure 3 – The results of calculations on the study of the effect of the number of blades at constant fill factor. (σ=const, *l*=3.3 м)

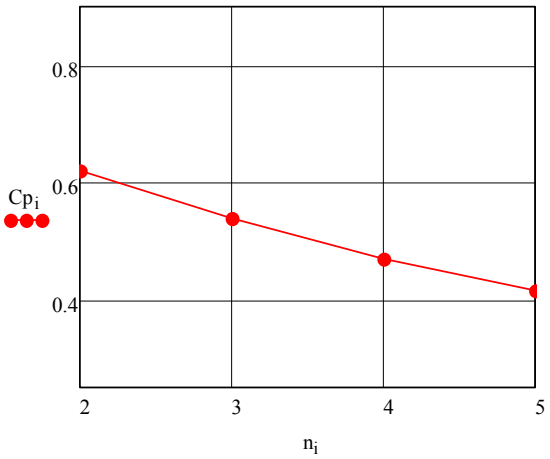

Figure 4 – The dependence of C_p on number of blades at their constant width (b=const, D=3.3 m,*l*=3.3 m)

4) *The effect of fill factor.* The fill factor is connected with two rotor design parameters: number of blades n_b and ratio of blade chord to rotor diameter b/D. It should be noted that when increasing the fill factor σ the value of rapidity z decreases, wherein C_p reaches its maximum value.

Having analyzed all the above mentioned data, the geometry of airfoil NASA-0021was determined.

In order to have a Darrieus rotor with straight blades of 1 kW power, with an average wind speed U, equal to 7 m/s, let's find a streamlined surface of rotor by formula:

$$S = \frac{2\,N_b}{C_p \rho U^3}$$

here N_b – capacity, W; C_p – wind energy efficiency, assumed equal 0,4; ρ – 1,29 kg/m^3 – air density.

The streamlined area of rotor of1kW capacity must be 11.3 m^2. If to take equal the rotor diameter D and the height of blade *l*, then D = *l*≈3,36m. During experimentally proved blade elongation λ=l/b=6-8 chord length of blade can range b=3,36/(6-8)=0,56-0,42 m and chord on average will be b=0,55m.

Since the maximum value of the coefficient C_p at different Re numbers is achieved for blades with a relative thickness of $0.15<\overline{c}<20$, let's take the relative thickness equal to 0,18. On this basis, the maximum thickness of blade, as a part of the length of chord must be 0.09m. And fill factor, in turn, will be equal to

$$\sigma = \frac{n_b b}{D} = 0.33.$$

It is important to note that the fill factor σ satisfies the conditions under which C_p reaches its maximum value.

Using the application packages for mathematical calculations we can obtain the area and perimeter of the cross section. For our rotor the wing perimeter is F=1,04m and the ratio of chord b is approximately equal to 2,1. The cross section area f_1=0.0154 m^2.

Figure 5 shows the preliminary design of machine with anti-icing system. Internal hydraulics and the movement of warm air through internal channels are described in detail in works [10,13,14].

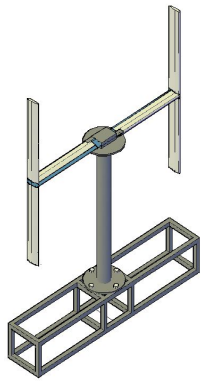

Figure 5 – Preliminary design of machine with anti-icing system

Conclusion

Now we are starting to design the wind power plant of carousel type with anti-icing system on the basis of above studies.

References

1. Solomin E.V. Wind Energy Plants GRTS-Vertical // Alternative Energy and Ecology. – 2010. № 1. – P. 10-15

2. Baklushin P.G., Vashkevich K.P., Samsonov V.V. Experimental Study of Aerodynamic Characteristics of Orthogonal Vane Wind wheels // Scientific Papers' Collection of Hydro project. –M., 1988. – Edition 129: Wind Power Stations. – 1988. – P. 98-105.

3. Voronin S.M., Babina L.V. Operation of Wind Turbineduring ChangingWind Direction // Alternative Energy and Ecology. – 2010. № 1. – P. 98-100

4. Gorelov D.N. The Analogy between the Flapping Wings and the Wind wheel with Vertical Rotation Axis // Applied Mechanics and Technical Physics. – 2009. – Vol. 50. – P. 152-155.

5. Turyan K.J., Strikland J., Barg D.E. Capacity of Wind Power Units with Vertical Rotation Axis // Aerospace techniques. – 1988. – P. 100-115.

6. Gorelov D.N., Kuzmenko U.N. Experimental Evaluation of Wind wheel Critical Power with Vertical Rotation Axis // Thermo physics and Aeromechanics. – 2001. – Vol. 8. – P. 329-334.

7. Jasinski W.J., Noe S.C., Selig M.C., Bragg M.B. Wind Turbine Performance under Icing Conditions // Trans ASME J Sol Energy Eng. – 1998. – Vol. 120. – P. 60–65.

8. Laakso T., Holttinen H., Ronsten G,.Tallhaug L., Horbaty R., Baring-Gould I. et al. State-of-the-Art of Wind Energy in Cold Climate. – 2003. – P. 1–56.

9. Dalili N., Edrisy A., Carriveau R. A Review of Surface Engineering Issues Critical to Wind Turbine Performance // Renewable and Sustainable Energy Reviews. – 2009. – Vol. 13. – P. 428-238.

10. Manatbayev R.K., Yershina Sh. A., Yershina A.K. Method for Thermally Protecting Operating Revolving Type Wind-Power Installation, Involves Causing Internal Natural Ventilation in Wind Unit by Centrifugal Force to Heat All Elements of Wind-Power Installation by Warm Air. Patent Number(s): RU2008137251-A; RU2447318-C2 International Patent Classification: F03D-003/00 Derwent Class Code(s): Q54 (Starting, ignition); X15 (Non-Fossil Fuel Power Generating Systems) Derwent Manual Code(s): X15-B01A6

11. Ivanov I.I., Ivanova G.A., Perfilov O.L. Model Studies of Wind Stations' Rotary Operation Wheels. Scientific Papers' Collection of Hydro project. –M., – 1988. – Edition 129: Wind Power Stations. – P. 106-113.

12. Gorelov D.N. Aerodynamics of Wind wheels with vertical rotation axis // Omsk: Printing center KAN. – 2012. – P. 68.

13. Yershina A.K., Manatbayev R.K. Organization of natural ventilation in side operating unit Darrieus // Energy. –Moscow. – 2013. – №1-2. – P. 63-66.

14. Yershina A.K., Manatbayev R.K. Determination of hydraulic resistance of a symmetric airfoil NASA -0021.KazNU Bulletin, Part of Mathematics, Mechanics, Informatics. – 2006. – №4 (51). – P. 56-58.

UDC 621.548

[1]Yershin Sh.A., [2]Yershina A.K., [3*]Manatbayev R.K., [3]Tulepbergenov A.K.

[1] Faculty of Mechanic-Mathematical, al-Farabi Kazakh National University, Almaty, Kazakhstan
[2]Kazakh State Women Pedogogical University, Almaty, Kazakhstan
[3] Physico-Technical Faculty, al-Farabi Kazakh National University, Almaty, Kazakhstan
[*]e-mail: rustem1977@mail.ru

Definition of aerodynamic characteristics wind turbine to Darrieus of system troposcino

Abstract: Recently the majority show interest in connection with a number of merits to vertically-axial wind turbine type to Darrieus. It is possible to tell that age such wind energy installations of 25-30 years whereas others types wind turbine (sailing, propeller) have seriously started to study almost 1,5 centuries. The theory of these wind turbine with sufficient completeness are resulted in known E. M.Fateyev's monograph.

In the present to article results of a theoretical substantiation for one of design kinds wind turbine are stated Darrieus - systems troposcino. This constructive form of the device to Darrieus becomes more and more popular. The general theory is constructed, almost all constructive and aerodynamic characteristics (linear speed, carrying power, front resistance are defined; wind power operating ratio; the moment of rotation of the turbine) this device. Thus, attempt to put basic bases of the theory of devices to Darrieus of system troposcino is made. This report shows main theoretical principles of troposkino wind-turbine. Theoretically were determined dynamical characteristics of the wind-turbine, such as: rotation moment, power, useful wind energy coefficient and physical model of the plant. The theoretical results were compared with well-known experimental data.

Key words: aerodynamic characteristics, wind turbine, wind turbine to Darrieus, system troposcino.

Introduction

The form troposcino (see Fig. 1) is rather close to a parabola described by the equation

$$x = r = r_m - \frac{9z^2}{16r_m} = \frac{3}{8}H - \frac{3}{2}\frac{z^2}{H}, \qquad (1)$$

where $r_m = \frac{3}{8}H$ – the maximum radius of rotation of the turbine (in considered by us of a design), - height. Therefore (1) it is possible to present the formula in a kind

$$r = r_m\left[1 - \left(\frac{z}{H/2}\right)^2\right]. \qquad (2)$$

In case of the turbine with direct blades "r" does not depend on "z" and $r_m = r_0$.

The area of the window formed in midlives metrically located pair of blades, is the area m sections of a surface of rotation of the turbine and is equal

$$F = \frac{4}{3}r_m H = \frac{H^2}{2}. \qquad (3)$$

Let's find total length of 2 blades. As it is known, the length $L_{1,2}$ of a curve on $[z_1, z_2]$ a piece is defined by the formula $L_{1,2} = \int_{Z_1}^{Z_2}\sqrt{(dx)^2 + (dz)^2}$. From here length of both blades is equal:

$$2L = 4\int_0^{H/2}\sqrt{1+\left(\frac{dx}{dz}\right)^2}dz = 4\int_0^{H/2}\sqrt{1+9\frac{z^2}{H^2}}dz = 2\left[\frac{H}{2}\sqrt{1+\frac{9}{4}} + \frac{H}{3}\ln\left(\frac{3}{2}+\sqrt{1+\frac{9}{4}}\right)\right] \approx 2,6H. \qquad (4)$$

Let's find the moment of force developed two blade by the turbine to Darrieus, executed in a kind troposcino which at us is replaced by a parabola (2). With that end in view we will define in the beginning components of a vector of speed of attack in the M point on the bent element of a wing of infinitesimal length System of co-ordinates it is located so that the direction of speed of a wind coincides with a direction of co-ordinate at, and a vertical axis of rotation wind turbine – with an axis z.

Method of research

Direction rotation wind turbine with some angular speed we will choose so that if to take a detached view of the turbine of a positive direction of an axis z, rotation will be counter-clockwise. We will consider instant position of blades developed concerning an axis x on a corner θ (Fig. 1 see). For simplification of the analysis (Fig. 2 see) we will choose three mutually perpendicular straight lines. Two of them are tangents to a blade surface in M. This is $AA^{'}$ point - a tangent to a parabola line, defines a blade bend, that is a corner γ between a straight line $AA^{'}$ and a vertical $NN^{'}$, and $BB^{'}$ - a tangent in the M point To a circle described in radius at rotation of the turbine. And, at last, the third straight line represents $CC^{'}$ a normal to the blade surface, directed to the M.

The point vector $\vec{V}$ of speed of attack represents a resultant from addition of two vectors. One of them is normal to a surface of the blade a component of a vector of speed of a wind $\vec{U}$ and is equal $\vec{U}\sin\theta\cos\gamma$ (Fig. 2), the second see - is directed on a tangent $BB^{'}$ and represents the sum: linear speed of rotation of a point $(\vec{r}\times\vec{\omega})$ of M plus a component of speed of the wind, designed on a direction $BB^{'}(\vec{U}\cos\theta)$. As a line on $BB^{'}$ which total speed $\vec{r}\times\vec{\omega}+\vec{U}\cos\theta$, and $CC^{'}$ on which the normal component of speed of a wind $\vec{U}\sin\theta\cos\gamma$ operates, are mutually perpendicular, their equally effective it is equal

Figure 1 – Wind turbine with the turbine to Darrieus of system troposcino

$$\left|\vec{V}\right| = \sqrt{U^2\sin^2\theta\cos^2\gamma + (r\omega + U\cos\theta)^2} \quad (5)$$

Also gives value of speed of attack of an air stream in point M the answer an angle of attack it will be defined by expression

$$tg\alpha = \frac{U\sin\theta\cos\gamma}{r\omega + U\cos\theta}. \quad (6)$$

From (5) and (6) it is easy to establish connection between an angle of attack and a blade angle of rotation:

$$\begin{aligned} \vec{V}\cos\alpha &= \vec{U}(\chi + \cos\theta) \\ \vec{V}\sin\alpha &= \vec{U}\sin\theta\cos\gamma. \end{aligned} \quad (7)$$

The moment created tangential making carrying power $\vec{R}_l$, is equal $M = rR_\tau = r\left|\vec{R}_l\right|\sin\alpha.$ Carrying power $\vec{R}_l$ is directed perpendicularly to a vector of speed of attack and connected with last means of factor of carrying power. Counteracting force is resistance of air to blade movement $\left|\vec{R}_D\right|$.

From here the moment created by an element dS of a wing, registers as follows:

$$dM_l = r\rho\frac{V^2}{2}в\left[C_y\sin\alpha - C_x\cos\alpha\right]dS, \quad (8)$$

Substituting values C_y and C_x for profile NASA-0021 in (8), we will receive

$$M_l = \rho\frac{V^2}{2}вr\left[\sqrt{2}\pi\sin^2\alpha - (0{,}014+\sin^2\alpha)\cos\alpha\right]dS \quad (9)$$

The decision (9) we will break into 2 separate problems

$$dM_l = dM_{l1} + dM_{l2},$$

where

$$dM_{l1} = \sqrt{2}вr\pi\frac{\rho V^2}{2}\sin^2\alpha dS, \quad (10)$$

$$dM_{l2} = -вr\frac{\rho V^2}{2}(0{,}014+\sin^2\alpha)\cos\alpha dS. \quad (11)$$

The first problem (10) dares simply enough. Addressing to (7), we will receive

$$dM_{l1} = \sqrt{2}\pi вr(z)\frac{\rho U^2}{2}\sin^2\theta\cos\gamma dz, \quad (12)$$

$$\text{As } \frac{dz}{dS} = \cos\gamma.$$

Using the formula (2), we will receive the following:

$$dM_{l1} = \sqrt{2}\pi в\frac{r_m\left(1-\bar{z}^2\right)H}{2}\rho\frac{U^2}{2}\sin^2\theta\cos\gamma d\bar{z}, \quad (13)$$

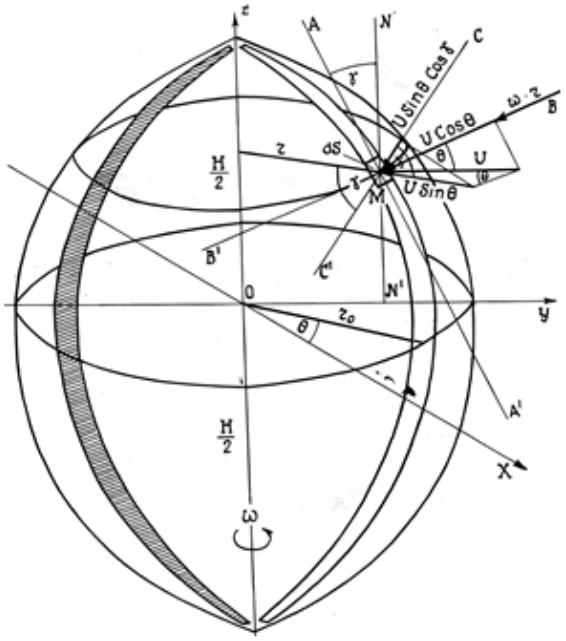

Figure 2 – The scheme of interaction of the blade troposcino with a wind stream

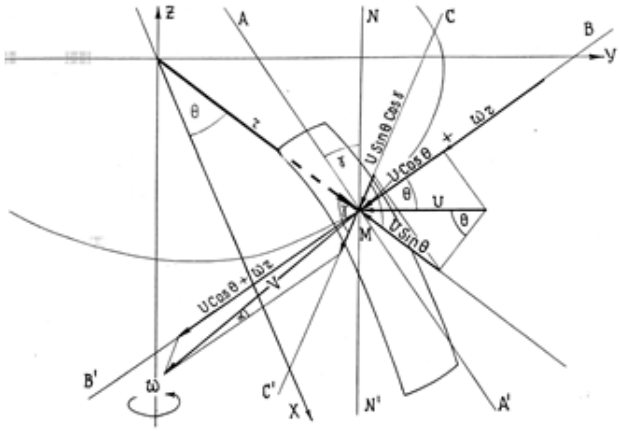

Figure 3 – A blade element troposcino for definition of speed and an angle of attack

where $\bar{z} = \frac{z}{H/2}$.

Dependence on $\cos\gamma$ co-ordinate to find easy. With that end in view we will write down the equation for a tangent in any point of a parabola:

$$tg\gamma = \frac{dx}{dz} = -3\frac{z}{H} = \frac{\sqrt{1-\cos^2\gamma}}{\cos\gamma}, \qquad (14)$$

$$\frac{1}{\cos\gamma} = \sqrt{1+9\left(\frac{z}{H}\right)^2} = \sqrt{1+\frac{9}{4}\bar{z}^2}. \qquad (15)$$

Substituting (15) in (13), we will receive

$$dM_{l1} = \frac{\sqrt{2}}{2}\pi H r_m в\rho\frac{U^2}{2}\sin^2\theta\frac{1-\bar{z}^2}{\sqrt{1+\frac{9}{4}\bar{z}^2}}d\bar{z} \qquad (16)$$

And, integrating last expression on $\bar{z}$, we will receive size of the rotary moment of the blade

$$M_{l1} = \frac{\sqrt{2}}{4}\pi H r_m в\rho U^2\sin^2\theta\int_{-1}^{1}\frac{1-\bar{z}^2}{\sqrt{1+\frac{9}{4}\bar{z}^2}}d\bar{z}\ . \qquad (17)$$

Tabular integral

$$\int_{-1}^{1}\frac{1-\bar{z}^2}{\sqrt{1+\frac{9}{4}\bar{z}^2}}d\bar{z} \approx 1{,}37\ .$$

Thus, for two blade turbines we will have:

$$2M_{l1} = 0{,}685\sqrt{2}\pi в r_m H\rho U^2\sin^2\theta. \qquad (18)$$

Average value of the rotary moment at one turn of the turbine we will receive, having integrated $2M_{l1}$ from zero to 2π and having divided on 2π:

$$M_{l1} = \frac{1}{\pi}\int_0^{2\pi}M_{l1}d\theta = 0{,}685\sqrt{2}в r_m H\rho U^2\int_0^{2\pi}\sin^2\theta d\theta$$

$$M_{l1} = 1{,}37\sqrt{2}\pi в r_m H\rho\frac{U^2}{2} \qquad (19)$$

Let's address now to the second problem (11). If to take out from a bracket and to take into consideration (5) and (7) expression (11) will become:

$$dM_{l2} = -вr(z)\frac{\rho U^2}{2}\times\left(1+0{,}014\frac{\sin^2\theta\cos^2\gamma+(\chi+\cos\theta)^2}{\sin^2\theta\cos^2\gamma}\right)\times\frac{\sin^2\theta\cos^2\gamma(\chi+\cos\theta)dS}{\sqrt{\sin^2\theta\cos^2\gamma+(\chi+\cos\theta)^2}}. \qquad (20)$$

Before to pass to the further procedure of the decision (20), we will receive some additional parities and communications. First of all we will notice that in a case troposcino degree of rapidity of the turbine changes on height

$$\chi(z) = \frac{\omega r(z)}{U} \qquad (21)$$

And it brings serious difficulties in the decision of a problem (10). They can be overcome if to take into consideration that the basic contribution to resistance of the air environment to blade movement is brought by the central part troposcino. And it occupies about 85 % of length of the blade. Really, from (2) follows

$$\bar{z} = \frac{z}{H/2} = \sqrt{1-\bar{r}} \qquad (22)$$

where $\bar{r} = \frac{r(z)}{r_m}$.

From here it is possible to estimate $\bar{z}$, for example, at reduction $\bar{r}$ in 3 times

$$\bar{z} = \sqrt{0{,}7} \approx 0{,}85. \qquad (23)$$

In view of (21), (22) it is possible to express dependence through size of rapidity of elements of the turbine $\chi(z)$

$$\bar{z} = \sqrt{1-\bar{\chi}}, \qquad (24)$$

where $\bar{\chi} = \frac{\chi(z)}{\chi_m}$, $\qquad \chi_m = \frac{\omega r_m}{U}$.

That circumstance that the basic contribution to turbine work is brought by the central part of blades (85 %) allows to soften nonlinearity of a parity (20). With that end in view we will remove the brackets and we will take out from under a root size $\chi + \cos\theta$. Then we will receive

$$dM_{l2} = -\varepsilon r(z)\frac{\rho U^2}{2}\times\left[\frac{1}{\sqrt{1+\left(\frac{\sin\theta\cos\gamma}{\chi+\cos\theta}\right)^2}} + 0,014\left(\frac{\chi+\cos\theta}{\sin\theta\cos\gamma}\right)^2\times\sqrt{1+\left(\frac{\sin\theta\cos\gamma}{\chi+\cos\theta}\right)^2}\right]\sin^2\theta\cos^2\gamma dS$$

The size estimation $\beta = \left(\frac{\sin\theta\cos\gamma}{\chi+\cos\theta}\right)^2$ shows that with reference to the central part troposcino, occupying 85 % of length of blades, it is possible to consider that $\beta << 1$. Really, in view of (21) and (15), we will β present size in a following kind that the operating conditions wind turbine demand we will $\chi_m \geq 3$, find

$$\beta = \left[\frac{\sin\theta}{\left(1+\frac{9}{4}\bar{z}\right)\left(\cos\theta+\chi_m\bar{\chi}\right)}\right]^2$$

$$\beta = \left[\frac{\sin\theta}{\left(1+0,85\frac{9}{4}\right)\left(\cos\theta+3\cdot 0,3\right)}\right]^2$$

Owing to the accepted assumption $\bar{z} = 0,85$ at $\bar{\chi} = \frac{r}{r_m} = 0,3$ taking into account

Whence follows, what even at the maximum value sinq=1, cosq = 0, It allows to spread out and in numbers $\frac{1}{\sqrt{1-\beta}}$ and $\sqrt{1-\beta}$ to be limited to first two members of these numbers

$$dM_{l2} = -\varepsilon r(z)\frac{\rho U^2}{2}\times\left[\begin{array}{l}1-\frac{1}{2}\left(\frac{\sin\theta\cos\gamma}{\chi_m\bar{\chi}+\cos\theta}\right)^2+\\ +0,014\left(\frac{\chi_m\bar{\chi}+\cos\theta}{\sin\theta\cos\gamma}\right)^2-0,007\end{array}\right]\times\sin^2\theta\cos^2\gamma dS = -\varepsilon r(z)\frac{\rho U^2}{2}\times$$

$$\times\left[\begin{array}{l}1,007\sin^2\theta\cos^2\gamma-\frac{1}{2}\frac{(\sin\theta\cos\gamma)^4}{(\chi_m\bar{\chi}+\cos\theta)^2}+\\ +0,014(\chi_m\bar{\chi}+\cos\theta)^2\end{array}\right]dS.$$

In square brackets, in comparison with two others, it is possible to neglect obviously, second member. As a result the decision breaks up again to 2 problems

$$dM_{l2} = dM'_{l2} + dM''_{l2}, \quad (25)$$

where

$$dM'_{l2} = -1,007\varepsilon r(z)\frac{\rho U^2}{2}\sin^2\theta\cos\gamma dz, \quad (26)$$

$$\frac{dz}{dS} = \cos\gamma, \text{ and}$$

$$dM_{l2}^{"} = -0{,}014 \text{в} r(z) \frac{\rho U^2}{2} \left(\cos\theta + \chi_m \bar{\chi}\right)^2 dS. \quad (27)$$

The decision of the first problem (26) to be reduced to already known decision (18) problems (12) and looks like

$$2M_{l2}^{'} = -0{,}577 r_m \text{в} H \frac{\rho U^2}{2} (1 - \cos 2\theta). \quad (28)$$

The problem (27) also easily gives in to the decision. For this purpose on the basis of (2) and (24) we will write down

$$\bar{z} = \frac{2z}{H} = \sqrt{1 - \bar{r}} = \sqrt{1 - \bar{\chi}} \quad (29)$$

Then (27) it is led to a kind

$$dM_{l2}^{"} = -0{,}014 \text{в} r_m \bar{r} \rho \frac{U^2}{2} (\cos\theta + \chi_m \bar{r})^2 \frac{dz}{\cos\gamma}$$

$$dM_{l2}^{"} = -0{,}014 \frac{\text{в} H}{4} r_m \rho U^2 (1 - \bar{z}^2) \left[\cos\theta + \chi_m (1 - \bar{z}^2)\right]^2 \sqrt{1 + \tfrac{9}{4} \bar{z}^2}\, d\bar{z} \quad (30)$$

Let's open square brackets in the second degree

$$dM_{l2}^{"} = -0{,}007 \text{в} r_m H \rho \frac{U^2}{2} \left[(\cos\theta + \chi_m)^2 (1 - \bar{z}^2) - 2\chi_m \times (\cos\theta + \chi_m) \bar{z}^2 (1 - \bar{z}^2) + \chi_m^2 \bar{z}^4 (1 - \bar{z}^2)\right] \sqrt{1 + \frac{9}{4} \bar{z}^2}\, d\bar{z} \quad (31)$$

For integration we will result (31) in a kind

$$dM_{l2}^{"} = A_0 (A_1 + A_2 y^2 + A_3 y^4 + A_4 y^6) \sqrt{1 + y^2}\, dy,$$

where $y = \frac{3}{2}\bar{z}$, $A_0 = -\frac{0{,}007}{3} \text{в} r_m H \rho U^2$, $A_1 = (\cos\theta + \chi_m)^2$,

$$A_2 = -\frac{4}{9}(\cos^2\theta + 4\chi_m \cos\theta + 3\chi_m^2),$$

$$A_3 = \frac{16}{81}(2\chi_m \cos\theta + 3\chi_m^2), \quad A_4 = -\frac{64}{729}\chi_m^2.$$

Integration leads to tabular integrals

$$I_1 = 2 \int_0^{\frac{3}{2}\sqrt{0{,}7}} \sqrt{1 + y^2}\, dy = 3{,}12;$$

$$I_2 = 2 \int_0^{\frac{3}{2}\sqrt{0{,}7}} y^2 \sqrt{1 + y^2}\, dy = 1{,}43;$$

$$I_3 = 2 \int_0^{\frac{3}{2}\sqrt{0{,}7}} y^4 \sqrt{1 + y^2}\, dy = 2{,}36;$$

$$I_4 = 2 \int_0^{\frac{3}{2}\sqrt{0{,}7}} y^6 \sqrt{1 + y^2}\, dy = 3{,}34.$$

Integration limits are limited by values $\overline{z} = -\sqrt{0,7}$ and $\overline{z} = \sqrt{0,7}$ (see (23)). As a result for two blade turbines it is had

$$2M''_{l2} = -\frac{0,014}{3} r_m в H \rho U^2 \left[3,12 \times (\chi_m + \cos\theta)^2 - 1,43 \frac{4}{9} \times \right.$$
$$\left. \times (\cos^2\theta + 4\chi_m \cos\theta + 3\chi_m^2) + 2,37 \frac{16}{81} (2\chi_m \cos\theta + 3\chi_m^2) - 3,34 \frac{64}{729} \chi_m^2 \right]$$

Let's open simple brackets and we will collect similar members. Then we will receive

$$2M''_{l2} = -\frac{0,014}{3} r_m в H \rho U^2 \times \left(2,48\cos^2\theta + 4,64\chi_m \cos\theta + 2,32\chi_m^2\right)$$

Let's unite with the decision (28)

$$2M_{l2} = 2(M'_{l2} + M''_{l2}) = -\frac{0,014}{3} r_m в H \rho U^2 \times \left[\begin{array}{l} 0,577 \frac{3}{0,014}(1 - \cos 2\theta) + 2,48\cos^2\theta + \\ +4,63\chi_m \cos\theta + 2,32\chi_m^2 \end{array} \right] \quad (32)$$

The received dependence expresses the counteracting moment of resistance of air to turbine rotation. The general rotary moment of the turbine consists of the algebraic sum positive (18) and the negative (32) moments of forces

$$2M_l = 2(M_{l1} + M_{l2}) = \frac{0,014}{3} r_m в H \rho U^2 \times \left\{ \left[\left(\frac{0,685\sqrt{2}\pi}{2} - 0,577 \right) \times \right. \right.$$
$$\left. \left. \times \frac{3}{0,014}(1 - \cos 2\theta) \right] - 1,24(1 + \cos 2\theta) - 4,63\chi_m \cos\theta - 2,32\chi_m^2 \right\} \quad (33)$$

Average value of the rotary moment operating on the turbine we will find, having integrated (33) from zero to 2π and 2π having divided on:

$$M_{turb} = \frac{1}{\pi} \int_0^{2\pi} M_l d\theta = \frac{0,028}{3} r_m в H \rho \frac{U^2}{2} \times (177 - 2,72\chi_m^2) \quad (34)$$

Capacity of the turbine is defined by product of angular speed of rotation of the turbine at the moment of forces

$$N_{turb} = \omega M_{turb}. \quad (35)$$

Substituting here dependence (34) and entering $\chi_m = \frac{\omega r_m}{U}$, we will receive

$$N_{turb} = \frac{0,028}{3} в H \rho \frac{U^3}{2} \chi_m (177 - 2,72\chi_m^2) \quad (36)$$

From here it is easy to define wind power operating ξ ratio if (35) to divide into capacity of the wind stream which is passing through by the turbine the area F

$$N_в = F\rho\frac{U^3}{2}. \quad (37)$$

Thus

$$\xi = \frac{N_{turb}}{N_в} = \frac{0,028}{3F}вH\chi_m(177 - 2,72\chi_m^2). \quad (38)$$

From last formula we will define value χ_m, at which the maximum value coefficient wind power uses is reached. $\xi_{\max}$ With that end in view we will equate the first derivative ξ on χ_m zero

$$\frac{d\xi}{d\chi_m} = 177 - 8,16\chi_m^2 = 0 \quad (39)$$

From here $\chi_m = 4,66$.

The area surfaces F we will find under the known formula for rotation bodies

$$F = 2\pi\int_{-1}^{1}\bar{r}(\bar{z})\sqrt{1+\left(\frac{d\bar{r}}{d\bar{z}}\right)^2}\,d\bar{z}.$$

Having substituted expression for $\bar{r}(\bar{z})$ under the formula (2), we will define

$$F = \frac{3\pi}{8}H^2\int_0^1(1-\bar{z}^2)\sqrt{1+\frac{9}{4}\bar{z}^2}\,d\bar{z}$$

Let's enter a new variable $y = \frac{3}{2}\bar{z}.$ Then

$$F = \frac{\pi H^2}{4}\int_0^{3/2}\sqrt{1+y^2}\,dy - \frac{\pi H^2}{9}\int_0^{3/2}y^2\sqrt{1+y^2}\,dy.$$

Again we come to tabular integrals I_1 and I_2 (see 28). Calculating these certain integrals, we will receive

$$F = 0,337\pi H^2. \quad (40)$$

Substituting expressions (39) and (40) in the formula (38), we will find

$$\xi_{\max} = 0,363. \quad (41)$$

Value $\xi_{\max}$ and size χ_m at which it is reached $\xi_{\max}$, lie close enough to the known data resulted on Fig. 4. On Fig. 4 skilled values of factor for ξ various types and designs wind turbine depending on degree their rapidity's taken $\chi = \frac{|\vec{\omega}|r_0}{|\vec{U}|}$ from [1,2] are resulted.

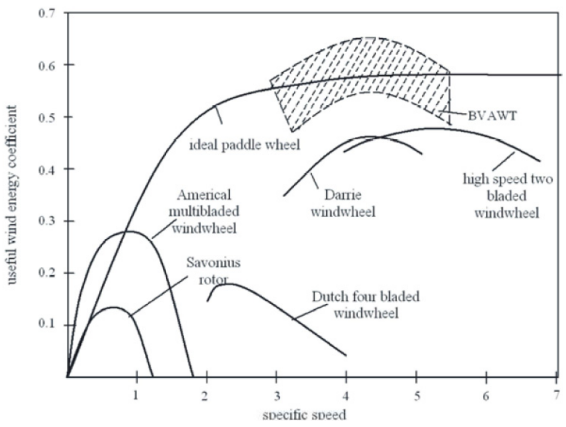

Figure 4 – Dependences of operating ratio of wind power x for various types and designs wind turbine from degree of their rapidity c.

References

1. Turyan K.Dzh., Striklend of J., X, Berg D.E. Capacit wind energy units with a vertical axis of rotation//the Space technics. – 1988. – No 8. – P. 105-121.

2.Yershina A.K., Yershin S.A., Zhapbasbaev U.K. Bas of the theory wind turbine to Darrieus. – Almaty. – 2001. – P. 104.

3.Yershin Sh., Yershina A., Manatbayev R., Tulepbergenov A. Bi-Darrie windturbine // ASME–ATI–UIT 2010 Conference on Thermal and Environmental lssues in Energy Systems. – Sorrento, Italy. – 2010. – P. 615-619.

UDC 539.17

[1*]Burtebayev N., [1]Burtebayeva J.T., [1]Duisebayev A., [1]Zholdybayev T., [1,2]Nassurlla M., [3]Spitaleri C., [4]Sakuta S.B., [5]Piasecki E., [5]Rusek K., [5]Trzcińska A., [5]Wolińska-Cichocka M., [6]Artemov S.V.

[1]Institute of Nuclear Physics of National Nuclear Center, Almaty, Kazakhstan,
[2]Al-Farabi Kazakh National University, Almaty, Kazakhstan,
[3] National Institute of Nuclear Physics, Sezione di Catania, Catania, Italy,
[4]National Research Center "Kurchatov Institute", Moscow, Russia,
[5]Heavy Ion Laboratory of Warsaw University, Warsaw, Poland,
[6]Institute of Nuclear Physics, Tashkent, Uzbekistan,
[*]e-mail: nburtebayev@yandex.ru

Scattering of ^{13}C ions by ^{12}C nuclei at energies close to the Coulomb barrier

Abstract: Angular distributions of the elastic and inelastic scattering of ^{13}C ions on ^{12}C nuclei were measured on the heavy-ion Warsaw Cyclotron at the energy of 32.5 MeV in the laboratory system. Elastic scattering in the forward hemisphere is well described by the standard optical model, while at the same time the possible rise of the cross section in the backward direction can be only reproduced with taking into account the contribution of the neutron transfer mechanism. The experimental data on elastic and inelastic scattering have been analyzed within the framework of the optical model and the Coupled Reaction Channels method via code FRESCO.
Key words: elastic scattering, optical model, potential parameters, differential cross sections, neutron transfer mechanism.

Introduction

Study of elastic scattering in the collision of light heavy ion nuclei at energies near the Coulomb barrier is of interest both in terms of establishing reliable values of the parameters of interaction potentials at low energies and determining the role of the cluster exchange mechanism in the scattering. Some of the key reactions for the carbon and oxygen burning stages are ^{12}C+^{12}C [1], ^{12}C+^{16}O [2, 3] and ^{16}O+^{20}Ne [4] leading to a synthesis of more heavy nuclei.

For the ^{12}C + ^{13}C system the neutron transfer mechanism ^{12}C (^{13}C, ^{12}C)^{13} C can manifest at backward angles. In this context, study of the cross sections in this area is of great interest for astrophysics since it allows us to estimate cross sections of the possible radiative capture ^{12}C(n, γ) ^{13}C reaction and its role in the evolution of the Universe immediately after the Big-Bang. It is expected that the neutron transfer reaction will be peripheral because of the Coulomb repulsion.

Previously elastic scattering ^{12}C + ^{13}C at an energy close to our was investigated in limited range of angles up to 60^0 [5]. Scattering in this system has been also investigated by Chua et al. [6, 7] in the energy range from E_{lab}=20 to 35.5 MeV. They got a reasonable agreement with the experimental data for these energies in the optical model. But their calculations do not predict the cross section rise at larger angles where the neutron exchange mechanism can be dominant.

In present work the differential cross sections of elastic and inelastic scattering for ^{12}C + ^{13}C system were measured at E_{lab} = 32.5MeV in the substantially extended angular range (up 120^0 in the center mass system) and the obtained experimental data were analyzed by coupled reaction channels method (CRC) taking into account coupling the elastic, inelastic as well as the neutron transfer mechanism.

Experimental Setup:

Angular distributions of elastic and inelastic scattering of ^{13}C ions by ^{12}C nuclei were measured using beam with the energy of 2.5 MeV/nucleon extracted from the Heavy Ion Laboratory Cyclotron (K = 160) of the Warsaw University.

The charged particles were detected and identified by four ΔE-E counter telescopes installed

 Printed in Kazakhstan

in the ICARE scattering chamber. The overall energy resolution was about 700 keV. The telescopes consisted of the ionization chamber as ΔE detector and the semiconductor silicon detector (E). The carbon foils with a thickness of about 150μg/cm^2 were used as a target. Their thicknesses were determined at the proton beam of the UKP-2 accelerator (Almaty, Kazakhstan) by measuring yield of γ-rays (E_γ = 1779 keV) depending on the protons energy loss during the passage through the target. For this purpose the narrow resonance with E_R = 992 keV in the reaction ^{27}Al(p, γ)^{28}Si was used. In this case the target was a fine film of aluminum oxide (Al_2O_3). An example of film thickness measurement is shown in the Fig. 1. Such method allows determining thicknesses of films in the interval of (10÷100) μg/cm^2 with the accuracy not worse than 5%.

A two-dimensional (ΔE-E) and single energy spectra of carbon produced in the ^{12}C+^{13}C collision are shown in Fig. 2 and 3 respectively.

The measured angular distributions for the elastic and inelastic scattering are shown in Fig. 4 by the red and black circles respectively.

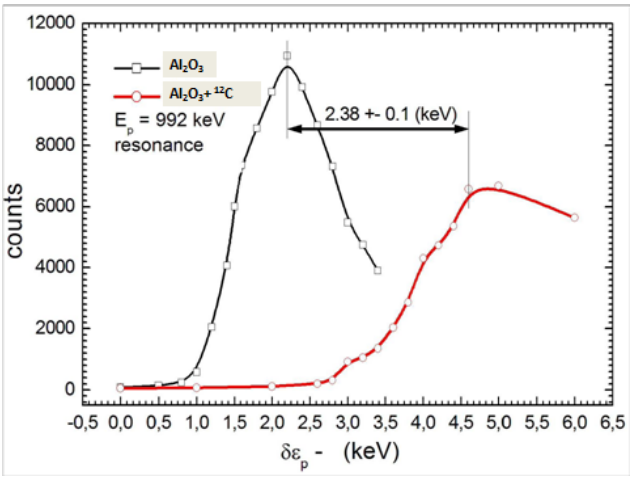

Figure 1 – The shift of the 992 keV resonance in reaction ^{27}Al (p, γ) ^{28}Si due to the energy loss of of protons in the carbon film.

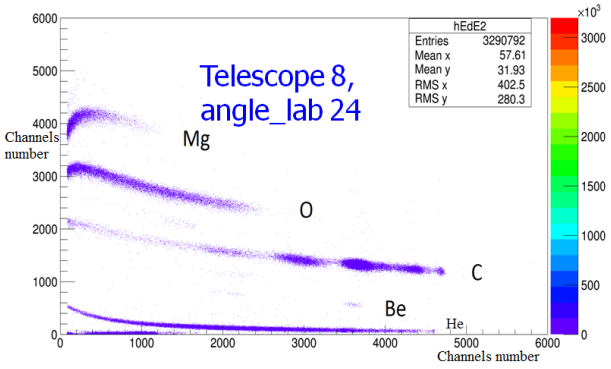

Figure 2 – The two-dimensional (ΔE-E) spectrum of charged nuclei produced from the collision of ^{12}C+^{13}C. The spectrum was measured at the angle of 24^0 in the laboratory system.

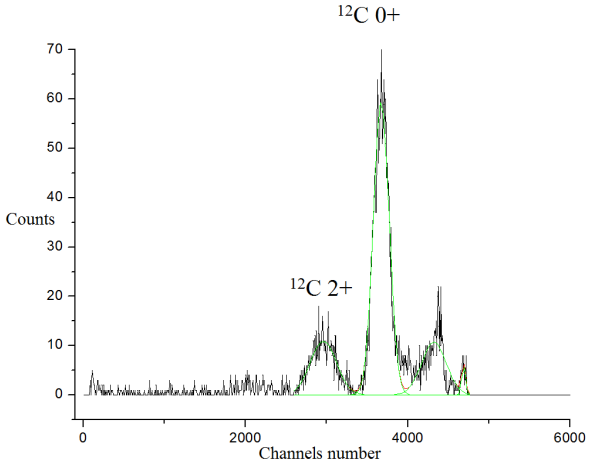

Figure 3 – The energy spectrum of carbon from the ^{12}C(^{13}C,^{13}C)^{12}C reaction.

Data Analysis

Experimental data of elastic scattering were analyzed within the framework of the optical model (OM). For all calculations, the Woods-Saxon form factor was used for both the real and imaginary potential

$$U = V + iW, \quad (1)$$

$$V = V_o\,[1+\exp\,(r-R_r)/a_r]^{-1} \quad (2)$$

$$W = W_o\,[1+\exp\,(r-R_i)/a_i]^{-1} \quad (3)$$

V_o and W_o, a_r and a_i, R_r and R_i being the depth, diffuseness and radii of the real and imaginary potentials, respectively. The radii are expressed in terms of the mass numbers A_1 and A_2 of the nuclei involved given by

$$R = r_o\,(A_1^{1/3}+A_2^{1/3}) \quad (4)$$

Parameters of optical potential (OP) were selected to achieve the best agreement between theoretical and the experimental angular distributions (see Table). The description of experimental data is shown in Fig. 4 by the blue line. It can be seen that OM well describes the differential cross section of elastic scattering in forward hemisphere. However, this model does not reproduce the smooth behavior of the experimental cross sections at the angles 50-90° and does not predict the rise cross sections at backward direction.

Table – Potential parameters

E (MeV)	V_0 (MeV)	r_V (fm)	a_V (fm)	W_0 (MeV)	r_W (fm)	a_W (fm)
32.5	73.1	1.03	0.699	35.22	1.19	0.211

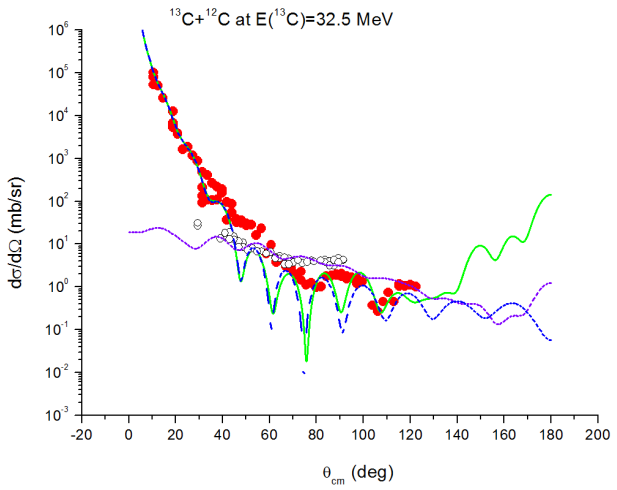

Figure 4 – The angular distributions of elastic and inelasic scattering of ^{13}C on ^{12}C measured at the 32.5 MeV. The red and white circles are experimental data for elastic and inelastic scattering respectively. Curves: the blue dash line is the optical model prediction; the green solid line represents the coupled reaction channels calculation of elastic scattering by code FRESCO with taking into account the neutron transfer mechanism; the violet dot line represents FRESCO calculation of inelastic scattering.

The experimental angular distributions show weak oscillations up to the angles of 100-120°. For the reaction ^{12}C (^{13}C, ^{12}C) ^{13}C, an important process affecting the scattering at large angles is the mechanism of one neutron transfer between the ^{13}C projectile nucleus and the ^{12}C target nucleus. To describe this mechanism we used the Coupled Reaction Channels method realized in the code FRESCO [8].

The theory of collisions that take into account the coupling of different reaction channels, called a multichannel theory. A variant of this theory, which without any approximation strictly takes into account the coupling between a limited numbers of channels and the influence of all other channels is discarded, called the coupled channels method. The method allows for coupling to rearrangement channels by including basis vectors classified according to different mass partitions.

Therefore, the relevant description of data in backward hemisphere needs to be taken into account the n-transfer mechanism for the system

$$A + (A' + x) \rightarrow A' + (A + x) \quad (5)$$

at allows reproducing the cross sections rise at large angles (see Fig. 5).

The angular distribution of inelastic scattering has been analyzed within the code FRESCO which took into account the coupling between the elastic and inelastic scattering as well as the neutron transfer. We assume that the rotation is the dominant mechanism for transition to the 2^+ level at the excitation energy of 4.43 MeV of the ^{12}C nucleus. The transition to this level was calculated using the form-factor:

$$V_\lambda(r) = -\frac{\delta_\lambda}{\sqrt{4\pi}}\frac{dU(r)}{dr}, \qquad (6)$$

where δ_λ is the length of the multipole (λ) deformation. In our case $\lambda = 2$ for the quadrupole transitions. The value of deformation length δ_2 =2.59 fm was extracted from the analysis of experimental data of inelastic scattering. This value corresponds to the deformation parameter $\beta_2 = 1.1$ ($\beta_2 = \delta_2/R_V$).

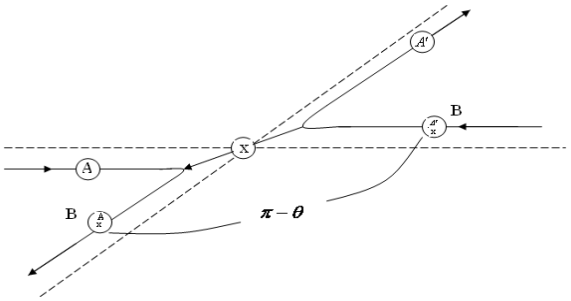

Figure 5 – Schematic representation for the transfer reaction

Conclusion

The experimental data on elastic and inelastic scattering have been analyzed within the framework of the optical model and the Coupled Reaction Channels method with code FRESCO taking into account the neutron transfer mechanism. As it seen from Fig. 4, OM does not provide cross sections enhancement in backward direction. Only taking into account the neutron transfer mechanism gives rise to cross sections at large angles. So, it is important to extend the measurements for angles greater than 120°. The value of deformation length δ_2 =2.59 fm was extracted from the analysis of experimental data of inelastic scattering by CRC.

References

1. Burtebayev N. *et al.* Investigation of $^{12}C+^{12}C$ reaction in a wide energy range // J. of Eurasia National University. –2010. – Vol. 79. – P. 131-135.

2. Burtebayev N., Nassurlla M. *et al.* Detailed Study For $^{12}C+^{16}O$ Nucler System // J. of Eurasia National University. – 2012. – Vol. 87. – P. 49-54.

3. Burtebayev N. *et al.* Analysis of alpha-cluster transfer in 16O + 12C and 12C + 16O at energies near Coulomb barrier // Nucl. Phys. A. – 2011. – Vol.859. – P. 29.

4. Burtebayev N., Nassurlla M. *et al.* Complex analysis of scattering 1p-shell nuclei in the framework of coupled channel method // J. Phys.:Conf. Ser. – 2015. – Vol. 590**. –** P**.** 012056.

5. Gary D., Westfall and Zaidi S.A.A. Reactions induced by ^{13}C on ^{12}C, O16, ^{28}Si, and ^{32}S // Physical Review C. – 1976. – Vol. 14. – P. 610.

6. Chua L.T., Gobbi A., Sachs M.W., Shapira D., Wieland R., Bromley D.A., Nuovo I. Cimento A. ibid. – 1978. – Vol. 47. – P. 430.

7. Chua L.T., Gobbi A., Sachs M.W., Shapira D., Wieland R., Bromley D.A., Nuovo I. Cimento A. An analysis of neutron transfer between identical cores with applications to the12C+13C system // Nuovo Cimento. – 1978. – Vol. 47. – P. 443

8. Thompson I.J., Comput. Coupled reaction channels calculations in nuclear physics // Phys. Rep. – 1988. – Vol. **7. –** P. 167.

UDC 530.145; 530.12; 539.12-17

[1*]Nurbakova G.S., [1]Habyl N., [2]Mukushev B.A.

[1]Physico-Technical Faculty, al-Farabi Kazakh National University, Almaty, Kazakhstan
[2]Shakarim State University, Semey, Republic of Kazakhstan
[*]e-mail: guliya_nurbakova@mail.ru

Angular decay distributions for cascade decay $B \to K^*(\to K\pi) + \overline{l}l$

Abstract: This article is devoted to the study of the $B \to K^*(\to K\pi) + \overline{l}l$ decay. The rare flavour changing neutral current decays are forbidden in the Standard Model (SM) at tree level. They proceed only via the loops in the perturbation theory. For this reason, these decays are sensitive to the possible effects of new physics beyond the Standard Model. The new heavy particles can contribute to the branching fractions and the angular decay distributions. It is generally believed that the decay mode $B \to K^*(\to K\pi)\mu^+\mu^-$ is one of the best modes to search for new physics beyond the standard model. The angular distribution enables the independent measurement of several observables as a function of the dilepton invariant mass.
Key words: B-meson, rare decay, two-fold angular distributions, four-fold angle distribution, polarization observables.

Introduction

The rare flavor changing neutral current (FCNC) decays proceed only via the loops in the perturbation theory. For this reason, these decays are sensitive to the possible effects of new physics beyond the SM. The new heavy particles can contribute to the branching fractions and the angular decay distributions. The angular distribution enables the independent measurement of several observables as a function of the dilepton invariant mass. Plenty of observables obtained in this manner enable unique tests of the standard model contributions.

In this paper we study the rare $B \to K^*(\to K\pi) + \overline{l}l$ decay. We derive the fourfold angular decay distribution by employing the helicity formalism in a model-independent way.

The rare exclusive decays are described by the effective Hamiltonian obtained from the SM-diagrams by using the operator product expansion and renormalization group techniques. It allows one to separate the short-distance contributions and isolate them in the Wilson coefficients which can be studied systematically within perturbative QCD. The long-distance contributions are contained in the matrix elements of local operators. Contrary to the short-distance contributions the calculation of such matrix elements requires nonperturbative methods and is therefore model dependent.

The rare decay $b \to s(d)l^+l^-$ can be described in terms of the effective Hamiltonian [1]:

$$H_{eff} = -\frac{G_F}{\sqrt{2}}\lambda_t \sum_{i=1}^{10} C_i(\mu) Q_i(\mu) \qquad (1)$$

where $C_i(\mu)$ and $Q_i(\mu)$ are the Wilson coefficients and local operators, respectively. $\lambda_t \equiv V_{ts(d)}^{\dagger} V_{tb}$ is the product of CKM elements. The standard set [1] of local operators for $b \to sl^+l^-$ transition is written as

$$\begin{aligned}
&Q_1 = \left(\overline{s}_{a_1}\gamma^\mu P_L c_{a_2}\right),\left(\overline{c}_{a_2}\gamma_\mu P_L b_{a_1}\right), && Q_2 = \left(\overline{s}\gamma^\mu P_L c\right),\left(\overline{c}\gamma_\mu P_L b\right),\\
&Q_3 = \left(\overline{s}\gamma^\mu P_L b\right)\sum\nolimits_q \left(\overline{q}\gamma_\mu P_L q\right), && Q_4 = \left(\overline{s}_{a_1}\gamma^\mu P_L b_{a_2}\right)\sum\nolimits_q \left(\overline{q}_{a_2}\gamma_\mu P_L q_{a_1}\right),\\
&Q_5 = \left(\overline{s}\gamma^\mu P_R b\right)\sum\nolimits_q \left(\overline{q}\gamma_\mu P_R q\right), && Q_6 = \left(\overline{s}_{a_1}\gamma^\mu P_R b_{a_2}\right)\sum\nolimits_q \left(\overline{q}_{a_2}\gamma_\mu P_R q_{a_1}\right),\\
&Q_7 = \frac{e}{16\pi^2} m_b \left(\overline{s}\sigma^{\mu\nu} P_R b\right) F_{\mu\nu}, && Q_8 = \frac{g}{16\pi^2} m_b \left(\overline{s}_{a_1}\sigma^{\mu\nu} P_R \mathbf{T}_{a_1 a_2} b_{a_2}\right)\mathbf{G}_{\mu\nu},\\
&Q_9 = \frac{e}{16\pi^2}\left(\overline{s}\gamma^\mu P_L b\right)\left(\overline{l}\gamma_\mu l\right), && Q_{10} = \frac{e}{16\pi^2}\left(\overline{s}\gamma^\mu P_L b\right)(\overline{l}\ \gamma_\mu\gamma_5 l),
\end{aligned} \qquad (2)$$

 Printed in Kazakhstan

where $\mathbf{G}_{\mu\nu}$ and $F_{\mu\nu}$ are the gluon and photon field strengths, respectively; $\mathbf{T}_{\mu\nu}$ are the generators of the SU(3) color group; a_1 and a_2 denote color indices (they are omitted in the color-singlet currents). The chirality projection operators are $P_{L,R} = (1 \mp \gamma_5)/2$ and m_b is the running mass in the MS scheme.

By using the effective Hamiltonian defined by Eq. (1) one can write the matrix element of the exclusive transitions $B \to K(K^*)l^+l^-$ as

$$M = \frac{G_F}{\sqrt{2}} \frac{\alpha \lambda_t}{\pi} \Big\{ C_9^{eff} < K(K^*) \,|\, \bar{s}\gamma^\mu P_L b \,|\, B > \left(\bar{l}\gamma_\mu l\right) - \frac{2m_b}{q^2} C_7^{eff} < K(K^*) \,|\, \bar{s} i\sigma^{\mu\nu} P_R b \,|\, B > \left(\bar{l}\gamma_\mu l\right) + C_{10} < K(K^*) \,|\, \bar{s}\gamma^\mu P_L b \,|\, B > \left(\bar{l}\gamma_\mu \gamma_5 l\right) \Big\}, \tag{3}$$

where $C_7^{eff} = C_7 - C_5/3 - C_6$. The Wilson coefficient C_9^{eff} effectively takes into account, first, the contributions from the four-quark operators Q_i $(i = 1,...,6)$ and, second, the nonperturbative effects coming from the $c\bar{c}$-resonance contributions which are as usual parametrized by a Breit-Wigner ansatz [2]:

$$\begin{aligned} C_9^{eff} = C_9 + C_0 \Bigg\{ & h(\hat{m}_c, s) + \frac{3\pi}{\alpha^2} k \sum_{V_i = \psi(1s), \psi(2s)} \frac{\Gamma\left(V_i \to l^+l^-\right) m_{V_i}}{m_{V_i}^{\ 2} - q^2 - i m_{V_i} \Gamma_{V_i}} \Bigg\} \\ & - \frac{1}{2} h(1, s)\left(4C_3 + 4C_4 + 3C_5 + C_6\right) \\ & - \frac{1}{2} h(0, s)\left(C_3 + 3C_4\right) + \frac{2}{9}\left(3C_3 + C_4 + 3C_5 + C_6\right), \end{aligned} \tag{4}$$

where $C_0 \equiv 3C_1 + C_2 + 3C_3 + C_4 + 3C_5 + C_6$. Here

$$h(\hat{m}_c, s) = -\frac{8}{9}\ln\frac{m_b}{\mu} - \frac{8}{9}\ln\hat{m}_c + \frac{8}{27} + \frac{4}{9}x - \frac{2}{9}(2+x)\left|1-x\right|^{1/2} \begin{cases} \left(\ln\left|\dfrac{\sqrt{1-x}+1}{\sqrt{1-x}-1}\right| - i\pi\right) & for \quad x \equiv \dfrac{4\hat{m}_c^{\ 2}}{s} < 1 \\ 2\arctan\dfrac{1}{\sqrt{x-1}} & for \quad x \equiv \dfrac{4\hat{m}_c^{\ 2}}{s} > 1, \end{cases}$$

$$h(0, s) = \frac{8}{27} - \frac{8}{9}\ln\frac{m_b}{\mu} - \frac{4}{9}\ln s + \frac{4}{9} i\pi,$$

where $m_c = m_c / m_B, s = q^2 / m_B^{\ 2}$ и $k = 1/C_0$.

Two-fold angular distributions

Let us consider the polar angle decay distribution differential in the momentum transfer squared q^2. The polar angle is defined by the angle between $\vec{q} = \vec{p}_1 - \vec{p}_2$ and $\vec{k}_1$ ($\ell^+\ell^-$ rest frame) as shown in Figure 1. One has

$$\frac{d^2\Gamma}{dq^2 d\cos\theta}=\frac{|\mathbf{p}_2|\upsilon}{(2\pi)^3 4m_1^3}\cdot\frac{1}{8}\sum_{pol}|M|^2=\frac{G_F^2}{(2\pi)^3}\left(\frac{\alpha|\lambda_t|}{2\pi}\right)^2\frac{|\mathbf{p}_2|\upsilon}{8m_1^2}$$
$$\times\frac{1}{8}\left\{H_{11}^{\mu\nu}\cdot tr\left[\gamma_\mu\left(\not{k}_1-m_\ell\right)\gamma_\nu\left(\not{k}_1+m_\ell\right)\right]+H_{22}^{\mu\nu}\cdot tr\left[\gamma_\mu\gamma_5\left(\not{k}_1-m_\ell\right)\gamma_\nu\gamma_5\left(\not{k}_1+m_\ell\right)\right]+\right.$$
$$\left.+H_{12}^{\mu\nu}\cdot tr\left[\gamma_\mu\left(\not{k}_1-m_\ell\right)\gamma_\nu\gamma_5\left(\not{k}_1+m_\ell\right)\right]+H_{21}^{\mu\nu}\cdot tr\left[\gamma_\mu\gamma_5\left(\not{k}_1-m_\ell\right)\gamma_\nu\left(\not{k}_1+m_\ell\right)\right]\right\}= \tag{5}$$
$$=\frac{G_F^2}{(2\pi)^3}\left(\frac{\alpha|\lambda_t|}{2\pi}\right)^2\frac{|\mathrm{P}_2|\upsilon}{8m_1^2}\cdot\frac{1}{2}\left\{L_{\mu\nu}^1\cdot\left(H_{11}^{\mu\nu}+H_{22}^{\mu\nu}\right)-\frac{1}{2}L_{\mu\nu}^2\cdot\left(q^2H_{11}^{\mu\nu}+\left(q^2-4m_\ell^2\right)H_{22}^{\mu\nu}\right)+L_{\mu\nu}^3\cdot\left(H_{12}^{\mu\nu}+H_{21}^{\mu\nu}\right)\right\},$$

where $|\mathbf{p}_2|=\lambda^{1/2}\left(m_1^2,m_2^2,q^2\right)/2m_1$ is the momentum of the $K(K^*)$ - meson given in the B-rest frame and $\beta_l=\sqrt{1-4m_l^2/q^2}$.

The Lorentz contractions in Eq. (5) can be evaluated in terms of helicity amplitudes as described in [3]. First, we define an orthonormal and complete helicity basis $\in^\mu(m)$ with the three spin 1 components orthogonal to the momentum transfer q_μ, i.e. $\in^\mu(m)q_\mu=0$ for $m=\pm0$, and the spin 0 (time)-component $m=t$ with $\in^\mu(t)=q^\mu/\sqrt{q^2}$. The orthonormality and completeness properties read

$$\begin{aligned}&\in_\mu^\dagger(m)\in^\mu(n)=g_{mn}, && (\text{ orthonormality})\\ &\in_\mu(m)\in_\nu^\dagger(n)g_{mn}=g_{\mu\nu}, \quad (m,n=t,\pm0) && (\text{ completeness})\end{aligned} \tag{6}$$

with $g_{mn}=diag(+,-,-,-)$. Using the completeness property we rewrite the contraction of the lepton and hadron tensors in Eq. (5) according to

$$L^{(k)\mu\nu}H_{\mu\nu}^{ij}=L_{\mu'\nu'}^{(k)}\in^{\mu'}(m)\in^{\dagger\mu}(m')g_{mm'}\in^{\dagger\nu'}(n)\in^{\nu}(n')g_{nn'}H_{\mu\nu}^{ij}=L_{mn}^{(k)}g_{mm'}g_{nn'}H_{m'n'}^{ij}, \tag{7}$$

where we have introduced the lepton and hadron tensors in the space of the helicity components

$$L_{mn}^{(k)}=\in^\mu(m)\in^{\dagger\nu}(n)L_{\mu\nu}^{(k)}, \qquad H_{mn}^{ij}=\in^{\dagger\mu}(m)\in^{\nu}(n)H_{\mu\nu}^{ij}. \tag{8}$$

The lepton tensors $L^{(k)}=(m,n)$ will be evaluated in the $\bar{\ell}\ell$-CM system whereas the hadron tensors $H^{ij}(m,n)$ will be evaluated in the B rest system.

The differential $(q^2,\cos\theta)$ distribution finally reads

$$\frac{d\Gamma\left(H_1\to H_2\bar{\ell}\ell\right)}{dq^2d(\cos\theta)}=\frac{3}{8}(1+\cos^2\theta)\cdot\frac{1}{2}\left(\frac{d\Gamma_U^{11}}{dq^2}+\frac{d\Gamma_U^{22}}{dq^2}\right)+\frac{3}{4}\sin^2\theta\cdot\frac{1}{2}\left(\frac{d\Gamma_L^{11}}{dq^2}+\frac{d\Gamma_L^{22}}{dq^2}\right)-\upsilon\cdot\frac{3}{4}\cos\theta\cdot\frac{d\Gamma_P^{12}}{dq^2}$$
$$+\frac{3}{4}\sin^2\theta\cdot\frac{1}{2}\frac{d\tilde{\Gamma}_U^{11}}{dq^2}-\frac{3}{8}(1+\cos^2\theta)\cdot\frac{d\tilde{\Gamma}_U^{22}}{dq^2}+\frac{2}{3}\cos^2\theta\cdot\frac{1}{2}\frac{d\tilde{\Gamma}_L^{11}}{dq^2}-\frac{3}{4}\sin^2\theta\cdot\frac{1}{2}\frac{d\tilde{\Gamma}_L^{22}}{dq^2}+\frac{3}{4}\frac{d\tilde{\Gamma}_S^{22}}{dq^2}. \tag{9}$$

Integrating over *cosθ* one obtains

$$\frac{d\Gamma\left(H_1 \to H_2 \overline{\ell}\ell\right)}{dq^2} = \frac{1}{2}\left(\frac{d\Gamma_U^{11}}{dq^2} + \frac{d\Gamma_U^{22}}{dq^2} + \frac{d\Gamma_L^{11}}{dq^2} + \frac{d\Gamma_L^{22}}{dq^2}\right) + \frac{1}{2}\frac{d\tilde{\Gamma}_U^{11}}{dq^2} - \frac{d\tilde{\Gamma}_U^{22}}{dq^2} + \frac{1}{2}\frac{d\tilde{\Gamma}_L^{11}}{dq^2} - \frac{d\tilde{\Gamma}_L^{22}}{dq^2} + \frac{3}{2}\frac{d\tilde{\Gamma}_S^{22}}{dq^2}, \quad (10)$$

where the partial helicity rates $d\Gamma_X^{ij}/dq^2$ and $d\tilde{\Gamma}_X^{ij}/dq^2\left(X = U, L, P, S; i, j = 1, 2\right)$ are defined as

$$\frac{d\Gamma_{X_{ij}}}{dq^2} = \frac{G_F^2}{\left(2\pi\right)^3}\left(\frac{\alpha\left|\lambda_t\right|}{2\pi}\right)^2 \frac{\left|\mathbf{p}_2 q^2 \upsilon\right|}{12m_1^2} H_X^{ij}, \qquad \frac{d\tilde{\Gamma}_{X_{ij}}}{dq^2} = \delta_{\ell\ell}\frac{d\Gamma_X^{ij}}{dq^2}, \qquad \delta_{\ell\ell} \equiv \frac{2m_\ell^2}{q^2}. \quad (11)$$

The four-fold angle distribution

The lepton-hadron correlation function $L_{\mu\nu}H^{\mu\nu}$ reveals even more structure when one uses the cascade decay $B \to K^*\left(\to K\pi\right)\overline{\ell}\ell$ to analyze the polarization of the K^*. The hadron tensor now reads

$$H_{\mu\nu}^{ij} = T_{\mu\alpha}^i \left(T_{\nu\beta}^i\right)^\dagger \frac{3}{2\left|\mathbf{p}_3\right|}\mathrm{Br}\left(K^* \to K\pi\right) p_{3\alpha'} p_{3\beta'} S^{\alpha\alpha'}\left(p_2\right) S^{\beta\beta'}\left(p_2\right), \quad (12)$$

where $S^{\alpha\alpha'}\left(p_2\right) = -g^{\alpha\alpha'} + p_2^\alpha p_2^{\alpha'}/m_2^2$ is the standard spin 1 tensor, $p_2 = p_3 + p_4, p_3^2 = m_K^2, p_4^2 = m_\pi^2$, and p_3 and p_4 are the momenta of the *K* and the π, respectively. The relative configuration of the (K,π)- and $\left(\overline{\ell}\ell\right)$-planes is shown in Fig. 1.

Following basically the same trick as in Eq. (8) the contraction of the lepton and hadron tensors may be written through helicity components as

$$\begin{aligned} L^{(k)\mu\nu}H_{\mu\nu}^{ij} &= \in^{\mu'}\left(m\right) \in_2^{\dagger\nu'}\left(n\right) L_{\mu'\nu'}^k g_{mn'} g_{nn'} \in^{\dagger\mu}\left(m'\right) \in^{\nu}\left(n'\right) H_{\mu\nu}^{ij} \\ &= L_{mn}^k g_{mn'} g_{nn'}\left(\in^{\dagger\mu}\left(m'\right) \in^{\dagger\alpha}\left(r\right) T_{\mu\alpha}^i\right)\left(\in^{\dagger\nu}\left(n'\right) \in_2^{\dagger\alpha}\left(s\right) T_{\nu\beta}^i\right)^\dagger \\ \times p_3 \in_2\left(r\right) \cdot p_3 \in_2^\dagger\left(s\right) \frac{3Br\left(K^* \to K\pi\right)}{2\left|\mathbf{p}_3\right|} &= \frac{3Br\left(K^* \to K\pi\right)}{2\left|\mathbf{p}_3\right|}\left(L_{tt}^k \left|H_t^{ij}\right|^2 \cdot \left(p_3 \in_2^\dagger\left(0\right)\right)^2\right) \\ &+ \sum_{m,n=\pm,0} L_{mn}^k H_m^i H_n^{\dagger j} \cdot p_3 \in_2\left(m\right) \cdot p_3 \in_2^\dagger\left(n\right) \\ &- \sum_{n=\pm,0} L_{tn}^k H_t^i H_n^{\dagger j} \cdot p_3 \in_2\left(0\right) \cdot p_3 \in_2^\dagger\left(n\right) \\ &- \sum_{m=\pm,0} L_{mt}^k H_m^i H_t^{\dagger j} \cdot p_3 \in_2\left(m\right) \cdot p_3 \in_2^\dagger\left(0\right). \end{aligned} \quad (13)$$

Using these results one obtains the full four-fold angular decay distribution

$$\frac{d\Gamma\left(B\to K^*\left(\to K\pi\right)\bar{l}l\right)}{dq^2 d\cos\theta d\left(\chi/2\pi\right)d\cos\theta^*}=Br\left(K^*\to K\pi\right)$$
$$\times\left\{\frac{3}{8}\left(1+\cos^2\theta\right)\cdot\frac{3}{4}\sin^2\theta^*\cdot\frac{1}{2}\left(\frac{d\Gamma_U^{11}}{dq^2}+\frac{d\Gamma_U^{22}}{dq^2}\right)+\frac{3}{4}\sin^2\theta\cdot\frac{3}{2}\cos^2\theta^*\cdot\frac{1}{2}\left(\frac{d\Gamma_L^{11}}{dq^2}+\frac{d\Gamma_U^{22}}{dq^2}\right)\right.$$
$$-\frac{3}{4}\sin^2\theta\cdot\cos 2\chi\cdot\frac{3}{4}\sin^2\theta^*\cdot\frac{1}{2}\left(\frac{d\Gamma_T^{11}}{dq^2}+\frac{d\Gamma_T^{22}}{dq^2}\right)+\frac{9}{16}\sin 2\theta\cdot\cos\chi\cdot\sin 2\theta^*\cdot\frac{1}{2}\left(\frac{d\Gamma_I^{11}}{dq^2}+\frac{d\Gamma_I^{22}}{dq^2}\right)$$
$$+\upsilon[-\frac{3}{4}\sin\theta\cdot\frac{3}{4}\sin^2\theta^*\cdot\frac{d\Gamma_P^{12}}{dq^2}-\frac{9}{8}\sin\theta\cdot\cos\chi\cdot\sin 2\theta^*\cdot\frac{1}{2}\left(\frac{d\Gamma_A^{12}}{dq^2}+\frac{d\Gamma_A^{21}}{dq^2}\right)$$
$$+\frac{9}{16}\sin\theta\cdot\sin\chi\cdot\sin 2\theta^*\cdot\left(\frac{d\Gamma_{II}^{12}}{dq^2}+\frac{d\Gamma_{II}^{21}}{dq^2}\right)]-\frac{9}{32}\sin 2\theta\cdot\sin\chi\cdot\sin 2\theta^*\cdot\left(\frac{d\Gamma_{IA}^{11}}{dq^2}+\frac{d\Gamma_{IA}^{22}}{dq^2}\right)$$
$$+\frac{9}{32}\sin^2\theta\cdot\sin 2\chi\cdot\sin^2\theta^*\cdot\left(\frac{d\Gamma_{IT}^{11}}{dq^2}+\frac{d\Gamma_{IT}^{22}}{dq^2}\right)+\frac{3}{4}\sin^2\theta\cdot\frac{3}{4}\sin^2\theta^*\cdot\frac{1}{2}\cdot\frac{d\tilde{\Gamma}_U^{11}}{dq^2}-\frac{3}{8}\left(1+\cos^2\theta\right)\cdot\frac{3}{4}\sin^2\theta^*\cdot\frac{d\tilde{\Gamma}_U^{22}}{dq^2}$$
$$+\frac{3}{2}\cos^2\theta\cdot\frac{3}{2}\cos^2\theta^*\cdot\frac{1}{2}\cdot\frac{d\tilde{\Gamma}_L^{11}}{dq^2}-\frac{3}{4}\sin^2\theta\cdot\frac{3}{2}\cos^2\theta^*\cdot\frac{d\tilde{\Gamma}_L^{22}}{dq^2}+\frac{3}{4}\sin^2\theta\cdot\cos 2\chi\cdot\frac{3}{4}\sin^2\theta^*\cdot\left(\frac{d\tilde{\Gamma}_T^{11}}{dq^2}+\frac{d\tilde{\Gamma}_T^{22}}{dq^2}\right)$$
$$-\frac{9}{8}\sin 2\theta\cdot\cos\chi\cdot\sin 2\theta^*\cdot\frac{1}{2}\left(\frac{d\tilde{\Gamma}_I^{11}}{dq^2}+\frac{d\tilde{\Gamma}_I^{22}}{dq^2}\right)+\frac{3}{2}\cos^2\theta^*\cdot\frac{3}{4}\frac{d\tilde{\Gamma}_S^{22}}{dq^2}+\frac{9}{16}\sin 2\theta\cdot\sin\chi\cdot\sin 2\theta^*\cdot\left(\frac{d\tilde{\Gamma}_{IA}^{11}}{dq^2}+\frac{d\tilde{\Gamma}_{IA}^{22}}{dq^2}\right) \quad (14)$$
$$\left.-\frac{9}{16}\sin^2\theta\cdot\sin 2\chi\cdot\sin^2\theta^*\cdot\left(\frac{d\tilde{\Gamma}_{IT}^{11}}{dq^2}+\frac{d\tilde{\Gamma}_{IT}^{22}}{dq^2}\right)\right\}$$

Integrating Eq. (14) over $\cos\theta^*$ and χ one recovers the two-fold $(q^2,\cos\theta)$ distribution of Eq. (9).

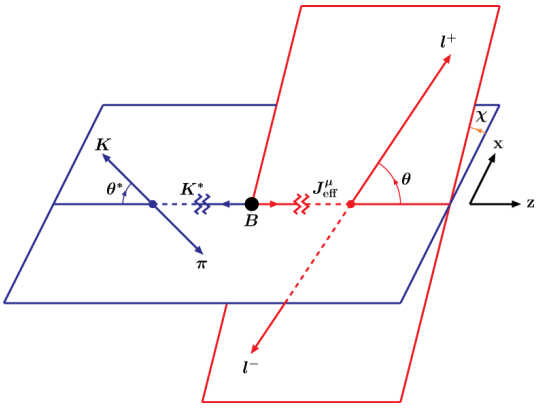

Figure 1 – Definition of angles in the cascade decay $B\to K^*(\to K\pi)\bar{\ell}\ell$

Conclusion

Note that a similar four-fold distribution has also been obtained in Refs. [4], [5] using, however, the zero lepton mass approximation. If there are sufficient data one can attempt to fit them to the full four-fold decay distribution and thereby extract the values of the coefficient functions $d\Gamma_X^{ij}/dq^2$ and, in the case $\ell = \tau$ the coefficient functions $d\tilde{\Gamma}_X^{ij}/dq^2$. Instead of considering the full four-fold decay distribution one can analyze single angle distributions by integrating out two of the remaining angles.

We have performed a detailed analysis of the decay process $B\to K^*(\to K\pi)\bar{\ell}\ell$ by using the helicity formalism to analyze the angular decay distribution.

Acknowledgements

This work was supported by the Ministry of Education and Science of the Republic of Kazakhstan, grant 3091/GF4, state registration No. 0115RK01041.

References

1. Buchalla G., Buras A.J., Lautenbacher M.E. Weak decays beyond leading logarithms // Rev. Mod. Phys. – 1996. – Vol.68. – P.1125-1144.

2. Ali A., Mannel T., Morozumi T. // Phys. Lett. B. – 1991. – Vol.273. – P. 505.

3. Körner J.G. and Schuler G.A. Exclusive semileptonic heavy meson decays including lepton mass effects // Z. Phys. C – 1990. – Vol.46. – P. 93.

4. Kruger F., Sehgal L.M., Sinha N. and Sinha R. Angular Distribution and CP Asymmetries in the Decays B->K^-pi^+e^-e^+ and B->pi^-pi^+e^-e^+ // Phys. Rev. D. – 2000. – Vol.61. – P. 114028.

5. Kim C.S., Kim Y.G., Lu C.D. and Morozumi T. Azimuthal Angle Distribution in $B \to K^*(\to K\pi)l^+l^-$ at low invariant $m_{l^+l^-}$ Region // Phys. Rev. D. – 2000. – Vol.62. – P. 034013

UDC 539.19

[1*]Seshavatharam U.V.S., [2]Lakshminarayana S.

[1]Honorary Faculty, I-SERVE, Alakapuri, Hyderabad-35, Telangana, India
[2]Departament of Nuclear Physics , Andhra University, Visakhapatnam-03, AP, India
[*]e-mail: seshavatharam.uvs@gmail.com

Towards a workable model of final unification

Abstract: Even though 'String theory' models and "quantum gravity' models are having a strong mathematical back ground and sound physical basis, they are failing in implementing the Newtonian gravitational constant in atomic and nuclear physics and thus seem to fail in developing a 'workable' model of final unification. In this context, extending Abdus Salam's old concept of 'nuclear strong gravitational coupling' we consider two very large pseudo gravitational constants assumed to be associated with electromagnetic and strong interactions. By combining the two microscopic pseudo gravitational constants with the Newtonian gravitational constant, we make an attempt to combine the old 'strong gravity' concept with 'Newtonian gravity' and try to understand and re-interpret the constructional features of nuclei, atoms and neutron stars in a unified approach. Finally we make a heuristic attempt to estimate the Newtonian gravitational constant from the known elementary atomic and nuclear physical constants. By exploring the possibility of incorporating the proposed two pseudo microscopic gravitational constants in current unified models, in near future, complete back ground physics can be understood and observable low energy predictions can be made.
Key words: Final unification, Schwarzschild interaction, Newtonian gravitational constant, Gravitational constants associated with electromagnetic and strong interactions.

Novelty and Significance of this paper

By introducing two pseudo gravitational constants, we make an attempt to combine the old 'strong gravity' concept with 'Newtonian gravity' and try to understand and re-interpret the constructional features of nuclei, atoms, and neutron stars in a unified approach and finally making an attempt to estimate the Newtonian gravitational constant from the known elementary atomic and nuclear physical constants.

Scope of this paper

Considering the two pseudo gravitational constants assumed to be associated with strong and electromagnetic interactions,

1. Currently believed generalized physical concepts like, proton-electron mass ratio, neutron life time, weak coupling constant, strong coupling constant, nuclear charge radius, root mean square radius of proton, melting points of proton and electron, nuclear charge radii, nuclear binding energy, nuclear stability, Bohr radius of hydrogen atom, electron and proton magnetic moments, Planck's constant, atomic radii, molar mass constant and Avogadro number etc. can be reviewed in a unified approach and can be simplified.

2. Significance of the ratio of nuclear gravitational constant and Newtonian gravitational constant can be understood and thereby magnitude of the Newtonian gravitational constant can be estimated in a unified approach.

3. Proceeding further, considering the ratio of nuclear gravitational constant and Newtonian gravitational constant, neutron star mass can be understood

 Printed in Kazakhstan

Table – Topics of this paper

S.No	Section heading
1	Introduction
2	Two basic assumptions of final unification
3	Important points pertaining to 'Schwarzschild interaction' and 'final unification'
4	To understand the role of Newtonian gravitational constant in nuclear physics
5	To understand the Planck's constant
6	Nuclear charge radius and root mean square radius of proton
7	To fit and understand the Fermi's weak coupling constant
8	Melting points of proton and electron
9	To fit and understand the atomic radii
10	'System of units' independent Avogadro number and Molar mass unit
11	To fit and understand the atomic radii
12	Mass and radius of a neutron star
13	Fitting and understanding the neutron life time
14	Understanding the Bohr radius, Reduced Planck's constant and magnetic moments of electron and proton
15	Understanding the nuclear charge radii
16	Discussion
17	Conclusion

1. Introduction

Even though 'String theory' models and "quantum gravity' models [1,2] are having a strong mathematical back ground and sound physical basis, they are failing in implementing the Newtonian gravitational constant [3] in atomic and nuclear physics and thus seem to fail in developing a 'workable' model of final unification.

According to Roberto Onofrio [4], weak interactions are peculiar manifestations of quantum gravity at the Fermi scale, and that the Fermi coupling constant is related to the Newtonian constant of gravitation. In his opinion, at atto-meter scale, Newtonian gravitational constant seems to reach a magnitude of $8.205\times10^{22}m^3kg^{-1}sec^{-2}$. In this context, in physics literature [5,6,7] one can see number of papers on 'strong gravity'. Based on the old and ignored scientific assumption put forward by Nobel laureate Abdus Salam, we developed and compiled many interesting relations assumed to be connected with nuclear physics, atomic physics and astrophysics. We are sure to say that, each and every relation is having its own mathematical beauty and we are working on deriving them at fundamental level. The main issue is: to understand the basics of final unification from hidden, unknown and un-identified physics! It is true that, from unification point of view, one cannot accept any relation without a derivation. It is also true that, practically, subject of 'true unification' is beyond the scope of current human understanding. Based on the concepts of : 'workability' and 'something is better than nothing', we appeal the readers to go through the following sections in a true scientific spirit.

Clearly speaking, in this paper, by introducing two pseudo gravitational constants, we make an attempt to combine the old 'strong gravity' concept with 'Newtonian gravity' and try to understand and re-interpret the constructional features of nuclei, atoms, and neutron stars in a unified approach and finally making an attempt to estimate the Newtonian gravitational constant from the known elementary atomic and nuclear physical constants.

2. Two basic assumptions of final unification

In our recent publication [8] (Proceedings of International Intradisciplinary Conference on the Frontiers of Crystallography (IICFC-2014)), qualitatively we proposed the following two assumptions with many possible applications. It may be noted that, current main stream physics is very silent on implementing the Newtonian gravitational constant in current microscopic physics. In this context, thinking that, 'something is better than nothing', we developed this subject. We are at 'half the way' and are sure to say that the subject under development is fruitful and needs experts' hands-on experience in ripening it.

Assumption-1: Magnitude of the gravitational constant associated with the electromagnetic interaction is, $G_e \cong (2.375 \pm 0.002) \times 10^{37}$ $m^3kg^{-1}sec^{-2}$.

Assumption-2: Magnitude of the gravitational constant associated with the strong interaction is, $G_s \cong (3.328 \pm 0.002) \times 10^{28}$ $m^3kg^{-1}sec^{-2}$.

Note-1: We choose the following semi empirical relations as 'reference relations' for constructing other semi empirical relations.

$$\frac{m_p}{m_e} \cong \left(\frac{G_s m_p^2}{\hbar c}\right)\left(\frac{G_e m_e^2}{\hbar c}\right) \text{ and } \left(\frac{G_s m_p m_e}{\hbar c}\right) \cong \left(\frac{\hbar c}{G_e m_e^2}\right) \quad (1)$$

$$m_p \cong \left(\frac{G_N}{G_e}\right)^{\frac{1}{6}}\left(\frac{\hbar c m_e^2}{G_N}\right)^{\frac{1}{4}} \cong \left(\frac{G_N}{G_e}\right)^{\frac{1}{6}}\sqrt{M_{pl} m_e} \quad (2)$$

where $M_{pl} \cong \sqrt{\hbar c / G_N}$ is the Planck mass.

Note-2: It may be noted that, with reference to the operating force magnitudes, protons and electrons cannot be considered as 'black holes'. But protons and electrons can be assumed to follow the relations that black holes generally believed to follow. Clearly speaking, in the study of black holes, Newtonian gravitational constant G_N plays a major role, whereas in the study of elementary particles, G_s and G_e play the key role. For detailed information, see the following section.

Note-3: Considering the above two assumptions,

1) Currently believed generalized physical concepts like, proton-electron mass ratio, neutron life time, weak coupling constant, strong coupling constant, nuclear charge radius, root mean square radius of proton, melting points of proton and electron, nuclear charge radii, nuclear binding energy, nuclear stability, Bohr radius of hydrogen atom, electron and proton magnetic moments, Planck's constant, atomic radii, molar mass constant and Avogadro number etc. can be reviewed in a unified approach and can be simplified.

2) Significance of the ratio of nuclear gravitational constant and Newtonian gravitational constant can be understood and thereby magnitude of the Newtonian gravitational constant can be estimated in a unified approach.

3) Proceeding further, considering the ratio of nuclear gravitational constant and Newtonian gravitational constant, neutron star mass can be understood.

3. Important points pertaining to 'Schwarzschild interaction' and 'final unification'

1) If it is true that c and G_N are fundamental physical constants, then (c^4/G_N) can be considered as a fundamental compound constant related to a characteristic limiting force [9].

2) Black holes are the ultimate state of matter's geometric structure.

3) Magnitude of the operating force at the black hole surface is of the order of (c^4/G_N).

4) Gravitational interaction taking place at black holes can be called as 'Schwarzschild interaction'.

5) Strength of 'Schwarzschild interaction' can be assumed to be unity.

6) Strength of any other interaction can be defined as the ratio of operating force magnitude and the classical or astrophysical force magnitude (c^4/G_N).

7) If one is willing to represent the magnitude of the operating force as a fraction of (c^4/G_N) i.e. X times of (c^4/G_N), where $X << 1$, then

$$\frac{X \text{ times of } (c^4/G_N)}{(c^4/G_N)} \cong X \rightarrow \text{Effective } G \Rightarrow \frac{G_N}{X} \quad (3)$$

If X is very small, $(1/X)$ becomes very large. In this way, X can be called as the strength of interaction. Clearly speaking, strength of any interaction is $(1/X)$ times less than the 'Schwarzschild interaction' and effective G becomes (G/X).

8) With reference to Schwarzschild interaction, for electromagnetic interaction, $X \approx 2.811 \times 10^{-48}$ and for strong interaction, $X \cong 2.0 \times 10^{-39}$.

9) Characteristic operating force corresponding to electromagnetic interaction is $(c^4/G_e) \approx 3.4 \times 10^{-4}$ N and characteristic operating force corresponding to strong interaction is $(c^4/G_s) \approx 242600$ N.

10) Characteristic operating power corresponding to electromagnetic interaction is $(c^5/G_e) \approx 10990$ J/sec and characteristic operating power corresponding to strong interaction is $(c^5/G_s) \approx 7.27 \times 10^{13}$ J/sec

11) As $\left[\left(c^4/G_e\right),\left(c^4/G_s\right)\right] << \left(c^4/G_N\right)$ and $\left[\left(c^5/G_e\right),\left(c^5/G_s\right)\right] << \left(c^5/G_N\right)$, protons and electrons can not be considered as 'black holes', but may be assumed to follow similar relations that black holes generally believed to follow.

12) According to S.W. Hawking [10], temperature of black hole takes the following expression.

$$T_B \cong \frac{\hbar c^3}{8\pi G_N k_B M_B} \tag{4}$$

where M_B and T_B represent the mass and temperature of a black hole respectively. It may be noted that, by combining the views of Hawking and Abhas Mithra [11] and by considering the proposed assumptions, melting points of elementary particles can be estimated and fitted.

4. To understand the role of Newtonian gravitational constant in nuclear physics

Let,

$$M_{pl} \cong \sqrt{\frac{\hbar c}{G_N}} \cong 1.220\ 93(7)\times 10^{19}\ \text{GeV}/c^2 \cong \text{Planck mass} \tag{5}$$

$$m_{npl} \cong \sqrt{\frac{\hbar c}{G_s}} \approx 546.7\ \text{MeV}/c^2 \cong \text{Nuclear Planck mass} \tag{6}$$

After developing many relations, to a very good accuracy, it is noticed that,

$$m_p \cong \left(\frac{m_e^6 M_{pl}}{m_{npl}^2}\right)^{\frac{1}{5}} \text{ and } m_e \cong \left(\frac{m_p^5 m_{npl}^2}{M_{pl}}\right)^{\frac{1}{6}} \tag{7}$$

In a simplified picture,

$$\left.\begin{aligned} m_e &\cong \left(\frac{G_N m_{npl}^2}{G_s m_p^2}\right)^{\frac{1}{12}} m_p \cong \left(\frac{G_N \hbar c m_p^{10}}{G_s^2}\right)^{\frac{1}{12}} \cong \left(\left(\frac{G_N}{G_s}\right)\left(\frac{\hbar c}{G_s}\right) m_p^{10}\right)^{\frac{1}{12}} \\ \rightarrow m_p &\cong \left(\frac{G_s^2 m_e^{12}}{G_N \hbar c}\right)^{\frac{1}{10}} \cong \left(\left(\frac{G_s}{G_N}\right)\left(\frac{\hbar c}{G_s}\right)^{-1} m_e^{12}\right)^{\frac{1}{10}} \\ \Rightarrow \hbar &\cong \left(\frac{G_s}{G_N}\right)\left(\frac{m_e}{m_p}\right)^{10}\left(\frac{G_s m_e^2}{c}\right) \end{aligned}\right\} \tag{8}$$

In this way, one can see the combined role of $\left(G_s, G_N\right)$ in understanding the mystery of rest masses of proton and electron. By fixing the magnitude of $\left(G_s\right)$, magnitude of $\left(G_N\right)$ can be fixed.

5. To understand the Planck's constant

Proceeding further, it is possible to show that,

$$h \cong \sqrt{\frac{m_p}{m_e}}\sqrt{\left(\frac{G_s m_p^2}{c}\right)\left(\frac{e^2}{4\pi\varepsilon_0 c}\right)} \tag{9}$$

$$hc \cong \sqrt{\frac{m_p}{m_e}}\sqrt{\left(G_s m_p^2\right)\left(\frac{e^2}{4\pi\varepsilon_0}\right)} \tag{10}$$

Note that, these two relations are free from arbitrary coefficients and seems to be connected with quantum theory of radiation. With further research, if one is able to derive these two relations, unification of quantum theory and gravity can be made practical and successful. Based on relation (9) and by considering the recommended values of elementary physical constants [12, 13],

$$\left.\begin{aligned} G_s &\cong \frac{4\pi\varepsilon_0 h^2 c^2 m_e}{e^2 m_p^3} \cong 3.329560807\times 10^{28}\ \text{m}^3\text{kg}^{-1}\text{sec}^{-2} \\ G_e &\cong \frac{\hbar^2 c^2}{G_s m_p m_e^3} \cong \left(\frac{\hbar}{h}\right)^2\left(\frac{e^2 m_p^2}{4\pi\varepsilon_0 m_e^4}\right) \cong \left(\frac{e^2 m_p^2}{16\pi^3\varepsilon_0 m_e^4}\right) \cong 2.374335471\times 10^{37}\ \text{m}^3\text{kg}^{-1}\text{sec}^{-2} \\ G_N &\cong \left(\frac{m_e}{m_p}\right)^{12}\left(\frac{G_s^2 m_p^2}{\hbar c}\right) \cong \left(\frac{m_e}{m_p}\right)^{14}\left(\frac{4\pi\varepsilon_0}{e^2}\right)^2\left(\frac{2\pi h^3 c^3}{m_p^2}\right) \cong 6.679856051\times 10^{-11}\ \text{m}^3\text{kg}^{-1}\text{sec}^{-2} \\ \text{and } m_{npl} &\cong \sqrt{\frac{\hbar c}{G_s}} \cong 546.6205673\ \text{MeV}/c^2 \end{aligned}\right\} \tag{11}$$

From this data it is very clear to say that, accuracy of G_N seems to depend only on the ratio of $\left(\frac{h}{\hbar}\right)$. It is a very important point to be noted here. In the forgoing sections, we use these values.

6. Nuclear charge radius and root mean square radius of proton

Nuclear charge radius [14] can be expressed with the following relation.

$$R_0 \cong \frac{2G_s m_p}{c^2} \cong 1.239290976\times10^{-15} \text{ m} \quad (12)$$

Considering this relation (12), magnitude of G_N can be estimated with the following relation.

$$G_N \cong \left\{\left(\frac{m_e}{m_p}\right)^{12}\left(\frac{c^3R_0^2}{4\hbar}\right)\right\} \cong 4.349311656\times10^{19}R_0^2 \quad (13)$$

By measuring the nuclear charge radii of stable atomic nuclides, (R_0, G_s) both can be estimated.

Root mean square radius of proton [12,13] can be expressed with the following relation.

$$R_p \cong \frac{\sqrt{2}G_s m_p}{c^2} \cong 0.8763110532\times10^{-15} \text{ m} \quad (14)$$

Considering this relation (14), magnitude of G_N can be estimated with the following relation.

$$G_N \cong \left\{\left(\frac{m_e}{m_p}\right)^{12}\left(\frac{c^3R_p^2}{2\hbar}\right)\right\} \cong 8.698623312\times10^{19}R_p^2 \quad (15)$$

See the following table-1.

Table 1 – RMS radius of proton Vs. Newtonian gravitational constant

RMS radius of proton (fm)	**Newtonian gravitational constant** $\left(10^{-11}\text{m}^3\text{kg}^{-1}\text{sec}^{-2}\right)$
0.8775	6.697994316
0.8768	6.68731232
0.8758	6.672067113
0.8751	6.661405819

7. To fit and understand the Fermi's weak coupling constant

To a great surprise, it is noticed that [12,13],

$$G_F \cong \left(\frac{m_e}{m_p}\right)^2 \hbar c R_0^2 \quad (16)$$

From above relations,

$$G_F \cong \left(\frac{m_e}{m_p}\right)^2\left(\frac{4G_s^2m_p^2\hbar}{c^3}\right) \cong \left(\frac{4G_s^2m_e^2\hbar}{c^3}\right) \cong 1.440210005\times10^{-62} \text{ J.m}^3 \quad (17)$$

Based on this relation (17), magnitude of G_N can be estimated with the following relation.

$$G_N \cong \left(\frac{m_e}{m_p}\right)^{10}\left(\frac{G_F c^2}{4\hbar^2}\right) \cong 6.659637481\times10^{-11} \text{ m}^3\text{kg}^{-1}\text{sec}^{-2} \quad (18)$$

where $G_F \cong 1.1663787\times10^{-5}(\hbar c)^3 \text{ GeV}^{-2} \cong 1.435850781\times10^{-62} \text{ Jm}^3$.

8. Melting points of proton and electron

From above concepts and relations, melting points of proton and electron can be estimated with the following relations.

Melting point of proton,

$$T_{proton} \cong \frac{\hbar c^3}{8\pi k_B G_s m_p} \cong 0.147 \text{ Trillion K} \quad (19)$$

This relation can be applied to quarks also. It may be noted that, RHIC have tentatively claimed to have created a quark–gluon plasma with an approximate temperature of 4 trillion degree Kelvin. A new record breaking temperature was set by ALICE at CERN on August, 2012 in the ranges of 5.5 trillion degree Kelvin. In June 2015, an international team of physicists have produced quark-gluon plasma at the Large Hadron Collider by colliding protons with lead nuclei at high energy inside the supercollider's Compact Muon Solenoid detector at a temperature of 4 trillion degree Kelvin [15]. These experimental temperatures are close to the predicted melting temperatures of Proton, up, down and strange quarks and seem to support the proposed pseudo gravitational constant assumed to be associated with strong interaction. Melting point of electron,

$$T_{electron} \cong \frac{\hbar c^3}{8\pi k_B G_e m_e} \cong 0.3786 \text{ Million K} \qquad (20)$$

Melting point of electron is 38827 times less than proton melting point. These two estimations are for experimental verification.

9. Nuclear stability and binding energy

Proton-neutron stability [16] can be understood with the following relation

Let A_s be the stable mass number of Z.

$$A_s \cong 2Z + k(2Z)^2 \cong 2Z + 0.0016(2Z)^2 \quad (\text{Or})$$
$$Z \cong \frac{\sqrt{4kA+1}-1}{4k} \text{ where } A \text{ is any mass number} \qquad (21)$$

where $k \cong \left(\frac{G_s m_p m_e}{\hbar c}\right) \cong 1.605\times10^{-3}$. See colum-2 of table-2. With even-odd corrections, accuracy can be improved. Close to stable atomic nuclides, nuclear binding energy [17] can be understood with the following relation.

For $(Z \geq 5)$,

$$BE \cong -\left(Z - 2 + \sqrt{\frac{Z}{30}}\right)\sqrt{\left(\frac{3}{5}\frac{e^2}{4\pi\varepsilon_0 R_p}\right)\left(\frac{3}{5}\frac{G_s m_p^2}{R_p}\right)} \qquad (22)$$
$$\cong -\left(Z - 2 + \sqrt{\frac{Z}{30}}\right)\times 19.8 \text{ MeV}$$

where R_p is the RMS radius of proton.

$-\left(\frac{3}{5}\frac{e^2}{4\pi\varepsilon_0 R_p}\right) \cong -0.986$ MeV and

$-\left(\frac{3}{5}\frac{G_s m_p^2}{R_p}\right) \cong -398.0$ MeV represent the respective self binding energies. See the following table-2.

Table 2 – Estimated stable mass numbers and their corresponding nuclear binding energy

Proton number	Estimated Stable mass number	Estimated binding energy in MeV		Proton number	Estimated Stable mass number	Estimated binding energy in MeV
6	12. 2	88.05		60	143.0	1176.4
16	33.6	291.6		70	171.4	1376.6
26	56.3	493.4		82	207.0	1616.7
40	90.2	775.3		92	238.2	1816.7
50	116.0	976.0		100	264.0	1976.5

10. 'System of units' independent Avogadro number and Molar mass unit

If, atoms as a whole believed to exhibit electromagnetic interaction, then molar mass constant and Avogadro number, both can be understood with the following simple relation.

$$G_e\left(m_{atom}\right)^2 \cong G_N\left(M_{mole}\right)^2 \qquad (23)$$

where m_{atom} is the unified atomic mass unit and M_{mole} is the molar mass unit or gram mole.

Thus it is very clear to say that, directly and indirectly 'gravity' plays a key role in understanding the molar mass unit.

$$\frac{M_{mole}}{m_{atom}} \cong \sqrt{\frac{G_e}{G_N}} \rightarrow M_{mole} \cong \sqrt{\frac{G_e}{G_N}} \times m_{atom} \qquad (24)$$

where $\sqrt{\frac{G_e}{G_N}} \cong 5.96\times10^{23}$ and $(0.00099 > M_{mole} < 0.001)$ kg

Based on these relations, "independent of system of units" and "independent of ad-hoc selection of exactly one gram", it may be possible to explore the correct physical meaning of the famous 'Molar mass unit' and 'Avogadro number' in a unified approach [18].

11. To fit and understand the atomic radii

Considering the geometric mean of the two assumed gravitational constants associated with proton and 'atom as whole', atomic radii can be fitted in the following way. By following the periodic arrangement of atoms and their electronic arrangement, accuracy can be improved.

$$R_{atom} \cong A_s^{1/3}\sqrt{\left(\frac{2G_s m_n}{c^2}\right)\left(\frac{2G_e m_{atom}}{c^2}\right)} \cong A_s^{1/3} * 33.0\times10^{-12} \text{ m} \cong A_s^{1/3} * 33.0 \text{ pico.meter} \quad (25)$$

where A_s is the stable atomic mass number of the atom, m_n is the average mass of nucleon and m_{atom} is the unified atomic mass unit. Note that, this relation resembles the famous relation for nuclear radii proposed by Rutherford [19]. See the following table-3.

Table 3 – Estimated atomic radii

Proton number	Stable Mass number	Estimated atomic radii (pico meter)	Reference data [20] (pico meter)
1	1	33.0	31
6	12	75.6	76
16	32	104.8	105
27	57	127.0	126
28	62	130.6	124
29	63	131.3	132
30	66	133.4	122

Proton number	Stable Mass number	Estimated atomic radii (pico meter)	Reference data [20] (pico meter)
40	90	147.9	175
47	107	156.7	145
60	142	172.2	201
70	172	183.5	187
81	203	193.9	145
89	227	201.3	215
92	238	204.5	196

12. Mass and radius of a neutron star

A) Mass of neutron star

According to G. Srinivasan [21]: "We began by remarking that the real stumbling block in determining the maximum mass of neutron stars is the equation of state of neutron star matter at densities above the nuclear density ~2.5x10^{14} g.cm^{-3}. After four decades of strenuous effort by several groups there is still considerable uncertainty concerning the equation of state: is the matter in the core of the star "stiff" or "soft"! This depends on whether or not Bose-Einstein Condensates, such as pion condensate or kaon condensate, occur at supranuclear densities, and whether asymptotically free quark matter occurs at even higher densities. Till this question is resolved all one can say is that the maximum mass of neutron stars is somewhere in the range (1.5 to 6.0) solar masses. It seems to us that the best one can do at present is to appeal to observation".

Let (M_{NS}, m_n) represent masses of neutron star [21] and neutron respectively.

$$\frac{G_N M_{NS} m_n}{\hbar c} \cong \sqrt{\frac{G_s}{G_N}} \rightarrow M_{NS} \cong \sqrt{\frac{G_s}{G_N}}\left(\frac{\hbar c}{G_N m_n}\right) \cong 3.17 \text{ Solar mass} \quad (26)$$

Alternatively, it is also noticed that,

$$\frac{M_{NS}}{M_{pl}} \cong \frac{G_s}{G_N} \text{ Or } \frac{G_N M_{NS}^2}{\hbar c} \cong \left(\frac{G_s}{G_N}\right)^2 \rightarrow G_N M_{NS} \cong G_s M_{pl} \Rightarrow M_{NS} \cong \left(\frac{G_s}{G_N}\right) M_{pl} \cong 5.46 \text{ Solar mass} \quad (27)$$

Interesting point to be noted is that, ratio of neutron star mass and Planck mass is of the order of $\left(\frac{G_s}{G_N}\right)$.

$$\frac{\text{Mass of neutron star}}{\text{Planck mass}} \cong \frac{M_{NS}}{\left(\sqrt{G_N\hbar/c^3}\right)} \cong \frac{G_s}{G_N} \qquad (28)$$

From astro-particle physics point of view, it can be given some consideration.

Note: Currently believed upper mass limit of Super massive black holes (SMBHs) [22] can be fitted with the following relation.

$$\frac{M_{SMBH}}{M_{pl}} \cong \frac{G_e}{G_N} \text{ Or } \frac{G_N M_{SMBH}^2}{\hbar c} \cong \left(\frac{G_e}{G_N}\right)^2$$
$$\rightarrow G_N M_{SMBH} \cong G_e M_{pl} \Rightarrow M_{SMBH} \cong \left(\frac{G_e}{G_N}\right) M_{pl} \cong \qquad (29)$$
$$\cong 7.74\times10^{39} \text{ kg} \approx 10^{10} \text{ Solar mass}$$

Point to be noted is that, ratio of upper limit of galactic black hole mass and Planck mass is of the order of $\frac{G_e}{G_N}$.

B) Radius of neutron star

Particle data group [13] recommended value of magnetic radius of neutron is around 0.86 fm. Qualitatively this can be compared with the following relation.

$$\frac{\sqrt{2}G_s m_n}{c^2} \cong 0.877 \text{ fm.} \qquad (30)$$

Let (R_{NS}, R_n) represent the radii [23,12] of neutron star and neutron respectively.

$$\frac{R_{NS}}{\left(\sqrt{2}G_s m_n/c^2\right)} \cong \frac{\text{Radius of neutron star}}{\text{Neutron magnetic radius}} \cong \sqrt{\frac{G_s}{G_N}}$$
$$\rightarrow R_{NS} \cong \sqrt{\frac{G_s}{G_N}}\left(\frac{\sqrt{2}G_s m_n}{c^2}\right) \cong 19.5 \text{ km} \qquad (31)$$

It may be noted that, observed masses of neutron stars are of the order of 2 Solar masses and radii are of the order of 11 km. In this context, important point to be noted is that, ratio of neutron star radius and neutron's characteristic radius is of the order of $\sqrt{\frac{G_s}{G_N}}$. It is also possible to say that, ratio of neutron star radius and Planck size is of the order of $\left(\frac{G_s}{G_N}\right)$.

It can be expressed in the following way.

$$\frac{\text{Radius of neutron star}}{\text{Planck length}} \cong \frac{R_{NS}}{\left(\sqrt{G_N\hbar/c^3}\right)} \cong \frac{G_s}{G_N} \qquad (32)$$

$$\frac{R_{NS}}{\left(\sqrt{\hbar G_N/c^3}\right)} \cong \frac{G_s}{G_N}$$
$$\rightarrow R_{NS} \cong \left(\frac{G_s}{G_N}\right)\sqrt{\frac{\hbar G_N}{c^3}} \cong \left(\sqrt{\frac{G_s}{G_N}} \times \sqrt{\frac{\hbar G_s}{c^3}}\right) \cong 8.1 \text{ km} \qquad (33)$$

where $\sqrt{\frac{\hbar G_s}{c^3}} \cong 3.61$ fm can be called as the nuclear Planck length. This can be compared with neutron's positively charged core of radius ~3 fm. Now the above relation (33) can be re-expressed in the following way.

$$\frac{\text{Radius of neutron star}}{\text{Nuclear Planck length}} \cong \frac{R_{NS}}{\left(\sqrt{G_s\hbar/c^3}\right)} \cong \sqrt{\frac{G_s}{G_N}} \qquad (34)$$

13. Fitting and understanding the neutron life time

It may be noted that, during beta-decay, by emitting one electron and one neutrino, neutron transforms to proton.

Let, t_n be the life time of neutron, m_n be the rest mass of neutron and $(m_n - m_p)$ be the mass difference of neutron and proton. Then, quantitatively it is possible to show that,

$$\frac{(m_n - m_p)}{m_n} \cong \left(\frac{G_e}{G_N}\right)^{\frac{1}{2}}\left(\frac{G_s m_n}{c^3 t_n}\right) \qquad (35)$$

Very interesting observation is that, the three gravitational constants seem to play a simultaneous role in deciding the neutron decay time and is for further analysis. Now,

$$t_n * (m_n - m_p)c^2 \cong \left(\frac{G_e}{G_N}\right)^{\frac{1}{2}}\left(\frac{G_s m_n^2}{c}\right) \qquad (36)$$

$$t_n \cong \left(\frac{G_e}{G_N}\right)^{\frac{1}{2}}\left(\frac{G_s m_n^2}{\left(m_n - m_p\right)c^3}\right) \cong 896.45 \text{ sec} \qquad (37)$$

With 1-2 % error, this obtained value can be compared with recommended [13] and experimental [24,25] neutron life times of $(878 \text{ to } 888)$ sec .

With reference to weak coupling constant and proposed gravitational constant associated with strong interaction,

$$t_n \cong \left(\frac{m_e}{m_p}\right)^{\frac{7}{2}} \frac{\sqrt{G_s G_F}}{2G_N\left(m_n - m_p\right)c} \qquad (38)$$

$$G_N \cong \left(\frac{m_e}{m_p}\right)^{\frac{7}{2}} \frac{\sqrt{G_s G_F}}{2t_n\left(m_n - m_p\right)c} \qquad (39)$$

Qualitatively, if one is willing to define the well believed strong coupling constant with the following relation,

$$\begin{cases} \alpha_s \cong \left(\dfrac{\hbar c}{G_s m_p^2}\right)^2 \cong 0.11519371 \quad \text{Or} \\ \sqrt{\alpha_s} \cong \left(\dfrac{\hbar c}{G_s m_p^2}\right) \cong 0.339401988, \end{cases} \qquad (40)$$

error in estimation of neutron life can be minimized and can be expressed with the following relation.

$$t_n \cong \left(\frac{G_e}{G_N}\right)^{\frac{1}{2}}\left(\frac{1}{\alpha_s}\right)^{\frac{1}{2}}\left(\frac{\hbar}{\left(m_n - m_p\right)c^2}\right) \cong \frac{303.41914 \text{ sec}}{\sqrt{\alpha_s}} \qquad (41)$$

With reference to recommended value [13] of $\alpha_s \cong 0.1185 \pm 0.0006$, obtained $t_n \cong 881.422$ sec

$$\alpha_s \cong \left(\frac{G_e}{G_N}\right)\left(\frac{\hbar}{t_n\left(m_n - m_p\right)c^2}\right)^2 \cong \left(\frac{303.41914 \text{ sec}}{t_n}\right)^2 \qquad (42)$$

With reference to recommended value [13,26,27] of $t_n \cong (880.3 \pm 1.1)$ sec, obtained $\alpha_s \cong 0.1188$

14. Understanding the Bohr radius, Reduced Planck's constant and magnetic moments of electron and proton

Energy conservation point of view, qualitatively and quantitatively, we noticed the following relation.

$$\begin{gathered} \frac{G_e m_e^2}{2a_0} \cong \frac{e^2}{4\pi\varepsilon_0\left(2G_s m_p / c^2\right)} \cong \frac{e^2}{4\pi\varepsilon_0 R_0} \\ \Rightarrow a_0 \cong \left(\frac{4\pi\varepsilon_0 G_e m_e^2}{e^2}\right)\left(\frac{G_s m_p}{c^2}\right) \end{gathered} \qquad (43)$$

where $a_0 \cong 0.53$ A° is the Bohr radius of hydrogen atom and $\frac{G_s m_p}{c^2} \cong 0.61965$ fm and $R_0 \cong \frac{2G_s m_p}{c^2} \cong 1.24$ fm is the nuclear charge radius. Now, potential energy of electron corresponding to Bohr radius can be expressed with the following relation.

$$\left(E_{pot}\right)_{a_0} \cong -\frac{e^2}{4\pi\varepsilon_0 a_0} \cong -\left(\frac{e^2}{4\pi\varepsilon_0 G_e m_e^2}\right)\frac{e^2}{4\pi\varepsilon_0\left(G_s m_p / c^2\right)} \qquad (44)$$

Now the basic question to be understood is : How to understand the 'discreteness'?. Important quantum mechanical result of Bohr's theory is that, maximum number of electrons that can be accommodated in any orbit is $2n^2$ where $n = 1, 2, 3, \ldots$. Based on this result, it can be interpreted that, in any orbit, probability of finding any one electron out of $2n^2$ electrons is $\left(\frac{1}{2n^2}\right)$. By following this interpretation and with reference to electron's total energy of 13.6 eV, 'discrete total energy' of electron in any orbit can be expressed with the following relation.

$$\left(E_{tot}\right)_n \cong -\left(\frac{1}{2n^2}\right)\frac{e^2}{4\pi\varepsilon_0 a_0} \cong -\left(\frac{1}{2n^2}\right)\left(\frac{e^2}{4\pi\varepsilon_0 G_e m_e^2}\right)\frac{e^2}{4\pi\varepsilon_0\left(G_s m_p/c^2\right)}$$
$$\cong -\left(\frac{1}{n^2}\right)\left(\frac{e^2}{4\pi\varepsilon_0 G_e m_e^2}\right)\frac{e^2}{4\pi\varepsilon_0\left(2G_s m_p/c^2\right)} \cong -\left(\frac{1}{n^2}\right)\left(\frac{e^2}{4\pi\varepsilon_0 G_e m_e^2}\right)\left(\frac{e^2}{4\pi\varepsilon_0 R_0}\right) \quad (45)$$

where $R_0 \cong 1.24$ fm.

Clearly speaking, in any orbit,

$$\frac{\text{Total energy of electron}}{\text{Nuclear potential}} \cong \left(\frac{1}{n^2}\right)\left(\frac{e^2}{4\pi\varepsilon_0 G_e m_e^2}\right) \quad (46)$$

Based on relation (43) and with reference to Bohr's theory of hydrogen atom,

$$\left(\frac{\hbar}{m_e}\right) \cong \frac{\sqrt{G_s m_p}\sqrt{G_e m_e}}{c} \cong \frac{\sqrt{G_s G_e}\sqrt{m_p m_e}}{c} \quad (47)$$

Now, revolving electron's magnetic moment can be expressed as follows.

$$\mu_e \cong \frac{e\hbar}{2m_e} \cong \frac{e\sqrt{G_s G_e}\sqrt{m_p m_e}}{2c} \quad (48)$$

Proceeding further, with reference to strong interaction and the proposed strong interaction gravitational constant, magnetic moment of proton can be expressed with the following relation.

$$\mu_p \cong \gamma * \left(\frac{eG_s m_p}{2c}\right) \cong \gamma * 1.488142\times10^{-26} \text{ J.Tesla}^{-1} \quad (49)$$

where γ is a coefficient of the order of unity and its approximate value is 0.952.

It may be noted that, by considering a proportionality ratio of $\left(\frac{\mu_p}{\mu_e}\right)$, planet earth's dipole magnetic moment can be expressed with the following relation.

$$\mu_{earth} \cong \left(\frac{\mu_p}{\mu_e}\right) * \left(\frac{eG_s M_{earth}}{2c}\right) \cong 8.15\times10^{22} \text{ J.Tesla}^{-1} \quad (50)$$

where $M_{earth} \cong 6\times10^{24}$ kg.

With further study and analysis, if one is willing to consider the proportionality ratio as a function of planetary physical and magnetic parameters, it may be possible to understand the weak and strong planetary magnetic moments.

15. Understanding the nuclear charge radii

For atomic number greater than 23, nuclear charge radii [30] can be fitted with the following relation.

$$R_{(Z,A)} \cong \left\{Z^{1/3} + \left(\sqrt{Z(A-Z)}\right)^{1/3}\right\}\left(\frac{G_s m_p}{c^2}\right) \quad (51)$$

where $Z \geq 23$ and $\frac{G_s m_p}{c^2} \cong 0.61965$ fm

This relation seems to be best applicable for medium, heavy and super heavy atomic nuclides. See the following table-4.

By refining the relation (51) with reference to lower atomic numbers and by knowing the nuclear charge radii of various atomic nuclides, magnitude of G_s can be estimated from nuclear experimental data.

Table 4 – To fit the nuclear charge radii

Proton number	Mass number	Neutron number A-Z	Estimated charge radii from relation (51)	Charge radii from reference [30]	%Error w.r.t relation (51)
20	40	20	3.364	3.4776	3.27
21	45	24	3.458	3.5459	2.49
22	48	26	3.522	3.5921	1.96
23	51	28	3.583	3.6002	0.47
24	52	28	3.621	3.6452	0.66
25	55	30	3.680	3.7057	0.70
26	56	30	3.716	3.7377	0.59
27	59	32	3.771	3.7875	0.43
28	60	32	3.806	3.8118	0.16
29	63	34	3.859	3.8823	0.61
30	66	36	3.910	3.9491	0.99
31	69	38	3.960	3.9973	0.93
32	72	40	4.009	4.0576	1.20
33	75	42	4.057	4.0968	0.98
34	76	42	4.087	4.1395	1.27
35	79	44	4.133	4.1629	0.73
36	86	50	4.207	4.1835	-0.57
37	87	50	4.236	4.1989	-0.88
38	88	50	4.264	4.224	-0.95
39	89	50	4.292	4.243	-1.14
40	90	50	4.319	4.2694	-1.15
41	93	52	4.360	4.324	-0.83
42	92	50	4.371	4.3151	-1.30
44	104	60	4.491	4.5098	0.41
45	103	58	4.503	4.4945	-0.20
46	108	62	4.554	4.5563	0.06
47	109	62	4.578	4.5638	-0.31
48	114	66	4.627	4.6087	-0.39
49	115	66	4.650	4.6156	-0.75
50	120	70	4.697	4.6519	-0.98
51	121	70	4.720	4.6802	-0.86
52	130	78	4.787	4.7423	-0.95
53	127	74	4.788	4.75	-0.81
54	136	82	4.853	4.7964	-1.18
55	133	78	4.854	4.8041	-1.04
56	138	82	4.897	4.8378	-1.22
57	139	82	4.918	4.855	-1.31
58	140	82	4.940	4.8771	-1.28
59	141	82	4.961	4.9174	-0.88
60	142	82	4.981	4.9123	-1.41
62	144	82	5.022	4.9524	-1.41
63	145	82	5.042	4.9663	-1.52
64	160	96	5.130	5.1734	0.83
65	159	94	5.141	5.06	-1.60
66	148	82	5.101	5.0455	-1.09

Proton number	Mass number	Neutron number A-Z	Estimated charge radii from relation (51)	Charge radii from reference [30]	%Error w.r.t relation (51)
67	165	98	5.198	5.2022	0.08
68	170	102	5.235	5.2789	0.83
69	169	100	5.245	5.2256	-0.38
70	176	106	5.290	5.3215	0.58
71	175	104	5.300	5.37	1.30
72	178	106	5.327	5.3371	0.18
73	181	108	5.354	5.3507	-0.06
74	184	110	5.381	5.3658	-0.28
75	185	110	5.399	5.3596	-0.73
76	192	116	5.441	5.4126	-0.53
77	191	114	5.451	5.3968	-1.00
78	194	116	5.476	5.4236	-0.97
79	197	118	5.502	5.4371	-1.18
80	198	118	5.519	5.4463	-1.33
81	205	124	5.559	5.4759	-1.52
82	208	126	5.584	5.5012	-1.50
83	209	126	5.601	5.5211	-1.44
84	208	124	5.610	5.5584	-0.92
86	212	126	5.650	5.5915	-1.05
87	212	125	5.662	5.5915	-1.27
88	214	126	5.682	5.6079	-1.33
90	232	142	5.773	5.7848	0.20
92	238	146	5.818	5.8571	0.66
94	239	145	5.846	5.8601	0.24
95	243	148	5.872	5.9048	0.56
96	244	148	5.887	5.8429	-0.75

16. Discussion

It may be noted that,

1) Mostly, old 'strong gravity' models seem to focus on understanding 'quark confinement,' 'basic hadron mass spectrum' and 'coupling constants'.

2) In this paper, we tried our level best in implementing the Newtonian gravitational constant along with two pseudo microscopic gravitational constants and proposed many interesting applications starting from 'electron mass' and 'neutron star mass'.

3) Relations (5) to (8) show the potential and combined role of (G_s, G_N) in nuclear and particle physics.

4) Relations (9) and (10) show the potential role of (G_s) in quantum theory of radiation.

5) Relations (12) to (23) seem to show the potential applications of (G_s, G_e) in nuclear and particle physics.

6) Relations (23), (24) and (25) clearly demonstrate the combined role of (G_s, G_e) in understanding the Avogadro number, molar mass constant and atomic radii.

7) Relations (26) to (34) seem to extend the scope of applicability of the proposed assumptions in astrophysics starting from neutron stars to galactic nuclei.

8) Relations (35) to (39) seem to play a key role in understanding the combined role of (G_s, G_e, G_N).

9) Relations (40) to (42) seem to play a key role in understanding the strong coupling constant and can be estimated from neutron life time and neutron-proton mass difference.

10) Relations (43) to (49) seem to play a key role understanding the origin of quantum mechanics and magnetic moments of electron and proton.

11) Relation (50) seems to play a key role in understanding the dipole magnetic moment of planet earth in a unified approach.

12) Relation (51) seems to play a key role in fitting and understanding the role of G_s in nuclear charge distribution.

13) Qualitatively and quantitatively in a heuristic approach we developed many characteristic relations among micro-macro physical constants with utmost possible accuracy.

14) Proceeding further, we proposed interesting and accurate analytical relations for estimating the Newtonian gravitational constant in a meaningful way and this procedure is beyond the scope of current research paradigm. One must admit this fact.

15) We admit the fact that, in this paper, we could not provide the required 'back ground physics' for understanding the proposed semi empirical relations. At the same time, one must accept the fact that, we presented all possible relations and relevant information using by which theoretically, one may be able to develop a unified and workable model of unification. We would like to inform that,

1) Based on the hierarchy of elementary physical constants,
2) Based on dimensional analysis,
3) Based on trial-error methods,
4) Based on simple mathematical functions,
5) Based on simplified computer programs,
6) Based on data fitting and
7) Based on data prediction

so far we could publish more than 20 papers on this subject. We admit that this procedure is against to the current 'scientific standards' and 'scientific procedures'. In this context, we would like to stress the fact that, even though string theory models are having strong mathematical back ground and sound physical reasoning, they are badly failing in coupling the gravitational and nuclear physical constants. Here, the problem is with 'our understanding and our perception' but not with 'scientific standards and procedures'. In the development of science and engineering, 'data fitting' and 'workability' are the two essential tools using by which physical models can be generated and validated in a progressive manner.

17. Conclusion

Considering the wide applicable range of the proposed two assumptions, we are confident to say that, with further research and analysis, 'hidden and left over physics' can easily be explored. In this context, we would also like to stress the fact that, with current understanding of String theory [28] or Quantum gravity [29], qualitatively or quantitatively, one cannot implement the Newtonian gravitational constant in microscopic physics. This 'draw back' can be considered as a characteristic 'inadequacy' of modern unification paradigm. Proceeding further, with reference to String theory models and Quantum gravity models, proposed two pseudo gravitational constants and presented semi empirical relations can be given some consideration in developing a 'workable model' of 'final unification'.

Acknowledgements

Author Seshavatharam U.V.S is indebted to professors K.V. Krishna Murthy, Chairman, Institute of Scientific Research in Vedas (I-SERVE), Hyderabad, India and Shri K.V.R.S. Murthy, former scientist IICT (CSIR), Govt. of India, Director, Research and Development, I-SERVE, for their valuable guidance and great support in developing this subject.

References

1. Ashoke Sen. Strong-weak coupling duality in four-dimensional string theory // International Journal of Modern Physics A. – 1994. – Vol. 9 (21). – P. 3707–3750.

2. Juan M., Maldacena Gravity. Particle Physics and Their Unification // Int.J.Mod.Phys. – 2000. – Vol. A15S1. – P. 840-852.

3. Schlamminger S. and Newman R.D. Recent measurements of the gravitational constant as a function of time // Phys. Rev. – 2015. – Vol. D 91. – P. 121101.

4. Roberto Onofrio. Proton radius puzzle and quantum gravity at the Fermi scale // EPL. – 2013. – Vol. 104. – P. 20002.

5. Abdus Salam., Strong Interactions., Gravitation and Cosmology. Publ. in: NATO Advanced Study Institute, Erice, June16-July 6, 1972.

6. Salam A., Sivaram C. Strong Gravity Approach to QCD and Confinement // Mod. Phys. Lett. – 1993. – Vol. A8(4). – P. 321- 326.

7. Sivaram C. et al. Gravity of Accelerations on Quantum Scales and its consequences. http://arxiv.org/abs/1402.5071.

8. Seshavatharam U.V.S. and Lakshminarayana S. Semi empirical procedure for estimating the Newtonian gravitational constant with elementary physical constants and Avogadro number.

Proceedings of International Intradisciplinary Conference on the Frontiers of Crystallography. – 2014. – P. 47- 60.

9. Gibbons G.W. The Maximum Tension Principle in General relativity // Found.Phys. – 2002. – Vol. 32. – P. 1891-1901.

10. Hawking S.W. Particle Creation by Black Holes // Commun.Math. Phys. – 1975. – Vol. 43. – P. 199–220.

11. Abhas Mitra. Why gravitational contraction must be accompanied by emission of radiation in both Newtonian and Einstein gravity // Phys. Rev. D. – 2006. – Vol. 74. – P. 024010.

12. Mohr P.J., Taylor B.N. and Newell D.B. CODATA Recommended Values of the Fundamental Physical Constants:2010 // by in Rev. Mod. Phys. – 2012. – Vol. 84. – P. 1527.

13. Olive K.A. et al. Review of Particle Physics // Chin. Phys. C. – 2014. – Vol. 38. – P. 090001.

14. Robert Hofstadter, Rudolf Mössbauer. The electron-scattering method and its application to the structure of nuclei and nucleons. Nobel Lecture, December 11, 1961.

15. Khachatryan V. *et al.* (CMS Collaboration). Evidence for Collective Multiparticle Correlations in p–Pb Collisions // Phys. Rev. Lett. – 2015. – Vol. 115. – P. 012301.

16. Chowdhury P.R. et al. Modified Bethe-Weizsacker mass formula with isotonic shift and new driplines // Mod. Phys. Lett. – 2005. – Vol. A20. – P.1605-1618.

17. Ghahramany N. et al. New approach to nuclear binding energy in integrated nuclear model // Journal of Theoretical and Applied Physics. – 2012. –Vol. 6. – P. 3.

18. Martin J.T. Milton A. New definition for the mole based on the Avogadro constant: a journey from physics to chemistry // Phil. Trans. R. Soc. A. – 2011. – Vol. 369. – P. 3993–4003.

19. Rutherfor E. The Scattering of α and β rays by Matter and the Structure of the Atom // Philos. Mag. – Vol. 6. – P. 21.

20. The Periodic Table of the Elements (including Atomic Radius).
www.sciencegeek.net/tables/AtomicRadius.pdf.

21. Srinivasan G. The Maximum Mass of Neutron Stars // Bulletin of Astronomic Society of India. – 2002. – Vol. 30. – P. 523-547.

22. Kohei Inayoshi. and Zoltan Haiman. Is there a maximum mass for black holes in galactic nuclei? arxiv: 1601.02611v1.

23. Sebastien Guillot. et al. Measurement of the Radius of Neutron Stars with High S/N Quiescent Low-mass X-ray Binaries in Globular Clusters. Astrophys.J. 772 (2013).

24. Yue A.T. et al. Improved Determination of the Neutron Lifetime // Phys. Rev. Lett. – 2013. – Vol. 111. – P. 222501.

25. Arimoto Y. et al. Development of time projection chamber for precise neutron lifetime measurement using pulsed cold neutron beams // Nuclear Instrument sand Methods in Physics Research A. – 2015. – Vol. 799. – P. 187.

26. Seshavatharam U.V.S. and Lakshminarayana S. Applications of gravitational model of possible final unification in both large and small scale physics // Prespacetime journal. – 2016. – Vol 7. – P. 405-421.

27. Seshavatharam U.V.S. and Lakshminarayana S. The Possible Role of Newtonian, Strong & Electromagnetic Gravitational Constants in Particle Physics // Prespacetime journal. – 2016. – Vol 7. – P. 857-888.

28. Ashoke Sen. Developments in Superstring theory. CERN Document server, hep-ph/9810356 (2009)
https://cds.cern.ch/record/368056/files/9810356.pdf.

29. Edward Witten. What Every Physicist Should Know About String Theory. GR Centennial Celebration, Strings 2015, Bangalore, India. (2105). http://member.ipmu.jp/yuji.tachikawa/stringsmirrors/2015/26-06-2015-Edward-Witten.pdf.

30. Angeli I., Marinovab K.P. Table of experimental nuclear ground state charge radii: An update. Atomic Data and Nuclear Data Tables. – 2013. – Vol. 99. – P. 69–95.

UDC 539.9.01

*Shalenov E.O., Dzhumagulova K.N., Ramazanov T.S., Gabdullina G.L.

Al-Farabi Kazakh National University, IETP, al-Farabi 71, 050040 Almaty, Kazakhstan
*e-mail: shalenov.erik@mail.ru

Influence of dynamic screening on the scattering cross sections of the particles in the dense nonideal plasmas of noble gases

Abstract: Within the dynamic screening potential model, elastic scattering processes between electrons and atoms in partially ionized plasmas were investigated using the method of phase functions. The phase shifts were calculated by solving the Calogero equation. Differential and total cross sections for the scattering of electrons on noble gas atoms were calculated and compared with experimental and other theoretical data. It was shown that the polarization potential is adequate for description the interaction between charged and neutral particles in partially ionized plasma. Analysis of the results showed that the phase shifts of electron atom scattering obtained with taking into account the dynamic screening are larger than the data obtained with consideration of static screening. The results can be used to calculate the various transport coefficients of the semiclassical dense plasma.
Key words: scattering cross section, dynamic interaction potential, dense nonideal plasma, phase shift, noble gases.

Introduction

Elastic scattering of electrons on atoms is a fundamental process that continuously attracts the attention of researchers. A large number of various theoretical and experimental studies of elementary processes is devoted to the elastic scattering of electrons on noble gas atoms. Reaction cross section are valuable since they provide information on how particles collide and interact. They are needed to describe transfer processes within partially ionized plasmas. For those practical applications where plasma is a working medium, one needs adequate data on physical properties of the system. Various theoretical methods are used in plasma investigations; one of them employs pseudopotential models that adequately describe the effective interaction between the plasma constituents. In the present work we consider collisional processes in plasmas of complex composition on the basis of the static potential and dynamic potential for the electron-atom interaction. In this work we used the effective potential of electron atom interaction presented in works [1-3] and considering the effects of screening and diffraction:

$$\Phi_{ea}(r) = -\frac{e^2\alpha}{2r^4(1-4\lambda\!\!\!^{-}_{ea}{}^2/r_D^2)}\left(e^{-Br}(1+Br)-e^{-Ar}(1+Ar)\right)^2, \qquad (1)$$

where

$$A^2 = \left(1+\sqrt{1-4\lambda\!\!\!^{-2}_{ea}/r_D^2}\right)\Big/ 2\lambda\!\!\!^{-}_{ea}{}^2,$$

$$B^2 = \left(1-\sqrt{1-4\lambda\!\!\!^{-2}_{ea}/r_D^2}\right)\Big/ 2\lambda\!\!\!^{-}_{ea}{}^2.$$

$\lambda\!\!\!^{-}_{ea} = \hbar\Big/\sqrt{2\pi\mu_{ea}k_BT} \approx \lambda\!\!\!^{-}_{e}$ is the de Broglie thermal wavelength; $\mu_{ea} = m_e m_a/(m_e+m_a)$ is the reduced mass of the atom and the electron; $r_D = \left(k_BT\Big/\left(8\pi e^2 n_e\right)\right)^{1/2}$ is the Debye length; n_e is the numerical density of electrons; T is the plasma temperature; k_B is the Boltzmanns constant, α is the atomic polarizability. Potential (1) is screened and has finite values at the distances close to zero.

Collision cross sections directly depend on the relative velocity of the colliding particles, contained in the equations for their calculation. The energy of the static interaction usually does not depend on this velocity. This consideration is not entirely correct, and accounting of the influence of the different dynamic effects, in particular, the dynamic screening of the incident charges field, on the interaction energy of the particles is more consistent

[4,5]. In work [5] the elastic differential cross sections of charges in a dense semiclassical plasma on the basis of the interaction potential, taking into account the effects of diffraction and the effect of dynamic screening were investigated. In work [6] phase shifts, differential, partial, total and transport scattering cross sections of charges in a nonideal semiclassical plasma on the basis of interaction potential, taking into account the effects of diffraction and the effect of dynamic screening were calculated.

This potential has been obtained by replacing the usual Debye length in the interaction potential (1) by the screening radius, depending on the relative velocity of the colliding particles [7]:

$$r_0 = r_D(1+\upsilon^2/\upsilon_{Th}^2)^{1/2}, \qquad (2)$$

here υ is the relative velocity of the colliding particles, υ_{Th} is the thermal velocity. Then the energy of the electron-atom interaction, which takes into account dynamic screening, in a dimensionless form is:

$$\Phi_{ea}^{dyn}(r) = -\frac{e^2\alpha}{2r^4(1-4\lambda_{ea}^{\,2}/r_0^{\,2})}\left(e^{-Br}(1+Br)-e^{-Ar}(1+Ar)\right)^2 \qquad (3)$$

where

$$A^2 = \left(1+\sqrt{1-4\lambda_{ea}^2/r_0^2}\right)\Big/2\lambda_{ea}^{\,2},$$

$$B^2 = \left(1-\sqrt{1-4\lambda_{ea}^2/r_0^2}\right)\Big/2\lambda_{ea}^{\,2}.$$

In the case, when the influence of the scattering center is not large, the calculation of the scattering cross sections can be carried out in the Born approximation [8]. In work [5] basing on the results obtained by the Born method, it was shown that dynamic screening increases the differential scattering cross sections in comparison with the Debyes static screening, especially at small scattering angles. At large scattering angles differential cross sections converge.

The method of partial waves [8-9] gives more accurate quantum mechanical solution of the problem of the scattering cross section estimation. In this method the scattering cross sections are calculated on the basis of the scattering phases of the waves with different values of the orbital quantum number. For large values the scattering phase can be found from the semiclassical representation of a particle moving in the field of a fixed force center. Another method for the scattering phase calculation is called as the phase-function method, it reduces to solving of the first order differential equation for the phase function [8].

Method and parameters

The method of phase functions is used for the investigation of scattering processes, see Ref. [2,6]. The mathematical background of this method is given by the following fact which is well known in the theory of differential equations: a linear homogeneous equation of the second order (the Schrdinger equation, in our case) can be reduced to a non-linear equation of the first order, i.e. to the Ricatti equation, in our case. The monograph [10] provides a detailed description of this method. Thus, within this approach we solved a first-order differential equation for the scattering phase, i.e. the Calogero equation:

$$\frac{d}{dr}\delta_l(k,r) = -\frac{1}{k}\frac{2m}{\hbar^2}\Phi^{\alpha\beta}(r)\left[\cos\delta_l(k,r)j_l(kr)-\sin\delta_l(k,r)n_l(kr)\right]^2,\ \ \delta_l(k,0)=0, \qquad (4)$$

where l is orbital quantum number; $\delta_l(k,0)$ is the phase function; $\Phi^{\alpha\beta}(r)$ is the interaction potential; k is the wave number of the particle; $j_l(kr)$ and $n_l(kr)$ are regular and irregular solutions of the Schrödinger equation. The phase shift is the asymptotical value of the phase function at the large distances:

$$\delta_l(k) = \lim_{r\to\infty}\delta_l(k,r). \qquad (5)$$

Note that in the Calogero equation there is an obvious relation between the interaction potential and the scattering phase shift. Besides, it is quite

easy to solve this equation numerically. In the present work we employed the Runge-Kutta method of fourth order.

If the scattering phase shifts are known, one can calculate the total cross section for the elastic scattering of plasma particles according to [8]:

$$Q^{\alpha\beta}(k) = \frac{4\pi}{k^2}\sum_{l=0}(2l+1)\sin^2\delta_l^{\alpha\beta}, \qquad (6)$$

The wave number is rebated to the energy of the incident particle, $k^2 = \mu_{ea}E/\hbar^2$.

In this work for hydrogen plasma the following dimensionless parameters were used:

$$\Gamma = \frac{e^2}{a\,k_B T}, \qquad (7)$$

is the coupling parameter; the average distance between particles is $a = \left(3/4\pi n\right)^{1/3}$, $n = n_e + n_i$ density of charged particles;

$$r_s = \frac{a}{a_B}, \qquad (8)$$

is the density parameter ($a_B = \hbar^2/m_e e^2$ is the Bohr radius).

Method and parameters

The results of studies of the collisional processes within the static model (1) have been previously obtained and presented in [11-12]. The comparison with results obtained on the basis of the Debye and Deutsch models, which take into account one of two effects, screening or diffraction, respectively, was presented there. In this paper, we present the data obtained in the framework of the potential (1) for comparison with the results obtained on the basis of a new dynamic interaction potential (3), taking into account the dynamic screening and the effect of diffraction. The goal of this work is to identify the differences in the characteristics of the collisional processes associated with the use of the dynamic screening in the charged particles interaction.

Equation (4) was solved numerically. Figures 1 and 2 show the dependences of the phase function of the electron atom scattering on the distance obtained in the framework of the models of static and dynamic screening. As can be seen in Figures 1 and 2, the obtained phase functions demonstrate proper asymptotic behavior, at large distances they tend to some steady-state value, which is actually the phase shift. Phase shifts calculated within the dynamic potential (3) are larger then phase shifts derived within the static model (1), since the dynamic screening of the field is weaker than the static one.

Figure 3 shows the dependences of the differential cross sections of the electron-atom scattering on the scattering angle obtained in the framework of the models of static and dynamic screening. As can be seen in Figure 3, the differential cross sections calculated within the dynamic potential (3) lay higher then differential cross sections derived from the static model (1).

Figures 4 and 5 present the total cross sections for the scattering on the basis of static and dynamic potentials of the electrons on neutral He, Ne, respectively. The comparison of our results with the data obtained in experimental and other theoretical works shows that the dynamic potential used in the present work describes adequately the interaction of the electrons with atoms.

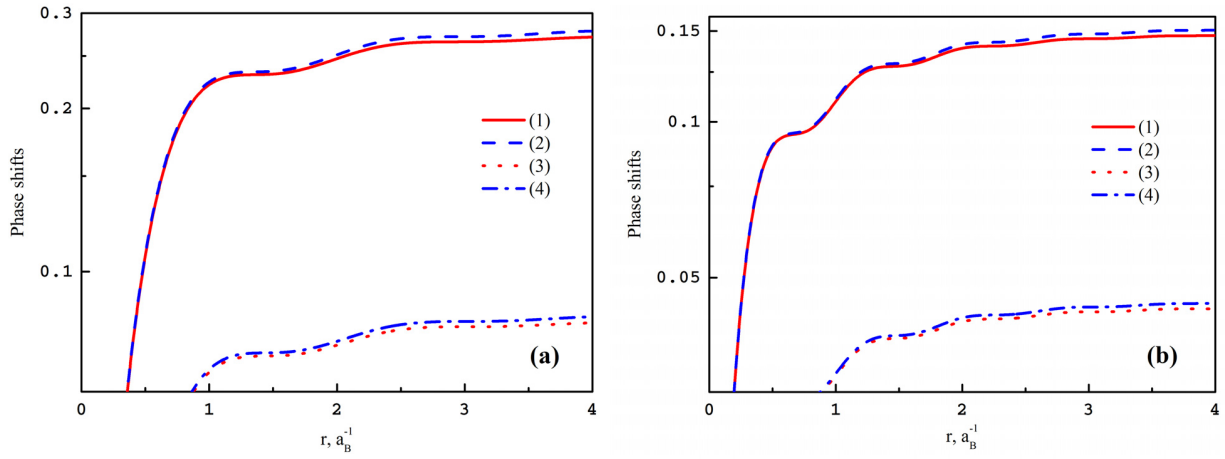

Figure 1 – Phase functions of electron-atom scattering in the dense plasma of noble gases.
a) $\Gamma = 0{,}5$, $r_s = 10$, $k = 2a_B^{-1}$.
1 – On the basis of the static potential on the hydrogen atom; 2 – On the basis of the dynamic potential on the hydrogen atom;
3 – On the basis of the static potential on the helium atom; 4 – On the basis of the dynamic potential on the helium atom;
b) $\Gamma = 0{,}5$, $r_s = 10$, $k = 4a_B^{-1}$.
1 – On the basis of the static potential on the hydrogen atom; 2 – On the basis of the dynamic potential on the hydrogen atom;
3 – On the basis of the static potential on the helium atom; 4 – On the basis of the dynamic potential on the helium atom;

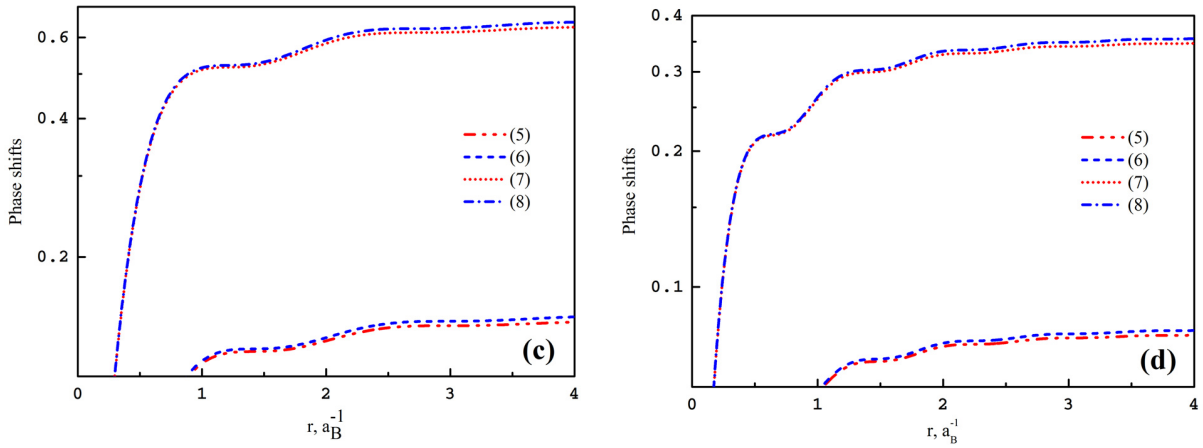

Figure 2 – Phase functions of electron-atom scattering in the dense plasma of noble gases.
c) $\Gamma = 0{,}5$, $r_s = 10$, $k = 2a_B^{-1}$.
5 – On the basis of the static potential on the neon atom; 6 – On the basis of the dynamic potential on the neon atom;
7 – On the basis of the static potential on the argon atom; 8 – On the basis of the dynamic potential on the argon atom;
d) $\Gamma = 0{,}5$, $r_s = 10$, $k = 4a_B^{-1}$.
5 – On the basis of the static potential on the neon atom; 6 – On the basis of the dynamic potential on the neon atom;
7 – On the basis of the static potential on the argon atom; 8 – On the basis of the dynamic potential on the argon atom;

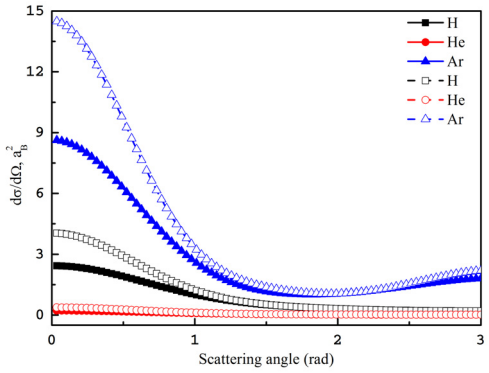

Figure 3 – Differential cross sections of the electron-atom scattering depending on the scattering angle, $\Gamma = 0{,}7$, $r_s = 4$, $k = 0{,}8a_B^{-1}$. Open symbol – on the basis of the dynamic potential; Solid symbol – on the basis of the static potential;

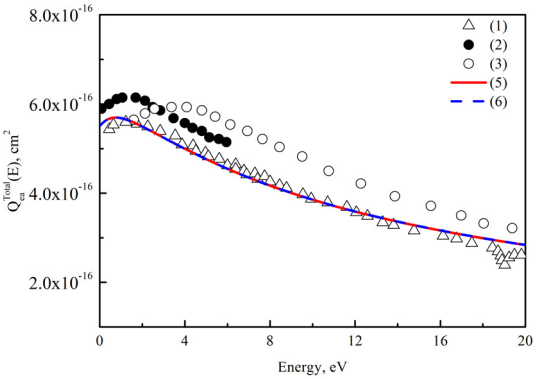

Figure 4 – Total cross sections for electron scattering on the helium atom on the basis of static and dynamic potentials. 1 – [13]; 2 – [14]; 3 – [15]; 4 – on the basis of the dynamic potential; 5 – on the basis of the static potential.

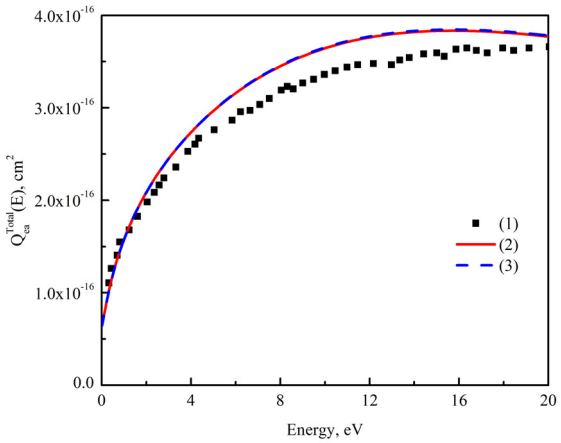

Figure 5 –Total cross sections for electron scattering on the neon atom on the basis of static and dynamic potentials. 1 – [16]; 2 – on the basis of the static potential; 3 – on the basis of the dynamic potential.

Conclusion

Based on the dynamic model of the charged particles interaction in nonideal semiclassical plasma phase shifts, differential and total scattering cross sections of the particles of noble gases were investigated. Quantum mechanical method has been used for their calculation. Analysis of the results showed that the phase shifts of electron atom scattering obtained with taking into account the dynamic screening are larger than the data obtained with consideration of static screening. The comparison of our results with the data obtained in the experiments and other theoretical works shows that the dynamic potential used in the present work adequately described the elastic scattering of the electron on atoms of noble gases.

The results can be used to calculate the various transport coefficients of the semiclassical dense plasma. Knowledge of these characteristics plays a major role in the design of technical installations associated with the use of the dense nonideal plasma, for example, inertial confinement fusion facilities.

References

1. Ramazanov T.S., Dzhumagulova K.N. and Omarbakiyeva Y.A.. Effective polarization interaction potential chargeatom for partially ionized dense plasma // Phys. Plasmas. – 2005. – Vol. 12. – P. 092702.

2. Ramazanov T.S., Dzhumagulova K.N., Omarbakiyeva Yu.A., Ropke G. Effective polarization potential and scattering processes in a partially ionized plasma // Contrib. Plasma Phys. – 2007. – Vol. 47. – P. 267.

3. Dzhumagulova K.N., Shalenov E.O. and Ramazanov T.S. Elastic scattering of low energy electrons in partially ionized dense semiclassical plasma // Phys. Plasmas. – 2015. – Vol. 22. – P. 082120.

4. Kim C.-G.and Jung Y.-D. Quantum dynamic screening effects on the elastic collisions in strongly coupled semiclassical plasmas // Phys. Plasmas. – 2012. – Vol. 19. – P. 014502.

5. Dzhumagulova K.N., Gabdullina G.L. and Shalenov E.O. Dynamic interaction potential and the scattering cross sections of the semiclassical

plasma particles // Physics of Plasmas – 2013. – Vol. 20. – 042702.

6. Dzhumagulova K.N., Shalenov E.O., Ramazanov T.S. and Gabdullina G.L. Phase shifts and scattering cross sections of the particles of nonideal semiclassical plasmas based on the dynamic interaction potential // Contrib. Plasma Phys. –2015. – Vol. 55. – P. 230.

7. Kremp D., Schlanges M. and Kraeft W.-D.. Quantum Statistics of Nonideal Plasmas. – Berlin: Springer, 2005. – P. 497.

8. Landau L.D. and Lipschitz E.M. Quantum mechanics (nonrelativistic theory). – Moscow: Nauka, 1989. – P. 768.

9. Drukarev G.F. The Theory of Electron-Atom Collisions, Translated from the Russian edition (1962) by S. Chomet, Hasted J.B., Translation Ed. Academic Press, New York, (1965)

10. Babikov V.V.. The Method of Phase Functions in Quantum Mechanics. – Moscow: Nauka, 1988. – P. 224. (in Russian)

11. Ramazanov T.S., Dzhumagulova K.N. and Akbarov A.Zh. Cross sections and transport coefficients of dense partially ionized semiclassical plasma // J. Phys. A: Math. Gen. – 2006. – Vol. 39. – P. 4335–4340.

12. Ramazanov T.S., Dzhumagulova K.N., Gabdullin M.T. and Akbarov A.Zh. A scattering cross-section and ionization equilibrium of a dense metal plasma // J. Phys. A: Math. Theor. – 2009. – Vol. 42. – P. 214049.

13. Golden D.E., Bandel H.W. Absolute total electron-helium-atom scattering cross sections for low electron energies // Phys. Rev. – 1965. – Vol. 138. – P. 14.

14. Cromton R.W., Elford M.T., Jory R.L. The Momentum Transfer Cross Section for Electrons in Helium // Australian J.Phys. – 1967. – Vol. 20. – P. 369.

15. Ramsauer C. Der Zeemaneffekt im Palladiumspektrum // Ann.Physik – 1921. – Vol. 66. – P. 546.

16. Salop A., Nakano H.H. Total Electron Scattering Cross Sections in O2 and Ne // Phys. Rev. A – 1970. – Vol. 2. – P. 127.

UDC 533.9.004.14; 621.039.6

[1*]Zhukeshov A.M., [1]Ibraev B.M., [2]Giniyatova Sh.G.,
[3]Useinov B.M., [4]Nikulin V.Ya., [1]Gabdullina A.T., [1]Amrenova A.U.

[1]IETP, al-Farabi Kazakh National University, Almaty, Kazakhstan
[2]Faculty of Physics and Technology, L.N.Gumilyov Eurasian National University, Astana, Kazakhstan
[3]North Kazakhstan State University named M. Kozybaev, Petropavlovsk, Kazakhstan
[4]Lebedev Physics Institute, Moscow, Russia
[*]e-mail: zhukeshov@physics.kz

Parameters calculation and design of vacuum camera for «Plasma focus» facility

Abstrac: Evaluation of discharge current magnitude and circuit discharge dynamics was performed on the basis of electrodynamic model for designed «Plasma focus» facility. This work investigates dependence of plasma focus current, plasma conductivity and electrons temperature on electrical engineering parameters of reactor (voltage, capacity and size of electrode system). Using obtained data, calculation of electrode system geometry was carried out. Vacuum camera for experimental research is descripted. Vacuum system of the pilot reactor uses fore vacuum unit and sensor system based on thermocouple and magnetic discharge manometers by Agilent technology. Promising ways to study the plasma focus were showed to solve applied physical problems.
Key words: plasma, vacuum camera, plasma focus, electrodynamic, electrode.

Introduction

So far, attempts of scientists to solve the problem of thermonuclear fusion are generally related to magnetic systems. Tokamaks (ITER project), laser inertial fusion, traps, etc. are exploered for this purpose. All those methods are being developed for tens of years, thousands of scientific papers were published, but no acting reactor is constructed yet.

First of all, it is caused by serious technical difficulties, but there are also fundamental reasons.

One of them is inability to take into consideration coordinated of all individual plasma particles [1] even at low concentration of particle in. In such situation alternative approach to solve this problem is study plasma self-organization taking into account collective. Matters of plasma self-organization in various plasma facilities are just beginning to be examined. For the first time, strata-type structuring of plasma was observed during Z-pinch experiments [2]. Structuring in plasma accelerators was also detected [3, 4].

In high-temperature dense plasma, self-organized structures shapes as filaments, alternating bands and other organized objects [5]. Obviously, presence of such objects indicates fundamental structuring property of dense hot plasma. In that case, they will play a decisive role in the work of fusion facilities.

Another approach for fusion facilities design is the method based on generation of plasma in apparatuses of plasma-focus type. On the basis of dynamic structures research in various plasma focus facilities, the authors of the project study the matter of design for new-type reactors based on focusing of plasma beams in small area with high density. The idea is that since the system is centrally symmetric this allow to compress plasma to the high dense due to contribution of strong magnetic field of parallel discharge currents and its geometry. For this purpose, shapes of both cathode and anode should be chosen in the way which provides plasma focus in localized area above anode. Magnetic fields focus plasma filaments into bunch which diameter has the size of several millimeters. When the bunch becomes dense enough, the temperature is the order of 100 million degrees that is sufficient for beginning of fusion. Formed in the focus area, the plasma bunch is self-organized structure and conditions of its formation should be thoroughly examined.

Experimental device and measured methods

Pilot fusion reactor «Plasma focus», developed by us, includes plasma focus chamber, capacitive energy storage, high-voltage discharger and current supplies. As capacitive energy storage, we use capacitor bank of 24 capacitors IK-50 with voltage of 30 kV and total capacity of 72 *mk*F as well as capacitor bank of 4 capacitors IK-50 with voltage of 5 kV and total capacity of 600 *mk*F.

We use two types of central electrode-cathode for plasma focus – in the first case, cylinder with diameter of 3 cm, wall thickness of 3 mm and length of 10 cm; in the second case, it presents solid round of the same sizes. External electrode – 6 cylinders circularly at distance of 2 – 3 cm from the center.

Let's briefly consider the theory of the process. During discharge of capacitor bank, current flows through the gas wherein current's plasma sheath is produced passing through the gas toward internal electrode (cathode). Current flows create strong magnetic field. The magnetic field pushes current's plasma sheath along chamber electrodes and presses the current sheath toward the system axis until plasma focus is produced. All stages and parameters of the process (formation of current sheath and magnetic field, processes of current sheath compression, formation of shock wave and plasma focus) depend on electrical engineering parameters [5].

This work investigates dependence of plasma focus current, plasma conductivity and electrons temperature on electrical engineering parameters of reactor (voltage, capacity and size of electrode system). From experimental data analysis, it is found that at given voltage, maximum value of plasma focus current depends on plasma pressure. In the beginning, with pressure increasing (3–6) torr, the current increases almost linearly, reaches its maximum value at the pressure of 6 torr. and then drops down. Increase of current with respect to pressure is caused by the fact that the time of plasma sheath motion is less than quarter period of capacitor bank discharge. Asymmetric breakdown leads to pressure increase. As a result plasma sheath compresses into cord with large inductance, and value of current decreases. From literature data analysis it could be concluded that plasma focus current depends on capacitor bank voltage. Besides, with voltage increasing, the current increases almost linearly that allows us to introduce the value $Y = \frac{dL}{dt}$ as a proportionality factor.

Thus, from the expression $I = \frac{1}{Y}U$, one can conclude that maximal current is determined by capacitor bank voltage and magnitude of circuit inductance change per time. The magnitude is determined by size of electrodes: anode and cathode, along with longitudinal velocity $\frac{dz}{dt}$ of current's sheath. To obtain the highest values for plasma focus current, we need optimum correlation between sizes of anode and cathode and magnitude of longitudinal velocity. With increase of longitudinal velocity of current's plasma sheath, the magnitude of $\frac{dL}{dt}$ initially increases almost linearly, then hits zero value and grows further. Optimum range for velocity values at our facility is velocity value of current's sheath $(4–5)\cdot 10^3$ m/s (more precise data will be obtained by probes). Maximal calculated value of plasma focus current is 3.03 MA at capacitor bank voltage of 30 kV, pressure p = (4–6) torr and current's plasma sheath velocity $\frac{dz}{dt} = 0.417 \cdot 10^4$ m/s; and the minimal one is 2.53 MA at voltage of 25 kV.

Conductivity calculation. Conductivity of plasma depends on electrical engineering parameters: capacitor bank voltage, current, sizes of anode and cathode and discharge time of capacitor bank. If magnitude of inductance change $\frac{dL}{dt}$ is considered constant during discharge (5 mks), conductivity of plasma can be considered constant. The conductivity was calculated using well-known formula where plasma pulse time only changes at specified values of voltage. Calculation showed $9.2 \cdot 10^3$ $\mathrm{Om^{-1}m^{-1}}$ for conductivity value.

Temperature calculation. The temperature was calculated under two conditions: in the first case, the temperature was calculated under condition that ionization degree is approximately equals 50% corresponding to current's plasma sheath_formation time. Herewith, electrical conductivity of plasma is only determined by temperature of electrons. Temperature of electrons was determined using Spitzer formula. Calculation showed that order of

magnitude of plasma temperature is 10 eV. In the second case, the temperature was evaluated under condition of constant velocity of radial compression during formation of plasma focus from equality of gas-kinetic and magnetic pressure. Temperature calculation showed 63.7 eV for its maximum value at current of 3.03 MA. The minimum value is 45.2 eV at current of 2.53 MA, wherein concentration of electrons is $n_e = 10^{13}\,\mathrm{m}^{-3}$.

Thus, temperature of plasma will increase by about 6 times in the period from formation of current's plasma sheath till creation of plasma focus.

Calculation for magnetic field intensity. Value of magnetic field intensity that appears during formation of CPS can be evaluated from equality of gas-kinetic and magnetic pressure. Calculations show $H = 1.6 \cdot 10^2$ A/m. As plasma sheath moves, its radius reduces to cord size resulting the sharp increase of magnetic field intensity. For precise calculation of magnetic field intensity, we should measure the magnitude of current's plasma sheath radial compression. Thickness of skin layer makes 1.2 cm.

Energy calculation. Energy saved in capacitor bank provides ohmic heating, magnetic energy, work of ponderomotive forces and motion kinetic energy of particles. Energy of $2 \cdot 10^3$ J providing heating of plasma is determined by ohmic losses and it is insignificant. Magnetic energy value is about 80 kJ.

Calculations for the facility using capacitor bank IM-150 with maximum voltage of 5 kV and capacity of 150 *mk*F per battery showed 300 kA for maximum current and order of 1 eV for plasma focus temperature.

Dependence of discharge current on battery capacity when using capacitors IK-50 is shown in Figure 1.

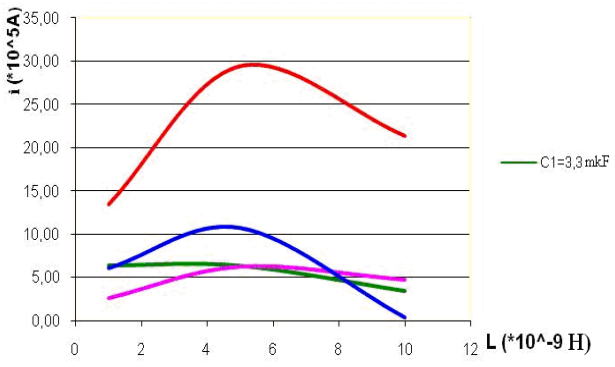

Figure 1 – Discharge curves of current for IK-type capacitors

Figure 2 presents similar diagrams for dependence of discharge current on battery capacity when using capacitors IM-150. As it is seen, maximum value of current can be obtained when system inductance is about 6 nH regardless of capacitor type. Wherein, maximum discharge current differs essentially: being 3MA for IK-50 capacitors, it results 300 kA for IM-150 capacitors and actually allmost does not depend on capacity value.

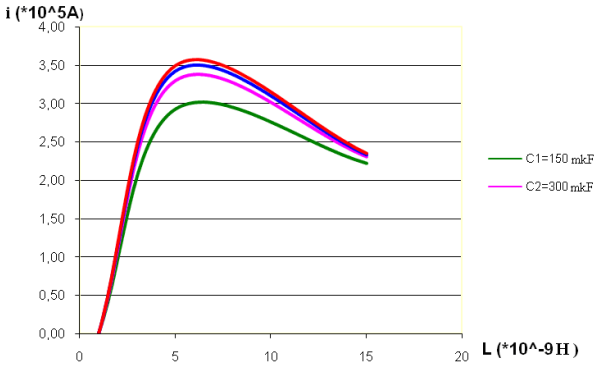

Figure 2 – Discharge curves of current for IM-type capacitors

Conclusions

«Plasma Focus» facility supposes use of high vacuum and presence of high-vacuum flanges with large diameter. Here, discharge currents can hit hundreds of kiloamperes therefore major requirement is sufficient thickness of chamber walls. Observation glass and diagnostic jacks should be also provided.

The designed facility supposes use of high vacuum and presence of high-vacuum flanges with large diameter. Here, discharge currents can hit hundreds of kiloamperes therefore major requirement is sufficient thickness of chamber walls. Observation glass and diagnostic jacks should be also provided.

Due to complication in design of such chamber in vitro, ready chamber of TMN-500 turbo molecular pump was used. Presence of two flanges by 18 cm and one flange by 30 cm in the facility allows total implementation of experiment conditions. The chamber wall thickness makes over 1 cm and ultimate vacuum is the order of 10^{-9} torr

Vacuum system of the pilot reactor uses fore vacuum unit and sensor system based on thermocouple and magnetic discharge manometers by Agilent technology. Vacuum control is managed

via digital controller 600 of the above trademark. Vacuum improving work and chamber vacuum test are in progress.

Acknowledgment

This work was supported by the Ministry of Education and Science of KR, grant №3207 GF4.

References

1. Smirnov V.P. Issledovanija po termojadernomu sintezu // Vestnik RAN. – 1974. – T. 73. – S. 6-14.

2. Kvarchava I.F., Kervalidze K.H., Gvaladze Ju.S., Zukakishvili G.G. Prostranstvenno-periodicheskie struktury plazmy, voznikajushhie v bystryh sil'notochnyh razrjadah // Jadernyj sintez. – 1965. – T.5. – № 5. – S.181-191.

3. Francis Y.C., Elkridge R., Smith J., Martin A., Cassibry J., Wu S.T. A Plasma Accelerator Concept for Application to Magnetized Target Fusion // Z-Pinches Conference. – Florence: Alabama university press. – 2006. – P. 456-467.

4. Voronin A.V., Aleksandrov S.E., Ajushin B.B. Snabzhenie toplivom central'noj zony Globus-M s pomoshh'ju plazmennoj pushki // Materialy dokladov 36-oj mezhdunarodnoj konferencii po fizike plazmy i UTS. – Zvenigorod, 2009. – S. 75-78

5. Burcev V.A., Gribkov V.A., Filippova T.I. Vysokotemperaturnye pinchevye obrazovanija. // Itogi nauki i tehniki. Ser. Fizika plazmy. – 1981. – T. 2. – S. 226.

UDC 539.17

*Burkova N.A., Tkachenko A.S.

Faculty of physics and technology, al-Farabi Kazakh National University,
Almaty, Kazakhstan
*e-mail: natali.burkova@gmail.com

Algebraic basics for high spin elastic scattering

Abstract. The analytics was implemented for the scattering processes with channel spin structure 1/2, 3/2 and 5/2. For the first time the parameterization of differential cross sections by orbital momentums $\ell = 0$, 1, 2, … for the quartet and quintet spin channels has been performed. The presentation is given in a universe form and may be applied for the phase shift analyses for the scattering of nuclei or elementary particles. Same amplitudes are used in the construction of the polarization characteristics as vector and tensor polarization. The following isotopes are in field of interests: $^{7}B(3/2^{-})$, $^{9}B(3/2^{-})$, $^{11}B(3/2^{-})$, $^{12}B(1^{+})$, $^{13}B(3/2^{-})$, $^{5}Li(3/2^{-})$, $^{6}Li(1^{+})$, $^{7}Li(3/2^{-})$, $^{9}Li(3/2^{-})$, $^{10}Li(1^{-})$, $^{9}C(3/2^{-})$, $^{11}C(3/2^{-})$ and protons, neutrons, deuterons as impact particles.

Key words: elastic scattering, spin channel, probability amplitude, cross section, partial wave.

Introduction

Of particular interest to the two-particle photodisintegration and radiative capture reactions $A + \gamma \rightleftarrows a + b$ is due to the fact that these processes are directly related to the most advanced research in nuclear astrophysics (thermodynamics of the Universe [1], nucleosynthesis of chemical elements in the Sun and stars, the Big Bang theory [2]), as well as the physics of nuclear reactors and nuclear fusion.

Currently, with implementation of the novel method of inverse Compton scattering (ICPB) for the generating a quasi-monochromatic beams of photons experimental capabilities have reached a new level and is continuously expanding.

It should also be noted, that in $A + \gamma \rightleftarrows a + b$ reactions both the discrete spectrum and continuous spectrum are involved. Thus, for the sequential description of $a + b$ scattering channel necessary to have the interaction potential. The parameters for such phenomenological potentials might be reconstructed as fitting the data on the cross sections of elastic scattering.

By now the scattering theory of both classical and quantum, is one of the most developed fields of theoretical physics. Mathematical formalism for the non-relativistic collision theory has been developed well and is represented in numerous original papers and reviews [3-8], university textbooks [9-10] and monographs [11-12].

However, for the practical application of this theory there are real difficulties connected with the fact that characteristics such as, for example, the *density matrix* and *scattering matrix* contain a defined set of some parameters, the number of which greatly increases when account is taken of the spin structure of the particles involved in the processes. In this context, the relevance of a particular task on the construction of the scattering matrix and the calculation of its elements is associated with the minimization of the number of parameters used. This requires an analysis of all the known symmetry properties of the system under study

Parameterization of differential cross sections

For practical calculations of the differential cross sections of scattering processes in a wide range of energies the elastic channels is enough to take into account, that is, with good accuracy, to consider only the spin-orbit potential V_{ls}, neglecting the spin-spin interaction. In this case, the matrix M is written explicitly:

$$M_{sv v'}(\theta) = \sqrt{\pi} k^{-1} [-C(\theta)\delta_{v v'} + i\sum_{J\ell} (2\ell+1)^{1/2} C^{Jv}_{sv\ell 0} C^{Jv}_{sv'\ell m} \cdot \exp(2i\sigma_{\ell})(1 - U^{J^{\pi}}_{s\ell}) Y^{m}_{\ell}(\theta, 0)], \quad (1)$$

 Printed in Kazakhstan

where S –spin channel, ν and ν' – corresponding spin projections on Z axis, $C(\theta)$ – Coulomb scattering amplitude, ℓ and ℓ' – orbital quantum numbers in initial and final channels, $C^{jm}_{j_1 m_1 j_2 m_2}$ – Clebsh-Gordan coefficients [13], σ_ℓ – coulomb phase shifts, $U^{J^\pi}_{s'\ell' s\ell}$ – scattering matrix, $Y^{m'}_{\ell'}(\theta,0)$ – angular functions. Note that with increasing values of the spin channel increases its contribution to the total differential cross section.

Here we oriented on the future research of the elastic scattering processes of particles with spin numbers 1 and 3/2. As a participants the following isotopes are in field of interests: $^7\mathrm{B}(3/2^-)$, $^9\mathrm{B}(3/2^-)$, $^{11}\mathrm{B}(3/2^-)$, $^{12}\mathrm{B}(1^+)$, $^{13}\mathrm{B}(3/2^-)$, $^5\mathrm{Li}(3/2^-)$, $^6\mathrm{Li}(1^+)$, $^7\mathrm{Li}(3/2^-)$, $^9\mathrm{Li}(3/2^-)$, $^{10}\mathrm{Li}(1^-)$, $^9\mathrm{C}(3/2^-)$, $^{11}\mathrm{C}(3/2^-)$, $d(1^+)$, as well as some elementary particles, for example, tau-lepton τ (1).

The differential cross section for elastic scattering of two particles system with spin structure 1 + 3/2 accounting spin-orbit splitting is:

$$\frac{d\sigma(\theta)}{d\Omega} = \frac{1}{6}\frac{d\sigma_{1/2}}{d\Omega} + \frac{1}{3}\frac{d\sigma_{3/2}}{d\Omega} + \frac{1}{2}\frac{d\sigma_{5/2}}{d\Omega}, \qquad (2)$$

where the indices and related to the *doublet*, *quartet* and *quintet* scattering states corresponding to the total spin channel $S = 1/2$, $S = 3/2$ and $S = 5/2$. For the partial cross sections 28 amplitudes have been analytically calculated.

Partial cross sections in (2) is the combination of amplitudes *X=A, B, C…*, defined as a following

$$X = f_c\delta_{\nu\nu'} + \frac{1}{2ik}\sum_{\ell=m} X_j\, e^{2i\sigma_\ell} P_\ell{}^m(\cos\theta). \qquad (3)$$

Angular functions $Y^m_\ell(\theta,0)$ are converted to the Legendre polynomials $P_\ell{}^m(\cos\theta)$ [13], $m = \nu - \nu'$. Within the selection rules X_j is the sum of all possible amplitudes α^j with appropriate algebraic coefficients C_j given in Tables 1-3:

$$X_j = \sum_j \alpha^j C_j, \qquad (4)$$

$$\alpha^j = 1 - U^{J^\pi}_{s\ell}. \qquad (5)$$

Coulomb scattering amplitude is rewritten in the following form

$$f_c(\theta) = -\left(\frac{\gamma}{2k\sin^2(\theta/2)}\right)\exp\left(i\gamma\ln\left[\sin^{-2}(\theta/2)\right] + 2i\sigma_0\right), \qquad (6)$$

where γ – Coulomb parameter; k – the wave number of the relative particle motion, $k^2 = 2\mu E/\hbar^2$. Coulomb parameter is represented as:

$$\gamma = \frac{\mu Z_1 Z_2 e^2}{k\hbar^2}, \qquad (7)$$

where Z – particle charges in units e, μ – reduced mass E – energy of scattering particles in center mass.

The differential cross section of elastic scattering in the doublet state ($S = 1/2$) is well known [3, 9, 10]:

$$\frac{d\sigma_{1/2}}{d\Omega} = \left(\left|A_{1/2}\right|^2 + \left|B_{1/2}\right|^2\right). \qquad (8)$$

The corresponding coefficients are given in Table 1. There and after values m complete the construction of (3). Thus $m = 0$ for amplitude A and $m = 1$ for B in (8).

Table 1 – doublet spin channel C_j coefficients

X	j	
	$\ell+1/2$	$\ell-1/2$
$A_{1/2}$	$\ell+1$	ℓ
$B_{1/2}$	$-\sqrt{\ell(\ell+1)}$	$\sqrt{\ell(\ell+1)}$

The differential cross section of elastic scattering in the quartet state ($S=3/2$) is:

$$\frac{d\sigma_{3/2}}{d\Omega}=\frac{1}{2}\left(\left|A_{3/2}\right|^2+\left|B_{3/2}\right|^2+\left|C_{3/2}\right|^2+\left|D_{3/2}\right|^2+\left|E_{3/2}\right|^2+\left|F_{3/2}\right|^2+\left|G_{3/2}\right|^2+\left|H_{3/2}\right|^2\right). \quad (9)$$

Here amplitudes are calculated by formula (3) using Table 2 and complementary information: $m=0$ for amplitudes *A* and *B*; $m=1$ for *C, D and E*; $m=2$ for *F* and *G*; $m=3$ for *H*.

Table 2 – quartet spin channel C_j coefficients

X	j			
	$\ell+3/2$	$\ell+1/2$	$\ell-1/2$	$\ell-3/2$
$A_{3/2}$	$\frac{6(\ell+1)(\ell+2)}{2\ell+3}$	$\frac{2\ell(\ell+1)}{2\ell+3}$	$\frac{2\ell(\ell+1)}{2\ell-1}$	$\frac{6\ell(\ell-1)}{2\ell-1}$
$B_{3/2}$	$\frac{2(\ell+2)(\ell+3)}{2\ell+3}$	$\frac{6(\ell+1)(\ell+2)}{2\ell+3}$	$\frac{6\ell(\ell-1)}{2\ell-1}$	$\frac{2(\ell-1)(\ell-2)}{2\ell-1}$
$C_{3/2}$	$-\frac{6(\ell+2)}{2\ell+3}$	$\frac{2(\ell+3)}{2\ell+3}$	$-\frac{2(\ell-2)}{2\ell-1}$	$\frac{6(\ell-1)}{2\ell-1}$
$D_{3/2}$	$-\frac{2\sqrt{3}(\ell+2)}{2\ell+3}$	$-\frac{2\sqrt{3}(\ell+1)}{2\ell+3}$	$\frac{2\sqrt{3}\ell}{2\ell-1}$	$\frac{2\sqrt{3}(\ell-1)}{2\ell-1}$
$E_{3/2}$	$-\frac{2\sqrt{3}(\ell+2)(\ell+3)}{(\ell+1)(2\ell+3)}$	$-\frac{2\sqrt{3}(\ell+2)(\ell-3)}{\ell(2\ell+3)}$	$\frac{2\sqrt{3}(\ell+4)(\ell-1)}{(\ell+1)(2\ell-1)}$	$\frac{2\sqrt{3}(\ell-1)(\ell-2)}{\ell(2\ell-1)}$
$F_{3/2}$	$\frac{2\sqrt{3}}{2\ell+3}$	$-\frac{2\sqrt{3}}{2\ell+3}$	$-\frac{2\sqrt{3}}{2\ell-1}$	$\frac{2\sqrt{3}}{2\ell-1}$
$G_{3/2}$	$\frac{2\sqrt{3}(\ell+3)}{(\ell+1)(2\ell+3)}$	$-\frac{2\sqrt{3}(\ell+6)}{\ell(2\ell+3)}$	$-\frac{2\sqrt{3}(\ell-5)}{(\ell+1)(2\ell-1)}$	$\frac{2\sqrt{3}(\ell-2)}{\ell(2\ell-1)}$
$H_{3/2}$	$-\frac{2}{(\ell+1)(2\ell+3)}$	$\frac{6}{\ell(2\ell+3)}$	$-\frac{6}{(\ell+1)(2\ell-1)}$	$\frac{2}{\ell(2\ell-1)}$

A similar way, using the Table 3 can be calculated the amplitudes for the *quintet* spin channel $S=5/2$. The partial cross-section of the channel is a combination of 18 independent amplitudes.

$$\frac{d\sigma_{5/2}}{d\Omega}=\frac{1}{2}\left(\left|A_{5/2}\right|^2+\left|B_{5/2}\right|^2+\left|C_{5/2}\right|^2+\left|D_{5/2}\right|^2+\left|E_{5/2}\right|^2+\left|F_{5/2}\right|^2+\left|G_{5/2}\right|^2+\left|H_{5/2}\right|^2+\left|I_{5/2}\right|^2+\right.$$
$$\left.+\left|J_{5/2}\right|^2+\left|K_{5/2}\right|^2+\left|L_{5/2}\right|^2+\left|M_{5/2}\right|^2+\left|N_{5/2}\right|^2+\left|O_{5/2}\right|^2+\left|P_{5/2}\right|^2+\left|Q_{5/2}\right|^2+\left|R_{5/2}\right|^2\right) \quad (10)$$

Table 3 – quintet spin channel C_j coefficients

X	j		
	$\ell+5/2$	$\ell+3/2$	$\ell+1/2$
$A_{5/2}$	$\frac{10(\ell+1)(\ell+2)(\ell+3)}{(2\ell+3)(2\ell+5)}$	$\frac{2(\ell+1)(\ell+2)}{(2\ell+3)(2\ell+5)}$	$\frac{4\ell(\ell+1)(\ell+2)}{(2\ell+3)(2\ell-1)}$
$B_{5/2}$	$\frac{20(\ell+1)(\ell+3)(\ell+4)}{(2\ell+3)(2\ell+5)}$	$\frac{36\ell(\ell+2)(\ell+3)}{(2\ell+3)(2\ell+5)}$	$\frac{8(\ell+1)(\ell-3)^2}{(2\ell+3)(2\ell-1)}$
$C_{5/2}$	$\frac{4(\ell+3)(\ell+4)(\ell+5)}{(2\ell+3)(2\ell+5)}$	$\frac{20(\ell+2)(\ell+3)(\ell+4)}{(2\ell+3)(2\ell+5)}$	$\frac{40(\ell+3)(\ell+1)(\ell-1)}{(2\ell+3)(2\ell-1)}$
$D_{5/2}$	$-\frac{10(\ell+2)(\ell+3)}{(2\ell+3)(2\ell+5)}$	$\frac{2(\ell+2)(\ell+5)}{(\ell+3)(2\ell+5)}$	$-\frac{4(\ell+2)(\ell-2)}{(2\ell+3)(2\ell-1)}$
$E_{5/2}$	$-\frac{20\sqrt{2}(\ell+2)(\ell+3)}{(2\ell+3)(2\ell+5)}$	$-\frac{4\sqrt{2}(\ell+2)(3\ell+5)}{(2\ell+3)(2\ell+5)}$	$\frac{8\sqrt{2}(\ell+1)(\ell+2)}{(2\ell+3)(2\ell-1)}$
$F_{5/2}$	$-\frac{20\sqrt{2}(\ell+3)(\ell+4)}{(2\ell+3)(2\ell+5)}$	$-\frac{12\sqrt{2}(\ell+2)(\ell+3)(\ell-5)}{(\ell+1)(2\ell+3)(2\ell+5)}$	$\frac{8\sqrt{2}(\ell^2+4\ell-6)(\ell-3)}{\ell(2\ell+3)(2\ell-1)}$
$G_{5/2}$	$-\frac{4\sqrt{5}(\ell+3)(\ell+4)}{(2\ell+3)(2\ell+5)}$	$-\frac{12\sqrt{5}(\ell+2)(\ell+3)}{(2\ell+3)(2\ell+5)}$	$-\frac{8\sqrt{5}(\ell+1)(\ell-3)}{(2\ell+3)(2\ell-1)}$
$H_{5/2}$	$-\frac{4\sqrt{5}(\ell+3)(\ell+4)(\ell+5)}{(\ell+1)(2\ell+3)(2\ell+5)}$	$-\frac{4\sqrt{5}(\ell+2)(\ell+3)(\ell+4)(3\ell-5)}{\ell(\ell+1)(2\ell+3)(2\ell+5)}$	$-\frac{8\sqrt{5}(\ell+3)(\ell-1)(\ell-8)}{\ell(2\ell+3)(2\ell-1)}$
$I_{5/2}$	$\frac{20\sqrt{2}(\ell+3)}{(2\ell+3)(2\ell+5)}$	$-\frac{4\sqrt{2}(3\ell+10)}{(2\ell+3)(2\ell+5)}$	$-\frac{8\sqrt{2}(\ell+7)}{(2\ell+3)(2\ell-1)}$
$J_{5/2}$	$\frac{4\sqrt{10}(\ell+3)}{(2\ell+3)(2\ell+5)}$	$\frac{4\sqrt{10}(\ell+2)}{(2\ell+3)(2\ell+5)}$	$-\frac{8\sqrt{10}(\ell+1)}{(2\ell+3)(2\ell-1)}$
$K_{5/2}$	$\frac{20\sqrt{2}(\ell+3)(\ell+4)}{(\ell+2)(2\ell+3)(2\ell+5)}$	$-\frac{12\sqrt{2}(\ell+3)(\ell+10)}{(\ell+1)(2\ell+3)(2\ell+5)}$	$-\frac{8\sqrt{2}(\ell-3)\ (\ell^2-2\ell-18)}{\ell(\ell+2)(2\ell+3)(2\ell-1)}$
$L_{5/2}$	$\frac{4\sqrt{10}(\ell+3)(\ell+4)(\ell+5)}{(\ell+1)(\ell+2)(2\ell+3)(2\ell+5)}$	$\frac{4\sqrt{10}(\ell+3)(\ell+4)(\ell-10)}{\ell(\ell+1)(2\ell+3)(2\ell+5)}$	$-\frac{8\sqrt{10}(\ell+3)\ (\ell^2+6\ell-22)}{\ell(\ell+2)(2\ell+3)(2\ell-1)}$
$M_{5/2}$	$-\frac{4\sqrt{10}}{(2\ell+3)(2\ell+5)}$	$\frac{4\sqrt{10}}{(2\ell+3)(2\ell+5)}$	$\frac{8\sqrt{10}}{(2\ell+3)(2\ell-1)}$
$N_{5/2}$	$-\frac{20(\ell+4)}{(\ell+2)(2\ell+3)(2\ell+5)}$	$\frac{36(\ell+5)}{(\ell+1)(2\ell+3)(2\ell+5)}$	$-\frac{8(\ell+12)(\ell-3)}{\ell(\ell+2)(2\ell+3)(2\ell-1)}$
$O_{5/2}$	$-\frac{4\sqrt{10}(\ell+4)(\ell+5)}{(\ell+1)(\ell+2)(2\ell+3)(2\ell+5)}$	$\frac{4\sqrt{10}(\ell+15)(\ell+4)}{\ell(\ell+1)(2\ell+3)(2\ell+5)}$	$\frac{8\sqrt{10}(\ell^2-4\ell-42)}{\ell(\ell+2)(2\ell+3)(2\ell-1)}$
$P_{5/2}$	$\frac{20}{(\ell+2)(2\ell+3)(2\ell+5)}$	$-\frac{60}{(\ell+1)(2\ell+3)(2\ell+5)}$	$\frac{40(\ell-3)}{\ell(\ell+2)(2\ell+3)(2\ell-1)}$
$Q_{5/2}$	$\frac{20(\ell+5)}{(\ell+1)(\ell+2)(2\ell+3)(2\ell+5)}$	$-\frac{20(3\ell+20)}{\ell(\ell+1)(2\ell+3)(2\ell+5)}$	$\frac{40(\ell+17)}{\ell(\ell+2)(2\ell+3)(2\ell-1)}$

$R_{5/2}$	$-\sqrt{\frac{(\ell-5)!}{(\ell+5)!}}$	$20\sqrt{\frac{(\ell-5)!}{(\ell+5)!}}$	$-10\sqrt{\frac{(\ell-5)!}{(\ell+5)!}}$
X	j		
	$\ell-1/2$	$\ell-3/2$	$\ell-5/2$
$A_{5/2}$	$\frac{4\ell(\ell+1)(\ell-1)}{(2\ell+3)(2\ell-1)}$	$\frac{2\ell(\ell+1)(\ell-1)}{(2\ell-1)(2\ell-3)}$	$\frac{10\ell(\ell-1)(\ell-2)}{(2\ell-1)(2\ell-3)}$
$B_{5/2}$	$\frac{8\ell(\ell+4)^2}{(2\ell+3)(2\ell-1)}$	$\frac{36(\ell+1)(\ell-1)(\ell-2)}{(2\ell-1)(2\ell-3)}$	$\frac{20\ell(\ell-2)(\ell-3)}{(2\ell-1)(2\ell-3)}$
$C_{5/2}$	$\frac{40\ell(\ell+2)(\ell-2)}{(2\ell+3)(2\ell-1)}$	$\frac{20(\ell-1)(\ell-2)(\ell-3)}{(2\ell-1)(2\ell-3)}$	$\frac{4(\ell-2)(\ell-3)(\ell-4)}{(2\ell-1)(2\ell-3)}$
$D_{5/2}$	$\frac{4(\ell+3)(\ell-1)}{(2\ell+3)(2\ell-1)}$	$-\frac{2(\ell-1)(\ell-4)}{(2\ell-1)(2\ell-3)}$	$\frac{10(\ell-1)(\ell-2)}{(2\ell-1)(2\ell-3)}$
$E_{5/2}$	$-\frac{8\sqrt{2}\ell(\ell-1)}{(2\ell+3)(2\ell-1)}$	$\frac{4\sqrt{2}(\ell-1)(3\ell-2)}{(2\ell-1)(2\ell-3)}$	$\frac{20\sqrt{2}(\ell-1)(\ell-2)}{(2\ell-1)(2\ell-3)}$
$F_{5/2}$	$-\frac{8\sqrt{2}(\ell+4)(\ell^2-2\ell-9)}{(\ell+1)(2\ell+3)(2\ell-1)}$	$\frac{12\sqrt{2}(\ell+6)(\ell-1)(\ell-2)}{\ell(2\ell-1)(2\ell-3)}$	$\frac{20\sqrt{2}(\ell-2)(\ell-3)}{(2\ell-1)(2\ell-3)}$
$G_{5/2}$	$\frac{8\sqrt{5}\ell(\ell+4)}{(2\ell+3)(2\ell-1)}$	$\frac{12\sqrt{5}(\ell-1)(\ell-2)}{(2\ell-1)(2\ell-3)}$	$\frac{4\sqrt{5}(\ell-2)(\ell-3)}{(2\ell-1)(2\ell-3)}$
$H_{5/2}$	$\frac{8\sqrt{5}(\ell+9)(\ell+2)(\ell-2)}{(\ell+1)(2\ell+3)(2\ell-1)}$	$\frac{4\sqrt{5}(3\ell+8)(\ell-1)(\ell-2)(\ell-3)}{\ell(\ell+1)(2\ell-1)(2\ell-3)}$	$\frac{4\sqrt{5}(\ell-2)(\ell-3)(\ell-4)}{\ell(2\ell-1)(2\ell-3)}$
$I_{5/2}$	$-\frac{8\sqrt{2}(\ell-6)}{(2\ell+3)(2\ell-1)}$	$-\frac{4\sqrt{2}(3\ell-7)}{(2\ell-1)(2\ell-3)}$	$\frac{20\sqrt{2}(\ell-2)}{(2\ell-1)(2\ell-3)}$
$J_{5/2}$	$-\frac{8\sqrt{10}\ell}{(2\ell+3)(2\ell-1)}$	$\frac{4\sqrt{10}(\ell-1)}{(2\ell-1)(2\ell-3)}$	$\frac{4\sqrt{10}(\ell-2)}{(2\ell-1)(2\ell-3)}$
$K_{5/2}$	$-\frac{8\sqrt{2}(\ell+4)\ (\ell^2+4\ell-15)}{(\ell+1)(\ell-1)(2\ell+3)(2\ell-1)}$	$-\frac{12\sqrt{2}(\ell-2)(\ell-9)}{\ell(2\ell-1)(2\ell-3)}$	$\frac{20\sqrt{2}(\ell-2)(\ell-3)}{(\ell-1)(2\ell-1)(2\ell-3)}$
$L_{5/2}$	$-\frac{8\sqrt{10}(\ell-2)\ (\ell^2-4\ell-27)}{(\ell+1)(\ell-1)(2\ell+3)(2\ell-1)}$	$\frac{4\sqrt{10}(\ell-2)(\ell-3)(\ell+11)}{\ell(\ell+1)(2\ell-1)(2\ell-3)}$	$\frac{4\sqrt{10}(\ell-2)(\ell-3)(\ell-4)}{\ell(\ell-1)(2\ell-1)(2\ell-3)}$
$M_{5/2}$	$-\frac{8\sqrt{10}}{(2\ell+3)(2\ell-1)}$	$-\frac{4\sqrt{10}}{(2\ell-1)(2\ell-3)}$	$\frac{4\sqrt{10}}{(2\ell-1)(2\ell-3)}$
$N_{5/2}$	$\frac{8(\ell+4)(\ell-11)}{(\ell+1)(\ell-1)(2\ell+3)(2\ell-1)}$	$-\frac{36(\ell-4)}{\ell(2\ell-1)(2\ell-3)}$	$\frac{20(\ell-3)}{(\ell-1)(2\ell-1)(2\ell-3)}$
$O_{5/2}$	$-\frac{8\sqrt{10}(\ell^2+6\ell-37)}{(\ell+1)(\ell-1)(2\ell+3)(2\ell-1)}$	$-\frac{4\sqrt{10}(\ell-3)(\ell-14)}{\ell(\ell+1)(2\ell-1)(2\ell-3)}$	$\frac{4\sqrt{10}(\ell-3)(\ell-4)}{\ell(\ell-1)(2\ell-1)(2\ell-3)}$
$P_{5/2}$	$\frac{40(\ell+4)}{(\ell+1)(\ell-1)(2\ell+3)(2\ell-1)}$	$-\frac{60}{\ell(2\ell-1)(2\ell-3)}$	$\frac{20}{(\ell-1)(2\ell-1)(2\ell-3)}$
$Q_{5/2}$	$\frac{40(\ell-16)}{(\ell+1)(\ell-1)(2\ell+3)(2\ell-1)}$	$-\frac{20(3\ell-17)}{\ell(\ell+1)(2\ell-1)(2\ell-3)}$	$\frac{20(\ell-4)}{\ell(\ell-1)(2\ell-1)(2\ell-3)}$
$R_{5/2}$	$10\sqrt{\frac{(\ell-5)!}{(\ell+5)!}}$	$-5\sqrt{\frac{(\ell-5)!}{(\ell+5)!}}$	$\sqrt{\frac{(\ell-5)!}{(\ell+5)!}}$

Here $m=0$ for amplitudes *A, B* and *C*; $m=1$ for *D, E, F, G* and *H*; $m=2$ for *I, J, K* and *L*; $m=3$ for *M, N* and *O*; $m=4$ f or *P* и *Q*, $m=5$ for *R*.

Conclusion

Present work for the first time reported the formulas for the calculation of differential cross sections in scattering channels with spins 3/2 and 5/2 in addition to 1/2. The obtained representations are *universal* and can be used for a wide range of problems in nuclear and particle physics. Namely their different combinations depending on the spins of scattering particles cover cases $s_1+s_2=1+1/2,1+3/2,2+1/2$. Due to the fact that the orbital quantum number can take any value in (3), these formulas are applicable for the calculation of reactions proceeding at low and ultra - low astrophysical energies, as well as for the high-energy processes.

References

1 Ishhanov B.S., Kapitonov I.M., Judin N.P. Chasticy i atomnye jadra.– M.: Izdatel'stvo LKI. – 2007. – P. 584.

2 Kapitonov I.M., Ishhanov B.S., Tutyn' I.A. Nukleosintez vo Vselennoj. – M.: Librokom. – 2009. – P. 202.

3 Lane A.M., Thomas R.G. R–Matrix Theory of Nuclear Reactions // Reviews of Modern Physics. – 1958. – Vol. 30. – P. 257–353.

4 Ohlsen G.G. Polarization transfer and spin correlation experiments in nuclear physics // Rep. Prog. Phys. – 1972. – Vol 35. – P. 717–801.

5 Brown L., Stainer E., Arnold L.G. and Seyler R.G. Polarization and phase shifts in ^{7}Li(p,p)^{7}Li from 0.4 to 0.25 MeV and the structure of ^{8}Be // Nucl. Phys. – 1973. – Vol. A206. – P. 353–373.

6 Seyler R.G. Polarization from scattering polarized spin–1/2 on unpolarized spin–1 particles // Nucl. Phys. – 1969. – Vol. A124. – P. 253–272.

7 Nemec O.F., Jasnogorodskij A.M. Poljarizacionnye issledovanija v jadernoj fizike. – Kiev: Naukova Dumka. – 1980. – P. 347.

8 Kolybasov V.M. Obshhie svojstva matricy rassejanija i poljarizacionnye jeffekty v prjamyh reakcijah. – M.: MIFI. – 1971. – P. 129.

9 Davydov A.S. Teorija atomnogo jadra. – M.: Fizmatgiz. – 1958. – P. 612.

10 Sitenko A.G. Teorija jadernyh reakcij. – M: Jenergoatomizdat. – 1983. – P. 352.

11 Dubovichenko S.B. Svojstva legkih atomnyh jader v potencial'noj klasternoj modeli. – Almaty: Daneker. – 2004. – P. 247.

12 Dubovichenko S.B. Termojadernye processy Vselennoj. Tom 7. – Almaty: Izd. Astrofizicheskogo instituta im. V.G. Fesenkova "NCKIT" NKA RK. – 2011. – P. 402.

13 Varshalovich D.A., Moskalev A.N., Hersonskij V.K. Kvantovaja teorija uglovogo momenta. – L.: Nauka. – 1975. – P. 439.